INVESTIGATION OF THE ELECTRONIC STRUCTURE OF TRANSITION METAL COMPOUNDS BY PHOTOELECTRON SPECTROSCOPY WITH VARIABLE PHOTON ENERGY

by

Nikolas Kaltsoyannis

St. Catherine's College, Oxford

A thesis submitted to the Board of the Faculty of Physical Sciences for the Degree of Doctor of Philosophy at the University of Oxford

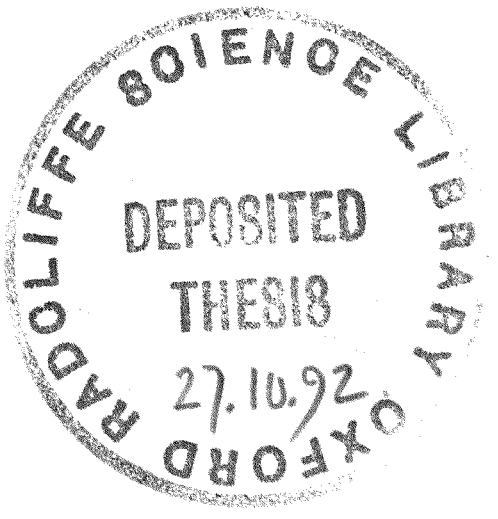

ABSTRACT

Investigation of the electronic structure of transition metal compounds by photoelectron spectroscopy with variable photon energy

by

Nikolas Kaltsoyannis, St. Catherine's College.

Submitted for the degree of Doctor of Philosophy, Trinity, 1992.

Relative partial photoionisation cross section (RPPICS) data have been obtained for a variety of transition metal compounds using synchrotron radiation in the incident photon energy range 17-115 eV. Cross section features such as p→d giant resonances, delayed maxima, Cooper minima and molecular shape resonances have been identified and interpreted in terms of the localisation properties of the ionising electrons.

The RPPICS behaviour of the photoelectron (PE) band corresponding to ionisation of the $1a_{1g}$ highest occupied molecular orbital (HOMO) of $[Mo(\eta\text{-}C_6H_5Me)_2]$ indicates that it is essentially metal-localised. The p→d giant resonant absorption enhancement of the cross section is found to be almost coincident in photon energy with a molecular shape resonance. Similar features in the $1e_{2g}^{-1}$ and $1e_{1g}^{-1}$ bands provide strong evidence for metal-ligand covalency in the associated MOs. In contrast, the monotonic fall off with increasing photon energy of the RPPICS of the $1e_{1u}^{-1}$ band is typical of ligand-localised MOs. Studies of the closely related $[M(\eta\text{-}C_7H_7)(\eta\text{-}C_5H_4R)]$ (M=Ti, Nb, Mo; R=H: M=Ta; R=Me) reveal a significant degree of both metal and ligand character to the $1e_2$ MOs, suggesting that neither the +1 nor the -3 formalism for the charge on the cycloheptatrienyl ring in its complexes is a good one, as they imply a metal- and ligand-localised $1e_2$ level respectively. Analysis of the occurrence and magnitude of shape resonances in all of these sandwich molecules suggests that they are governed chiefly by the amount of metal d orbital character in an MO.

The 5e MOs of PF_3, traditionally regarded as fluorine 2p lone pair MOs, have been shown to possess significant phosphorus 3p atomic orbital (AO) character. Comparison of the data obtained on PF_3 with those on $[Ni(PF_3)_4]$ indicates that the π back donation from the nickel 3d orbitals to the 7e lowest unoccupied MO of PF_3 also affects the composition of the 5e derived orbitals.

A combined experimental and theoretical study has resulted in an assignment of the PE spectrum of OsO_4 in which an osmium np AO (n=5 and/or 6) derived spin-orbit splitting of the lower ionisation energy (IE) $^2T_2$ primary ion state is found. RPPICS results obtained on $TiCl_4$, $TiBr_4$ and $ZrBr_4$ indicate that their PE spectra may be interpreted within a framework in which the primary ion state ordering is preserved on moving from chloride to bromide and from first to second row transition metal. Bromine-centred spin-orbit coupling produces the more complicated spectra of $TiBr_4$ and $ZrBr_4$. In all cases, the highest IE band shows RPPICS behaviour which indicates that it arises from the $2a_1$ MO, resolving the debate as to the assignment of the PE spectrum of $TiCl_4$. The He I and He II spectra of $[(CH_3)ReO_3]$ have been measured and Extended Hückel MO calculations performed upon both this molecule and ReO_3Cl. A consistent assignment of their spectra has been achieved, based upon that of OsO_4, and it is found that the methyl group represents a much greater perturbation to tetrahedral symmetry than does a chlorine atom.

The bonding between the metal and dithiolene fragments in $[Fe_2(CO)_6S_2C_2(CF_3)_2]$ has been shown to be primarily due to an interaction between the b_1 symmetry $Fe_2(CO)_6$ HOMO and the n. MO of the dithiolene, which is doubly reduced. In $[Ni(S_2C_2(CF_3)_2)_2]$, however, the closer energy match of metal and ligand valence orbitals results in monoanionic dithiolene groups and a more complex PE spectrum.

ACKNOWLEDGEMENTS

It would be wholly inappropriate to begin these acknowledgements in any other way than by extending my warmest thanks to my supervisor, Jennifer Green, for contributions far too numerous to detail here. She has been very closely involved with virtually every aspect of this work, bringing an insight and enthusiasm which I have been extremely fortunate to benefit from.

On the experimental front, three people deserve special thanks. Peter Scott synthesised 80% of the compounds described in Chapter Two, and was largely responsible for my interest in C7 ring chemistry. Michael MacDonald displayed an extraordinary amount of patience and skill in ensuring that the spectrometer in Daresbury functioned as well and as often as it did, and Kong Hung "Spud" Sze kept the Daresbury experiment running for 24 hours a day with me for many a long week, and made my life a whole lot simpler by completely revolutionising the data analysis process.

Other notable contributions in Daresbury were made by John West, Andy Hopkirk, Michel Siggel and Marion Hayes, together with the workshop and all of the machine staff of the Synchrotron Radiation Source. Thanks are also in order to the technical staff of the ICL, particularly the electronics department for putting up with my attempts to explain what was at fault with the PES machine. Pete Trevellick's help with numerous computing problems was also very much appreciated.

My thanks are extended to all of the people in the Green groups for providing such a pleasant working environment over the last four years. Peter Scott, Philip Mountford and Jason Hubert deserve a special mention in this respect. I am also deeply indebted to Jason for proof reading this work so diligently.

My family has been a great source of strength to me throughout all of my time in Oxford. Even if I was not always completely convinced I was doing the right thing, they were unswerving in their support. I would also like to take this opportunity to thank all of my friends at St. Catherine's, both past and present members, for making the last seven years in Oxford so enjoyable. One in particular has become very special to me, and I dedicate this work wholeheartedly to her.

The Molecular Challenge

Sir Ethylene, to scientists fair prey,
(Who dig and delve and peek and push and pry,
And prove their findings with equations sly)
Smoothed his ruffled orbitals, to say
"I stand in symmetry. Mine is a way
Of mystery and magic. Ancient, I
Am also deemed immortal. Should I die,
Π would be in the sky, and Judgement Day
Would be upon us. For all things must fail,
That hold our universe together, when
Bonds such as bind me fail, and fall asunder.
Hence I stand firm against the endless hail
Of scientific blows. I yield not."
Men and their computers stand and stare and wonder.

W.G.Lowe

CONTENTS

Chapter One Introduction

1.1	Introduction	1
1.2	The photoionisation process	2
1.3	Energetic aspects of photoelectron spectroscopy	2
	1.3.1 The calculation of ionisation energies	2
	1.3.1 (a) Koopmans' Theorem	2
	1.3.1 (b) ΔSCF and ΔSCF-CI calculations	3
	1.3.1 (c) The SCF-Xα approach	4
	1.3.1 (d) Ab initio Green's function calculations	5
	1.3.2 Vibrational fine structure in photoelectron bands	6
	1.3.3 Relativistic effects - spin-orbit coupling	7
	1.3.4 The Jahn-Teller effect	8
1.4	Band intensities	9
	1.4.1 General considerations	9
	1.4.2 Symmetry considerations	10
	1.4.3 Atomic photoionisation cross sections	11
	1.4.3 (a) Cooper minima	11
	1.4.3 (b) Delayed maxima	12
	1.4.3 (c) Inter-channel coupling - p→d and d→f giant resonances	14
	1.4.4 Molecular photoionisation cross sections	16
	1.4.4 (a) Cooper minima	18
	1.4.4 (b) Delayed maxima	18
	1.4.4 (c) Inter-channel coupling - p→d and d→f giant resonances	19
	1.4.4 (d) Shape resonances	20
1.5	The angular distribution of photoelectrons	21
1.6	The present work in context	23
1.7	Note on the arrangement of the Thesis	24
1.8	References for Chapter One	25

Chapter Two Electron localisation in transition metal sandwich compounds - [Mo(η-$C_6H_5Me)_2$] and [M(η-C_7H_7)(η-C_5H_4R)] (M=Ti, Nb, Mo; R=H : M=Ta; R=Me)

2.1 Introduction 31

2.2 [Mo(η-$C_6H_5Me)_2$] 32

2.2.1 Bonding and interpretation of the photoelectron spectrum 32

2.2.2 Results and discussion 36

2.2.2 (a) The $1a_{1g}^{-1}$ and $1e_{2g}^{-1}$ bands 36

2.2.2 (b) The $1e_{1u}^{-1}$ and $1e_{1g}^{-1}$ bands 41

2.2.2 (c) Shape resonances in [M(η-$C_5H_5)_2$] and [M(arene)$_2$] 43

2.3 [M(η-C_7H_7)(η-C_5H_4R)] (M=Ti, Nb, Mo; R=H) (M=Ta; R=Me) 45

2.3.1 Electronic structure of mixed sandwich molecules 45

2.3.2 Results and discussion 49

2.3.2 (a) [Mo(η-C_7H_7)(η-C_5H_5)] 51

2.3.2 (b) [Nb(η-C_7H_7)(η-C_5H_5)] 59

2.3.2 (c) [Ta(η-C_7H_7)(η-C_5H_4Me)] 67

2.3.2 (d) [Ti(η-C_7H_7)(η-C_5H_5)] 75

2.3.3 Summary of the results from the mixed ring species 79

2.4 Analysis of the ionisation energy data of some group V metal sandwich molecules 81

2.5 References for Chapter Two 85

Chapter Three Trifluorophosphine and nickel tetrakis(trifluorophosphine)

3.1 Introduction 88

3.2 Results and discussion 90

3.2.1 Trifluorophosphine 90

3.2.2 Nickel tetrakis(trifluorophosphine) 100

3.2.2 (a) On the nature of nickel→PF_3 back donation 103

3.3 Conclusions 105

3.4 References for Chapter Three 106

Chapter Four Tetrahedral co-ordination in formally d^0 transition metal complexes - OsO_4, the group IVA tetrahalides $TiCl_4$, $TiBr_4$ and $ZrBr_4$, $[(CH_3)ReO_3]$ and ReO_3Cl

4.1 Introduction 108

4.2 Osmium tetroxide 109

4.2.1 Bonding and interpretation of the photoelectron spectrum 110

4.2.2 RPPICS results 114

4.2.3 Assignment of the photoelectron spectrum of OsO_4 121

4.3 Titanium tetrachloride 127

4.3.1 Bonding and interpretation of the photoelectron spectrum 127

4.3.2 RPPICS results and discussion 129

4.4 Titanium tetrabromide and zirconium tetrabromide 140

4.4.1 Bonding and interpretation of the photoelectron spectra 140

4.4.2 RPPICS results and discussion 144

4.4.2 (a) $TiBr_4$ 144

4.4.2 (b) $ZrBr_4$ 154

4.4.3 Summary of the results from $TiBr_4$ and $ZrBr_4$ 162

4.5 $[(CH_3)ReO_3]$ and ReO_3Cl 162

4.5.1 $[(CH_3)ReO_3]$ 162

4.5.2 ReO_3Cl 169

4.6 Summary and conclusions 175

4.7 References for Chapter Four 176

Chapter Five Complexes of the 3,4-bis(trifluoromethyl)-1,2-dithiolene ligand - $[Fe_2(CO)_6S_2C_2(CF_3)_2]$ and $[Ni(S_2C_2(CF_3)_2)_2]$

5.1 Introduction 179

5.2 $S_2C_2(CF_3)_2$ 180

5.3 $[Fe_2(CO)_6S_2C_2(CF_3)_2]$ 183

5.3.1 Bonding and interpretation of the photoelectron spectrum 183

5.3.2 RPPICS results 190

5.4 $[Ni(S_2C_2(CF_3)_2)_2]$ 200

5.5 Summary and conclusions 206

5.6 References for Chapter Five 208

Chapter Six Experimental details

6.1 Synthesis 210

6.1.1 Chapter Two 210

6.1.2 Chapter Three 210

6.1.3 Chapter Four 210

6.1.4 Chapter Five 211

6.2 The photoelectron spectra and RPPICS calculations 211

6.2.1 The spectrometer 211

6.2.2 Calibration 215

6.2.3 Errors 216

6.2.4 Data analysis 217

6.3 He I and He II photoelectron spectra 218

6.3.1 The spectrometer 218

6.3.2 Calibration 219

6.4 References for Chapter Six 220

Appendix One Molecular orbital theory and the Extended Hückel method

A1.1 Fundamentals of molecular orbital theory 221

A1.2 The extended Hückel method 225

A1.2.1 Description of the programs used for performing extended Hückel calculations 230

A1.3 Input data used in the EHMO calculations described in this Thesis 232

A1.4 References for Appendix One 241

Appendix Two Relative partial photoionisation cross section data tables

A2.1 Rppics of bands A-D in the PE spectrum of $[Mo(\eta\text{-}C_6H_5Me)_2]$ 243

A2.2 Rppics of bands A-D in the PE spectrum of $[Mo(\eta\text{-}C_7H_7)(\eta\text{-}C_5H_5)]$ 244

A2.3 Rppics of bands A-D in the PE spectrum of $[Nb(\eta\text{-}C_7H_7)(\eta\text{-}C_5H_5)]$ 245

A2.4 Rppics of bands A-D in the PE spectrum of $[Ta(\eta\text{-}C_7H_7)(\eta\text{-}C_5H_4Me)]$ 246

A2.5 Rppics of bands A-C in the PE spectrum of $[Ti(\eta\text{-}C_7H_7)(\eta\text{-}C_5H_5)]$ 247

A2.6 Rppics of bands A-F in the PE spectrum of PF_3 248

A2.7 Rppics of bands A-E in the PE spectrum of OsO_4 250

A2.8 Rppics of bands A-E in the PE spectrum of $TiCl_4$ 252

A2.9 Rppics of bands A-F in the PE spectrum of $TiBr_4$ 253

A2.10 Rppics of bands A-G in the PE spectrum of $ZrBr_4$ 255

A2.11 Rppics of bands A-F in the PE spectrum of $[Fe_2(CO)_6S_2C_2(CF_3)_2]$ 257

ABBREVIATIONS

AO	Atomic orbital
BR	Branching ratio
CI	Configuration interaction
CNDO	Complete neglect of differential overlap
DV	Discrete variational
EHMO	Extended Hückel molecular orbital
ESR	Electron spin resonance
eV	Electron volt
FCF	Franck-Condon Factor
hν	Incident photon energy
HF	Hartree-Fock
HOMO	Highest occupied molecular orbital
HS	Hartree-Slater
IE	Ionisation energy
INDO	Intermediate neglect of differential overlap
IR	Infra-red
KE	Kinetic energy
LCAO	Linear combination of atomic orbitals
LS	Russell-Saunders coupling scheme
LUMO	Lowest unoccupied molecular orbital
M	Metal atom
Mb	Mega-barns
Me	Methyl
MNDO	Modified neglect of differential overlap
MO	Molecular orbital
PE	Photoelectron
PES	Photoelectron spectroscopy

R	Alkyl group
RPPICS	Relative partial photoionisation cross section(s)
SCF	Self-consistent-field
SCK	super-Coster-Kronig
TGM	Toroidal grating monochromator
UV	Ultra-violet
ε	Continuum wavefunction
ζ	Spin-orbit coupling constant

CHAPTER ONE

INTRODUCTION

1.1 Introduction

The technique of photoelectron spectroscopy (PES) is of central importance in the elucidation of the electronic structure of matter. It provides the most direct source of experimental information on the valence electrons in molecules, and is useful for testing the predictions of molecular orbital (MO) calculations.

PES was not alone amongst photon-matter experiments in undergoing significant changes as access to synchrotron radiation sources became more widespread in the mid to late 1970s. With the use of suitable monochromators, light of almost any desired wavelength (from the near ultra-violet to hard X-ray) can be obtained, greatly increasing the information that may be derived from the PES experiment. The study of photoionisation cross sections and photoelectron (PE) asymmetry parameters as a function of incident photon energy offers enhanced possibilities for unequivocal spectral assignment, together with a better understanding of electronic structure - and the photoionisation process in general - than can be obtained from conventional laboratory-based light sources.

This Thesis describes the results of gas-phase PE spectroscopic studies on the valence electronic structures of a range of transition metal complexes, using synchrotron radiation over the energy range 17-115 eV. It is not the purpose of this Introduction to provide a complete account of the technique of gas-phase PES, as a number of standard texts and reviews exists [1-10]. Instead, aspects of the experiment directly relevant to the results presented in this Thesis are explored in Sections 1.2-1.5, in particular those concerned with the use of synchrotron radiation in PES. Finally the present work is placed in context in Section 1.6.

1.2 The photoionisation process

In the PES experiment, monochromatic radiation, hν, causes ionisation of gas-phase molecules and the properties of the ejected electrons are measured. These include their kinetic energies (KEs) and angular distribution with respect to the incident photon beam. Einstein's equation gives the ionisation energy (IE) of the PE as the difference between the energy of the incident photons and the measured PE KE

$$IE = h\nu - KE \quad (1.1)$$

A PE spectrum is a plot of IE against the number of electrons having that IE. As the molecular ion may be generated in a variety of excited states as well as the ground state, a series of peaks is observed in the spectrum. There is a number of spectral features which aid the process of assignment and interpretation, and these are discussed at some length in the following Sections.

1.3 Energetic aspects of photoelectron spectroscopy

1.3.1 The calculation of ionisation energies

One of the principle pieces of information derived from the PES experiment is the IEs of a molecule. It is clearly of great importance to be able to compare experimentally determined IEs with the results of theoretical calculations, for it is only through a combined approach that a complete picture of electronic structure can be obtained. A number of theoretical techniques exists for the calculation of IEs, several of which are outlined briefly below.

1.3.1(a) Koopmans' Theorem [11]

Koopmans' Theorem equates atomic or molecular orbital IEs with the negative of one electron self-consistent-field (SCF) orbital energies obtained in Hartree-Fock (HF) calculations

$$IE = -\varepsilon_i \quad (1.2)$$

To a first approximation, PE spectra may be interpreted on the basis of this theorem, although there is a number of well documented sources of error within it. In the first instance, the approach invokes the frozen orbital approximation, which means that orbital relaxation in the molecular ion is ignored. This leads to an overestimation of IEs in that orbital relaxation stabilises the molecular ion relative to the neutral molecule.

An inherent failing of HF calculations is that the effect on the molecular wavefunction of a particular choice of co-ordinates for one electron is not dependent upon the choices of co-ordinates for all of the other electrons. In other words, the technique makes no allowance for electron correlation - the tendency for electrons to avoid each other on account of their charged nature. Thus all SCF-HF-MO energies are overestimates of the true MO energy, an effect which is greater for neutral species than for the molecular ion. Consequently the neglect of electron correlation leads to an underestimate of IEs.

The final source of error is that the HF approach is non-relativistic, and Koopmans' Theorem will be in error whenever relativistic effects play a significant part in determining electron energies.

In spite of the above problems, Koopmans' Theorem works remarkably well in many cases in predicting at least the ordering of valence MO energy levels. This is due in no small part to a self-cancellation of the errors involved in the approach. Frequently, however, Koopmans' Theorem gives both quantitatively and qualitatively inaccurate estimates of the ordering of ionic levels, even for small systems such as N_2 [12]. Its use in interpreting transition metal compound PE spectra is somewhat limited, although it often provides a useful starting point for more accurate assignments.

1.3.1(b) ΔSCF and ΔSCF-CI calculations

These involve calculating HF-SCF wavefunctions for the molecular ground state and all relevant molecular ion states, from which IEs are computed as energy differences. The technique therefore incorporates relaxation effects in that the energy levels of the

molecular ion are determined, but cannot take account of electron correlation due to the nature of the HF method. Correlation may be included, however, by carrying out configuration interaction (CI) calculations upon each excited ionic state [13]; the ΔSCF-CI approach.

The ΔSCF technique has been applied to transition metal complexes by Veillard [14] and by Hillier and co-workers [15-23]. The calculations have revealed that relaxation effects are greater for mainly metal-localised MOs than for ligand-based ones (resulting in a decrease of metal-based IEs relative to ligand-based ones) and that the energy ordering of ion states is reproduced much better than by application of Koopmans' Theorem. The more recent work on $[Ni(\eta^3\text{-}C_3H_5)_2]$, $[Ni(CN)_4]^{2-}$, $[Co(CN)_6]^{3-}$, $[Fe(CN)_6]^{4-}$ and $[Pd(acac)_2]$ (acac = O-CH-CH-CH-O) [21-23] has shown that introduction of electron correlation via CI leads to a significant increase in the IEs of metal d-based MOs relative to the ligand MOs, supporting the expectation that relaxation and correlation effects oppose one another.

1.3.1(c) The SCF-Xα approach

This approach was first suggested by Slater and co-workers [24, 25] and involves the use of an approximate exchange term proportional to the one-third power of the local electron density to replace the exact exchange term in rigorous SCF-HF calculations. The approximate exchange term includes a coefficient, α, which may be varied to obtain best results and which typically takes values in the region of 0.7.

In the SCF-Xα approach, the eigenvalues are given by $(\partial E_{X\alpha}/\partial n_i)$, the differential change in orbital energy with occupation number. IEs are estimated by so-called transition state energies - the orbital energy obtained when the occupancy of an orbital is reduced to one half its value in the un-ionised system. Unlike a Koopmans' Theorem consideration of the HF method, which emphasises the ground state, the Xα technique treats the ground and ionised states equally and gives better IEs.

Although initially applied to atoms and small molecules, SCF-Xα calculations are now performed almost routinely upon realistic transition metal complexes and are of significant value in aiding the assignment of PE spectra. Calculations on [M(η-

$C_5H_5)_2(CO)_2]$ (M=Ti, Zr) [26] give IEs for the valence MOs which are a maximum of 1 eV different to the experimental values. The PE band corresponding to ionisation of the predominantly (η-C_5H_5) e_1 symmetry MOs is resolved into three components in the zirconium complex whereas only one band is observed in the titanium analogue, in agreement with the calculations which predict a spread of ca. 1 eV for these ionisations in $[Zr(\eta\text{-}C_5H_5)_2(CO)_2]$ but only 0.34 eV in $[Ti(\eta\text{-}C_5H_5)_2(CO)_2]$. The agreement between the experimentally determined IEs of cis $[Pt(CH_3)_2$(cyclooctadiene)] with an SCF-Xα calculation on the model complex $[Pt(CH_3)_2(C_2H_4)_2]$ is within 0.3 eV [27]. Furthermore, the calculation predicts a 24% C=C character to the highest occupied molecular orbital (HOMO), consistent with the observation of vibrational fine structure in the first PE band.

The technique is not always so successful, however. The IEs obtained from calculations on $[Fe(\eta\text{-}C_5H_5)(CO)]_2(\mu\text{-}CO)_2$ and $[Fe(\eta\text{-}C_5H_5)(CO)]_2(\mu\text{-}CO)(\mu\text{-}CH_3)$ are overestimates of the experimentally measured values by ca. 2.5 eV [28]. Nonetheless the ordering of the valence MOs correlates very well between experiment and theory.

1.3.1(d) Ab initio Green's function calculations

To avoid carrying out individual calculations on both the un-ionised and the various ionic states (as required by ΔSCF-CI), Green's function techniques have been applied to calculate IEs directly. Green's functions are operators which describe the propagation of a particle under the influence of a potential, and were first employed by Cederbaum and co-workers to calculate IEs of small molecules such as $(CN)_2$ and H_2CO [29]. Accuracy to within ca. 0.2 eV was obtained for these systems, and extension to a range of organic molecules [30, 31] gives IEs to within ca. 0.5 eV. The technique takes both relaxation and correlation effects into account.

To date only Hillier and co-workers have applied this approach to transition metal complexes, on which it has proved to be extremely successful. A comparison of ΔSCF, ΔSCF-CI and Green's function calculations on $[Ni(\eta\text{-}C_3H_5)_2]$ [21] has revealed that the most accurate estimate of valence IEs and most satisfactory assignment of the PE spectrum stem from the latter approach. The inclusion of electron correlation increases the IEs of

metal-localised MOs with respect to ligand MOs when the ΔSCF and Green's function methods are compared. This is also the conclusion from calculations on $[Pd(acac)_2]$ [23] in which pseudopotentials are employed to mimic the effect of core electrons, and from comparisons of Koopmans' Theorem, ΔSCF, ΔSCF-CI and Green's function calculations on $[Ni(CN)_4]^{2-}$, $[Co(CN)_6]^{3-}$ and $[Fe(CN)_6]^{4-}$ [22].

In general, then, it would appear that calculational methods have progressed to the point at which, in most cases, the ordering of valence MOs obtained from PES is reproduced very well. Furthermore, impressively accurate estimates of IEs have been obtained in many transition metal complexes, lending the theoretical approaches increased credibility.

1.3.2 Vibrational fine structure in photoelectron bands

Photoionisation may give rise to molecular ions in their ground vibrational state or one of a number of vibrationally excited states, and it is important to distinguish between adiabatic ($v''=0 \rightarrow v'=0$) and vertical ($v''=0 \rightarrow v'_{max}$) ionisation processes. (v'' = vibrational quantum number of the neutral molecule, v' = vibrational quantum number of the molecular ion, v'_{max} = vibrational quantum number at the PE band maximum. In the PES experiment, the neutral molecules are almost invariably in the vibrationless v''=0 level). Unless otherwise stated, all IE data presented in this Thesis refer to vertical processes.

If the molecular ion is unstable with respect to dissociation, its vibrational levels are unquantised and a broad, featureless PE band is observed. If this is not the case, vibrational fine structure may be distinguished. Invoking the Born-Oppenheimer approximation - separating the nuclear and electronic motions - the relative intensity of a v'' → v' transition is given by the Franck-Condon Factor (FCF) - the square of the overlap integral between the wavefunctions of v'' and v'

$$FCF = [\langle \chi_{v''} | \chi_{v'} \rangle]^2 \quad (1.3)$$

If there is little difference between the potential energy surfaces of the neutral molecule and the molecular ion, the only significant FCF will be for the v"=0 → v'=0 transition and a single sharp peak is observed in the PE spectrum. Significant changes in potential energy surfaces result in v"=0 → v'>0 transitions being the most intense, leading to different PE band profiles. In the case of small molecules, the distinct vibrational energy levels of the molecular ion may well be resolved, producing a vibrational progression in the PE spectrum. In the majority of transition metal complexes discussed in this Thesis, the PES experiment does not resolve the separate vibrational levels of the molecular ion. Instead a broadening of PE bands is observed.

In many cases it is possible to derive important information as to the type of MO giving rise to particular vibrational behaviour. The most likely cause of a significant change in potential energy surface between neutral molecule and molecular ion is if the MO from which ionisation is occurring is strongly bonding or antibonding. Vibrational progressions are therefore most commonly associated with bonding/antibonding MOs. This is not an inviolate rule, however, in that nominally non-bonding electrons may have a significant effect on the geometry in the neutral and ionic molecules, which may well give rise to vibrational progressions. A classic example is the formally metal-oxygen non-bonding $1t_1$ MO of OsO_4 (Chapter Four), the associated $^2T_1$ ion state of which displays extensive vibrational fine structure in the PE spectrum.

In order that the FCF for a vibrational transition be non-zero, the direct product of the symmetry representations of $\chi_{v"}$ and $\chi_{v'}$ must span the totally symmetric irreducible representation of the molecular point group. As $\chi_{v"}$ is almost invariably totally symmetric, only totally symmetric vibrations may normally be excited on ionisation.

1.3.3 Relativistic effects - spin-orbit coupling

The Schrödinger equation does not provide a description of electronic structure which satisfies the principles of special relativity. For situations in which relativistic effects are important, the Dirac equation must be used [32]. This introduces electron spin,

providing an a priori basis for application of spin-orbit coupling as a perturbation on non-relativistic wavefunctions.

There are two main ways in which solutions of the relativistic wave equation differ from their HF counterparts. First, all wavefunctions are contracted towards the nucleus owing to the increase in electron mass at relativistic speeds. Secondly, radial solutions with the same n and **l** quantum numbers but differing j values have different radial wavefunctions and different eigenvalues. It is therefore necessary to give n, **l** and j when specifying a relativistic subshell.

It is through the latter effect that relativity manifests itself most markedly on valence PE spectra. Qualitatively, the effects of spin-orbit coupling on atomic and molecular ion states can be established using group theoretical techniques. The multiple levels obtained by removing an electron from a closed shell species must be classified using double group symbols [33, 34]. If the direct product of the spin and orbital representations of the ionised subshells spans two or more double group representations, spin-orbit coupling can in principle lift the degeneracy of the relevant molecular ion states. It is important to note that the many electron spin-orbit operator can connect states belonging to the same double group irreducible representation but produced by different orbital ionisation processes. Hence CI can occur between ion states of different orbital symmetries.

1.3.4 The Jahn-Teller effect

The Jahn-Teller Theorem states that a non-linear molecule in an orbitally degenerate ion state will distort so as to lower the symmetry and remove the degeneracy [35]. This distortion is brought about by excitation of one of the Jahn-Teller active degenerate vibrational modes of the undistorted molecule. When the distortion is small and the vibrational intervals sufficiently large, a single band profile showing a Jahn-Teller vibrational progression may be observed. When the distortion is large and the individual vibrational levels are unresolved, the band profile may show two or more separate maxima, each corresponding to a distinct electronic state of the molecular ion.

A molecular ion in an orbitally degenerate state may also be susceptible to spin-orbit coupling. If this is the larger of the two perturbations, non-Kramers degeneracies in the molecular ion may be lifted via vibronic distortions, e.g. U' states in cubic systems [36-38] which cannot split under spin-orbit coupling but may do so when Jahn-Teller distortions are also possible. When spin-orbit coupling and Jahn-Teller splittings are of comparable magnitude, complicated behaviour is expected.

1.4 Band intensities

1.4.1 General considerations

One of the main tools available for the interpretation of PE spectra - and certainly the one with which this Thesis is most concerned - is a knowledge of band intensities and the way in which they vary as the energy of the ionising radiation is altered. The intensity of a PE band is proportional to the photoionisation cross section of the associated orbital at the energy of the incident radiation. It has been shown [39, 40] that the cross section for photoionisation of a system in state i by a photon beam of energy hν, leaving the system in a final state f consisting of photoelectrons of energy ε and ions in state j, is given by

$$\sigma_{ij}(\varepsilon) = \left(\frac{4\pi\alpha a_0^2}{3g_i}\right)\left(\varepsilon + I_{ij}\right)\left|M_{if}\right|^2 \qquad (1.4)$$

where α is the fine structure constant (1/137), a_0 the Bohr radius and g_i the number of degenerate sublevels of the initial state. The PE energy ε and IE I_{ij} are expressed in Rydbergs. The matrix element is given by [41]

$$\left|M_{if}\right|^2 = \frac{4}{\left(I_{ij}+\varepsilon\right)^2}\sum_{i,f}\left|\left\langle f\left|\sum_{\mu}\exp(ik_v.r_\mu)\nabla_\mu\right|i\right\rangle\right|^2 \qquad (1.5)$$

where r_μ is the position co-ordinate of the μth electron, k_v the propagation vector of the photon ($|k_v|=(2\pi\nu)/c$), all wavefunctions are normalised and the summation over i,f is over the degenerate initial and final states.

The major concentration of the wavefunction amplitude occurs at a distance r_μ from the nucleus, of the order of the Bohr radius. Hence for incident photon energies lower than several keV, $k_v.r_\mu$ is small enough so that $\exp(ik_v.r_\mu)$ may be approximated by unity. This is known as the "dipole approximation" and the matrix element becomes

$$|M_{if}|^2 = \frac{4}{(I_{ij}+\varepsilon)^2}\sum_{i,f}\left|\langle f\left|\sum_\mu \nabla_\mu\right|i\rangle\right|^2 = \sum_{i,f}|\langle f|\, r_\mu|i\rangle|^2 \qquad (1.6)$$

so that the calculation of photoionisation cross sections reduces to a problem of finding initial and final state wavefunctions.

1.4.2 Symmetry considerations

In order that the photoionisation dipole matrix element be non-zero, the direct product $\Gamma_i\times\Gamma_d\times\Gamma_\varepsilon$ must contain the totally symmetric irreducible representation of the appropriate point group (i, d and ε refer to the initial state, the electric dipole operator and the continuum electron wavefunction respectively). In the atomic case, application of this condition in the Russell-Saunders (LS) coupling limit leads to the $\Delta l=\pm 1$ selection rule for photoionisation. Continuum ionisation channels are then defined for bound electrons, e.g. s→p and p→d are permitted, but s→d transitions are forbidden.

Although the direct product rule also applies in the molecular case, the anisotropy of the molecular potential field means that l is no longer well-defined, and non-zero matrix elements arise for transitions which would be disallowed in atoms.

1.4.3 Atomic photoionisation cross sections

The photoionisation of atoms is understood to a much better extent than is that of molecules, mainly due to the problems of constructing reliable wavefunctions for photoelectrons experiencing anisotropic molecular potentials. Thus many of the terms and concepts used in the description of molecular photoionisation come directly from atomic treatments.

In general, it is found that photoionisation cross sections decrease with increasing incident photon energy (and hence increasing PE KE). This arises because the interaction of the outgoing electron wavefunction with the ground electronic state decreases owing to the oscillatory nature of the former. The ionisation dipole matrix elements begin to cancel [42], and hence the cross section decreases. There is a number of effects which modify this monotonic cross section fall off, however, and these are discussed in the following Sections.

1.4.3 (a) Cooper minima

The photoionisation cross sections of many atomic orbitals (AOs) have well-defined minima at PE KEs ranging from just above threshold (e.g. 3s AO of sodium) to several hundred eV (e.g. 4d and 5d AOs of certain transition elements). This minimum is known as a Cooper minimum [43], and arises because the photoionisation dipole matrix element for a particular transition (e.g. the $3s \rightarrow \varepsilon p$ in the sodium case) goes through zero on account of positive and negative contributions exactly cancelling.

Cooper minima are often observed experimentally, and the following rules concerning their behaviour have been drawn up based upon these experiments and extensive calculations [43-52]

(i) Cooper minima appear only in $l \rightarrow l+1$ transitions

(ii) They occur only for outer and near outer subshells, and only for those whose wavefunctions possess radial nodes

(iii) They are generally not zero minima because even though the $l \rightarrow l+1$ dipole matrix element vanishes, the $l \rightarrow l-1$ does not (for all AOs other than s). In certain cases the

minimum is completely obscured by the $l \rightarrow l-1$ channel, although generally the $l \rightarrow l+1$ transitions dominate.

1.4.3 (b) Delayed maxima

The effective potential experienced by an electron in an atom may be approximated by the central field potential [53] and the radial wave equation is given by

$$\left[\frac{-d^2}{dr^2} + \frac{l(l+1)}{r^2} + V(r)\right]\Psi_{nl}(r) = E\,\Psi_{nl}(r) \qquad (1.7)$$

where the $(l(l+1)/r^2)$ term is the centrifugal repulsion term. For high angular momentum electrons, the effect of the centrifugal repulsion term is to create a so-called double-well potential, which has an intermediate range maximum which may be positive. This is illustrated schematically for a bound f electron in Figure 1.1, which also gives the potential for a continuum g electron. For the bound electron, at large distances from the ion core, there is little centrifugal repulsion ($\propto(1/r^2)$) and the Coulomb field of the ion core ($\propto(1/r)$) results in the potential being negative. As r becomes smaller, however, the repulsion becomes more significant and the potential more positive before penetration of the core electrons results in the Coulomb attraction becoming dominant, with a large drop in potential. At very small r, the rapid increase in centrifugal repulsion produces a positive potential.

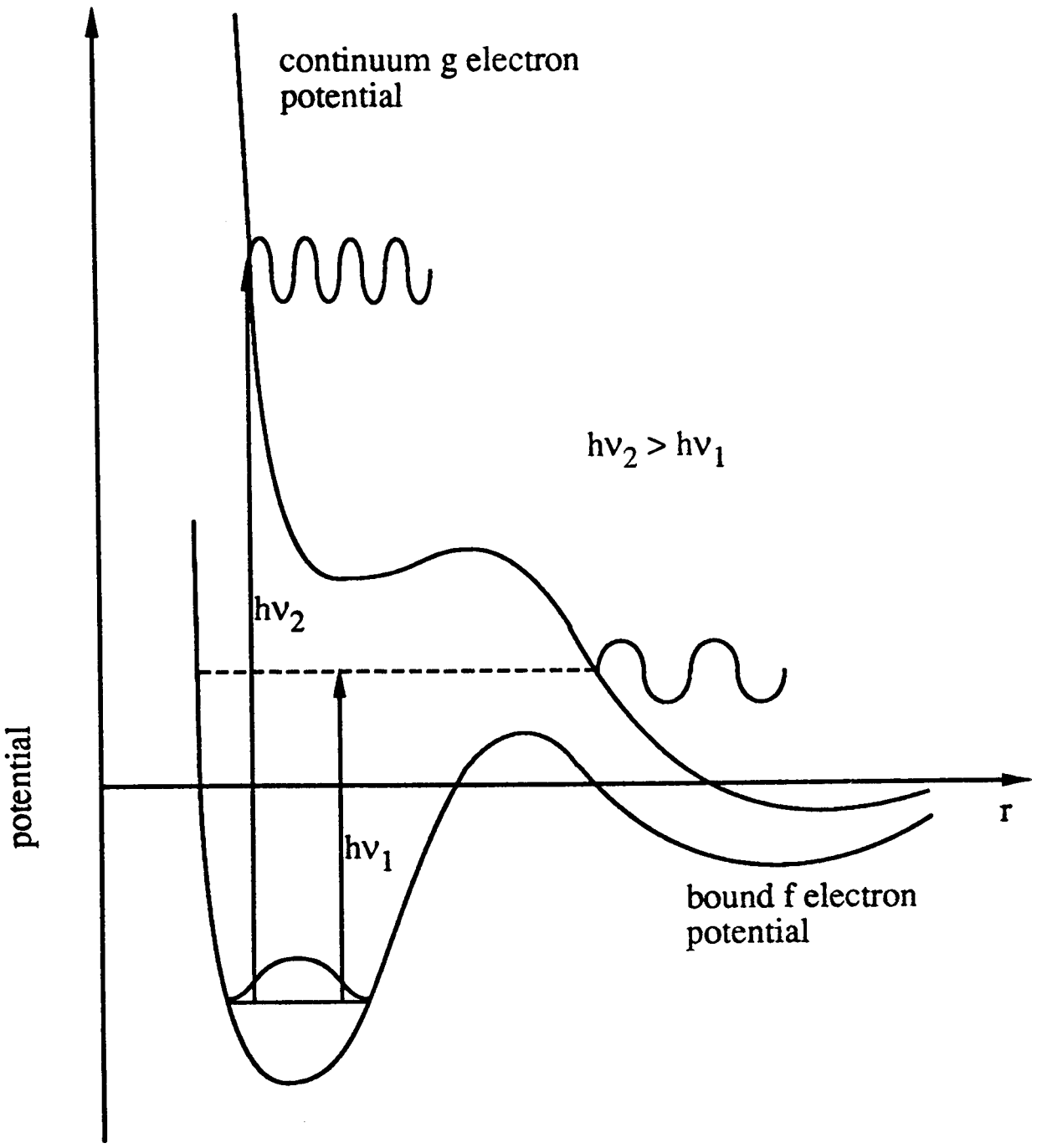

Figure 1.1 : schematic representation of the radial electrostatic potential for a bound f electron and a continuum g electron, illustrating the origin of delayed maxima

The main channel for ionisation of an f electron is via a free electron g wave. The height of the centrifugal barrier in the potential of the g wave is bigger than that of the f electron, and the depth of its inner well is smaller.‡ Due to the form of its potential, the continuum g function cannot penetrate into the atom (where the f wavefunction has most of its amplitude) at low PE KEs. Consequently the ionisation dipole matrix element is low. As the PE KE rises, penetration by the continuum g wave becomes more effective and the

‡ Generally speaking, the depth of the inner well in the radial potential of an electron experiencing a central field potential increases with increasing atomic number.

photoionisation cross section rises. At high energies, the εg wavefunction continues to move in toward the nucleus, and cancellation begins to occur due to its oscillatory nature. This results in a decrease in the cross section, producing an overall cross section behaviour which rises from threshold, maximises and subsequently falls away.

Hence the delayed maximum phenomenon is related to the final angular momentum of the PE. It is strongest for f→g transitions, very much weaker for p→d and virtually non-existent for s→p ionisation. The experimental cross section of the 4d AO of silver shows a pronounced maximum at ca. 45 eV photon energy, attributed to the 4d→εf delayed maximum [54].

1.4.3 (c) Inter-channel coupling - p→d and d→f giant resonances

Inter-channel coupling corresponds to electron correlation in either the initial or final state. An example is the cross section of the 3s AO of argon, which shows an experimental Cooper minimum [55], at odds with HF calculations which predict no minimum. It is believed that inter-channel coupling between the ^1P state arising from the $3s^13p^6\varepsilon p$ configuration and that from the $3s^23p^5\varepsilon d$ is responsible for the minimum, in that the 3s→εp dipole matrix element is small with respect to that of the 3p→εd and hence only a small degree of inter-channel coupling can cause significant modification of the 3s photoionisation cross section. The extremely large xenon 4d AO cross section in the region of its delayed maximum is mirrored by much smaller enhancements of the 5s and 5p cross sections [56].

One of the most significant effects of inter-channel coupling is seen in the cross sections of transition metal d and lanthanide and actinide f orbitals in the vicinity of the free atom np and nd IEs, and is referred to as p→d and d→f giant resonant absorption. When bound, d and f wavefunctions have nearly all of their amplitude in the inner well of their potential (Figure 1.1), which results in very large probabilities for photoabsorption transitions from inner p to valence d (or inner d to valence f) AOs, as they exist in the same region of space. This spatial proximity results in strong exchange interactions between the np or nd hole and the nd^{n+1} or nf^{n+1} states, and the energies of the configurations are

spread out over a wide range (ca. 10 to 20 eV [57]), many of which lie above the np or nd ionisation thresholds.

The possible fates of the absorption intermediate in a generalised p→d resonance are illustrated in the scheme below. Autoionisation (3) may occur, as may a super-Coster-Kronig (SCK) decay (4) in which a valence d electron is ionised [58, 59]. Inter-channel coupling between the corresponding states produced via the direct ionisation process (1) and the photoabsorption (2)/SCK decay (4) route strongly modifies the cross section of the nd AO.

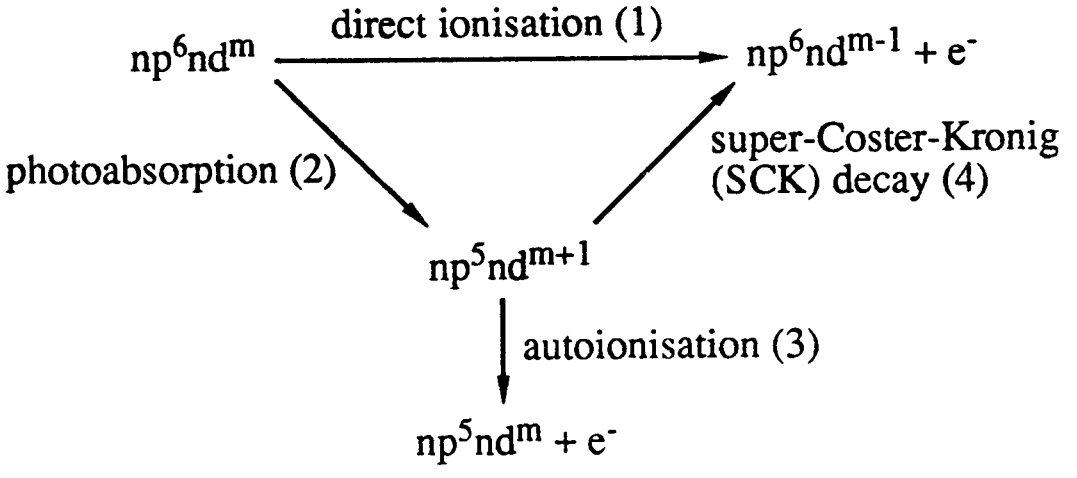

These resonances may be treated analytically using the approach of Fano [60, 61], who showed that, for a single resonance interacting with a single continuum channel, the cross section in the vicinity of the resonance is described by three parameters, the resonance energy E_r, the resonance width Γ and the line profile index q. The latter measures the relative contributions of the direct and resonant ionisation channels. Large q values imply large photoabsorption/SCK decay probabilities.

The cross section $\sigma(E)$ as a function of photon energy E in the vicinity of a resonance is given by

$$\sigma(E) = \sigma_0 \frac{(q + \varepsilon)^2}{(1 + \varepsilon^2)} \quad (1.8)$$

where $\varepsilon = (E-E_r)/0.5\Gamma$ and σ_0 is the background cross section, assumed to be constant in the region of the resonance. As described earlier, photoionisation cross sections tend to decrease with increasing incident photon energy, and hence the assumption of constant σ_0 is not generally valid. A modification to equation (1.8) is made

$$\sigma(E) = \sigma_0 (1 - X(E_1 - E)) \frac{(q + \varepsilon)^2}{(1 + \varepsilon^2)} \quad (1.9)$$

in which X is a parameter which determines the percentage decrease in σ_0 per eV and E_1 is the lower photon energy limit of the fit.

The photoionisation cross sections of the 3d AOs of chromium [62] and manganese [63-65] show very large intensity enhancements just above the 3p ionisation thresholds due to the inter-channel coupling described above. Satisfactory fits of equation (1.8) to the experimental data have been obtained. Similar effects have been observed in the 4d AO cross sections of barium, lanthanum and cerium [66].

1.4.4 Molecular photoionisation cross sections

The model most commonly used in interpreting molecular photoionisation cross sections is the Gelius model [67, 68], in which the one electron cross section σ_j for the jth MO is given by

$$\sigma_j = \sum_{A,i} P_{j,i,A} \sigma_i^A \quad (1.10)$$

where the summation is carried out over all of the AOs ϕ_i^A, on the different atoms, A, which contribute to the MO Φ_j. The σ_i^A are one electron atomic cross sections and the $P_{j,i,A}$ are factors describing the effective occupancy of the MO. In a properly normalised linear combination of atomic orbitals (LCAO) approach

$$P_{j,i,A} = (c_{j,i,A})^2 \quad (1.11)$$

where $c_{j,i,A}$ is the coefficient of the AO ϕ_i^A in Φ_j. In this model the molecular photoionisation cross sections are directly related to the atomic cross sections of the AOs contributing to the appropriate MO, and the overlap population does not contribute to the photoionisation cross sections.

The model is valid when

(a) the contribution of the overlap electron density to the cross section is negligible and

(b) the effects of the anisotropy of the molecular ion potential on the outgoing electron wavefunction are small or

(c) the PE KE is high.

The third condition implies (a) and (b) since

(i) a large PE KE leads to a low ionisation dipole matrix element at large distances from the nuclei as positive and negative contributions cancel, due to the rapidly oscillating continuum wavefunction and

(ii) the molecular potential field will cause less perturbation to a continuum wavefunction if it has high energy.

Hence the Gelius model facilitates interpretation of the photoionisation cross sections of MOs in terms of those of their constituent AOs. This has the dual advantage that these atomic features are comparatively well understood, and that cross section features derived from molecular effects can be more easily distinguished.

Photoionisation cross section calculations on small molecules using the Gelius model have concluded that the dominant factors are indeed the AO cross sections [69, 70] and that overlap effects are small. Even at comparatively low incident photon energies, it would appear that the Gelius model may be applied with some confidence. In all of the previous work on the project with which this Thesis is concerned, an interpretation of the experimental results in terms of the Gelius model has proved extremely successful [71-77]. Throughout this Thesis, therefore, the Gelius model is used as a basis for interpreting MO photoionisation cross sections.

1.4.4 (a) Cooper minima

Cooper minima have been observed in many MO photoionisation cross sections. Figure 1.2 shows the experimentally determined cross sections of the $7t_2$ and 2e MOs of CCl_4 (from Carlson et al. [78]). These MOs are essentially chlorine 3p lone pair MOs, and as such are expected to have cross section behaviour similar to that of the chlorine 3p AO. Both MO cross sections go through a minimum at ca. 43 eV photon energy, corresponding to PE KEs of 31 and 34 eV for the $7t_2$ and 2e MOs respectively. This is in good agreement with calculations on atomic chlorine, which predict the Cooper minimum of the 3p AO to occur at a PE KE of ca. 30 eV [52], and with the experimental value for argon of 34 eV.

The photoionisation cross section of the $2\pi_g^{-1}$ HOMO of CS_2 (an essentially sulphur lone pair MO) shows a minimum at 40 eV photon energy [79], in good agreement with calculations which place that of the 3p AO of sulphur at 36 eV [52]. The predominantly halogen lone pair 1π MOs of the hydrogen halides HX (X=Cl, Br, I) have a pronounced cross section minimum which is echoed, to a much lesser extent, in the 3σ H-X bonding MO in HCl and HI, though not in HBr [80].

The reduced rate of cross section fall off of the d bands of $[Cr(CO)_6]$ at high photon energy with respect to those of the equivalent bands of $[Mo(CO)_6]$ and $[W(CO)_6]$ [71, 74] is explained by the lack of a Cooper minimum in 3d AO cross sections. This is also found to be the case in the d bands of ferrocene in comparison with its second and third row congenors [71, 75].

1.4.4 (b) Delayed maxima

The iodine 4d AO cross section in CH_3I shows a maximum some 30 eV above its ionisation threshold of 58 eV [81]. An extremely elegant example of the delayed maximum effect is seen in the f band of uranocene ($[U(\eta\text{-}C_8H_8)_2]$) [72, 76], in which the cross section rises sharply between 24 and 39 eV photon energy. The large He II/He I relative intensity increases of f bands in actinide PE spectra have been established for some considerable time [10], but this represents the first variable photon energy confirmation of the effect.

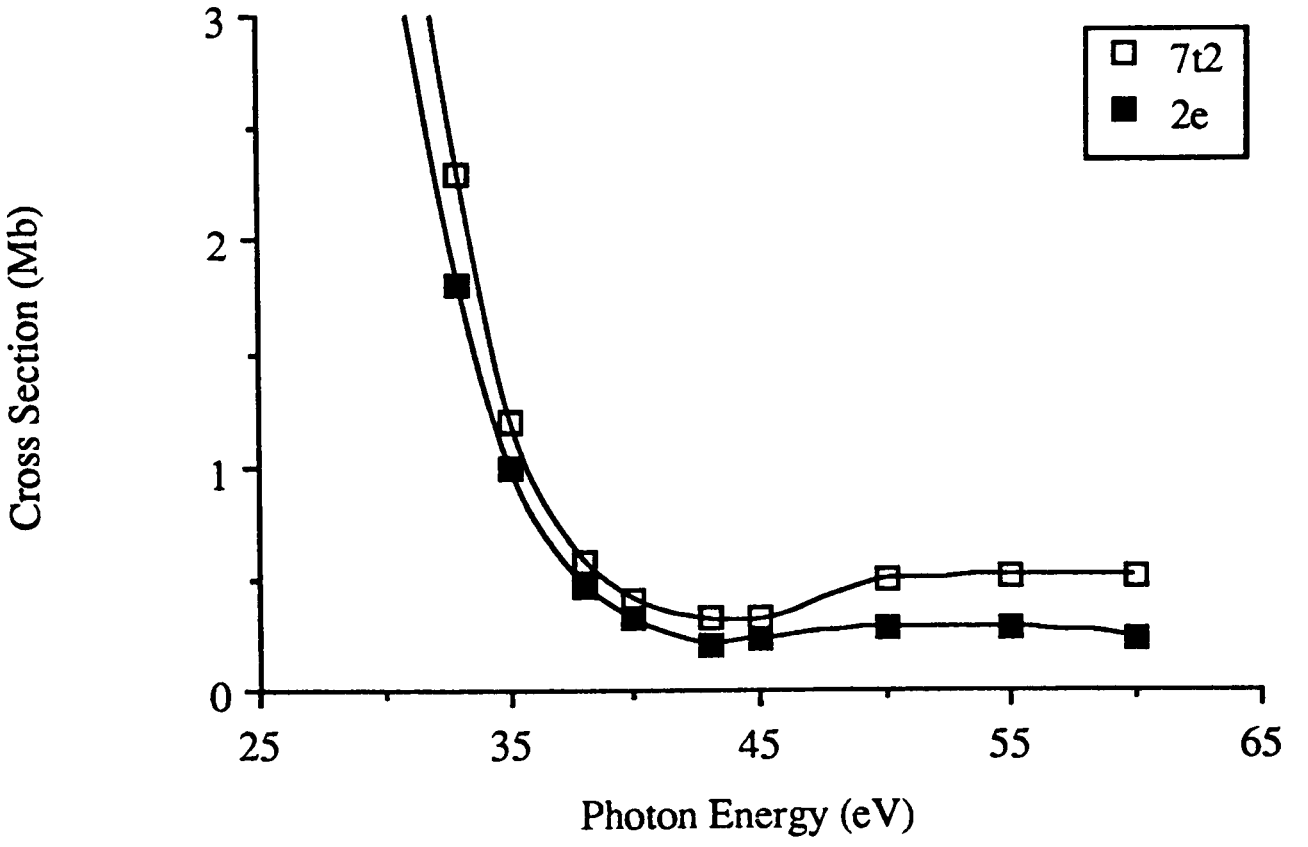

Figure 1.2 : experimentally determined cross sections for the $7t_2$ and 2e (chlorine 3p lone pair-based) MOs of CCl_4 [78]

1.4.4 (c) Inter-channel coupling - p→d and d→f giant resonances

To date, the only reported effects of giant resonant absorption on MO photoionisation cross sections of gas-phase transition metal compounds have come from the on-going project with which this Thesis is concerned, although solid state examples exist [82-84]. It has been observed in a wide range of compounds, including $[M(\eta\text{-}C_6H_6)_2]$ (M=Cr, Mo) [71], $[M(CO)_6]$ (M=Cr, Mo, W) [71, 74], $[M(\eta\text{-}C_5H_5)_2]$ (M=Fe, Ru, Os) [71, 72, 75], $[U(\eta\text{-}C_8H_8)_2]$ [72, 76], $[Ni(PF_3)_4]$ [72, 77] and $[(\eta\text{-}C_5H_4{}^iPr)MoS]_4$ [73], and may now be regarded as a well established effect in variable photon energy PES. In many cases the cross section enhancements of MOs with substantial metal d (or f) AO character can be fitted to the Fano functions given earlier (equations (1.8) and (1.9)), lending further weight to the Gelius model and to Fano functions as a description of the resonance process.

1.4.4 (d) Shape resonances

Shape resonances have no direct equivalent in atomic photoionisation, being critically dependent upon the form of the potential of the molecular ion. This itself is determined in part by the physical shape of the molecule, from which the name of the effect derives. Shape resonances manifest themselves as increases in cross section, which are frequently sharp and generally at relatively low PE KEs.

The total electrostatic potential experienced by a PE as it escapes from a molecular ion is a combination of a multi-centre Coulomb attractive term and a repulsive term, analogous to the centrifugal repulsion in an atomic potential (Section 1.4.3 (b)), although the l quantum number is not strictly defined in molecules. In a manner similar to the delayed maximum effect in atoms (Section 1.4.3 (b)), the intermediate range barrier in its electrostatic potential prevents the continuum wavefunction, at low PE KEs, from occupying the region of space in which the bound electron has most of its amplitude, resulting in a low ionisation dipole matrix element. Only as the free electron KE increases does the continuum wavefunction penetrate into the molecular electron density and increase the ionisation probability for this channel. As the PE KE increases still further, its interaction with the bound electron wavefunction decreases due to its oscillatory nature.

An alternative explanation of shape resonances is to consider that the bound electron possesses an intermediate range maximum in its potential, analogous to that shown for a f electron in Figure 1.1. Initially, the electron is excited into a quasi-bound antibonding MO, which exists within the inner well of the effective electrostatic potential. At low PE KEs, the excited electron has a low probability of penetrating the intermediate range maximum and escaping from the molecule - i.e. the probability of the system decaying to form molecular ion plus free electron is small. As the PE KE increases, there is an increased probability of the quasi-bound electron penetrating the barrier and escaping the molecule. As the bound and quasi-bound states are localised within the same region of space, there is good overlap between them, and hence once there is sufficient energy to overcome the barrier a large increase in cross section may occur.

The large increase in the cross section of the $3\sigma_g$ MO of N_2 at an incident photon energy of 28 eV is attributed to a shape resonance involving the σ_u symmetry continuum ionisation channels [85-88]. No equivalent peak is seen in the $1\pi_u$ or $2\sigma_u$ cross sections, as u→u transitions are symmetry forbidden.

1.5 The angular distribution of photoelectrons

The differential cross section for the angular distribution of PEs for an $|i\rangle \rightarrow |j, \varepsilon\rangle$ electric dipole photoionisation process by elliptically polarised light (such as is generated by a synchrotron source) is given by [89]

$$\frac{d\sigma_{ij}(\varepsilon)}{d\Omega} = \frac{\sigma_{ij}(\varepsilon)}{4\pi}\left(1 + \frac{\beta_{ij}(\varepsilon)}{4}(3P\cos 2\theta + 1)\right) \quad (1.12)$$

where θ is the angle between the PE direction and the polarisation vector of the incident radiation, σ_{ij} is the photoionisation cross section, β is the asymmetry parameter and P is the degree of polarisation of the radiation, defined by

$$P = \frac{(I_y - I_x)}{(I_y + I_x)} \quad (1.13)$$

with I_x and I_y being the intensity of light polarised in the photon-PE plane and at 90° to it respectively. β contains all of the PE angular distribution information for the electric dipole photoionisation process, and must lie in the range $-1<\beta<2$ so that the differential cross section is positive.

Each continuum ionisation channel has a characteristic β value, e.g. for atomic $ns\rightarrow\varepsilon p$ ionisations $\beta=2$ while for $np\rightarrow\varepsilon s$ $\beta=0$. Where more than one ionisation channel is open, the resultant value of β is dependent upon their relative phase differences and amplitudes. As both of these are dependent upon the incident photon energy, so is β. Indeed the photon energy dependence of β has proved to be a very sensitive indicator of phenomena such as resonances and Cooper minima, as the relative strengths of the

different ionisation channels vary rapidly in such circumstances. Figure 1.3 shows the β values for the $7t_2$ and 2e MOs of CCl_4 [78], the cross section data for which are given in Figure 1.2. It can be seen that the changes in β in the region of the Cooper minima in these bands (35-50 eV) are more dramatic than those in the cross section values. There are many examples of this effect [80, 90-93].

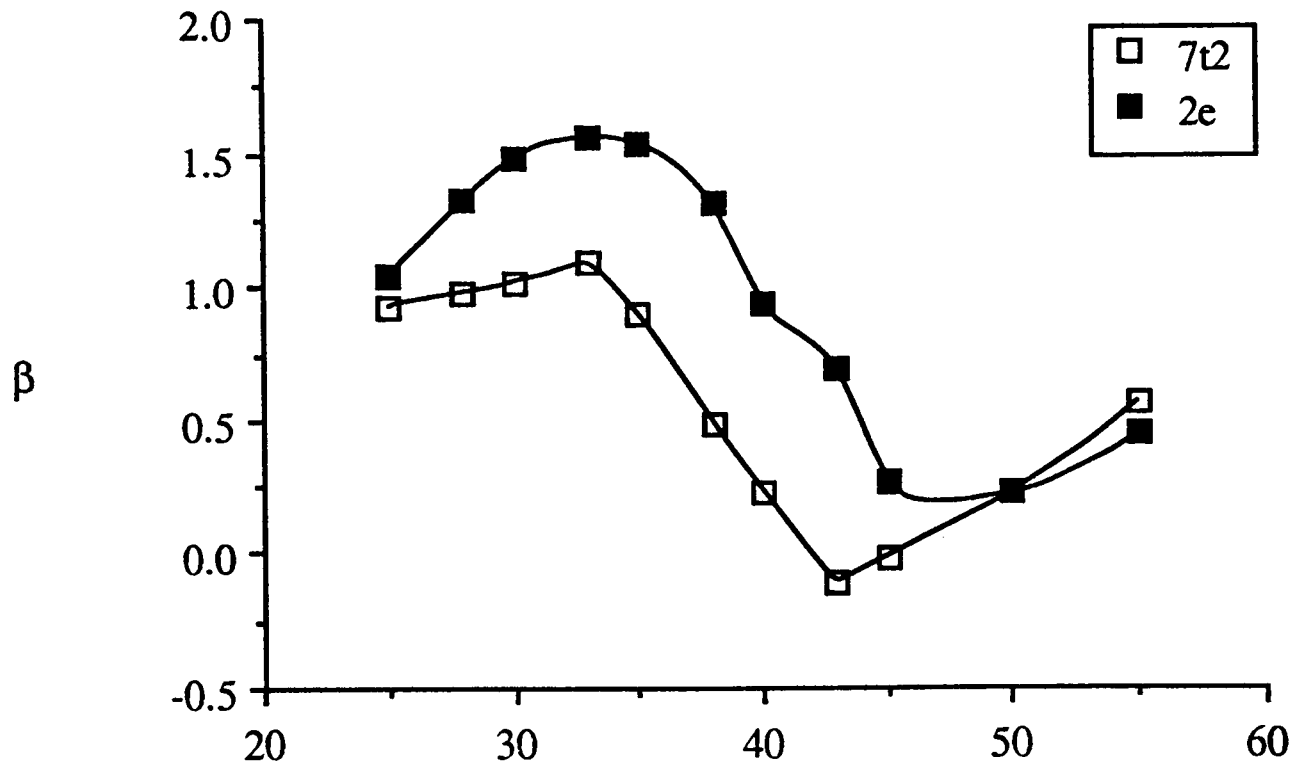

Figure 1.3 : experimentally determined β values for the $7t_2$ and 2e (chlorine 3p lone pair-based) MOs of CCl_4 [78]

It may be seen from equation (1.12) that the PE flux is dependent upon β for all ejection angles except the so-called "magic angle", given by

$$\theta = \frac{\cos^{-1}(1/3P)}{2} \quad (1.14)$$

at which the cross section for a particular ionisation process may be directly observed. All of the data presented in this Thesis are cross section data, and no attempt was made to

measure β values for any of the systems studied. Hence all measurements were made at the "magic angle", as detailed in Chapter Six.

1.6 The present work in context

This Thesis is concerned primarily with the interpretation of relative partial photoionisation cross section (RPPICS) data of the valence MOs of transition metal complexes. These are photoionisation cross sections not placed on an absolute scale, as no measure of the absolute pressure of the ionising gas can be made in the experiment. This is described in more detail in Chapter Six.

One of the initial aims [71] of extending the technique of gas-phase PES of transition metal complexes to synchrotron radiation was to evaluate the empirically derived relative intensity rules [10] for interpreting discharge lamp spectra. Furthermore, it was hoped to assess the validity of the Gelius model as an approach to understanding MO cross sections. Consequently the first targets for investigation were "classic" compounds; high symmetry systems which were well understood theoretically and which had unambiguously assigned PE spectra. These included $[M(\eta\text{-}C_6H_6)_2]$ (M=Cr, Mo) [71], $[M(CO)_6]$ (M=Cr, Mo, W) [71, 74], $[M(\eta\text{-}C_5H_5)_2]$ (M=Fe, Ru, Os) [71, 72, 75] and $[U(\eta\text{-}C_8H_8)_2]$ [72, 76].

This has proved to be an extremely successful exercise in that it has been possible to understand the RPPICS of these systems largely from the standpoint of the Gelius model. The increase in relative intensity of bands corresponding to ionisation from metal d-based MOs over ligand-based MOs as the ionising radiation is altered from He I to He II [9] has been shown to be due in no small part to the occurrence of p→d and shape resonances in the region of He II photon energy. The dramatic increase in relative intensity of f bands in actinide PE spectra between He I and He II has been more thoroughly probed by studying uranocene with synchrotron radiation, in which the delayed maximum effect is clearly illustrated. Work on the sulphur-containing molecules $[(\eta\text{-}C_5H_4{}^iPr)MoS]_4$ and $[W(S_2C_2(CF_3)_2)_3]$ [73] has confirmed that the collapse of sulphur-based bands in He II spectra arises from the Cooper minimum in the 3p AO.

The assumption that He II PE spectra give intensity ratios reflecting the degeneracies of the MOs from which the ionised electrons originate [1] has been shown to be incorrect. The data obtained on $[Cr(\eta\text{-}C_6H_6)_2]$ reveal that it is only due to a shape resonance at an incident photon energy of 42 eV that the $1a_{1g}/1e_{2g}$ branching ratios (BRs) are approximately proportional to their degeneracies in the He II spectrum. A similar conclusion was drawn from the study of ferrocene and osmocene, illustrating the potential pitfalls of drawing quantitative conclusions from relative band intensities in He II spectra.

The work described in this Thesis represents a departure from the majority of the previous studies, in that the variable photon energy experiment has been applied to systems which are less well understood. Armed with a better understanding of the way in which transition metal MO cross sections vary with photon energy, a number of chemically important questions has been addressed. The oxidation state of the cycloheptatrienyl ligand in its transition metal complexes has been investigated in a study of electron localisation in sandwich molecules of the form $[M(\eta\text{-}C_7H_7)(\eta\text{-}C_5H_4R)]$ (M=Ti, Nb, Ta, Mo). An investigation of the MO cross sections of PF_3 and a comparison with those of $[Ni(PF_3)_4]$ has sought to probe the π acidity of the PF_3 ligand. The superficially straightforward but ultimately highly complicated tetrahedral molecules OsO_4, $TiCl_4$, $TiBr_4$ and $ZrBr_4$ have been studied, and a further attempt has been made to assess the bonding mode of the dithiolene ligand $S_2C_2(CF_3)_2$ in its transition metal complexes. Taken together, these investigations illustrate the value of synchrotron radiation-based PES to the determination of the electronic structures of transition metal compounds.

1.7 Note on the arrangement of the Thesis

A number of Extended Hückel Molecular Orbital (EHMO) calculations has been performed. The input data for these calculations are collected in Appendix One, which also provides a brief introduction to MO theory in general and the EHMO method in particular. Relative partial photoionisation cross section data for the compounds studied with synchrotron radiation are given in graphical form in the appropriate Chapters. To avoid unnecessary congestion, these data are tabulated in Appendix Two.

1.8 References for Chapter One

[1] J. H. D. Eland: *Photoelectron Spectroscopy* Butterworths, London (1984).

[2] D. W. Turner, C. Baker, A. D. Baker and C. R. Brundle: *Molecular Photoelectron Spectroscopy* Wiley-Interscience, London (1970).

[3] J. W. Rabalais: *Principles of Ultraviolet Photoelectron Spectroscopy* Wiley-Interscience, New York (1977).

[4] T. A. Carlson: *Photoelectron and Auger Spectroscopy* Plenum Press, New York (1975).

[5] D. Briggs: *Handbook of X-ray and Ultraviolet Photoelectron Spectroscopy* Heyden, London (1977).

[6] C. R. Brundle and A. D. Baker (eds): *Electron Spectroscopy, Theory, Techniques and Applications* Academic Press, London (1977 to 1981).

[7] P. K. Ghosh: *Introduction to Photoelectron Spectroscopy* Wiley-Interscience, New York (1983).

[8] C. Furlani and C. Cauletti: *Structure and Bonding* **35** (1977) 119.

[9] A. H. Cowley: *Prog. Inorg. Chem.* **26** (1979) 46.

[10] J. C. Green: *Structure and Bonding* **43** (1981) 37.

[11] T. Koopmans: *Physica* **1** (1934) 104.

[12] P. E. Cade, K. D. Sales and A. D. Wahl: *J. Chem. Phys.* **44** (1966) 1973.

[13] I. H. Hillier: *Pure Appl. Chem.* **51** (1979) 2183.

[14] A. Veillard and J. Demuynck: *Modern Theoretical Chemistry* Plenum Press, New York (1977).

[15] S. Evans, M. F. Guest, I. H. Hillier and A. F. Orchard: *J. Chem. Soc., Farad. Trans. II* **70** (1974) 417.

[16] J. A. Connor, L. M. R. Derrick, M. B. Hall, I. H. Hillier, M. F. Guest, B. R. Higginson and D. R. Lloyd: *Mol. Phys.* **28** (1974) 1193.

[17] I. H. Hillier, M. F. Guest, B. R. Higginson and D. R. Lloyd: *Mol. Phys.* **27** (1974) 215.

[18] M. F. Guest, I. H. Hillier, B. R. Higginson and D. R. Lloyd: *Mol. Phys.* **29** (1975) 113.

[19] M. B. Hall, I. H. Hillier, J. A. Connor, M. F. Guest and D. R. Lloyd: *Mol. Phys.* **30** (1975) 839.

[20] M. Doran, I. H. Hillier, E. A. Seddon, K. R. Seddon, V. H. Thomas and M. F. Guest: *Chem. Phys. Lett.* **63** (1979) 612.

[21] D. Moncrieff, I. H. Hillier, V. R. Saunders and W. von Niessen: *Inorg. Chem.* **24** (1985) 4247.

[22] S. Smith, D. A. Taylor, I. H. Hillier, M. A. Vincent, M. F. Guest, A. A. MacDowell, W. von Niessen and D. S. Urch: *J. Chem. Soc., Farad. Trans. II* **84** (1988) 204.

[23] N. A. Burton, I. H. Hillier and J. Kendrick: *Chem. Phys. Lett.* **155** (1989) 195.

[24] J. S. Slater: *Phys. Rev.* **81** (1951) 385.

[25] J. S. Slater: *The Calculation of Molecular Orbitals* Wiley, New York (1979).

[26] M. Casarin, E. Ciliberto, A. Gulino and I. Fragala: *Organometallics* **8** (1989) 900.

[27] D. S. Yang, G. M. Bancroft, J. D. Bozek, R. J. Puddephatt and J. S. Tse: *Inorg. Chem.* **29** (1990) 2487.

[28] M. V. Andreocci, M. Bossa, C. Cauletti, R. Paolesse, G. Ortaggi, T. Vondrak, M. N. Piancastelli, N. Casarin, M. Dal Colle and G. Granozzi: *J. Organomet. Chem.* **366** (1989) 343.

[29] L. S. Cederbaum and W. Domcke: *Adv. Chem. Phys.* **36** (1977) 205.

[30] W. von Niessen, W. P. Kraemer and L. S. Cederbaum: *J. Electron Spectr. Relat. Phenom.* **8** (1976) 179.

[31] W. von Niessen, L. S. Cederbaum, W. P. Kraemer and G. H. F. Diercksen: *J. Am. Chem. Soc.* **98** (1978) 2066.

[32] R. E. Moss: *Advanced Quantum Mechanics* Chapman and Hall, London (1973).

[33] F. A. Cotton: *Chemical Applications of Group Theory (3rd edition)* Wiley-Interscience, New York (1991).

[34] J. A. Salthouse and M. J. Ware: *Point Group Character Tables and Related Data* Cambridge University Press, London (1972).

[35] H. A. Jahn and E. Teller: *Proc. Roy. Soc. London* **A161** (1937) 220.

[36] J. C. Green, M. L. H. Green, P. J. Joachim, A. F. Orchard and D. W. Turner: *Phil. Trans. Roy. Soc. Lond. A* **268** (1970) 111.

[37] P. Burroughs, S. Evans, A. Hamnett, A. F. Orchard and N. V. Richardson: *J. Chem. Soc., Farad. Trans. II* **70** (1974) 1895.

[38] S. Evans, J. C. Green, P. J. Joachim, A. F. Orchard, D. W. Turner and J. P. Maier: *J. Chem. Soc., Farad. Trans. II* **68** (1972) 905.

[39] D. R. Bates: *Mon. Not. Roy. Astr. Soc.* **106** (1946) 432.

[40] S. T. Manson: *Adv. Electron Electr. Phys.* **41** (1976) 73.

[41] H. A. Bethe and E. E. Saltpeter: *Quantum Mechanics of One- and Two-Electron Atoms* Springer-Verlag, Berlin (1957).

[42] W. Heitler: *Quantum Theory of Radiation* Oxford University Press, London (1954).

[43] J. W. Cooper: *Phys. Rev. Lett.* **13** (1964) 762.

[44] J. W. Cooper: *Phys. Rev.* **128** (1962) 681.

[45] S. T. Manson and J. W. Cooper: *Phys. Rev.* **165** (1968) 126.

[46] E. J. McGuire: *Phys. Rev.* **175** (1968) 20.

[47] F. Combet-Farnoux and Y. Heno: *C.R. Acad. Sci. Ser. B* **264** (1967) 138.

[48] F. Combet-Farnoux: *J. Phys. (Paris)* **32** (1971) (C4) 7.

[49] D. J. Kennedy and S. T. Manson: *Phys. Rev. A* **5** (1972) 227.

[50] T. N. Chang: *J. Phys. B* **8** (1975) 743.

[51] S. T. Manson: *J. Electron Spectr. Relat. Phenom.* **1** (1973) 413.

[52] J. J. Yeh and I. Lindau: *At. Data Nucl. Data Tables* **32** (1985) 1.

[53] R. D. Cowan: *The Theory of Atomic Structure and Spectra* Chemical Abstracts Service, Columbus, Ohio (1981).

[54] M. O. Krause, W. A. Svensson, T. A. Carlson, G. Leroi, D. E. Ederer, D. M. P. Holland and A. C. Parr: *J. Phys. B* **18** (1985) 4069.

[55] R. G. Houlgate, J. B. West, K. Codling and G. V. Marr: *J. Electron Spectr. Relat. Phenom.* **9** (1976) 205.

[56] J. B. West, P. R. Woodruff, K. Codling and R. G. Houlgate: *J. Phys. B* **9** (1976) 407.

[57] J. L. Dehmer, A. F. Starace, U. Fano, J. Sugar and J. W. Cooper: *Phys. Rev. Lett.* **26** (1971) 1521.

[58] L. C. Davis and L. A. Feldkamp: *Phys. Rev. A* **17** (1978) 2012.

[59] L. C. Davis and L. A. Feldkamp: *Phys. Rev. B* **23** (1981) 6239.

[60] U. Fano: *Phys. Rev.* **124** (1961) 1866.

[61] U. Fano and J. W. Cooper: *Phys. Rev. A* **137** (1965) 1364.

[62] R. Bruhn, E. Schmidt, H. Schröder and B. Sonntag: *J. Phys. B* **15** (1982) 2807.

[63] R. Bruhn, E. Schmidt, H. Schröder and B. Sonntag: *Phys. Lett.* **90A** (1982) 41.

[64] M. O. Krause, T. A. Carlson and A. Fahlman: *Phys. Rev. A* **30** (1984) 1316.

[65] P. H. Kobrin, U. Becker, C. M. Truesdale, D. W. Lindle, H. G. Kerkhoff and D. A. Shirley: *J. Electron Spectr. Relat. Phenom.* **34** (1984) 129.

[66] M. Richter, M. Meyer, M. Pahler, T. Prescher, E. von Raven, B. Sonntag and H. E. Wetzel: *Phys. Rev. A* **39** (1989) 5666.

[67] U. Gelius in *Electron Spectroscopy* North-Holland, Amsterdam (1972).

[68] U. Gelius and K. Siegbahn: *Faraday Discuss. Chem. Soc.* **54** (1972) 257.

[69] V. G. Yarzhensky, V. I. Nefedov, M. Y. Amusia, N. A. Cherepkov and L. V. Chernysheva: *J. Electron Spectr. Relat. Phenom.* **19** (1980) 123.

[70] P. R. Hilton, S. Nordholm and N. S. Hush: *J. Electron Spectr. Relat. Phenom.* **18** (1980) 101.

[71] G. Cooper: *D. Phil. Thesis* Oxford (1987).

[72] C. M. Redfern: *D. Phil. Thesis* Oxford (1988).

[73] N. Kaltsoyannis: *Part II Thesis* Oxford (1989).

[74] G. Cooper, J. C. Green, M. P. Payne, B. R. Dobson and I. H. Hillier: *J. Am. Chem. Soc.* **109** (1987) 3836.

[75] G. Cooper, J. C. Green and M. P. Payne: *Mol. Phys.* **63** (1988) 1031.

[76] J. B. Brennan, J. C. Green and C. M. Redfern: *J. Am. Chem. Soc.* **111** (1989) 2373.

[77] J. B. Brennan, J. C. Green, C. M. Redfern and M. A. MacDonald: *J. Chem. Soc., Dalton Trans.* (1990) 1907.

[78] T. A. Carlson, M. O. Krause, F. A. Grimm, P. Keller and J. W. Taylor: *J. Chem. Phys.* **77** (1982) 5340.

[79] T. A. Carlson, M. O. Krause and F. A. Grimm: *J. Chem. Phys.* **77** (1982) 1701.

[80] T. A. Carlson, A. Fahlman, M. O. Krause, P. R. Keller, J. W. Taylor, T. Whitley and F. A. Grimm: *J. Chem. Phys.* **80** (1984) 3521.

[81] G. M. Bancroft, B. W. Yates, K. H. Tan and L. L. Coatsworth: *J. Chem. Soc., Chem. Commun.* (1984) 1613.

[82] S. V. Didziulis, S. L. Cohen, A. A. Gewirth and E. I. Solomon: *J. Am. Chem. Soc.* **110** (1988) 250.

[83] K. D. Butcher, S. V. Didziulis, B. Briat and E. I. Solomon: *J. Am. Chem. Soc.* **112** (1990) 2231.

[84] K. D. Butcher, M. S. Gebhard and E. I. Solomon: *Inorg. Chem.* **29** (1990) 2067.

[85] J. L. Dehmer and D. Dill: *J. Chem. Phys.* **65** (1976) 5327.

[86] N. Padial, G. Csanak, B. V. McCoy and P. W. Langhoff: *J. Chem. Phys.* **69** (1978) 2992.

[87] J. W. Davenport: *Phys. Rev. Lett.* **36** (1976) 945.

[88] T. Gustafsson: *Surf. Sci.* **94** (1980) 593.

[89] V. Schmidt: *Phys. Lett. A* **45** (1973) 63.

[90] M. N. Piancastelli, P. R. Keller, J. W. Taylor, F. A. Grimm, T. A. Carlson, M. O. Krause and D. Lichtenberger: *J. Electron Spectr. Relat. Phenom.* **34** (1984) 205.

[91] A. W. Potts, I. Novak, G. V. Quinn, B. R. Dobson and I. H. Hillier: *J. Phys. B* **18** (1985) 3177.

[92] R. M. Holmes and G. V. Marr: *J. Phys. B* **18** (1980) 3177.

[93] P. R. Keller, J. W. Taylor, F. A. Grimm and T. A. Carlson: *Chem. Phys.* **90** (1984) 147.

CHAPTER TWO

ELECTRON LOCALISATION IN TRANSITION METAL SANDWICH COMPOUNDS - $[Mo(\eta\text{-}C_6H_5Me)_2]$ AND $[M(\eta\text{-}C_7H_7)(\eta\text{-}C_5H_4R)]$ (M=Ti, Nb, Mo; R=H : M=Ta; R=Me)

2.1 Introduction

Although a substantial chemistry of $(\eta\text{-}C_7H_7)$-M derivatives of the group IV to VI metals (except Ta) is known, the nature of the $(\eta\text{-}C_7H_7)$-M bond is not understood in detail. Indeed, the formal oxidation state of the η-cycloheptatrienyl ligand in its complexes is open to debate [1], as both a +1 and a -3 formal charge satisfy the Hückel 4n+2 rule for aromaticity. It was therefore decided to conduct a PE spectroscopic study of complexes of the type $[M(\eta\text{-}C_7H_7)(\eta\text{-}C_5H_4R)]$ using synchrotron radiation, in order to assess the localisation properties of the valence electrons. Sandwich compounds are particularly well suited to this, since they sublime readily to give PE spectra with well separated bands of metal, ligand and mixed metal/ligand character. By comparing features in the cross sections of metal-based ionisation bands with those of more ligand-based bands, a measure of the degree of metal character in the valence MOs can be obtained.

The bonding in bis-arene complexes is less uncertain than in the isoelectronic $[M(\eta\text{-}C_7H_7)(\eta\text{-}C_5H_4R)]$ systems, and has been investigated by a variety of techniques, including PES [2-4], electron spin resonance (ESR) spectroscopy [4], ab initio SCF [5] and SCF-Xα [6] calculations and gas-phase electronic absorption spectroscopy [7, 8]. By studying such a well understood class of compound, it was hoped to establish a sound basis for interpreting the results from the mixed ring species. The electronic structure of bis-arene systems is such that they too have MOs ranging from almost completely metal-localised to essentially ligand-based. $[Cr(\eta\text{-}C_6H_6)_2]$ and $[Mo(\eta\text{-}C_6H_6)_2]$ have already been the subject of a variable photon energy PE spectroscopic investigation [9], but while good data were obtained for the chromium compound, those on $[Mo(\eta\text{-}C_6H_6)_2]$ were less satisfactory. This provided further incentive to acquire a good data set on a second row bis-arene

system, and it was decided to study [Mo(η-$C_6H_5Me)_2$] rather than [Mo(η-$C_6H_6)_2$] on account of the greater volatility of the former.

2.2 [Mo(η-$C_6H_5Me)_2$]

2.2.1 Bonding and interpretation of the photoelectron spectrum

A qualitative MO scheme for [Mo(η-$C_6H_6)_2$], in D_{6h} symmetry, is given in Figure 2.1. The axis system employed is shown below. [Cr(η-$C_6H_6)_2$] has been shown to have an eclipsed formation in both the solid [10] and gas [11] phases and [Mo(η-$C_6H_6)_2$] is assumed to have the same structure. The MO diagram for [Mo(η-$C_6H_5Me)_2$] will not differ significantly and, if it is taken to have $D_{\infty h}$ symmetry (an approximation made in many treatments [12]), the symmetry labels for the MOs are the same as for [Mo(η-$C_6H_6)_2$]. Only those arene π orbitals which interact most with the metal valence orbitals are included.

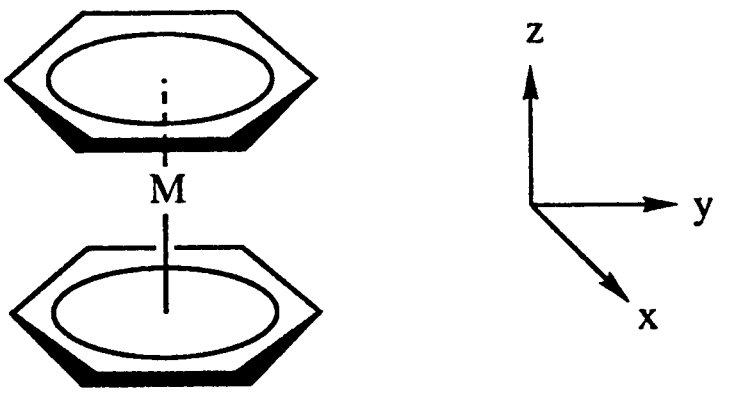

In both D_{6h} and $D_{\infty h}$ symmetries, the metal d orbitals split into three sets; d_{z^2} (a_{1g}), d_{xz}, d_{yz} (e_{1g}) and $d_{x^2-y^2}$, d_{xy} (e_{2g}), which are of σ, π and δ symmetry respectively with respect to the metal-ring axes. The σ orbital is essentially metal-carbon non-bonding (due to the fact that the nodal cone of the d_{z^2} orbital intersects the metal-directed lobes of the p orbitals of the rings close to their region of maximum electron density [4]), the π orbitals strongly antibonding and the δ orbitals metal→carbon back-bonding in nature. Metal-carbon bonding is also generated through interaction of the metal d-based e_{1g} orbitals with the occupied e_{1g} ligand set.

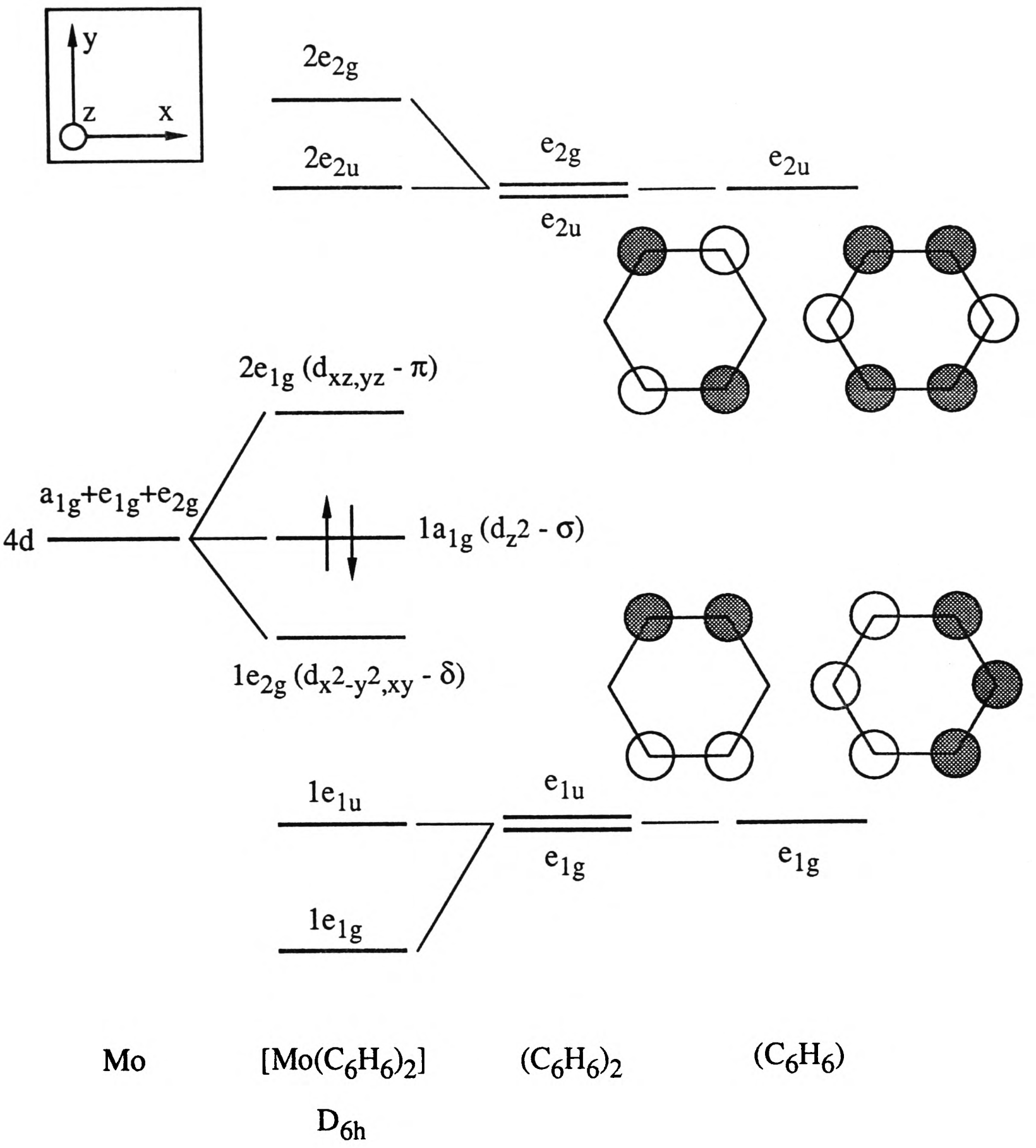

Figure 2.1 : qualitative MO diagram for [Mo(η-C_6H_6)$_2$]. Shadings indicate the phases of the carbon $2p_z$ AOs

Figure 2.2 shows the PE spectrum of [Mo(η-$C_6H_5Me)_2$], obtained with synchrotron radiation at photon energies of 30 and 50 eV. The assignment of the spectrum is as given by previous workers [3]. Bands E and F can be assigned by analogy with the PE spectrum of toluene [13], E1 to ionisations from ligand carbon-carbon σ and the totally symmetric π bonding MOs, E2 to carbon-carbon and carbon-hydrogen σ bonding orbitals, E3 to deeper lying carbon-hydrogen bonding MOs and F to ionisations from MOs with substantial carbon 2s character. Below 10.5 eV are four bands, two of which (bands C and D) overlap significantly. Band A is assigned to the metal-based $1a_{1g}$ HOMO. Band B is assigned to the $1e_{2g}$ set of MOs; the greater width of this band implies greater vibrational excitation in the molecular ion, reflecting the metal→carbon back-bonding character of these MOs (Chapter 1.3.2). Bands C and D are assigned to the $1e_{1u}$ and $1e_{1g}$ complex MOs respectively. The metal-carbon bonding nature of the $1e_{1g}$ set results in their being stabilised with respect to the non-bonding $1e_{1u}$ MOs, and consequently they have the higher IE. IEs and assignments are summarised in Table 2.1.

Table 2.1 : assignment of the PE spectrum of [Mo(η-$C_6H_5Me)_2$] [3]

Band	IE (eV) [a]	Ion state	Related MO
A	5.32	$^2A_{1g}$	$1a_{1g}$
B	6.33	$^2E_{2g}$	$1e_{2g}$
C	9.05	$^2E_{1u}$	$1e_{1u}$
D	9.75	$^2E_{1g}$	$1e_{1g}$
E1, E2, E3, F	> 10.5		ligand σ and π

[a] Data from reference [3]

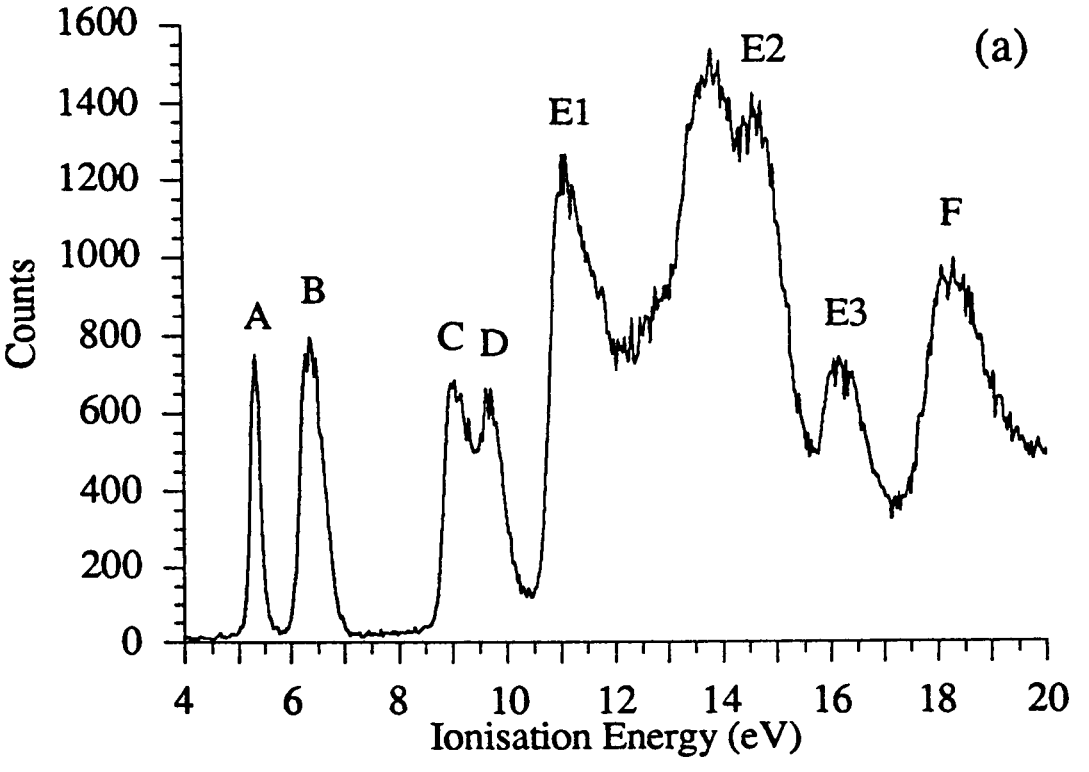

Figure 2.2 : the PE spectrum of [Mo(η-$C_6H_5Me)_2$], acquired at (a) 30 and (b) 50 eV

2.2.2 Results and discussion

The PE spectrum of [Mo(η-$C_6H_5Me)_2$] has been obtained over the incident photon energy range 24-100 eV. Band areas have been derived for bands A-D, and their RPPICS have been calculated. The large number of MOs ionising above an IE of 10.5 eV makes detailed assignment impossible, and no attempt was made to produce cross sections for bands E and F. The RPPICS of bands A-D are shown in Figure 2.3 and will be discussed in two parts. First, the predominantly metal d ionisations - the $1a_{1g}^{-1}$ (A) and $1e_{2g}^{-1}$ (B) bands - and second the $1e_{1u}^{-1}$ (C) and $1e_{1g}^{-1}$ (D) bands.

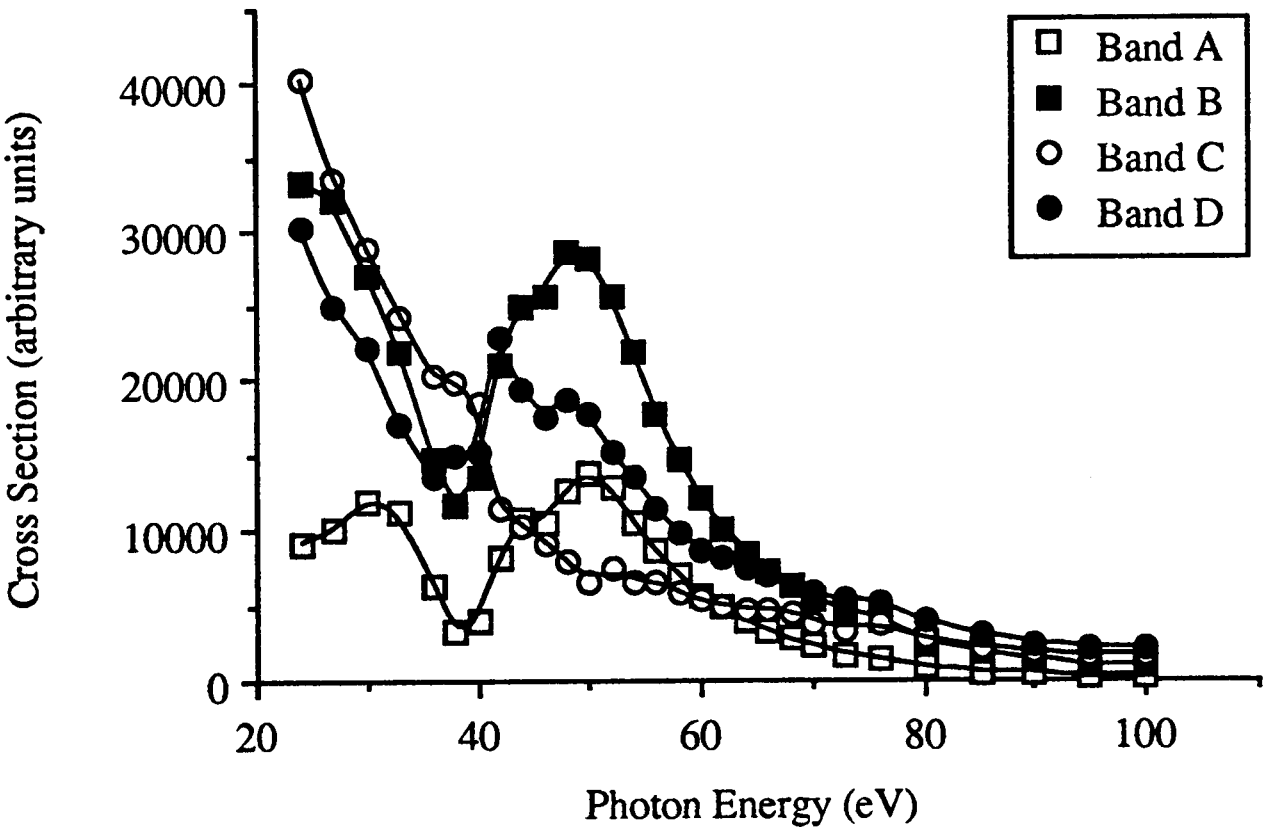

Figure 2.3 : RPPICS of bands A-D in the PE spectrum of [Mo(η-$C_6H_5Me)_2$]

2.2.2 (a) The $1a_{1g}^{-1}$ and $1e_{2g}^{-1}$ bands

The RPPICS of bands A and B are given in Figure 2.4 (a) and their renormalised BRs in Figure 2.4 (b). The RPPICS of both bands show features close to the 4p ionisation potentials of free molybdenum ($^2P_{3/2}$ = 42 eV, $^2P_{1/2}$ = 45 eV [14]), which are attributable to resonant photoemission of 4d electrons in the vicinity of 4p→4d giant resonant absorption (Chapter 1.4.3 (c)). This is represented by the equation

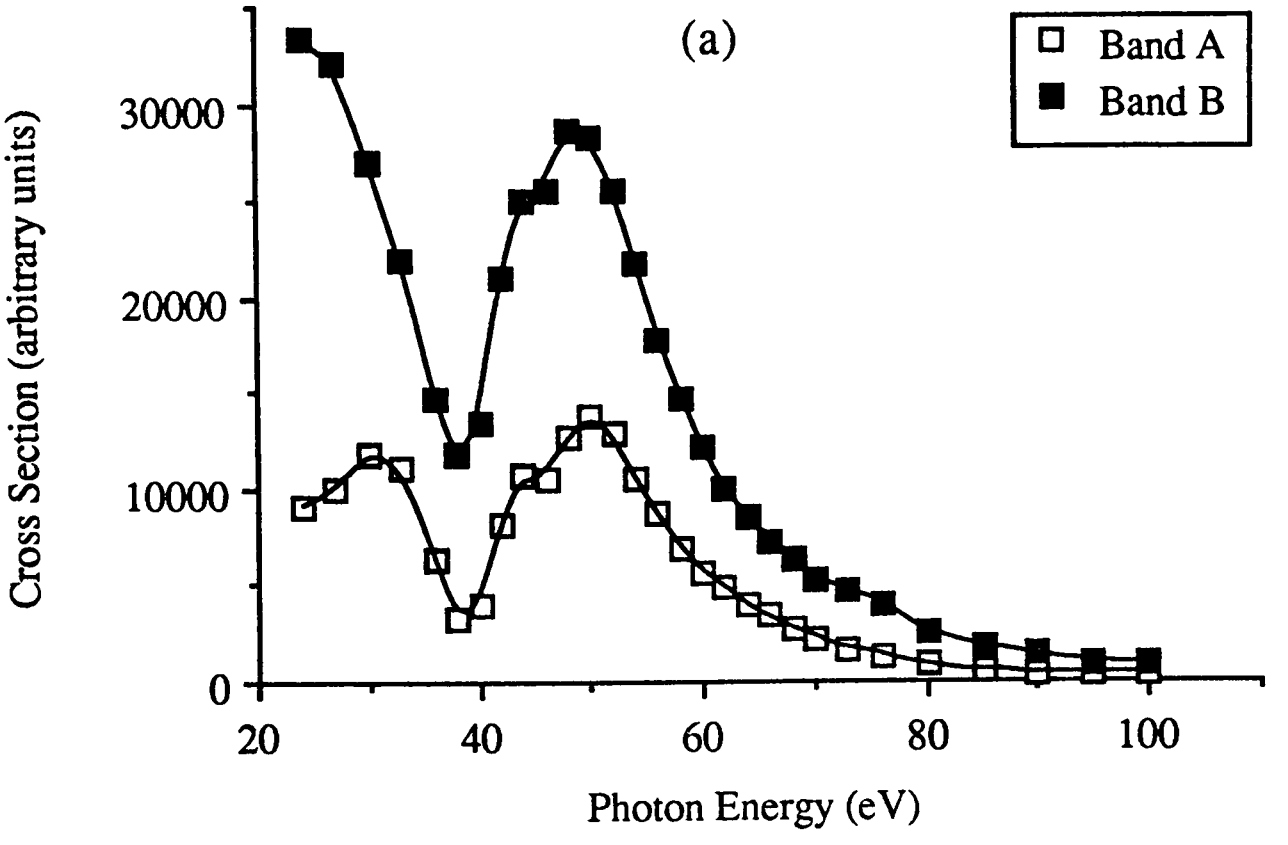

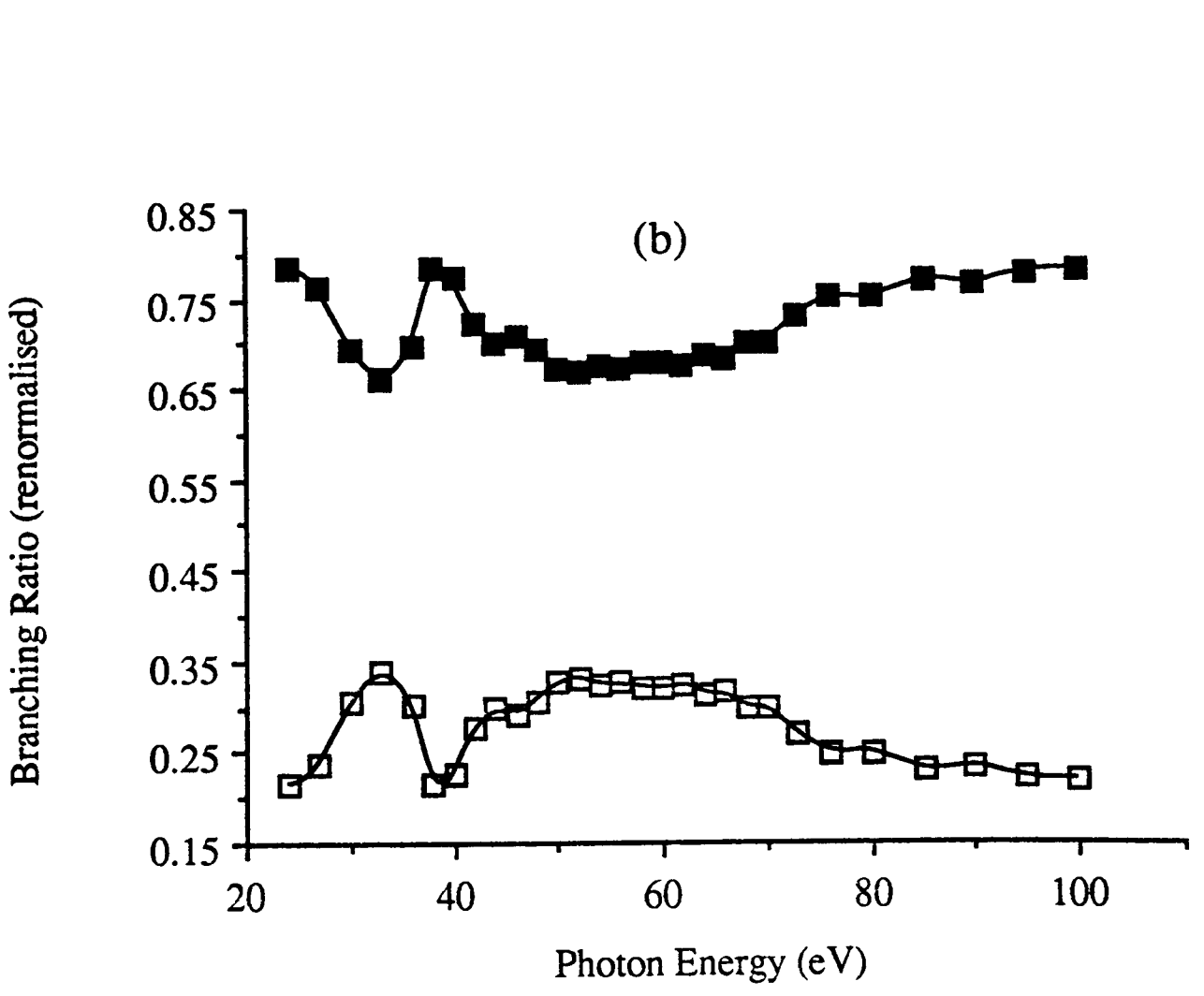

Figure 2.4 : (a) RPPICS and (b) renormalised BRs of bands A and B in the PE spectrum of $[Mo(\eta\text{-}C_6H_5Me)_2]$

$$(4p)^6(1e_{2g})^4(1a_{1g})^2(2e_{1g})^0 + h\nu \rightarrow (4p)^5(1e_{2g})^4(1a_{1g})^2(2e_{1g})^1$$

The irreducible representations of the $4p^5$ configuration transform as $(A_{1u} + E_{1u})$ in $D_{\infty h}$ symmetry, so that the states arising from the $(4p)^5(1e_{2g})^4(1a_{1g})^2(2e_{1g})^1$ configuration are given by the direct product

$$(A_{1u} + E_{1u}) \times E_{1g} = {}^1E_{1u} + {}^1A_{1u} + {}^1A_{2u} + {}^1E_{2u} + {}^3E_{1u} + {}^3A_{1u} + {}^3A_{2u} + {}^3E_{2u}$$

The electric dipole selection rule allows transitions only to $A_{1u} + E_{1u}$ excited states, and in the LS coupling limit we have the additional constraint that $\Delta S = 0$, so that the allowed final states are ${}^1A_{1u} + {}^1E_{1u}$. The 4p and $2e_{1g}$ orbitals are in close spatial proximity to each other and, as for atomic np→nd giant resonant absorption [15], exchange interactions in the excited states will be large. Owing to the resultant singlet-triplet splitting, almost all of the p→d oscillator strength lies above the 4p IEs. Autoionisation

$$(4p)^5(1e_{2g})^4(1a_{1g})^2(2e_{1g})^1 \rightarrow (4p)^5(1e_{2g})^4(1a_{1g})^2(2e_{1g})^0 + e^-$$

is therefore possible, along with the super-Coster-Kronig (SCK) (Chapter 1.4.3 (c)) decay processes

$$(4p)^5(1e_{2g})^4(1a_{1g})^2(2e_{1g})^1 \rightarrow \begin{cases} (4p)^6(1e_{2g})^3(1a_{1g})^2(2e_{1g})^0 + e^- \\ (4p)^6(1e_{2g})^4(1a_{1g})^1(2e_{1g})^0 + e^- \end{cases}$$

the final states of which are identical to those produced by direct photoionisation of the $1e_{2g}$ or $1a_{1g}$ MOs

$$(4p)^6(1e_{2g})^4(1a_{1g})^2(2e_{1g})^0 + h\nu \rightarrow \begin{cases} (4p)^6(1e_{2g})^3(1a_{1g})^2(2e_{1g})^0 + e^- \\ (4p)^6(1e_{2g})^4(1a_{1g})^1(2e_{1g})^0 + e^- \end{cases}$$

Inter-channel coupling in the corresponding final states in the direct and resonance ionisation processes should lead to two overlapping Fano profiles (Chapter 1.4.3 (c)), resulting from absorption to the $^1A_{1u}$ and $^1E_{1u}$ excited states, for the RPPICS of the $1e_{2g}^{-1}$ and $1a_{1g}^{-1}$ bands.

Fano resonance profiles with sloping background cross sections were fitted to the experimentally determined RPPICS of bands A and B, using equation (1.9). The values of the Fano parameters obtained are given in Table 2.2. Satisfactory fits were obtained to two Fano profiles having identical line profile indices. (N.B. when fitting two profiles to equation (1.9), the Fano function fitting program constrains the q values of both profiles to be the same).

Table 2.2 : Fano parameters obtained from the RPPICS of bands A and B in the PE spectrum of $[Mo(\eta\text{-}C_6H_5Me)_2]$

Band	q	E_r (eV)	σ_0	Γ	X	hν range (eV)
A	1.83	42.0	2612	8.63	0.025	40-70
		48.0		8.08		
B	1.15	42.6	11486	11.15	0.029	40-65
		48.0		0.92		

Three explanations present themselves as to why two Fano profiles were required to produce adequate fits

(a) the splitting of the $^1A_{1u}$ and $^1E_{1u}$ states of the $(4p)^5(1e_{2g})^4(1a_{1g})^2(2e_{1g})^1$ configuration is significant

(b) spin-orbit coupling in the 4p subshell

(c) the presence of a molecular shape resonance (Chapter 1.4.4 (d)) in the same photon energy range as the p→d resonance.

Spin-orbit coupling, which is generally small for second row transition metals, is disfavoured by the RPPICS data obtained on $[Ru(\eta\text{-}C_5H_5)_2]$ [16] in which a single Fano profile was sufficient to fit the data on the $1a_1'^{-1}$ and $1e_2'^{-1}$ bands. (The $1a_1'$ $[M(\eta\text{-}C_5H_5)_2]$ and $1a_{1g}$ $[M(arene)_2]$ MOs and the $1e_2'$ $[M(\eta\text{-}C_5H_5)_2]$ and $1e_{2g}$ $[M(arene)_2]$ MOs have similar localisation properties. The former are almost metal-carbon non-bonding, whilst the latter are metal→carbon back-bonding). Metal-based spin-orbit coupling effects will be greater in ruthenium complexes than molybdenum, reflecting the trend in the neutral atoms (e.g. the 4p IEs of ruthenium are at 49 and 53 eV [14]).

Large excited state splitting remains a possibility, although a coincident shape resonance is the most likely explanation. The features with maxima at 42 eV in the RPPICS of the $1a_{1g}^{-1}$ and $1e_{2g}^{-1}$ bands of $[Cr(\eta\text{-}C_6H_6)_2]$ are almost certainly due to a shape resonance [9, 17], occurring as they do at the same photon energy as the shape effect in the metal d band RPPICS of $[Cr(CO)_6]$ [18]. A molecular shape resonance in the equivalent bands of $[Mo(CO)_6]$ was not observed, but it was noted that the large p→d resonance may well be obscuring the effect. The RPPICS data of bands C and D, which are discussed below, provide good evidence to suggest that two resonance phenomena are occurring almost coincidentally. Consequently the Fano parameters given in Table 2.2 are suspect, as the equation from which they are derived (equation (1.9)) assumes that the direct ionisation channel interacts with only one resonance channel [19, 20]. Further examination of these resonance features is given below.

The cross section of band A rises from 24 eV to a maximum at 30 eV. A maximum was found in the RPPICS of the $1a_1'^{-1}$ band of $[Ru(\eta\text{-}C_5H_5)_2]$ at an incident photon energy of 24 eV, which was attributed to the delayed maximum phenomenon (Chapter 1.4.3 (b)). The photon energy of this maximum was found to be ca. 4.5 eV higher than that predicted by calculations on atomic ruthenium [21]. Similar calculations on atomic molybdenum predict that the delayed maximum of the 4d subshell should occur at a PE KE of ca. 15 eV. It might be expected that the $1a_{1g}^{-1}$ band would have a similar value for any

delayed maximum, as the evidence suggests that this MO is almost entirely molybdenum 4d in character [4, 8]. The RPPICS maximum in band A occurs at a PE KE of 24.7 eV (the IE of band A is 5.3 eV), ca. 10 eV higher than the predicted value. Given the magnitude of this discrepancy, it may be that a shape effect is once again the cause of this feature.

The BR plot (Figure 2.4 (b)) of bands A and B clearly shows this low photon energy feature in band A, and indicates that both of the RPPICS maxima occur more strongly in band A than band B. Another interesting feature of this plot is the gain in intensity of band B relative to band A at high photon energies (70-100 eV). This illustrates the approaching Cooper minimum (Chapter 1.4.3 (a)) in the cross section of the molybdenum 4d subshell (calculated to occur at a PE KE of 82 eV [21]), an effect that will be seen more prominently in the cross section of band A on account of the significant carbon 2p AO contribution to the $1e_{2g}$ MOs (band B).

All of the evidence presented supports the assertion that the $1a_{1g}$ MO contains almost pure metal d orbital character, while the $1e_{2g}$ set has a significant carbon 2p contribution. The relative magnitudes of the p→d resonance phenomena in the $1a_{1g}^{-1}$ and $1e_{2g}^{-1}$ bands and the cross section behaviour in the region of the molybdenum 4d Cooper minimum suggest very strongly that the metal $4d_{z2}$ atomic orbital remains largely unaltered on complex formation.

2.2.2 (b) The $1e_{1u}^{-1}$ and $1e_{1g}^{-1}$ bands

The RPPICS and renormalised BRs of bands C and D are presented in Figure 2.5, from which it can be seen that band C ($1e_{1u}^{-1}$) has only very small features in the generally monotonic cross section fall off with increasing photon energy, behaviour typical of ligand-localised ionisations. The steep fall off at low photon energies is reduced somewhat in the shape and p→d resonance region, with a small maximum at 52 eV, but it is clear that the RPPICS of band C is markedly different from those of bands A, B and D.

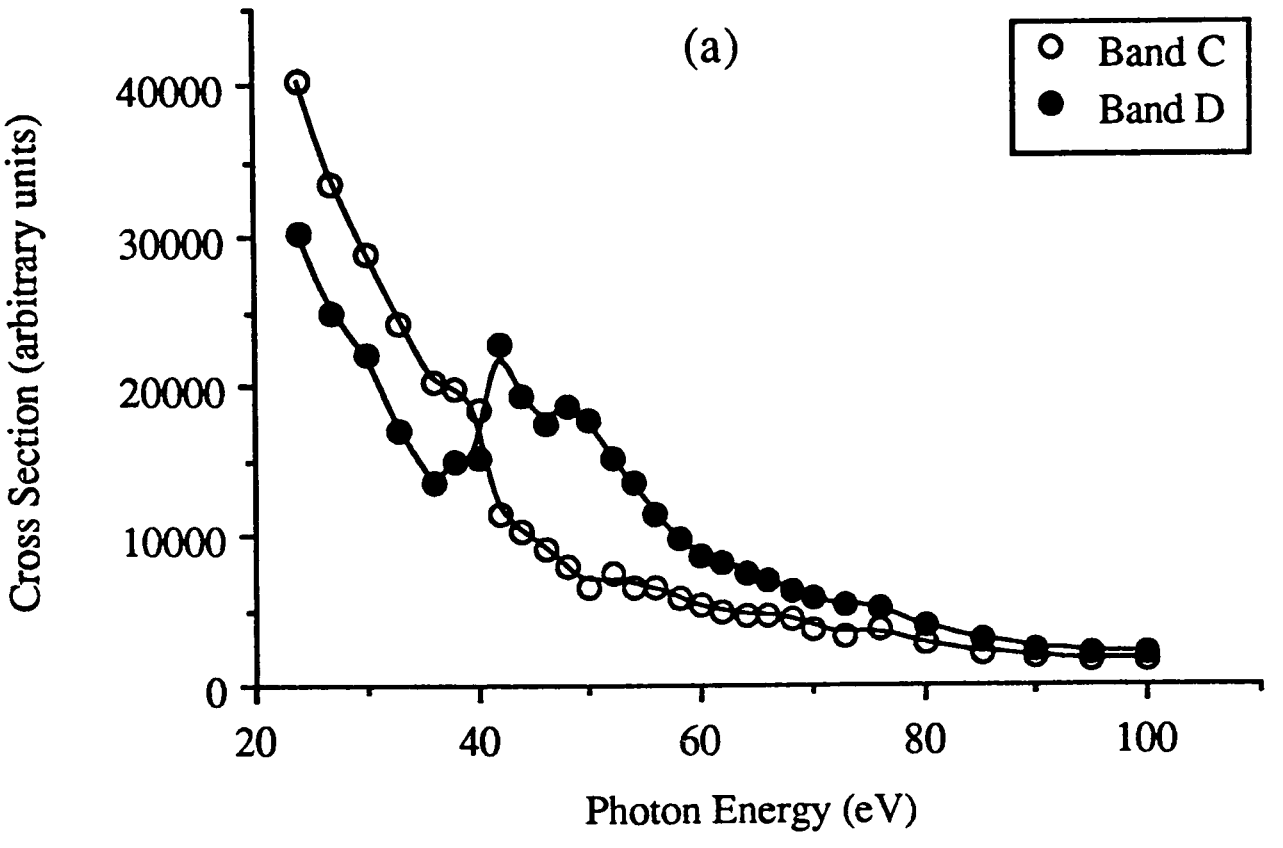

Figure 2.5 : (a) RPPICS and (b) renormalised BRs of bands C and D in the PE spectrum of $[Mo(\eta\text{-}C_6H_5Me)_2]$

Band D has a pronounced feature in its cross section in the photon energy range 36-70 eV, similar to those of bands A and B. The BR plot of the $1e_{1u}^{-1}$ and $1e_{1g}^{-1}$ bands (Figure 2.5 (b)) strikingly illustrates the metal d contribution to the $1e_{1g}$ MOs. The key difference between the RPPICS of the metal-based ionisations and those stemming from more ligand-based MOs is the relative magnitudes of the two contributory resonance phenomena. The shape effect, which produces a low photon energy shoulder to the main RPPICS maxima at ca. 50 eV in bands A and B, is the dominant feature in the RPPICS of band D, in line with the much reduced metal d content of the $1e_{1g}$ MOs with respect to the $1e_{2g}$ and $1a_{1g}$ MOs. The RPPICS of band D leave little doubt that the cross section enhancement of bands A and B in the photon energy range 40-70 eV arises from two resonance effects, and thus the Fano parameters obtained on these bands must be regarded with a great deal of caution.

2.2.2 (c) Shape resonances in $[M(\eta\text{-}C_5H_5)_2]$ and $[M(arene)_2]$

The possible continuum channels available for ionisation of electrons from the valence MOs of $[Mo(\eta\text{-}C_6H_5Me)_2]$ are given in Table 2.3.

Table 2.3 : possible channels for ionisation from the valence MOs of $[Mo(\eta\text{-}C_6H_5Me)_2]$

Molecular orbital	Continuum ionisation channels
$1a_{1g}$	$\varepsilon a_{1u} + \varepsilon e_{1u}$
$1e_{2g}$	$\varepsilon e_{1u} + \varepsilon e_{2u} + \varepsilon e_{3u}$
$1e_{1u}$	$\varepsilon a_{1g} + \varepsilon a_{2g} + \varepsilon e_{1g} + \varepsilon e_{2g}$
$1e_{1g}$	$\varepsilon a_{1u} + \varepsilon a_{2u} + \varepsilon e_{1u} + \varepsilon e_{2u}$

An important point to notice is that all of the g symmetry MOs can ionise solely into u symmetry continuum channels, while the $1e_{1u}$ MO has only g symmetry channels available. It may well be that the shape resonance occurring in band D at 42 eV and in bands A and B as a low photon energy shoulder to the p→d resonance maximum at 50 eV

is symmetry controlled, in that the only band in which it does not occur is the $1e_{1u}^{-1}$ band (band C). Alternatively, it may be dependent upon the metal d orbital content of the MO from which ionisation is occurring. One of the possible ways of envisaging shape resonances is that the ionising electron is initially excited to a quasi-bound antibonding MO (Chapter 1.4.4 (d)), a state which then decays into the molecular ion plus PE. Good overlap between bound and quasi-bound MOs is an important factor in the process, and it may well be that the quasi-bound intermediate MO(s) in this shape resonance are strongly localised in the region occupied by the metal atom. Consequently only MOs with significant metal AO (in the case of the valence MOs, metal d AO) content will experience the shape resonance. The possibility that the resonance is both symmetry- and metal d AO content controlled cannot be discounted.

If the RPPICS maximum of band A at 30 eV is due to a shape resonance, it cannot be simply a symmetry controlled effect, in that it is not mirrored in any other band. It is possible, however, that it is controlled by the metal d AO content of the ionising MO, and is not seen in any of the other bands because the carbon 2p AO content dominates their RPPICS at such low incident photon energies to the point at which any metal d AO derived shape effect is swamped.

There is a maximum in the RPPICS of the $1a_1'^{-1}$ and $1e_2'^{-1}$ bands of the metallocenes $[M(\eta\text{-}C_5H_5)_2]$ (M = Fe, Ru, Os [16]) between 38-50 eV which is stronger in the $1a_1'^{-1}$ bands than the $1e_2'^{-1}$. As indicated earlier, the valence MOs of the metallocenes are very similar to those of bis-arene compounds in terms of their localisation properties. It is curious, therefore, that there should be no shape effect in either of the e_1 bands of the metallocenes. One possible explanation for this is that the higher incident photon energy shape resonance of $[Mo(\eta\text{-}C_6H_5Me)_2]$ does not occur in any of the bands of $[M(\eta\text{-}C_5H_5)_2]$, but that the one seen at 30 eV in band A of $[Mo(\eta\text{-}C_6H_5Me)_2]$ does, albeit at higher incident photon energies. This explanation is supported by two observations. First, the small shape resonance in the metallocene $1e_2'^{-1}$ bands is visible by virtue of the fact that the carbon 2p AO contribution to the RPPICS of these bands is smaller at the higher incident photon energies, and does not swamp the metal d AO derived effects as is the case

in band B of [Mo(η-$C_6H_5Me)_2$] at 30 eV. Secondly, there are very large maxima at 42 eV in the RPPICS of the $e_1''^*$ metal-ligand antibonding MOs, populated by one and two electrons respectively in the 19- and 20-electron [Co(η-$C_5H_5)_2$] and [Ni(η-$C_5H_5)_2$] complexes [22]. As these MOs are much more metal-localised than their bonding counterparts, a correlation between metal d AO character and the existence of this particular shape resonance seems probable.

2.3 [M(η-C_7H_7)(η-C_5H_4R)] (M=Ti, Nb, Mo; R=H) (M=Ta; R=Me)

2.3.1 Electronic structure of mixed sandwich compounds

The bonding in mixed sandwich molecules has been the subject of a number of both theoretical and experimental investigations [1, 3, 4, 12, 23-27], but only those aspects relevant to this work will be considered here. The X-ray crystal structures of [M(η-C_7H_7)(η-C_5H_5)] (M=Ti [28], V [29] and Cr [25]) show that the hydrocarbon rings are planar and parallel, and it may be reasonably assumed that the second and third row compounds discussed here have similar structures. The molecules may be assigned in the $C_{\infty v}$ point group [3, 12], and a qualitative MO diagram is given in Figure 2.6, based on the following axis system

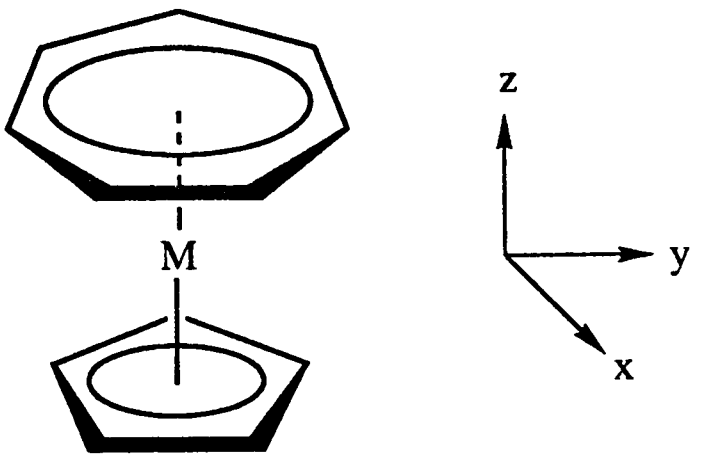

The MOs are filled up to and including the $1e_2$ set in all four compounds. In [Nb(η-C_7H_7)(η-C_5H_5)] and [Ta(η-C_7H_7)(η-C_5H_4Me)], there is one electron in the $1a_1$ level, which is doubly occupied in [Mo(η-C_7H_7)(η-C_5H_5)]. The metal d orbitals are once again split into three sets, but the ligand contributions to these levels are different to the

analogous MOs of the bis-arene compounds. Figure 2.7 shows the relative energies of the pπ MOs in cyclic C_nH_n (n=5-7) systems, calculated using the Hückel approach [30]. It can be seen that the ring e MOs become progressively more stabilised with increasing ring size. This is of central importance in that the e_1 and e_2 ligand levels in [M(η-C_7H_7)(η-C_5H_5)] species are no longer of the same energy for the two rings, as is the case in the bis-arene systems. The relative energies of the ligand e orbitals and the metal d orbitals are such that the main contribution to metal-ligand bonding for the cyclopentadienyl rings is from the π MOs (e_1), whereas the δ MOs (e_2) are the more important for the seven-membered ring.

Symmetry permits mixing of both ring e_1 levels with the metal e_1 orbitals, and with each other. On energy grounds the (η-C_7H_7) e_1 orbitals are expected to be the principal contributor to the $1e_1$ complex MOs, and the (η-C_5H_5) e_1 levels to be the main contributor to the $2e_1$.

The (η-C_7H_7) e_2 orbital content of the $1e_2$ complex MOs is of key importance in determining the nature of the (η-C_7H_7)-M bond. If these MOs are found to be largely metal-localised, the conclusion must be that there is relatively little metal→carbon back-bonding (the (η-C_7H_7) ring is functioning more as a +1 ligand) whereas if a substantial ligand contribution is revealed, the metal-ligand δ interaction is strong (the (η-C_7H_7) ring is functioning more as a -3 ligand).

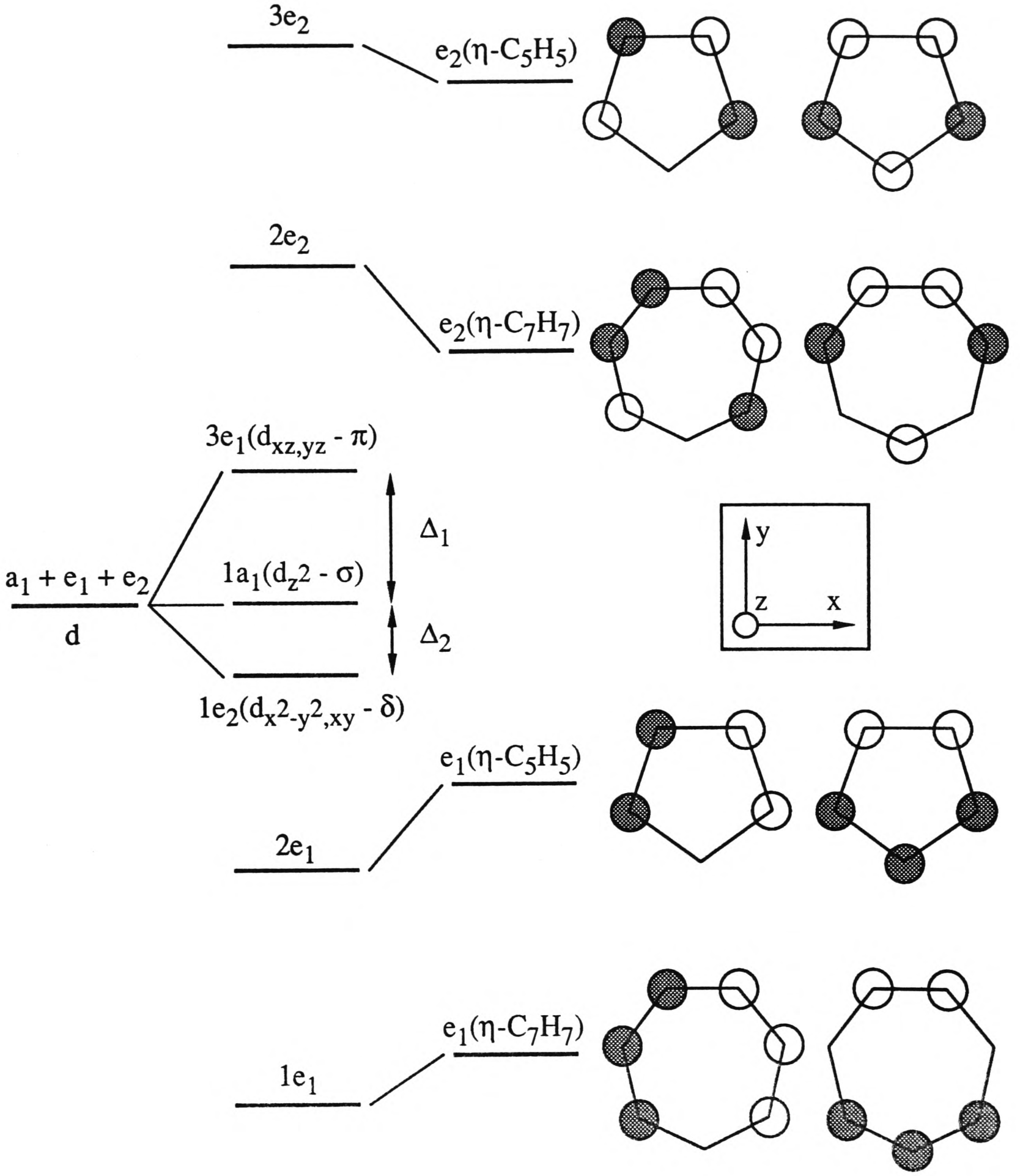

Figure 2.6 : qualitative MO diagram for [M(η-C_7H_7)(η-C_5H_5)] compounds

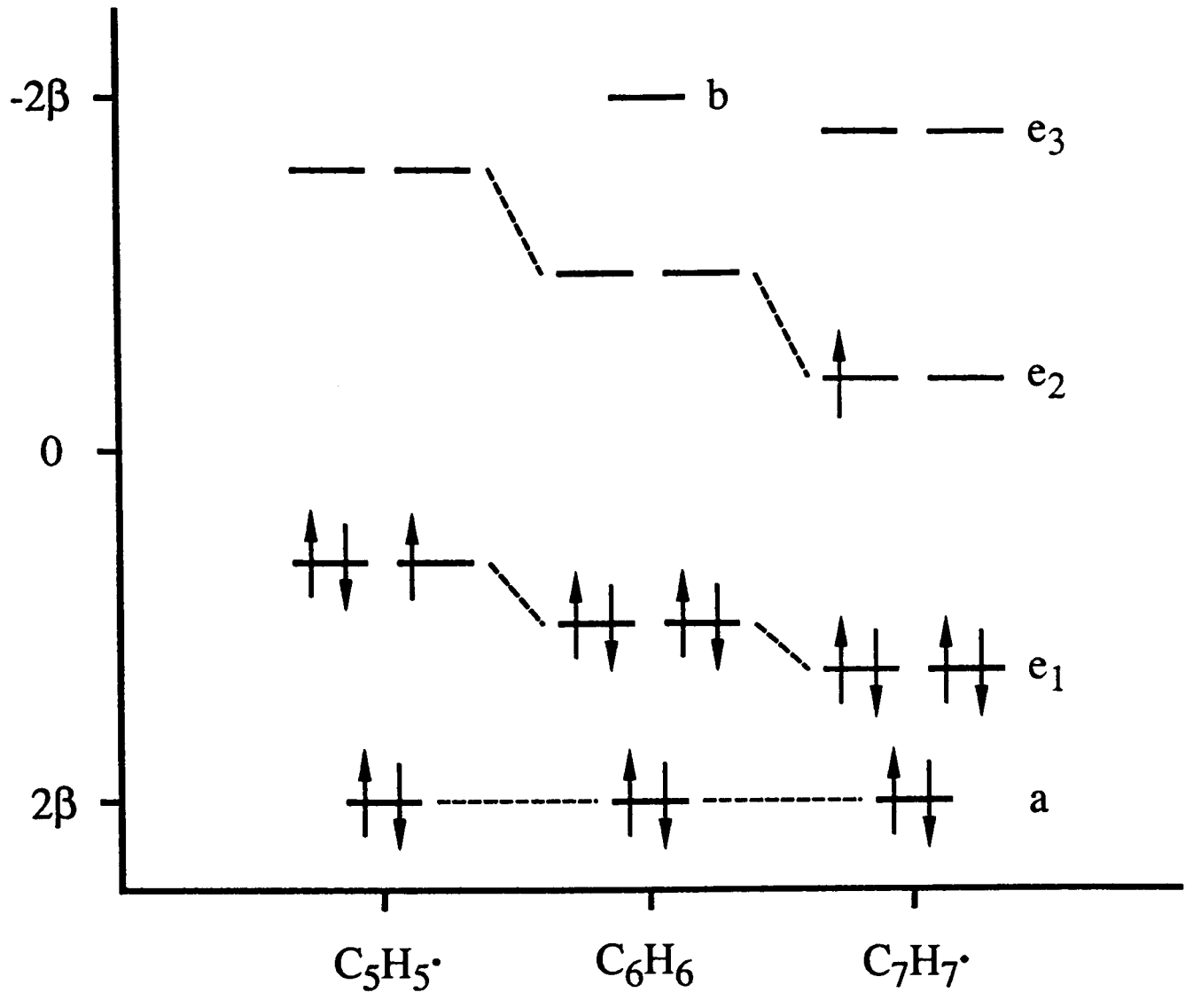

Figure 2.7 : Hückel energies of the carbocyclic ring π orbitals

The +1 formalism for the charge on the (η-C_7H_7) ring is attractive, as it leaves the ring with six pπ electrons, isoelectronic with (η-cyclopentadienyl) and arene rings. Thus [Ti(η-C_7H_7)(η-C_5H_5)] was considered to contain a Ti(0) (d^4) metal centre [31]. Subsequent evidence, however, suggested that the unipositive formalism was misleading. An extensive series of compounds [M(η-C_7H_7)L_2X] (M=Ti, Zr) exists, where L=O-, N- and P- donor ligands and X=halides and alkyl groups. The typically "harder" L ligands (ethers, amines) are more tightly bound than the "softer" phosphine ligands [1, 32], suggesting that the metal centre is more d^0 than d^4 in character. A similar conclusion can be drawn from the infra-red stretching frequency of the CO adduct in [Nb(η-C_7H_7)(η-C_5H_4Me)CO]$^+$ [27, 32], which at 2086 cm^{-1} is beyond the range found for cationic Nb(III) complexes of the type [Nb(η-C_5H_5)L_4X]$^+$ [33]. The evidence from a helium discharge lamp PE spectroscopic study of [Ti(η-C_7H_7)(η-C_5H_5)] [1] also favoured a d^0

titanium centre (i.e. a -3 charge for the seven-membered ring). This work is considered further below.

In the light of the discussion surrounding the localisation properties of the $1e_2$ MOs, together with the advent of a new, high-yield synthetic route into [M(η-C_7H_7)(η-C_5H_5)] systems [32], it was decided to undertake a more extensive PE spectroscopic study of these compounds than had been possible previously, with the aim of establishing the degree of metal-ligand mixing in the $1e_2$ MOs.

2.3.2 Results and discussion

The PE spectra of [M(η-C_7H_7)(η-C_5H_5)] (M=Ti, Nb and Mo) and [Ta(η-C_7H_7)(η-C_5H_4Me)] have been measured over the incident photon energy ranges given in Table 2.4. Table 2.5 presents IE data and band assignments. The IE data for [M(η-C_7H_7)(η-C_5H_5)] (M=Nb and Mo) and [Ta(η-C_7H_7)(η-C_5H_4Me)] are taken from their He I spectra, measured by the author prior to the synchrotron study, while those in parentheses are from the original reports. Those for [Ti(η-C_7H_7)(η-C_5H_5)] are taken from reference [1].

Table 2.4 : incident photon energy ranges used in acquisition of the PE spectra of [M(η-C_7H_7)(η-C_5H_5)] (M=Ti, Nb and Mo) and [Ta(η-C_7H_7)(η-C_5H_4Me)]

Compound	Incident photon energy range (eV)
[Ti(η-C_7H_7)(η-C_5H_5)]	20 - 80
[Nb(η-C_7H_7)(η-C_5H_5)]	21 - 80
[Mo(η-C_7H_7)(η-C_5H_5)]	21 - 80
[Ta(η-C_7H_7)(η-C_5H_4Me)]	20 - 95

As for [Mo(η-C_6H_5Me)$_2$], no attempt was made to measure RPPICS for bands ionising above ca. 11 eV.

Table 2.5 : vertical IEs and band assignments for [M(η-C_7H_7)(η-C_5H_5)] (M=Ti, Nb and Mo) and [Ta(η-C_7H_7)(η-C_5H_4Me)]

Compound	Band	IE (eV)	Ion state	Related MO
[Ti(η-C_7H_7)(η-C_5H_5)][a]	A	6.85	$^2E_2$	$1e_2$
	B	8.74	$^2E_1$	$2e_1$
	C	9.90	$^2E_1$	$1e_1$
		>11		ligand σ and π
[Nb(η-C_7H_7)(η-C_5H_5)][b]	A	5.85 (5.98)	$^1A_1$	$1a_1$
	B	7.00 (7.11)	$^3E_2$	$1e_2$
	B'	7.36 (7.50)	$^1E_2$	$1e_2$
	C	8.77 (8.78)		$2e_1$
	C'	9.23 (9.13)		$2e_1$
	D	10.22 (10.4)		$1e_1$
		>11		ligand σ and π
[Mo(η-C_7H_7)(η-C_5H_5)][b]	A	5.70 (5.87)	$^2A_1$	$1a_1$
	B	7.38 (7.55)	$^2E_2$	$1e_2$
	C	8.86 (8.93)		$2e_1$
	C'	9.25 (9.28)		$2e_1$
	D	10.38 (10.4)		$1e_1$
		>11		ligand σ and π
[Ta(η-C_7H_7)(η-C_5H_4Me)]	A	5.47	$^1A_1$	$1a_1$
	B	6.89	$^3E_2$	$1e_2$
	B'	7.21	$^1E_2$	$1e_2$
	C	8.73		$2e_1$
	C'	9.14		$2e_1$
	D	10.19		$1e_1$
		>11		ligand σ and π

[a] data from reference [1] [b] data in parentheses from reference [26]

2.3.2 (a) [Mo(η-C_7H_7)(η-C_5H_5)]

The PE spectrum of [Mo(η-C_7H_7)(η-C_5H_5)], recorded at 30 and 48 eV, is presented in Figure 2.8. The assignment (Table 2.5) is as given by previous workers, and is similar to that of [Mo(η-$C_6H_5Me)_2$]. The major difference is in the energies of the e_1 MOs, which are separated by 0.75 eV in [Mo(η-$C_6H_5Me)_2$] but lie 1.52 eV apart in [Mo(η-C_7H_7)(η-C_5H_5)], reflecting the relative energies of the e_1 levels of the five- and seven-membered rings. The shoulder to band C (labelled C') is more clearly visible in the He I spectrum, which is of slightly superior resolution to the spectra acquired using synchrotron radiation. The asymmetry of band C is probably due to a Jahn-Teller distortion localised on the cyclopentadienyl ring. The $1a_1^{-1}$ ionisation band is once again sharper than the other valence ionisation bands, indicating its non-bonding nature.

The RPPICS of bands A-D are presented in Figure 2.9 and will be discussed in two parts, as for [Mo(η-$C_6H_5Me)_2$]. The cross section data of bands A and B are given in Figure 2.10 (a) and their renormalised BRs in Figure 2.10 (b). They are very similar to those for [Mo(η-$C_6H_5Me)_2$], with both bands showing a substantial cross section enhancement in the region of the molybdenum 4p subshell ionisation potentials, and band A having another maximum at an incident photon energy of 30 eV. The BR plots confirm how alike the RPPICS behaviour is, as Figures 2.4 (b) and 2.10 (b) are almost identical, both in overall profile and numerical BR. It should be noted, however, that the cross section of band A at 21 eV is higher than that at 24 eV. This is not seen in [Mo(η-$C_6H_5Me)_2$] as the data begin at 24 eV‡, but is of central importance in determining the origin of the RPPICS maximum at 30 eV. This point is explored further below.

---

‡ Experimental difficulties preclude the acquisition of spectra on most compounds below incident photon energies of ca. 20 eV. At these energies, electrons are generated with very low KEs, resulting in high backgrounds which make reliable deconvolution problematic.

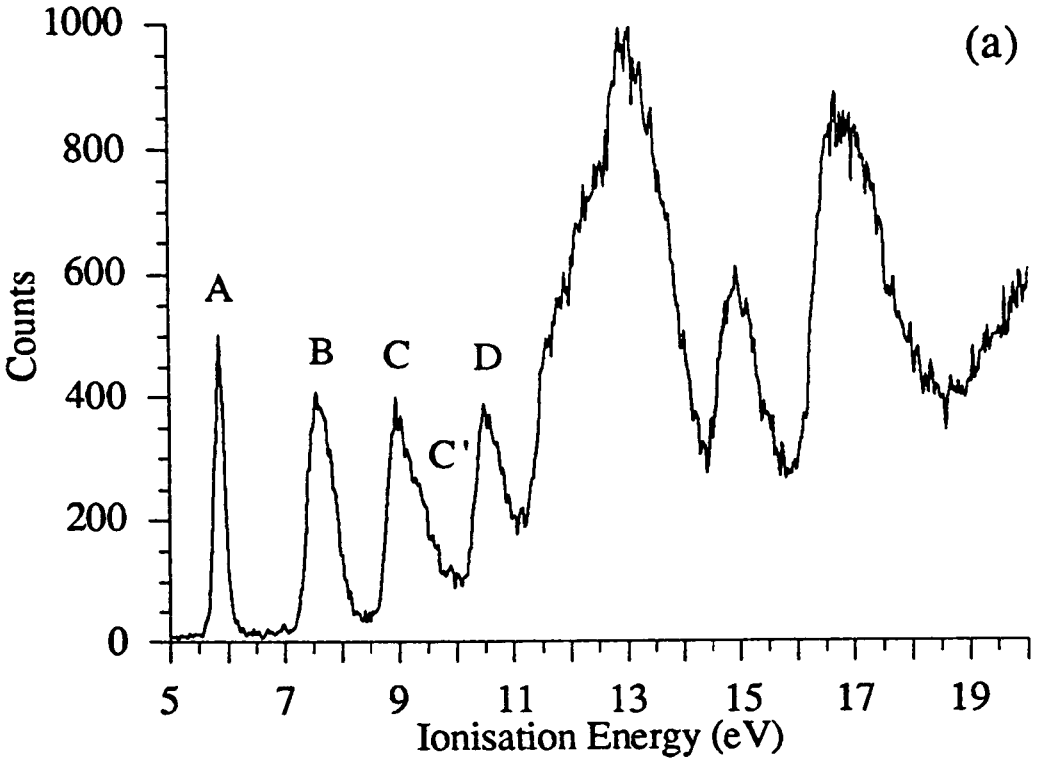

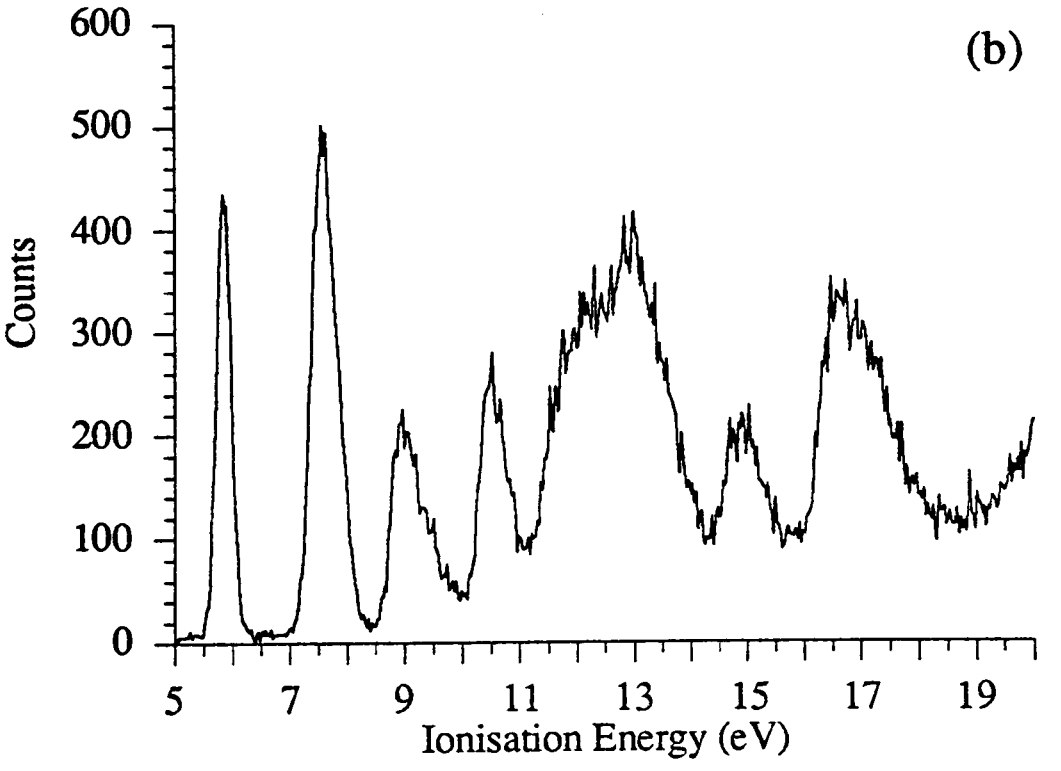

Figure 2.8 : the PE spectrum of [Mo(η-C_7H_7)(η-C_5H_5)], acquired at (a) 30 and (b) 48 eV

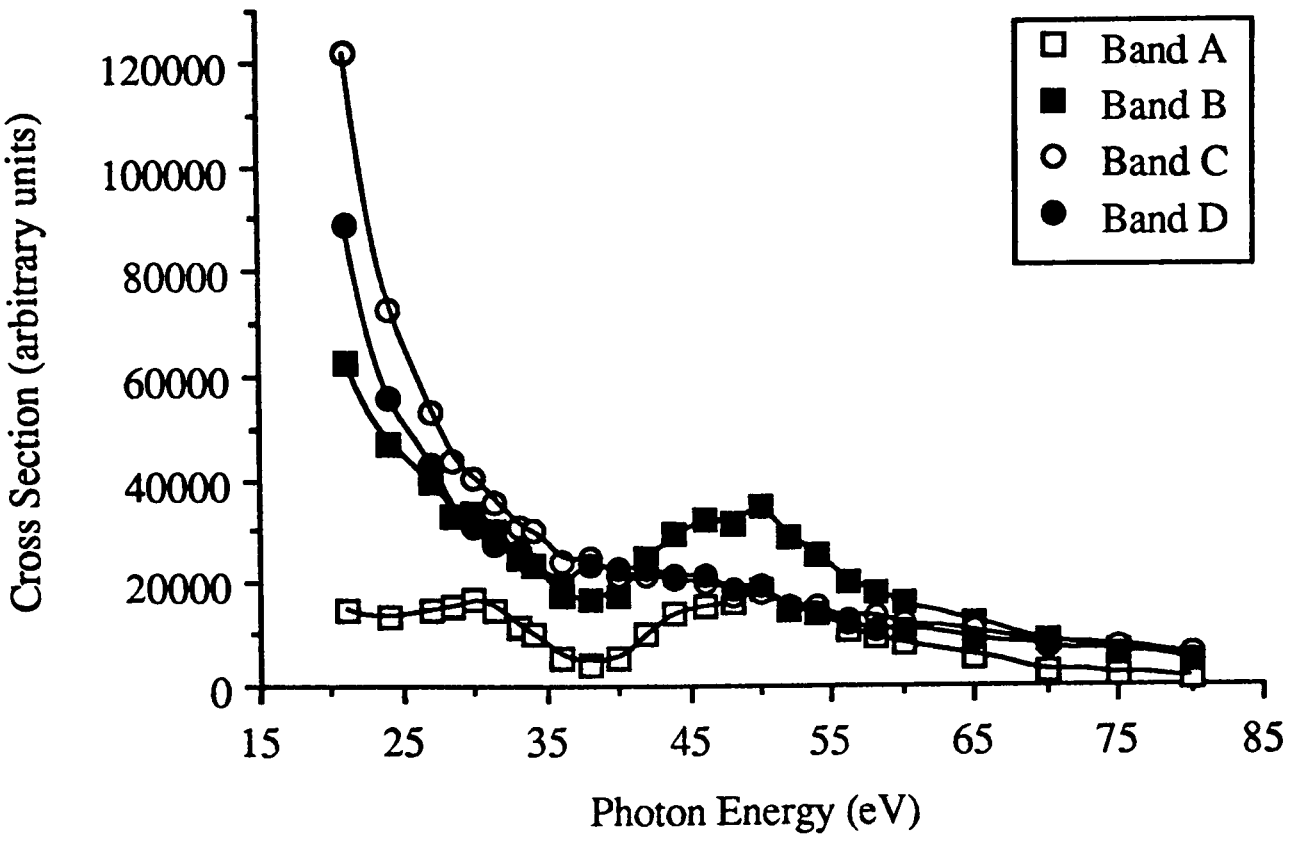

Figure 2.9 : RPPICS of bands A-D in the PE spectrum of [Mo(η-C_7H_7)(η-C_5H_5)]

The 4p→4d giant resonant absorption process for [Mo(η-C_7H_7)(η-C_5H_5)] is represented by the equation

$$(4p)^6(1e_2)^4(1a_1)^2(3e_1)^0 + h\nu \rightarrow (4p)^5(1e_2)^4(1a_1)^2(3e_1)^1$$

In $C_{\infty v}$ symmetry, the irreducible representations of the $4p^5$ configuration transform as (A_1 + E_1), so that the states arising from the $(4p)^5(1e_2)^4(1a_1)^2(3e_1)^1$ configuration are given by the direct product

$$(A_1 + E_1) \times E_1 = {}^1E_1 + {}^1A_1 + {}^1A_2 + {}^1E_2 + {}^3E_1 + {}^3A_1 + {}^3A_2 + {}^3E_2$$

Application of the dipole selection rule and assumption of Russell-Saunders coupling gives the allowed final states as $^1A_1$ and $^1E_1$. Autoionisation

$$(4p)^5(1e_2)^4(1a_1)^2(3e_1)^1 \rightarrow (4p)^5(1e_2)^4(1a_1)^2(3e_1)^0 + e^-$$

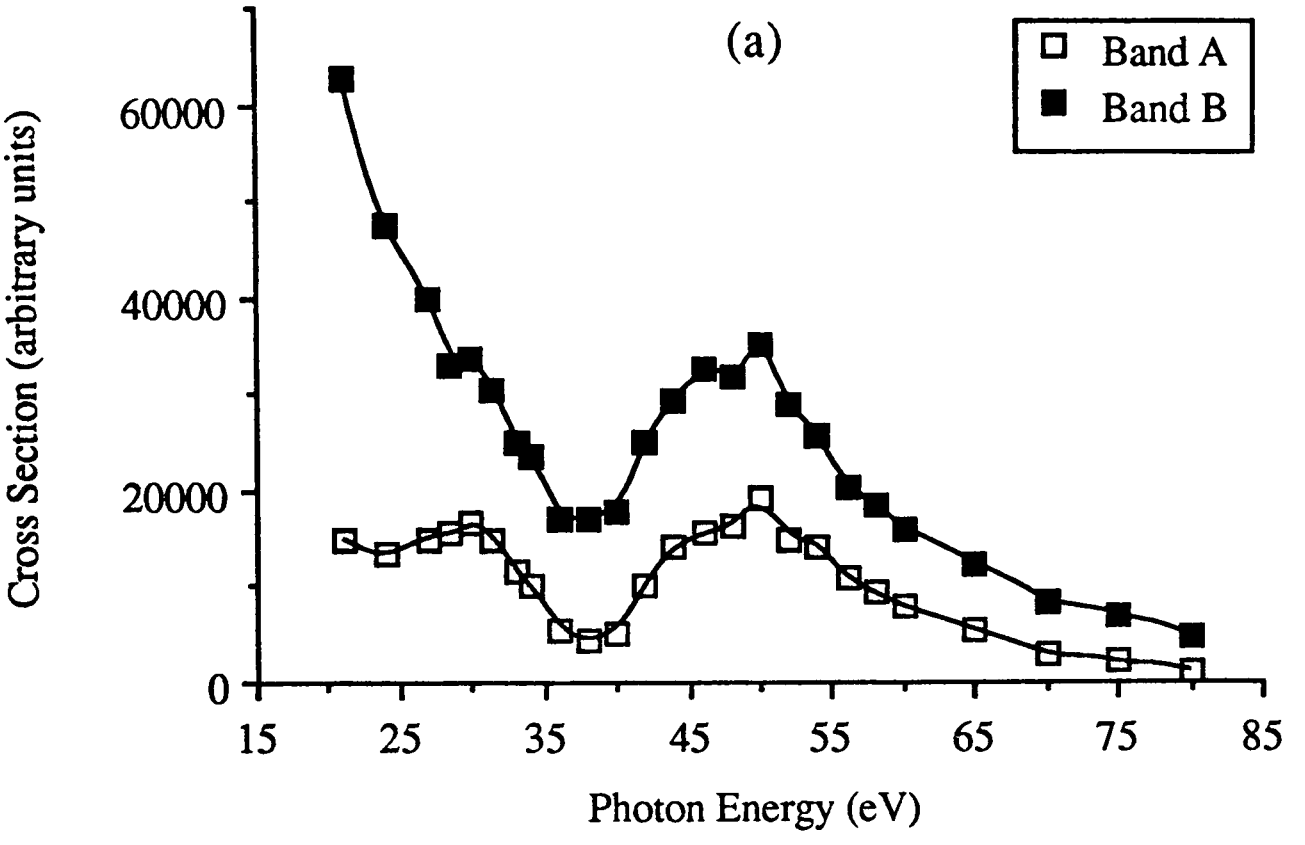

Figure 2.10 : (a) RPPICS and (b) renormalised BRs of bands A and B in the PE spectrum of [Mo(η-C_7H_7)(η-C_5H_5)]

is possible and, in a manner analogous to [Mo(η-$C_6H_5Me)_2$], inter-channel coupling in the final states produced by the SCK decay processes

$$(4p)^5(1e_2)^4(1a_1)^2(3e_1)^1 \rightarrow \begin{matrix}(4p)^6(1e_2)^3(1a_1)^2(3e_1)^0 + e^- \\ (4p)^6(1e_2)^4(1a_1)^1(3e_1)^0 + e^-\end{matrix}$$

and direct photoionisation

$$(4p)^6(1e_2)^4(1a_1)^2(3e_1)^0 + h\nu \rightarrow \begin{matrix}(4p)^6(1e_2)^3(1a_1)^2(3e_1)^0 + e^- \\ (4p)^6(1e_2)^4(1a_1)^1(3e_1)^0 + e^-\end{matrix}$$

should lead to two overlapping Fano profiles for the RPPICS of the $1e_2^{-1}$ and $1a_1^{-1}$ bands.

Fano resonance profiles with sloping background cross sections were fitted to the experimentally determined RPPICS of bands A and B, using equation (1.9). The values of the Fano parameters obtained are given in Table 2.6. Satisfactory fits were obtained to two Fano profiles with identical line profile indices.

Table 2.6 : Fano parameters obtained from the RPPICS of bands A and B in the PE spectrum of [Mo(η-C_7H_7)(η-C_5H_5)]

Band	q	E_r (eV)	σ_0	Γ	X	hν range (eV)
A	1.35	43.1	6401	8.26	0.024	38-70
		48.3		1.81		
B	0.76	41.6	17040	10.4	0.024	38-70
		49.8		0.14		

The distinct asymmetry of the RPPICS plots over the molybdenum 4p→4d giant resonance and the fact that two Fano profiles were required to obtain a good fit suggest

very strongly that there is a molecular shape resonance occurring in the same incident photon energy range as the p→d resonance. Shape resonances are dependent upon the potential field generated by a molecule (Chapter 1.4.4 (d)) and it may well be that the fields generated by [Mo(η-$C_6H_5Me)_2$] and [Mo(η-C_7H_7)(η-C_5H_5)] are sufficiently similar so that a shape effect would occur at similar photon energies. The arguments employed in discussing these effects in the analogous bands of [Mo(η-$C_6H_5Me)_2$] are equally applicable here, and the conclusion must once again be that the Fano parameters given in Table 2.6 are suspect. Nonetheless, the q values for bands A and B indicate that the magnitude of the p→d resonance is stronger in A than B, a conclusion that can be drawn from a qualitative inspection of Figure 2.10. This is in agreement with the prediction of significant carbon 2p AO contribution to the $1e_2$ MOs, but also indicates a substantial molybdenum 4d content. This will be discussed further following the presentation of the results for the other mixed sandwich molecules.

It is interesting that the RPPICS of band A show a maximum at 30 eV, precisely the same photon energy as the $1a_{1g}^{-1}$ band of [Mo(η-$C_6H_5Me)_2$]. Furthermore, the extra data point obtained on [Mo(η-C_7H_7)(η-C_5H_5)] over [Mo(η-$C_6H_5Me)_2$] (at 21 eV) indicates that the cross section has a minimum at 24 eV. This is strong evidence to suggest that the RPPICS maximum at 30 eV is caused not by the delayed maximum in the cross section of the 4d AO of molybdenum, but rather by a molecular shape resonance. The delayed maximum occurs at lower photon energy; indeed, an incident photon energy of 21 eV, corresponding to a PE KE of 15.3 eV, can be be taken as an upper limit to the value of the delayed maximum, in excellent agreement with the ca. 15 eV PE KE obtained from calculations on atomic molybdenum [21]. The shoulder on the RPPICS plot of band B at 30 eV may be due to the same shape resonance as the maximum in band A, but the effect is much smaller, indicating that this resonance is associated more with the $1a_1$ MO than the $1e_2$. The possibility that the shape resonance is also occurring in the $1e_2^{-1}$ band was discussed in relation to [Mo(η-$C_6H_5Me)_2$] (Section 2.2.2 (c)), and the observation of the RPPICS shoulder at 30 eV in [Mo(η-C_7H_7)(η-C_5H_5)] lends weight to that argument.

As noted above, the BR plot (Figure 2.10 (b)) is very similar to the equivalent plot for [Mo(η-$C_6H_5Me)_2$] (Figure 2.4 (b)) and may be explained in the same way. Both RPPICS maxima occur more strongly in band A than band B, and the cross section of the purely metal d-localised MO (band A) decreases in intensity relative to the mixed metal/ligand MO at high incident photon energies, in the region of the molybdenum 4d AO Cooper minimum.

The RPPICS and renormalised BRs of bands C and D are presented in Figure 2.11, from which it can be seen that both bands have cross section behaviour typical of ligand-localised MOs. This is more so in band C than band D, which shows a small cross section enhancement in the region of the molybdenum 4p→4d giant resonance, revealing a small metal d orbital contribution to the $1e_1$ MOs. This is most clearly illustrated in Figure 2.11 (b) (the origin of the slight gain in relative intensity of band C over band D at 58 eV is not clear)). This may well be indicative of a system in which the three MOs of e_1 symmetry mix to produce metal-ligand bonding ($1e_1$), non-bonding ($2e_1$) and antibonding ($3e_1$) levels.

Neither of these orbitals has features in its RPPICS which can be identified with the shape resonances found in the more metal-localised ionisations. This is an important piece of information in determining whether MO symmetry or metal d AO content is responsible for the shape resonances seen between 40-50 eV. In [Mo(η-$C_6H_5Me)_2$], the resonance is seen only in the RPPICS of the MOs with significant metal d AO character, which are also of g symmetry. The g/u symmetry notation is not defined in [M(η-C_7H_7)(η-C_5H_5)] and yet the shape resonance still occurs in bands A and B, though not in band D. The cross section behaviour of the $1e_1^{-1}$ band suggests that the associated MO has little molybdenum 4d AO character, leading to the conclusion that this shape resonance, like the one at lower incident photon energy, is governed primarily by the amount of metal d orbital contribution to the ionising MO.

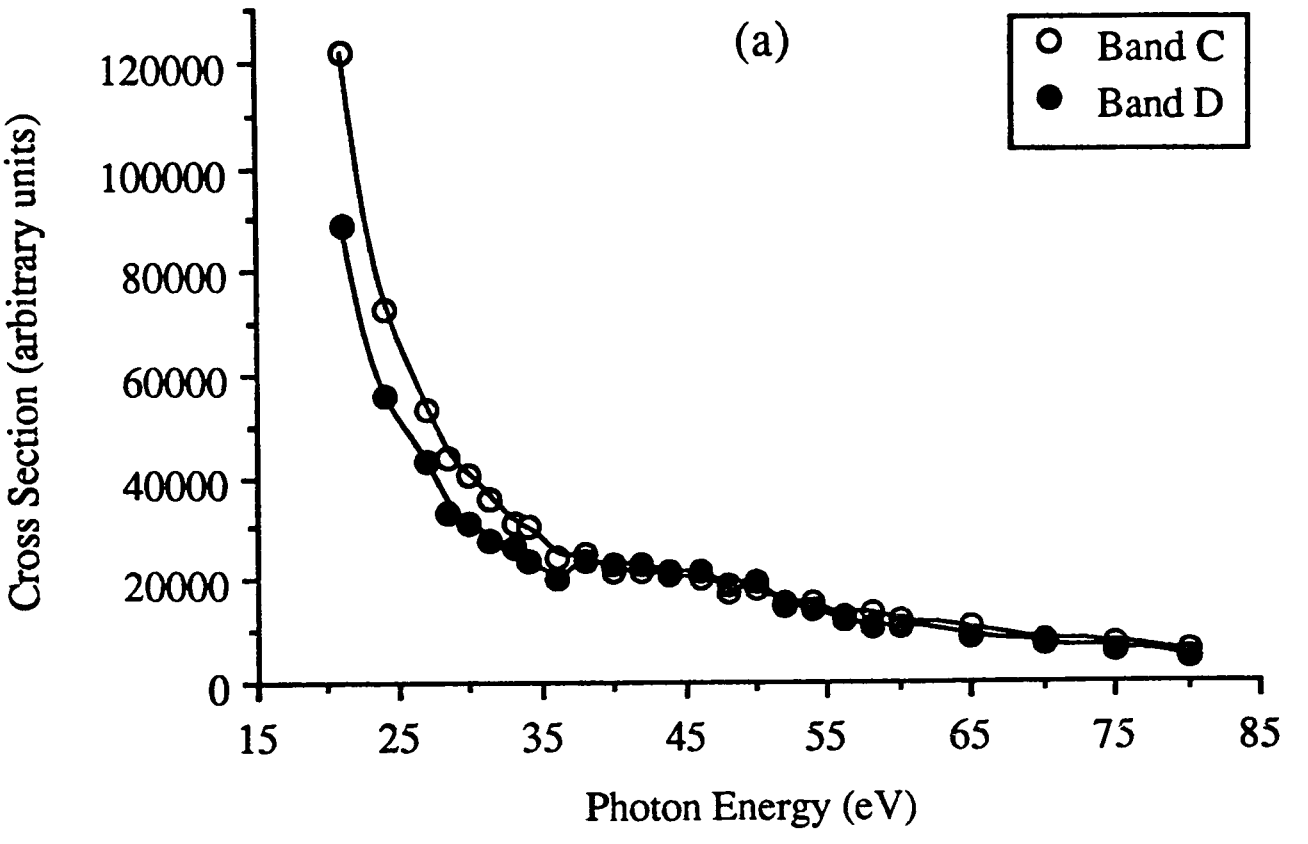

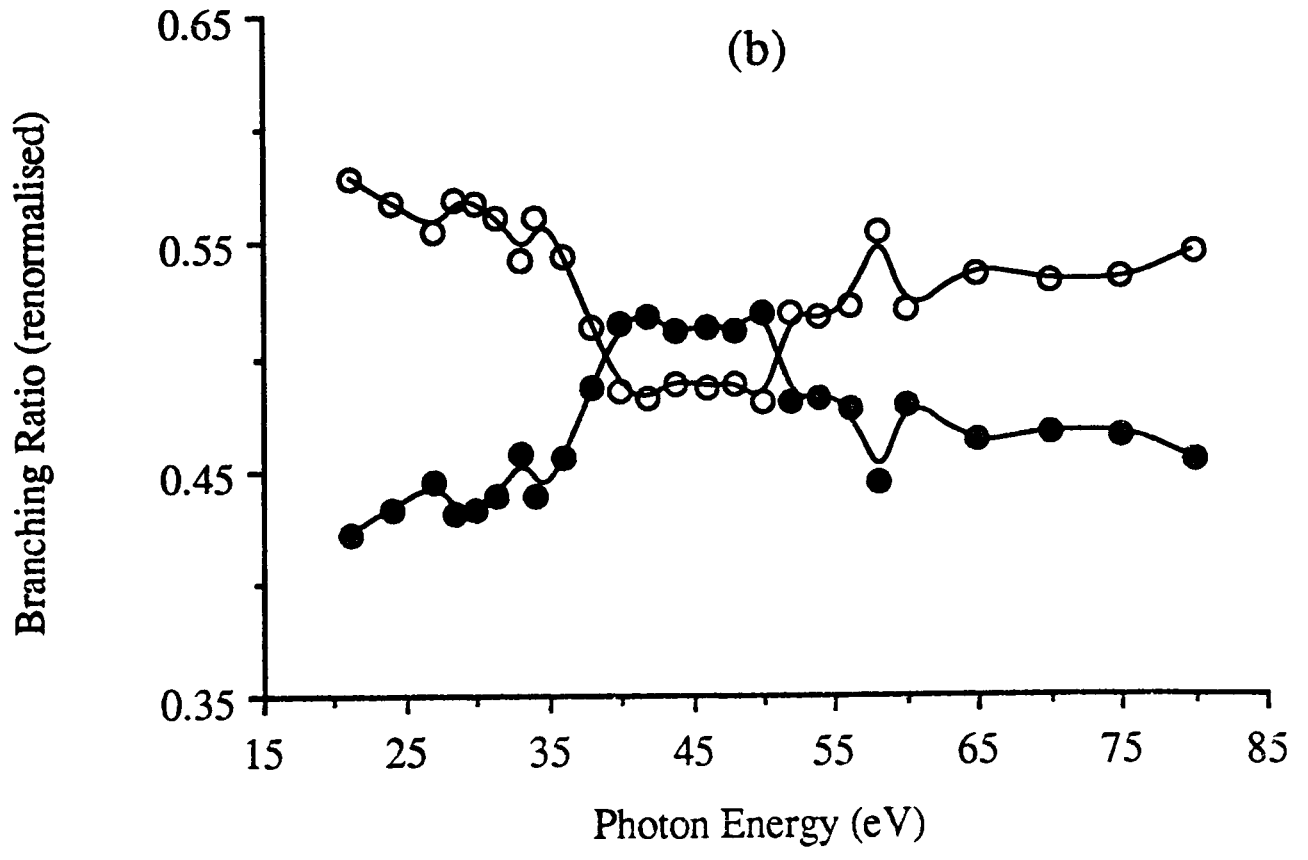

Figure 2.11 : (a) RPPICS and (b) renormalised BRs of bands C and D in the PE spectrum of $[Mo(\eta\text{-}C_7H_7)(\eta\text{-}C_5H_5)]$

2.3.2 (b) [Nb(η-C_7H_7)(η-C_5H_5)]

The PE spectrum of [Nb(η-C_7H_7)(η-C_5H_5)], recorded at 30 and 48 eV, is presented in Figure 2.12. The assignment is given in Table 2.5, and is as proposed by previous workers. The spectrum is very similar to that of [Mo(η-C_7H_7)(η-C_5H_5)], but the relative intensity of band A is lower than the $1a_1^{-1}$ ionisation of [Mo(η-C_7H_7)(η-C_5H_5)]. This arises from the $1a_1$ MO being singly occupied in [Nb(η-C_7H_7)(η-C_5H_5)], but doubly occupied in [Mo(η-C_7H_7)(η-C_5H_5)]. The asymmetry of band B, which is more pronounced in the He I spectrum [26], is a result of an exchange interaction between the unpaired electron remaining in the $1e_2$ MOs following ionisation with the electron in the $1a_1$ [27] (Section 2.4). That of band C, which is again not well resolved in the spectra acquired with synchrotron radiation, probably arises from a Jahn-Teller distortion, as for [Mo(η-C_7H_7)(η-C_5H_5)].

The RPPICS of bands A-D are presented in Figure 2.13. Figure 2.14 gives the RPPICS of bands A and B, together with their renormalised BRs. The data are similar to those for [Mo(η-$C_6H_5Me)_2$] and [Mo(η-C_7H_7)(η-C_5H_5)], with both bands showing cross section enhancements in the region of the niobium 4p subshell binding energies ($^2P_{3/2}$ = 38 eV, $^2P_{1/2}$ = 40 eV [14]) and band A having another maximum at 27 eV.

The 4p→4d giant resonant absorption process for [Nb(η-C_7H_7)(η-C_5H_5)] is represented by two equations

$$(4p)^6(1e_2)^4(1a_1)^1(3e_1)^0 + h\nu \rightarrow (4p)^5(1e_2)^4(1a_1)^2(3e_1)^0$$
$$(4p)^6(1e_2)^4(1a_1)^1(3e_1)^0 + h\nu \rightarrow (4p)^5(1e_2)^4(1a_1)^1(3e_1)^1$$

As for [Mo(η-C_7H_7)(η-C_5H_5)], the irreducible representations of the $4p^5$ configuration transform as ($A_1 + E_1$) so that the states arising from the $(4p)^5(1e_2)^4(1a_1)^2(3e_1)^0$ configuration are given by the direct product

$$(A_1 + E_1) \times A_1 = {}^2A_1 + {}^2E_1$$

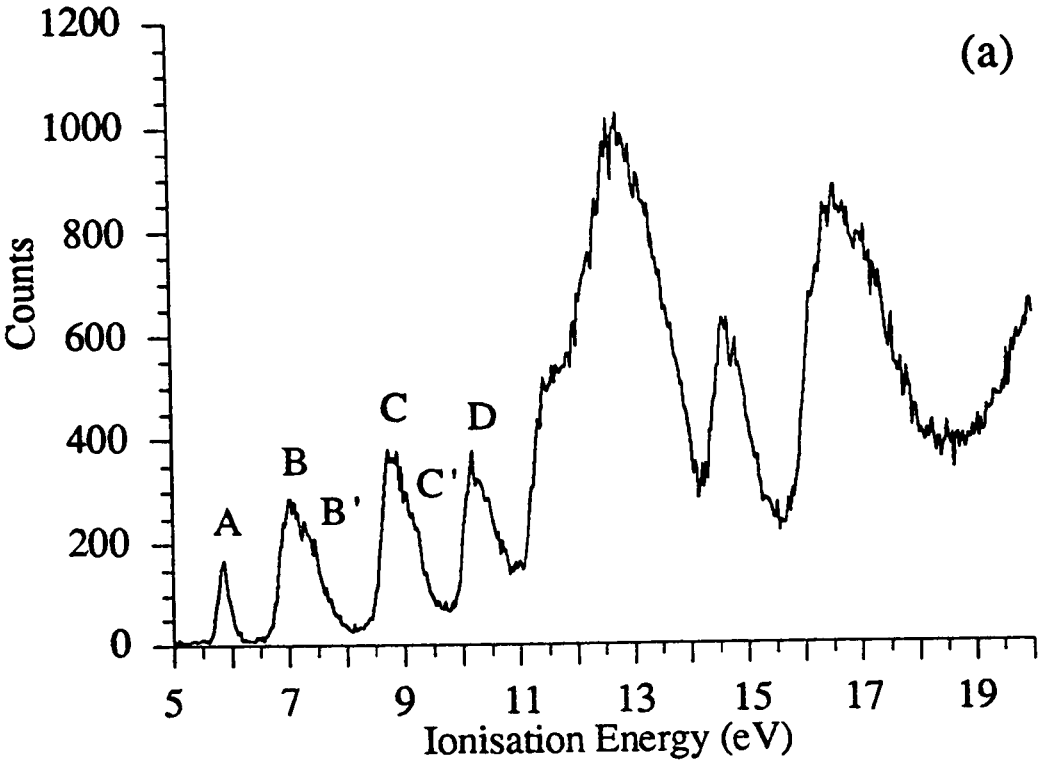

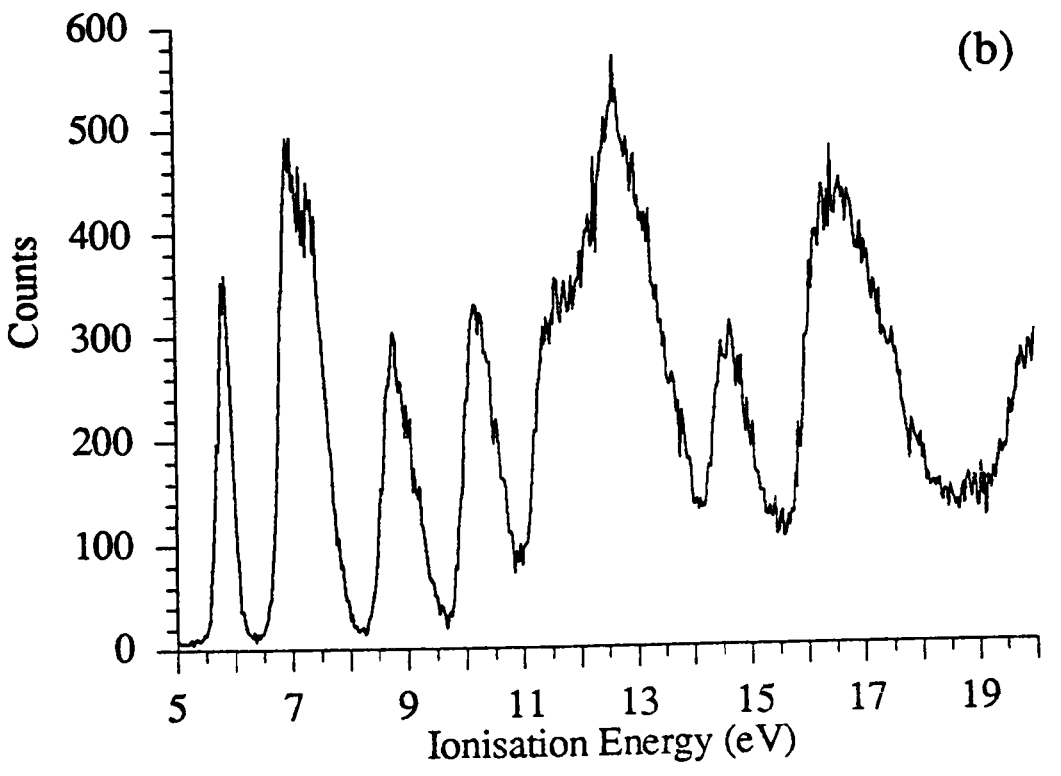

Figure 2.12 : the PE spectrum of [Nb(η-C_7H_7)(η-C_5H_5)], acquired at (a) 30 and (b) 48 eV

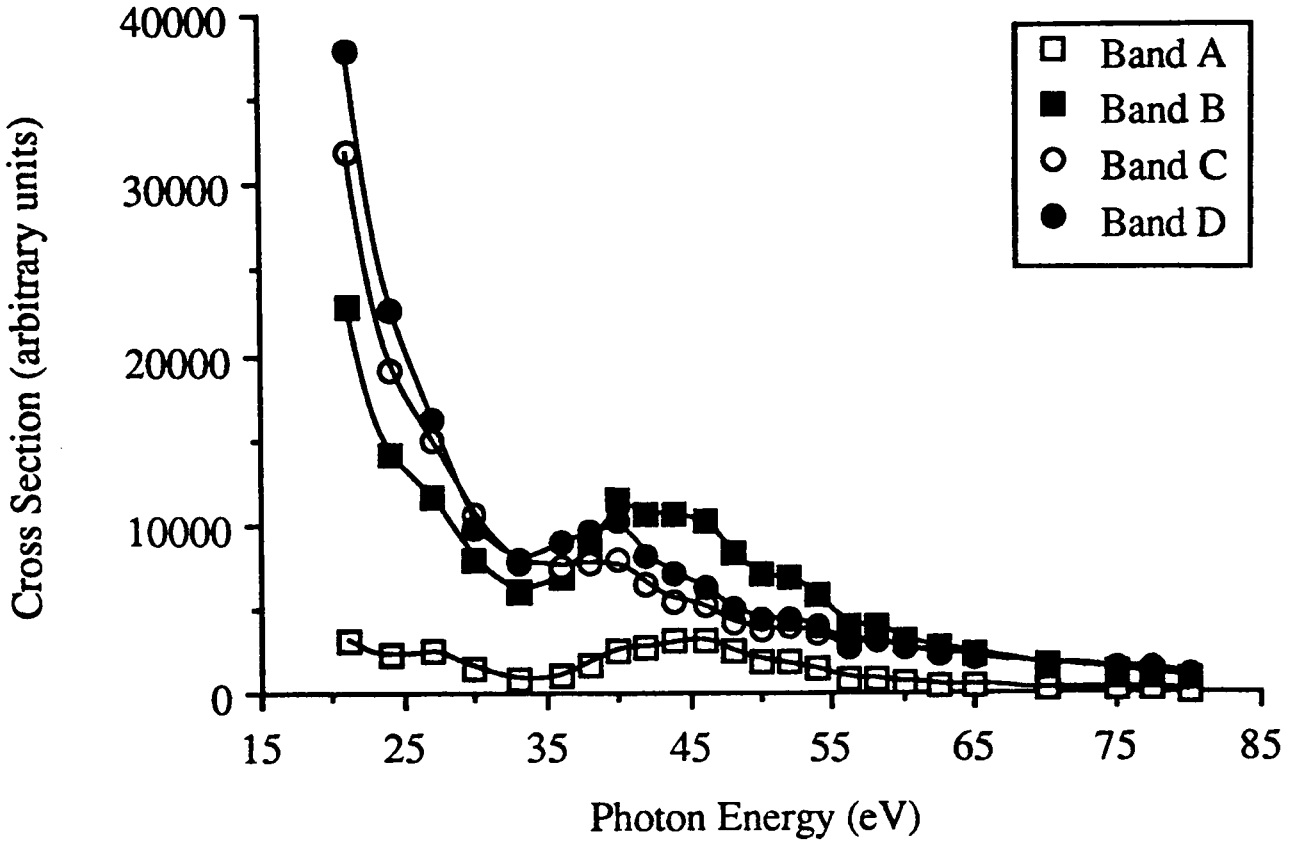

Figure 2.13 : RPPICS of bands A-D in the PE spectrum of [Nb(η-C_7H_7)(η-C_5H_5)]

both of which are permitted final states in absorption. The states arising from the $(4p)^5(1e_2)^4(1a_1)^1(3e_1)^1$ configuration are slightly more complicated. The metal d-localised states are given by the direct product

$$A_1 \times E_1 = E_1$$

and hence the states of the $(4p)^5(1e_2)^4(1a_1)^1(3e_1)^1$ configuration are given by the direct product

$$(A_1 + E_1) \times E_1 = {}^2E_1 + {}^2A_1 + {}^2A_2 + {}^2E_2 + {}^4E_1 + {}^4A_1 + {}^4A_2 + {}^4E_2$$

from which the allowed final states are $^2A_1$ and $^2E_1$. We therefore have four permitted final states, two $^2A_1$ and two $^2E_1$. Mixing may well occur between the two A_1 states and between the two E_1, but the numbers and symmetries of the states should not alter.

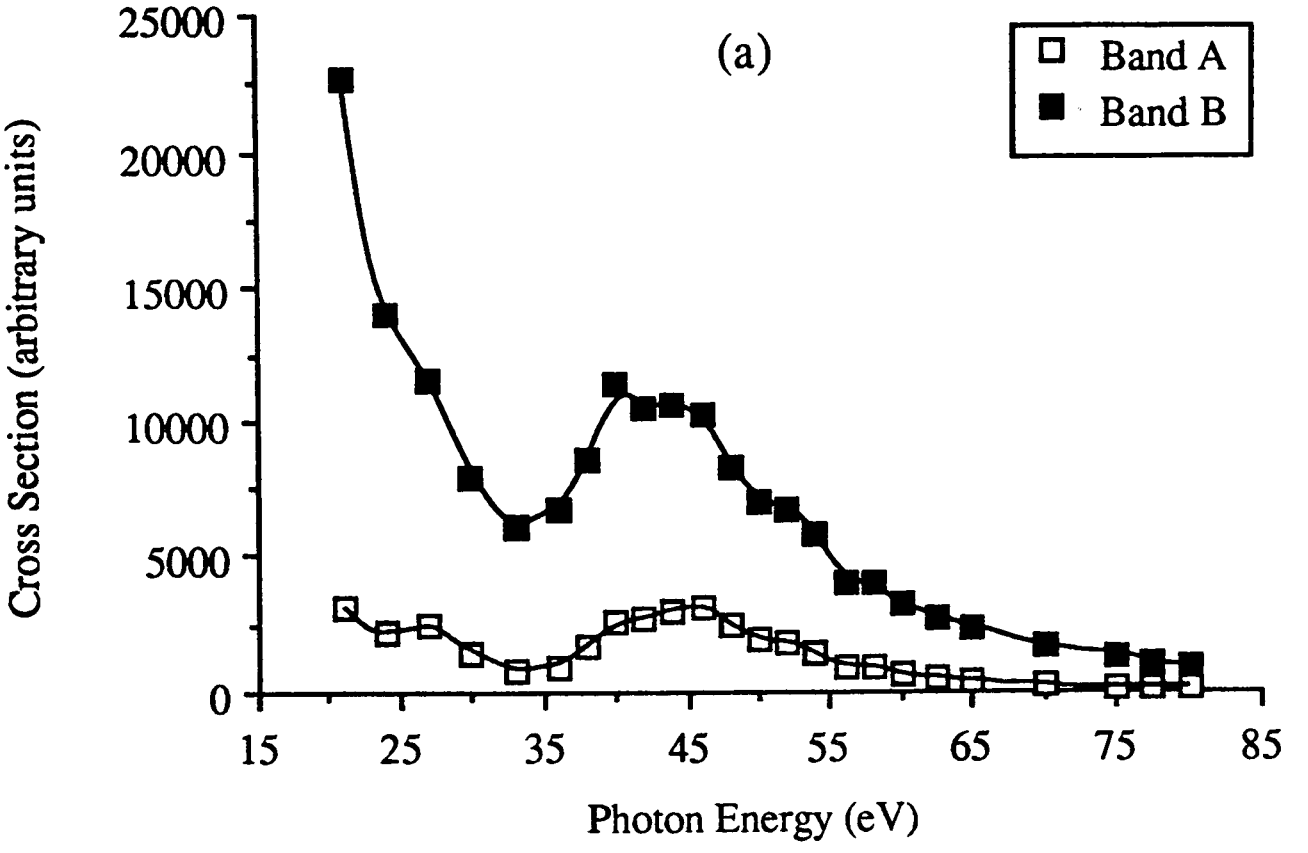

Figure 2.14 : (a) RPPICS and (b) renormalised BRs of bands A and B in the PE spectrum of $[Nb(\eta\text{-}C_7H_7)(\eta\text{-}C_5H_5)]$

Autoionisation

$$(4p)^5(1e_2)^4(1a_1)^1(3e_1)^1 \rightarrow (4p)^5(1e_2)^4(1a_1)^1(3e_1)^0 + e^-$$
$$(4p)^5(1e_2)^4(1a_1)^2(3e_1)^0 \rightarrow (4p)^5(1e_2)^4(1a_1)^1(3e_1)^0 + e^-$$

is possible, together with the SCK decay processes

$$(4p)^5(1e_2)^4(1a_1)^1(3e_1)^1 \rightarrow \begin{array}{l} (4p)^6(1e_2)^4(1a_1)^0(3e_1)^0 + e^- \\ (4p)^6(1e_2)^3(1a_1)^1(3e_1)^0 + e^- \\ (4p)^6(1e_2)^3(1a_1)^0(3e_1)^1 + e^- \end{array}$$

and

$$(4p)^5(1e_2)^4(1a_1)^2(3e_1)^0 \rightarrow \begin{array}{l} (4p)^6(1e_2)^4(1a_1)^0(3e_1)^0 + e^- \\ \\ (4p)^6(1e_2)^3(1a_1)^1(3e_1)^0 + e^- \end{array}$$

the final states of which (bar $(4p)^6(1e_2)^3(1a_1)^0(3e_1)^1$) are identical to those produced by direct photoionisation

$$(4p)^6(1e_2)^4(1a_1)^1(3e_1)^0 + h\nu \rightarrow \begin{array}{l} (4p)^6(1e_2)^4(1a_1)^0(3e_1)^0 + e^- \\ \\ (4p)^6(1e_2)^3(1a_1)^1(3e_1)^0 + e^- \end{array}$$

Four overlapping Fano profiles for the RPPICS of the $1e_2^{-1}$ and $1a_1^{-1}$ bands are therefore expected via inter-channel coupling between the corresponding final states in the SCK and direct ionisation processes, and the cross section behaviour may be further complicated by the existence of a final state that cannot be achieved through a simple direct photoionisation ($(4p)^6(1e_2)^3(1a_1)^0(3e_1)^1$). It is therefore expected that the RPPICS maxima of the metal-

based ionisations of [Nb(η-C_7H_7)(η-C_5H_5)] are the result of a complicated series of ionisation processes, which the expected molecular shape resonance will further affect.

There are four separate features within the RPPICS enhancement of band B over the photon energy range 36-65 eV. Detailed assignment of these is not possible, but it is likely that the shape resonance occurs at the same incident photon energy as in [Mo(η-C_7H_7)(η-C_5H_5)], and therefore that it is the origin of the first maximum (at 40 eV). It is curious that this maximum is not as strong in the RPPICS of band A, unlike the two molybdenum complexes discussed previously. It proved impossible to fit adequately Fano functions (using both one and two profiles - the Fano function fitting program can fit no more than two separate profiles) to the RPPICS of bands A and B. Given their complicated cross section behaviour - both expected and found - this is not a surprising result.

The low incident photon energy behaviour of band A is analogous to that found in [Mo(η-C_7H_7)(η-C_5H_5)]. It is curious that the maximum in the shape resonance occurs 3 eV lower in [Nb(η-C_7H_7)(η-C_5H_5)] (at 27 eV), but the minimum in the RPPICS of band A at 24 eV indicates that the subsequent maximum is not due to the delayed maximum in the niobium 4d AO cross section. This is calculated to occur at a PE KE of ca. 11 eV [21]. Once again the incident photon energy of 21 eV, corresponding to a PE KE of ca. 15 eV, places an upper limit on the experimental value of the delayed maximum, but in the absence of spectra below 21 eV no further conclusions can be drawn. The shape resonance may be mirrored in band B at 27 eV, but the effect is slight, supporting further the observation that the low photon energy shape resonance is stronger in the $1a_1^{-1}$ than the $1e_2^{-1}$ band.

The BR plot (Figure 2.14 (b)) reinforces the preceding discussion, and again emphasises the mixed metal/carbon AO nature of the $1e_2$ MOs. The BR of the purely metal-based MO ($1a_1$) decreases at high incident photon energies on account of the Cooper minimum in the niobium 4d AO cross section (calculated to occur at a PE KE of 79 eV [21]), as was observed for the molybdenum complex.

In general, then, the RPPICS behaviour of the $1a_1^{-1}$ and $1e_2^{-1}$ bands of [Nb(η-C_7H_7)(η-C_5H_5)] are qualitatively similar to their molybdenum analogues. Quantitative comparison is precluded by the wider range of intermediates accessible via giant resonant

absorption in the niobium system, and the further complications of the coincident molecular shape resonance. Nonetheless, examination of Figures 2.10 and 2.14 suggests that the metal d orbital content of the $1e_2$ MOs is approximately similar for both complexes.

Figure 2.15 presents the RPPICS and renormalised BRs of bands C and D. As with [Mo(η-C_7H_7)(η-C_5H_5)], the cross section variation of these two bands is somewhat different from those of bands A and B, but the slight RPPICS enhancement in band D of [Mo(η-C_7H_7)(η-C_5H_5)] in the p→d resonance region is stronger in the corresponding band of [Nb(η-C_7H_7)(η-C_5H_5)]. Band C, which displayed no metal d orbital contribution in [Mo(η-C_7H_7)(η-C_5H_5)], has a small cross section maximum at 40 eV, although both Figures 2.15 (a) and (b) indicate that the effect is weaker in the predominantly cyclopentadienyl-localised e_1 MOs than in their cycloheptatrienyl counterparts. These results suggest that the metal 4d AO content of the ring e_1 levels is slightly greater in [Nb(η-C_7H_7)(η-C_5H_5)] than [Mo(η-C_7H_7)(η-C_5H_5)]. What is most curious about Figure 2.15 (b) is the way in which band C gains in intensity relative to band D at low photon energies, in the region of the molecular shape resonance which is associated most strongly with band A. If the origin of this BR variation is the shape effect, it rather complicates the seeking of a pattern to the occurrence of shape resonances, as it is appearing here in the band with the least metal d orbital character.

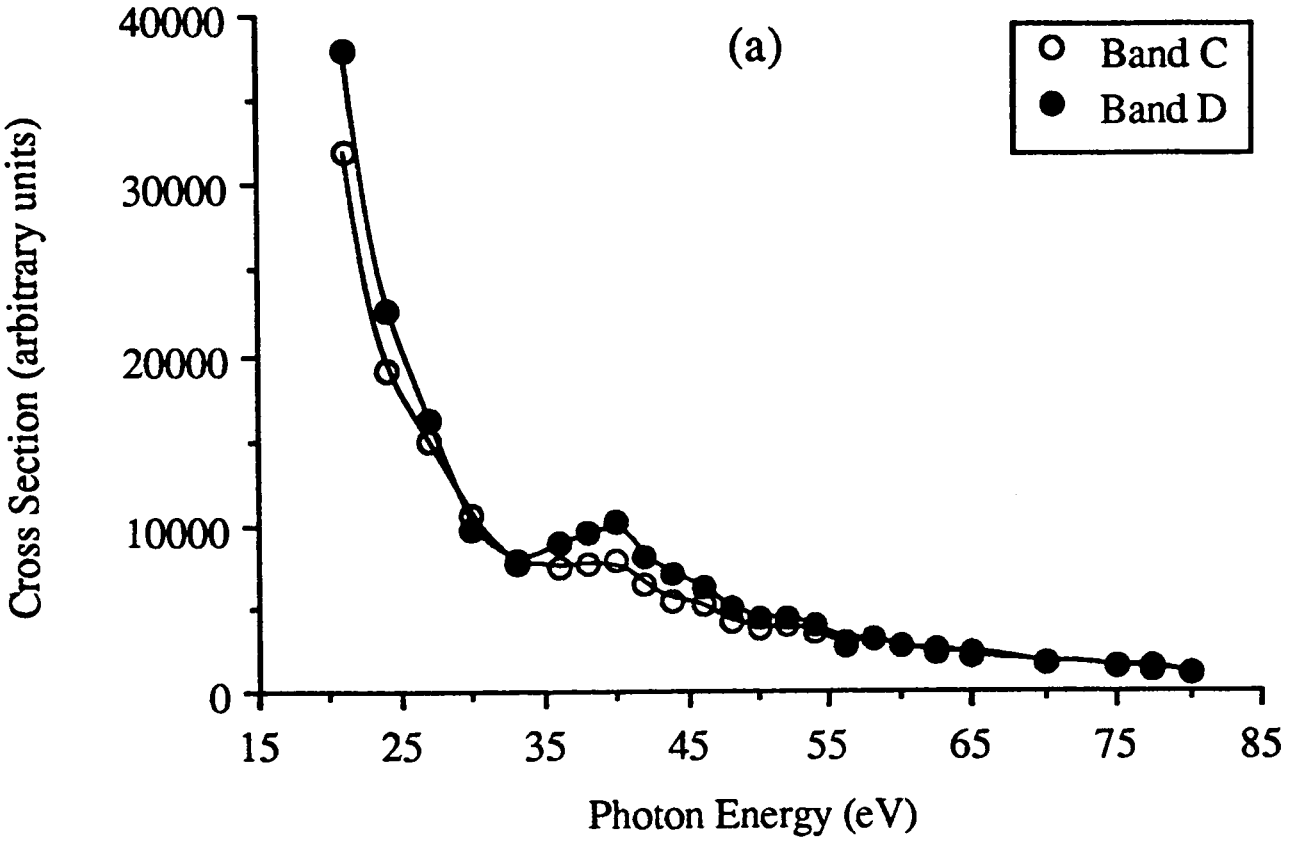

Figure 2.15 : (a) RPPICS and (b) renormalised BRs of bands C and D in the PE spectrum of $[Nb(\eta\text{-}C_7H_7)(\eta\text{-}C_5H_5)]$

2.3.2 (c) [Ta(η-C_7H_7)(η-C_5H_4Me)]

The recently synthesised [Ta(η-C_7H_7)(η-C_5H_4Me)] [32] is the first example of a cycloheptatrienyl-Ta complex, and hence its PE spectrum is reported for the first time. Figure 2.16 presents the He I spectrum, together with that obtained using synchrotron radiation at 50 eV. It can be readily assigned by comparison with the previously reported [M(η-C_7H_7)(η-C_5H_5)] spectra. The asymmetries of bands B and C are attributed to the same causes as in [Nb(η-C_7H_7)(η-C_5H_5)], to exchange and Jahn-Teller effects respectively. A comparison of the IE data now available for [M(η-C_7H_7)(η-C_5H_4R)] (M=V, Nb and Ta) is given in Section 2.4.

Figure 2.17 presents the RPPICS of bands A-D. It is a somewhat uninformative graph in that the cross sections overlap to the point at which it is difficult to distinguish them, but the purpose in including the Figure is merely to provide a comparison of the relative magnitudes of the cross sections. Figure 2.18 gives the RPPICS of bands A and B, plotted on separate graphs to allow the features to be seen more clearly, and Figure 2.19 their renormalised BRs. Both bands have cross section behaviour which is different from that seen in the complexes discussed so far, with four separate maxima over the 20-95 eV incident photon energy range employed. The data for band A are particularly striking.

In the region of the p→d giant resonance (ca. 35-65 eV) there are now two distinct RPPICS maxima in both bands A and B, at 42 and 52 eV, in contrast to the second row systems discussed thus far. This is in accord with the increased splitting of the IEs of the np subshell as n moves from 4 to 5. The $^2P_{3/2}$ and $^2P_{1/2}$ states are split by 2 eV in niobium and 3 eV in molybdenum while for atomic tantalum, $^2P_{3/2}$ = 38 eV, $^2P_{1/2}$ = 47 eV [14].

The 5p→5d giant resonant absorption process for [Ta(η-C_7H_7)(η-C_5H_4Me)] is represented by two equations

$$(5p)^6(1e_2)^4(1a_1)^1(3e_1)^0 + h\nu \rightarrow (5p)^5(1e_2)^4(1a_1)^2(3e_1)^0$$

$$(5p)^6(1e_2)^4(1a_1)^1(3e_1)^0 + h\nu \rightarrow (5p)^5(1e_2)^4(1a_1)^1(3e_1)^1$$

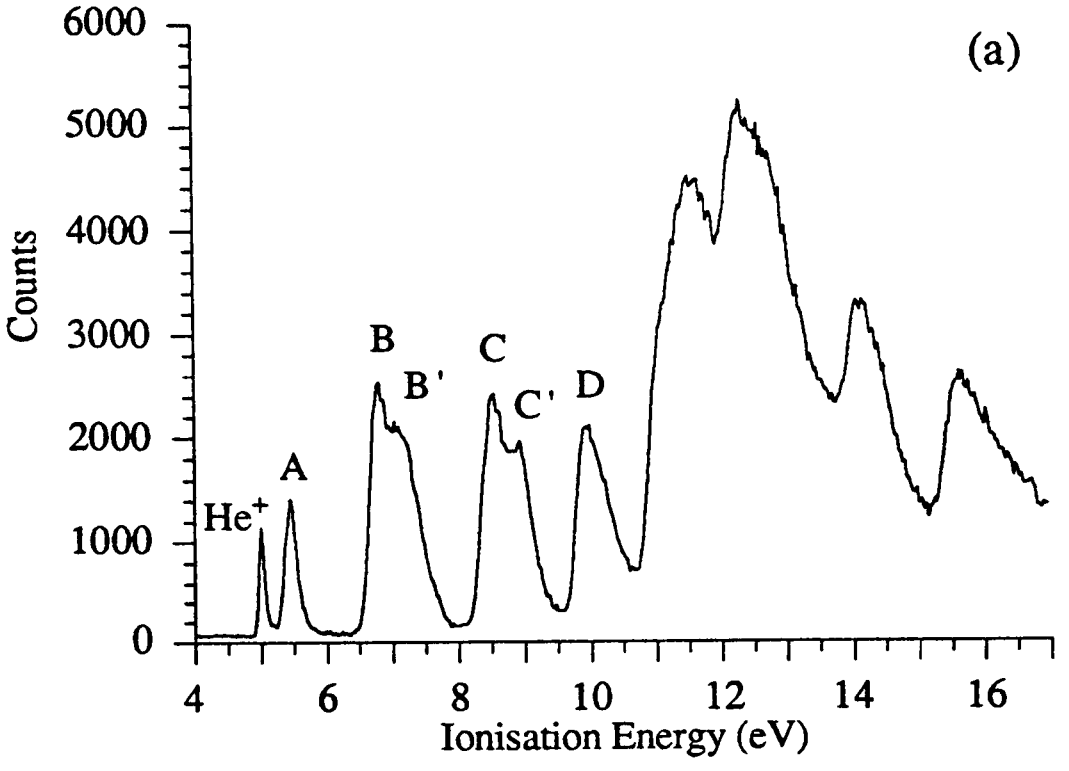

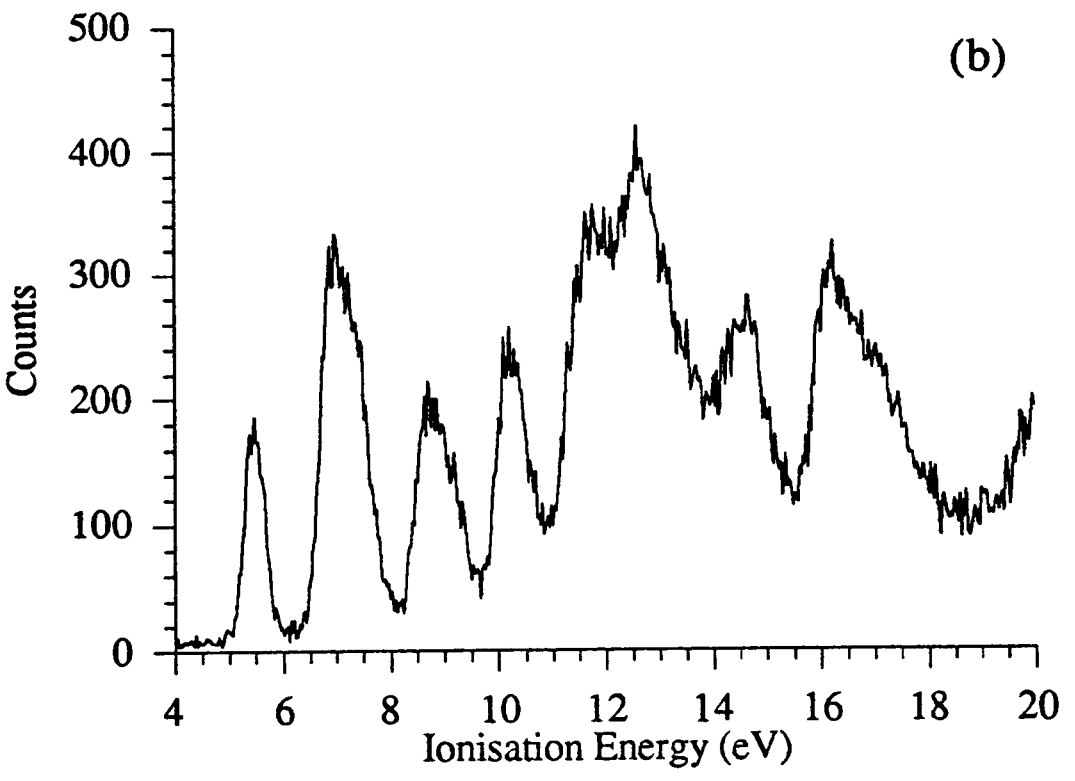

Figure 2.16 : the PE spectrum of [Ta(η-C_7H_7)(η-C_5H_4Me)], acquired at (a) 21.22 eV (helium discharge lamp) and (b) 50 eV (synchrotron radiation)

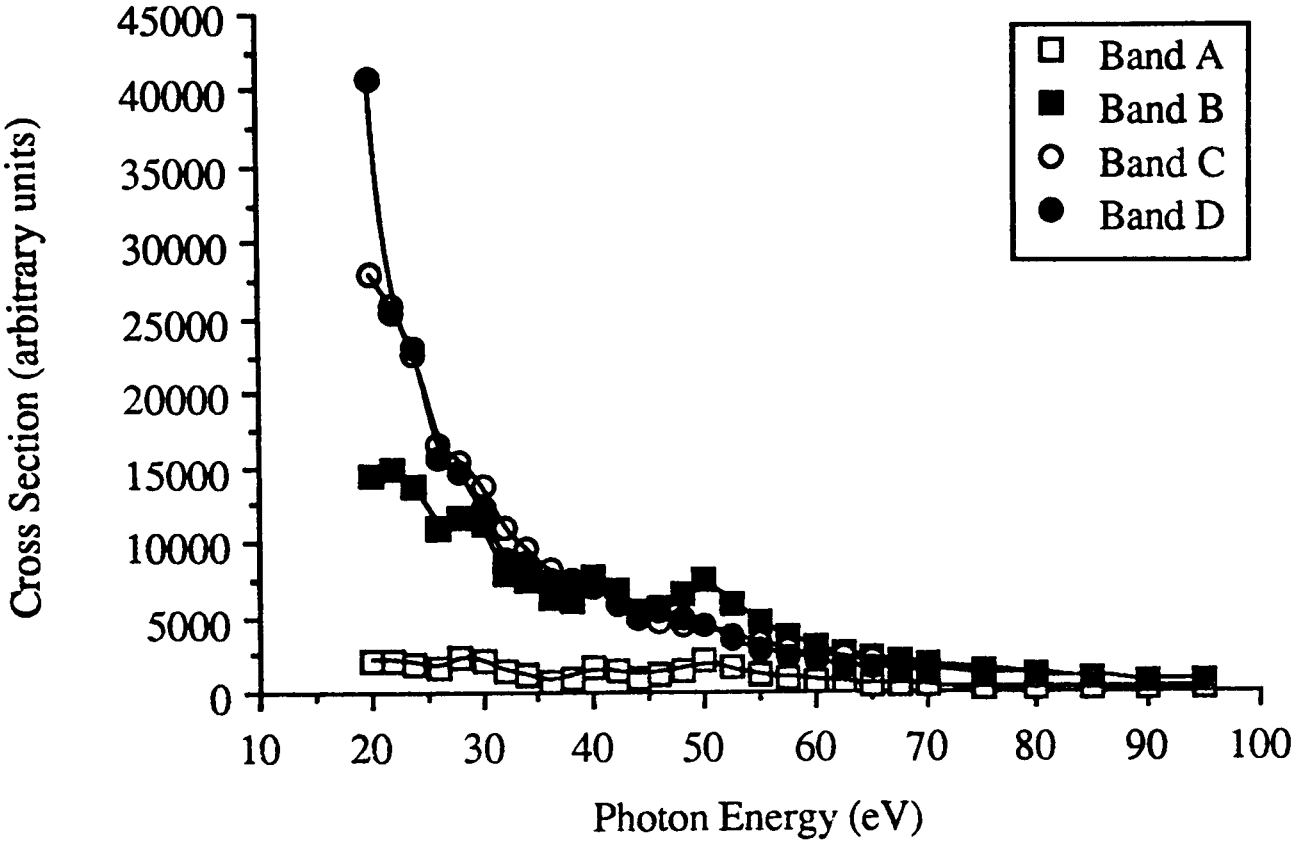

Figure 2.17 : RPPICS of bands A-D in the PE spectrum of [Ta(η-C_7H_7)(η-C_5H_4Me)]

in a manner analogous to [Nb(η-C_7H_7)(η-C_5H_5)]. A significant difference between the two systems arises because of the increase in spin-orbit coupling effects in the third row over the second row metals, to the point at which the LS coupling scheme is no longer valid. A treatment of the p→d resonances in [$W(CO)_6$] [9, 18], [Os(η-C_5H_5)$_2$] [9, 16] and [U(η-C_8H_8)$_2$] [22, 34] under the j-j coupling approach led in all cases to the prediction that the first RPPICS maximum should be more intense than the second. In all cases the reverse was found in practice, as is the situation in d→f photoabsorption spectra of lanthanide and actinide elements, e.g. thorium [35] and uranium [36]. The conclusion was that neither coupling scheme provides a valid approach, as the magnitude of exchange and spin-orbit effects are similar [37].

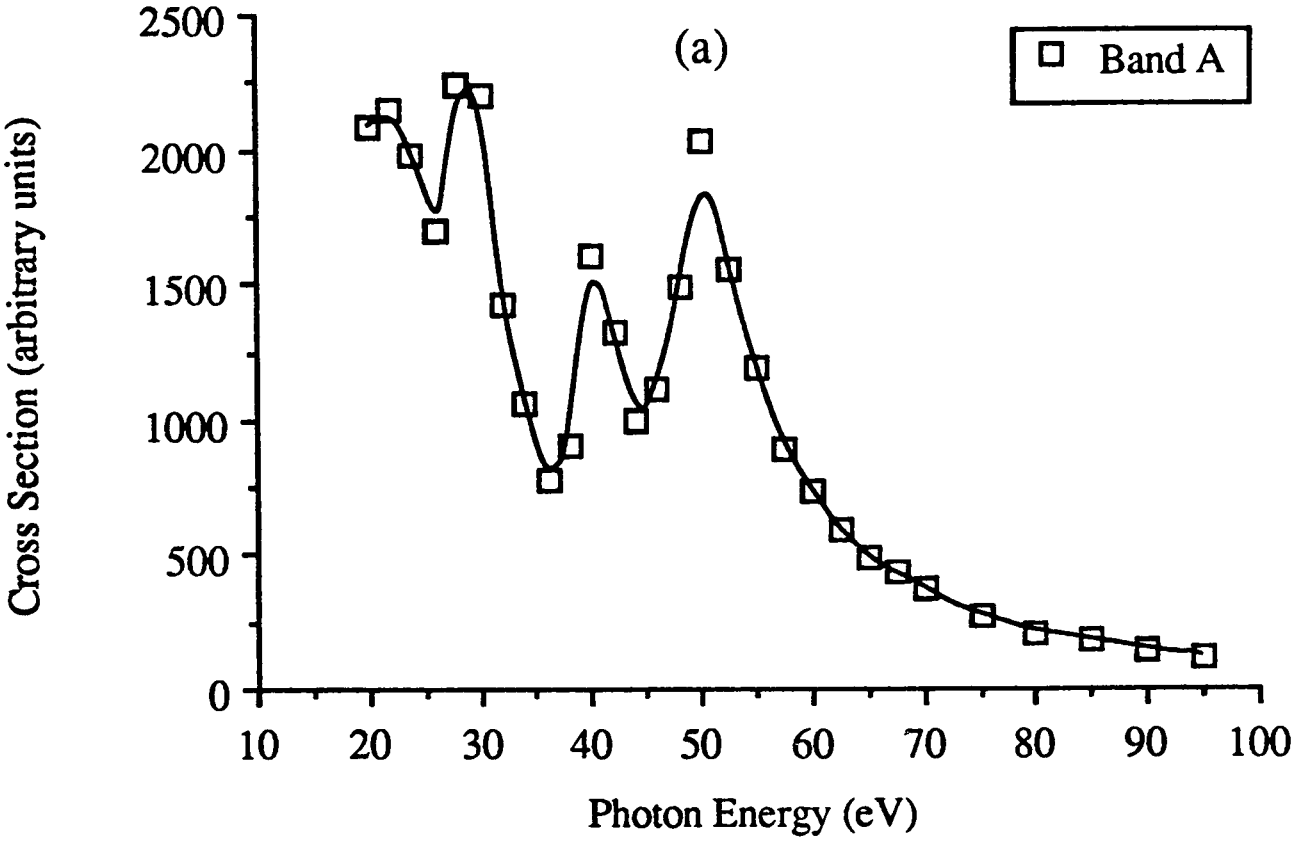

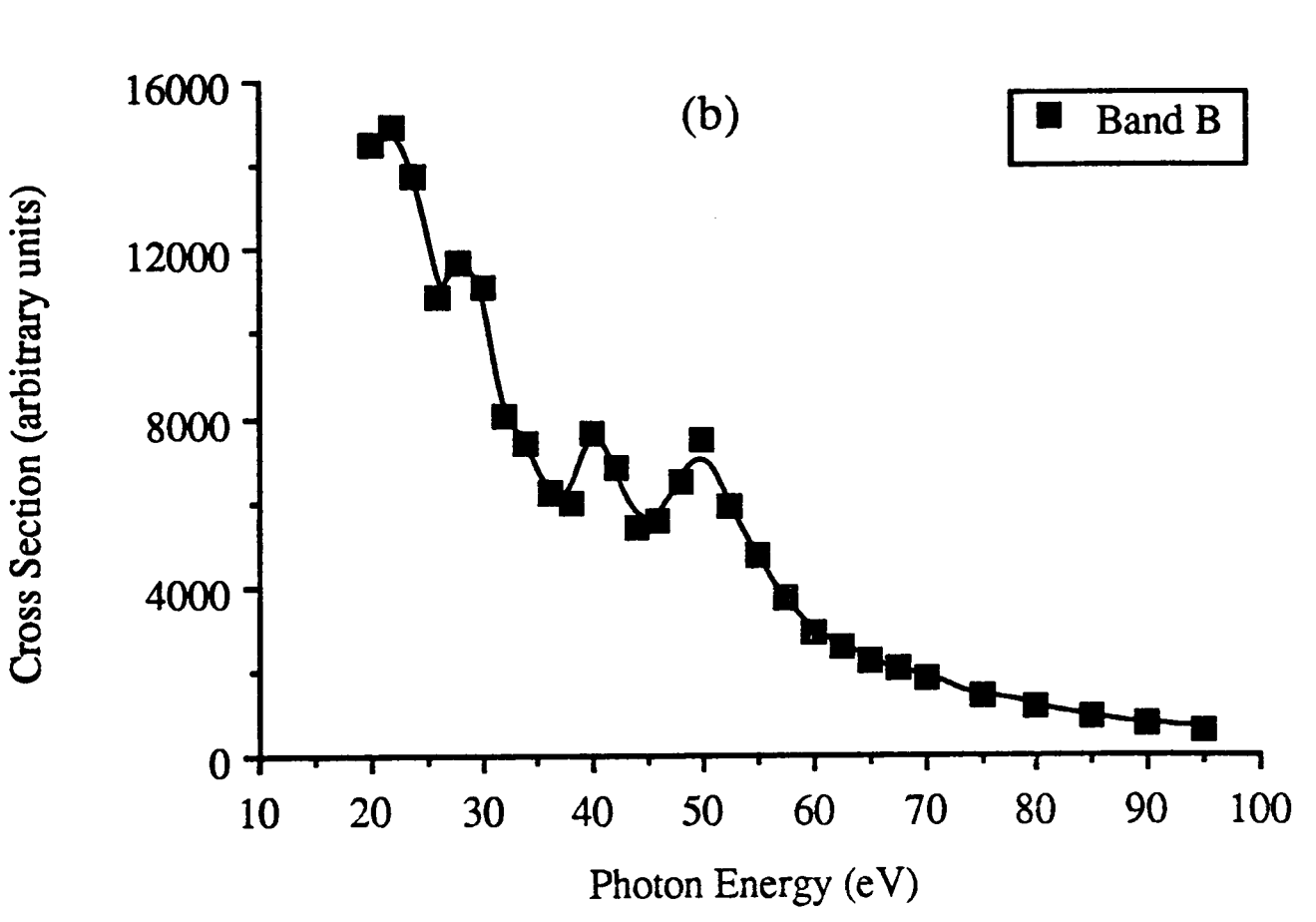

Figure 2.18 : RPPICS of (a) band A and (b) band B in the PE spectrum of $[Ta(\eta\text{-}C_7H_7)(\eta\text{-}C_5H_4Me)]$

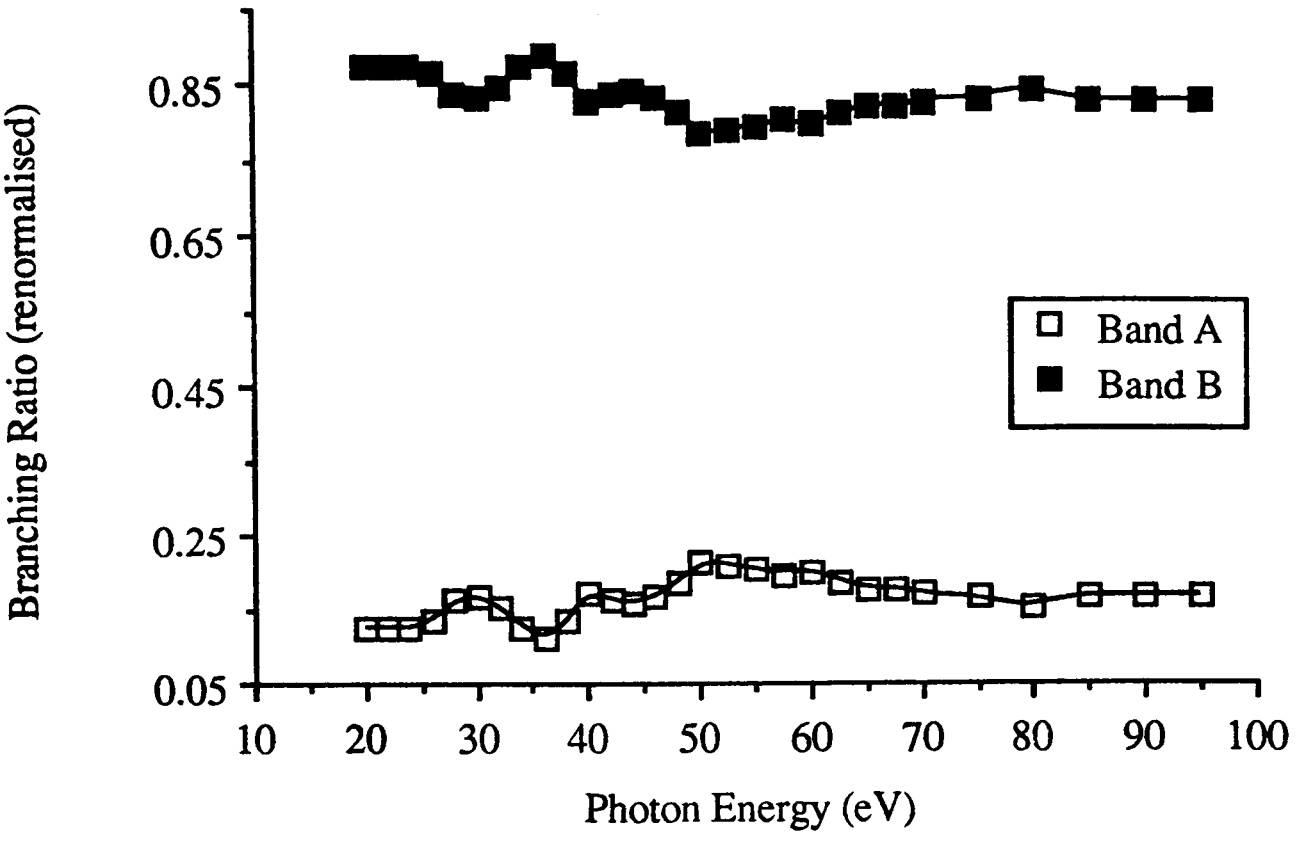

Figure 2.19 : renormalised BRs of bands A and B in the PE spectrum of [Ta(η-C_7H_7)(η-C_5H_4Me)]

Given this body of evidence, the fact that the second RPPICS maximum is again more intense than the first in both bands A and B, and the complications arising from the possibility of more than two open shells in the molecular ion ($(5p^5)(1e_2^4)(1a_1^1)(1e_1^1)$) and the expected molecular shape resonance, a group theoretical treatment of the p→d resonance in [Ta(η-C_7H_7)(η-C_5H_4Me)] under either coupling scheme is not rewarding.

The molecular potential field of [Ta(η-C_7H_7)(η-C_5H_4Me)] should not differ significantly from those of the complexes discussed so far, and a shape resonance might therefore be expected in both bands A and B at ca. 40 eV. The symmetric nature of both RPPICS enhancements suggests that if a shape resonance is occurring, it is coincident in photon energy with one of the p→d resonance maxima.

The RPPICS of both bands A and B fit very well to two Fano profiles having identical line profile indices, one profile being used to fit each of the separate maxima at 42

and 52 eV. The values obtained are given in Table 2.7. The validity of this exercise is tenuous, but if the potential errors in the approach are assumed to be the same for both bands A and B, the results may be used to quantify the percentage of tantalum 5d AO character in the $1e_2$ MOs. If the further assumption that the $1a_1$ MO is purely tantalum 5d in composition is made, a value of (0.15/1.06)×100% = 14% for the tantalum 5d AO contribution to the $1e_2$ MOs can be obtained, based on a comparison of the line profile indices for bands A and B. This conclusion of relatively little metal character in the $1e_2$ MOs is supported by a qualitative inspection of Figure 2.18.

Table 2.7 : Fano parameters obtained from the RPPICS of bands A and B in the PE spectrum of [Ta(η-C_7H_7)(η-C_5H_4Me)]

Band	q	E_r (eV)	σ_0	Γ	X	hν range (eV)
A	1.06	38.2	1019	1.62	0.027	34-62.5
		47.6		6.93		
B	0.15	37.2	7009	4.89	0.034	36-60
		45.1		6.78		

If a similar comparison is made for [Mo(η-C_7H_7)(η-C_5H_5)], the q values (Table 2.6, page 55) indicate a 56% molybdenum 4d contribution to the $1e_2$ MOs. Thus the RPPICS enhancement of the $1e_2^{-1}$ band over the p→d resonance region is smaller in [Ta(η-C_7H_7)(η-C_5H_4Me)] than either [Mo(η-C_7H_7)(η-C_5H_5)] (or [Nb(η-C_7H_7)(η-C_5H_5)]), suggesting a more ligand-localised set of MOs in the third row system.

There is a maximum in the RPPICS of both bands at 22 eV, which may be identified with the delayed maximum in the tantalum 5d AO cross section. Calculations predict that this maximum should occur at about the same PE KE as that of the 4d AO of niobium (ca. 10 eV) [21]. An incident photon energy of 22 eV corresponds to a PE KE of ca. 16.5 eV in band A and 15.1 eV in band B, which is somewhat higher than the predicted value. The data for [Ta(η-C_7H_7)(η-C_5H_4Me)] are the first to show a cross section maximum at these low incident photon energies, the previous RPPICS revealing only the

fall off following the delayed maximum. Hence of all of the estimates of the positions of the delayed maxima, the tantalum one is the most reliable.

The remaining feature in the RPPICS of bands A and B is the maximum at 28 eV. It is very likely that this is due to the molecular shape resonance seen at 27 eV in [Nb(η-C_7H_7)(η-C_5H_5)] and at 30 eV in [Mo(η-C_6H_6)$_2$] and [Mo(η-C_7H_7)(η-C_5H_5)]. Once again the effect is significantly greater in the $1a_1$ MO than the $1e_2$.

The BR data (Figure 2.19) indicate that the resonance features are stronger in the more metal-localised orbital. There is a slight gain in relative intensity of band B over band A at higher incident photon energies, but it is not as great as in the second row complexes. This is in agreement with calculation [21], which indicates that the Cooper minimum in the cross section of the 5d AO of tantalum occurs at a photon energy of ca. 190 eV, substantially higher than that of either niobium or molybdenum.

The RPPICS of bands C and D are given in Figure 2.20, together with their renormalised BRs. Unlike the equivalent e_1^{-1} bands in [Mo(η-C_7H_7)(η-C_5H_5)] and [Nb(η-C_7H_7)(η-C_5H_5)], the cross section behaviour is typical of essentially ligand-based MOs, with no RPPICS enhancement at incident photon energies corresponding to the resonance phenomena observed in the $1a_1^{-1}$ and $1e_2^{-1}$ bands. This is strong evidence to indicate very little tantalum 5d AO involvement in either of the e_1 ring MOs. Figure 2.20 (b) indicates that the relative areas of the two bands remain fairly equal over the photon energy range employed, in agreement with the assertion that each band corresponds to four electrons with similar localisation properties.

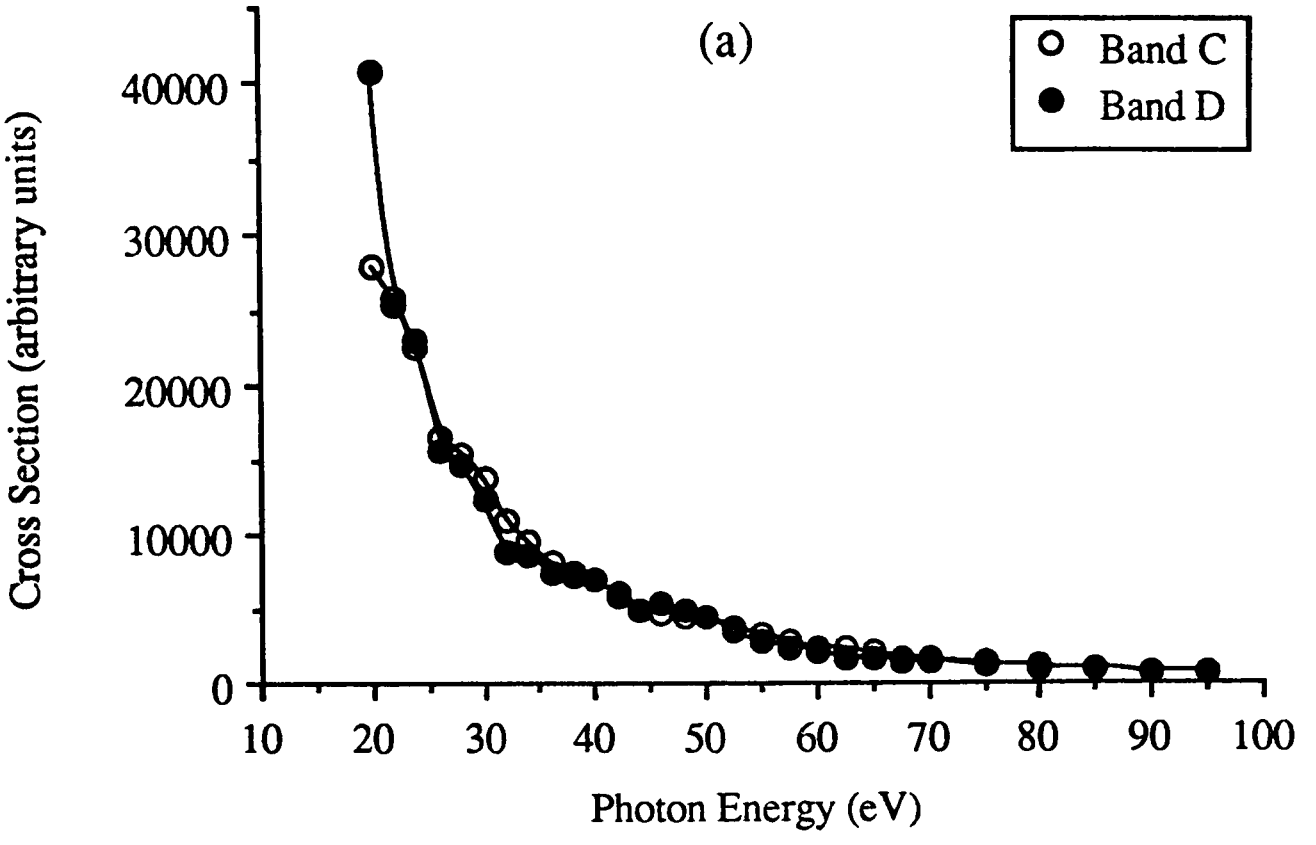

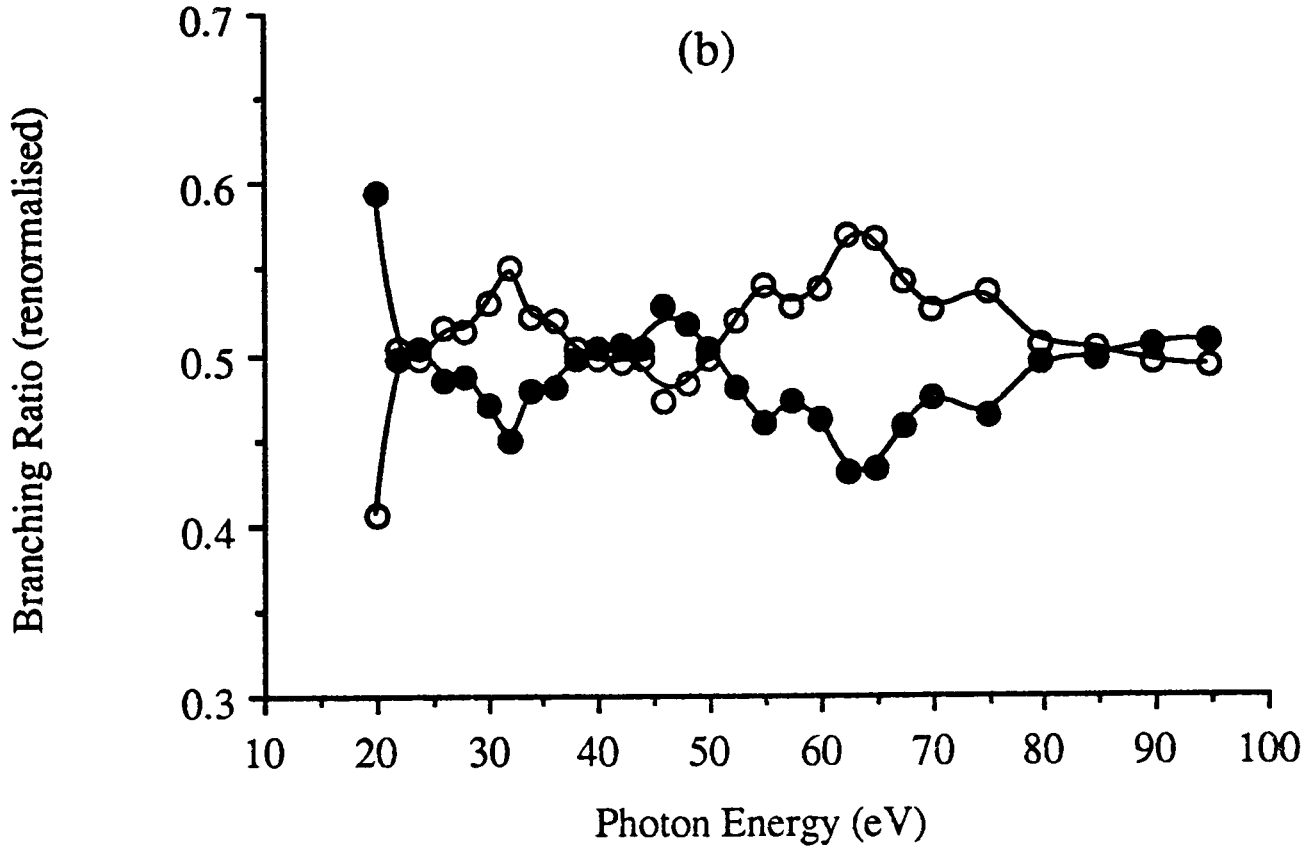

Figure 2.20 : (a) RPPICS and (b) renormalised BRs of bands C and D in the PE spectrum of [Ta(η-C_7H_7)(η-C_5H_4Me)]

2.3.2 (d) [Ti(η-C_7H_7)(η-C_5H_5)]

The He I and He II spectra of [Ti(η-C_7H_7)(η-C_5H_5)] have been reported before [1], and they are very similar to one another. This lack of change in the form of the spectrum as the incident photon energy is raised from 21.22 to 40.81 eV was taken as evidence of little or no titanium 3d AO character in the $1e_2$ MOs. Together with the chemical evidence discussed earlier, the discharge lamp spectra support the assertion of a Ti(IV) (d^0) metal centre with the oxidation state of the cycloheptatrienyl ring being -3. In the light of substantial RPPICS enhancements of the $1e_2^{-1}$ bands in [Mo(η-C_7H_7)(η-C_5H_5)], [Nb(η-C_7H_7)(η-C_5H_5)] and [Ta(η-C_7H_7)(η-C_5H_4Me)] in the p→d resonance regions, it was decided to investigate [Ti(η-C_7H_7)(η-C_5H_5)] using synchrotron radiation.

The PE spectrum of [Ti(η-C_7H_7)(η-C_5H_5)], recorded at 33 and 48 eV, is shown in Figure 2.21. [Ti(η-C_7H_7)(η-C_5H_5)] is a 16-electron complex and the HOMO is the $1e_2$ MO. Consequently only three bands are observed below an IE of ca. 11 eV. The change in the form of the spectrum as the incident photon energy is raised to 48 eV - just above the energy of the He IIα line - is quite dramatic, with the $1e_2^{-1}$ band (band A) undergoing a substantial increase in relative intensity. This is illustrated in Figure 2.22, which presents the RPPICS and BRs of bands A, B and C. It can be seen that it is only as the incident photon energy is increased above 42 eV that the p→d resonance takes effect, providing an elegant example of the advantages of access to a continuously tunable light source.

The 3p subshell of atomic titanium ionises at 38 ($^2P_{3/2}$) and 39 ($^2P_{1/2}$) eV [14]. The 3p→3d giant resonant absorption process for [Ti(η-C_7H_7)(η-C_5H_5)] is represented by two equations

$$(3p)^6(1e_2)^4(1a_1)^0(3e_1)^0 + h\nu \rightarrow (3p)^5(1e_2)^4(1a_1)^1(3e_1)^0$$

$$(3p)^6(1e_2)^4(1a_1)^0(3e_1)^0 + h\nu \rightarrow (3p)^5(1e_2)^4(1a_1)^0(3e_1)^1$$

The permitted final states arising from both of the intermediate configurations are $^1A_1$ + $^1E_1$, giving a total of four allowed states, as for [Nb(η-C_7H_7)(η-C_5H_5)].

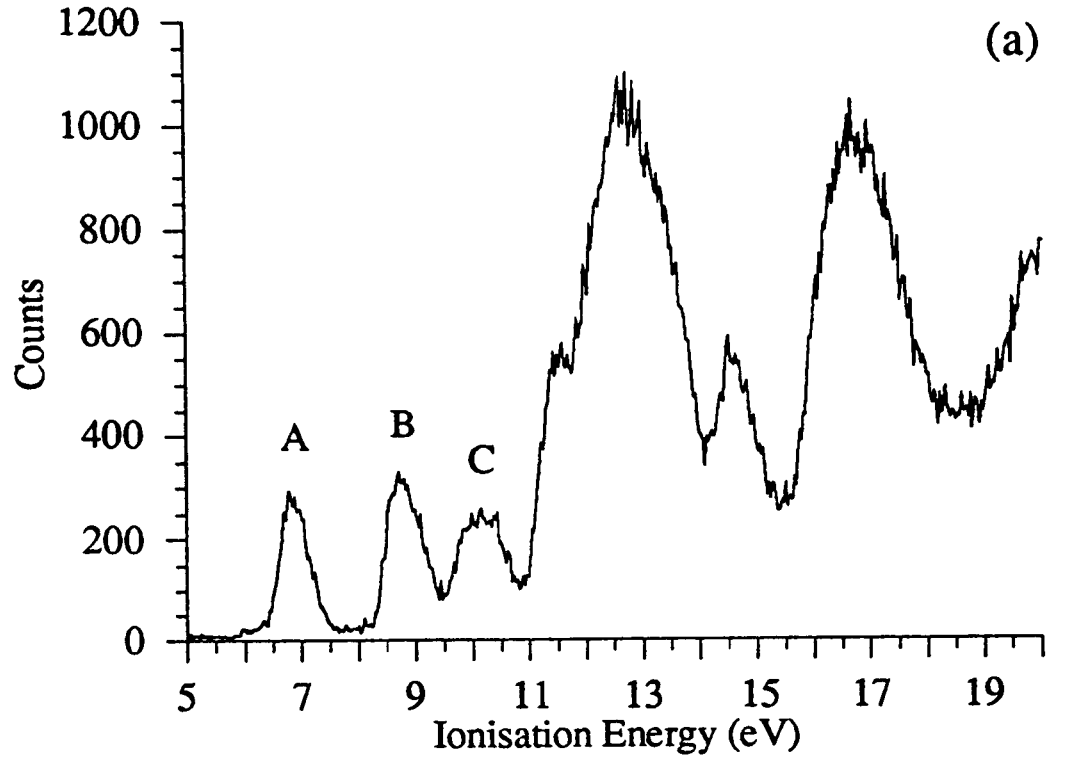

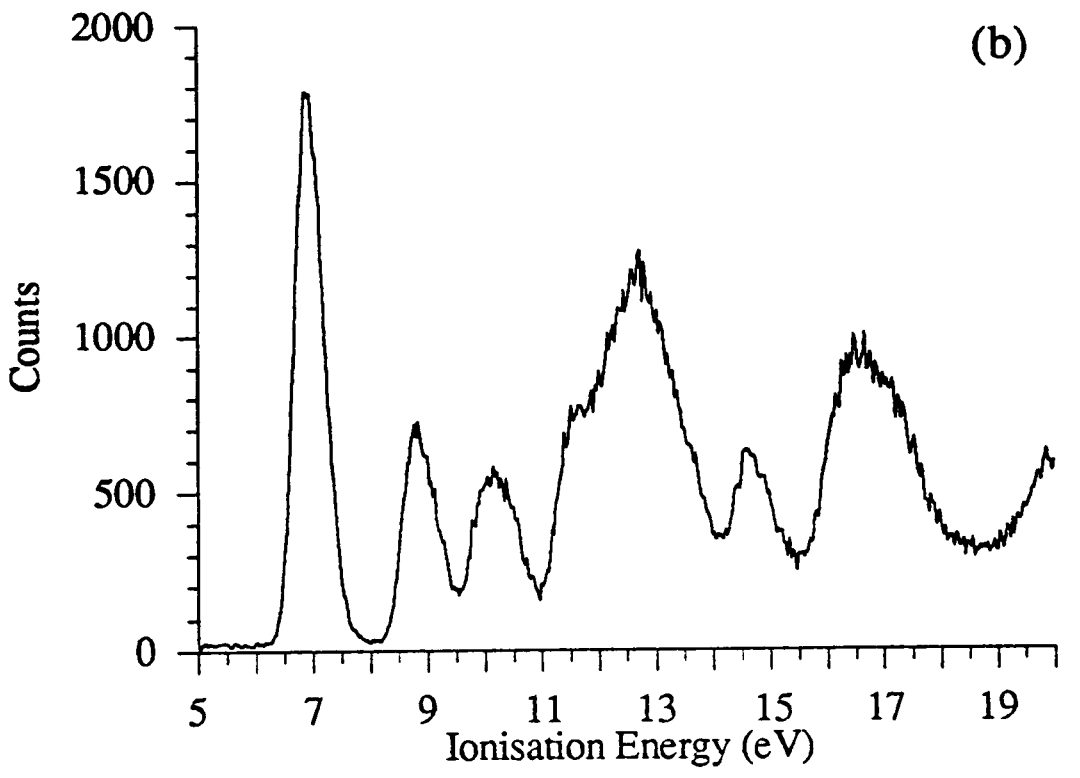

Figure 2.21 : the PE spectrum of [Ti(η-C_7H_7)(η-C_5H_5)], acquired at (a) 33 and (b) 48 eV

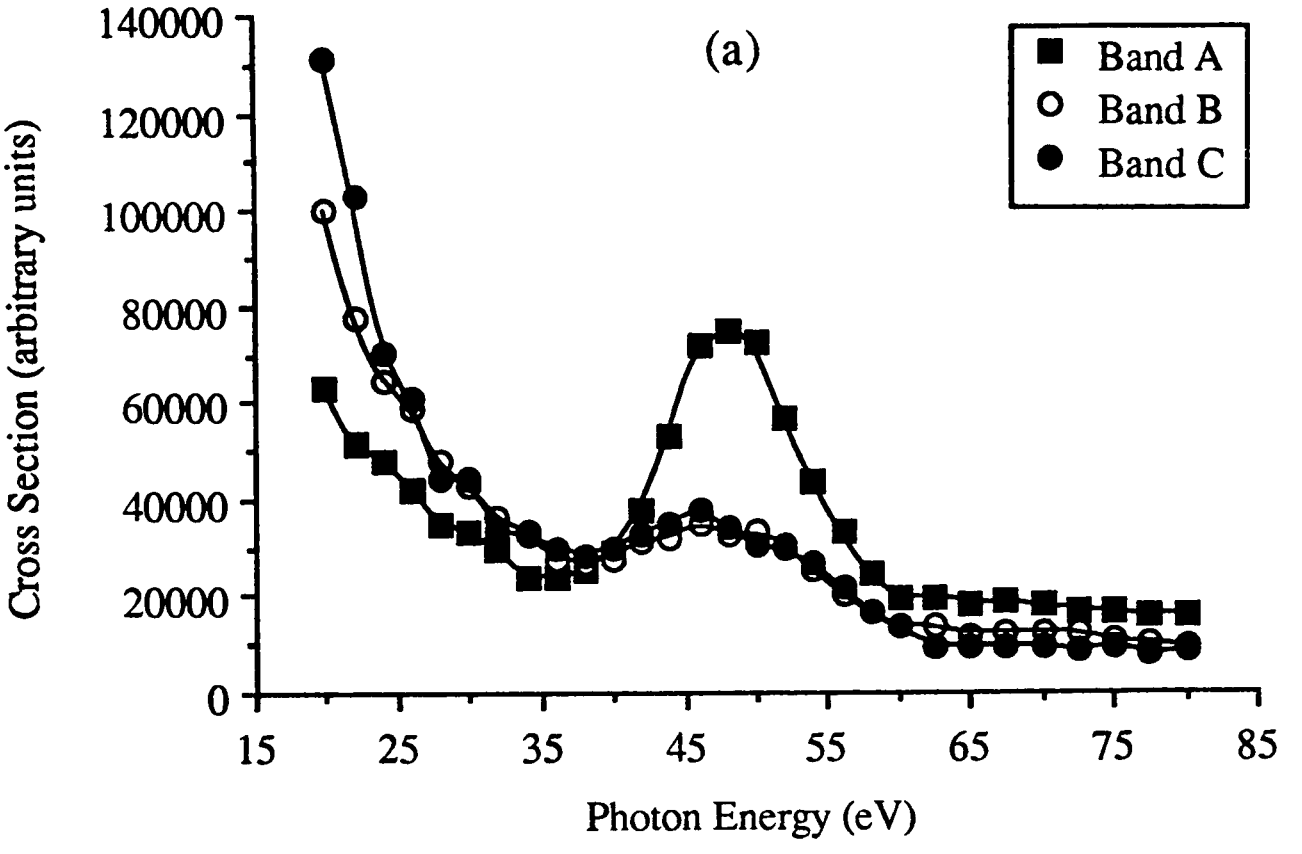

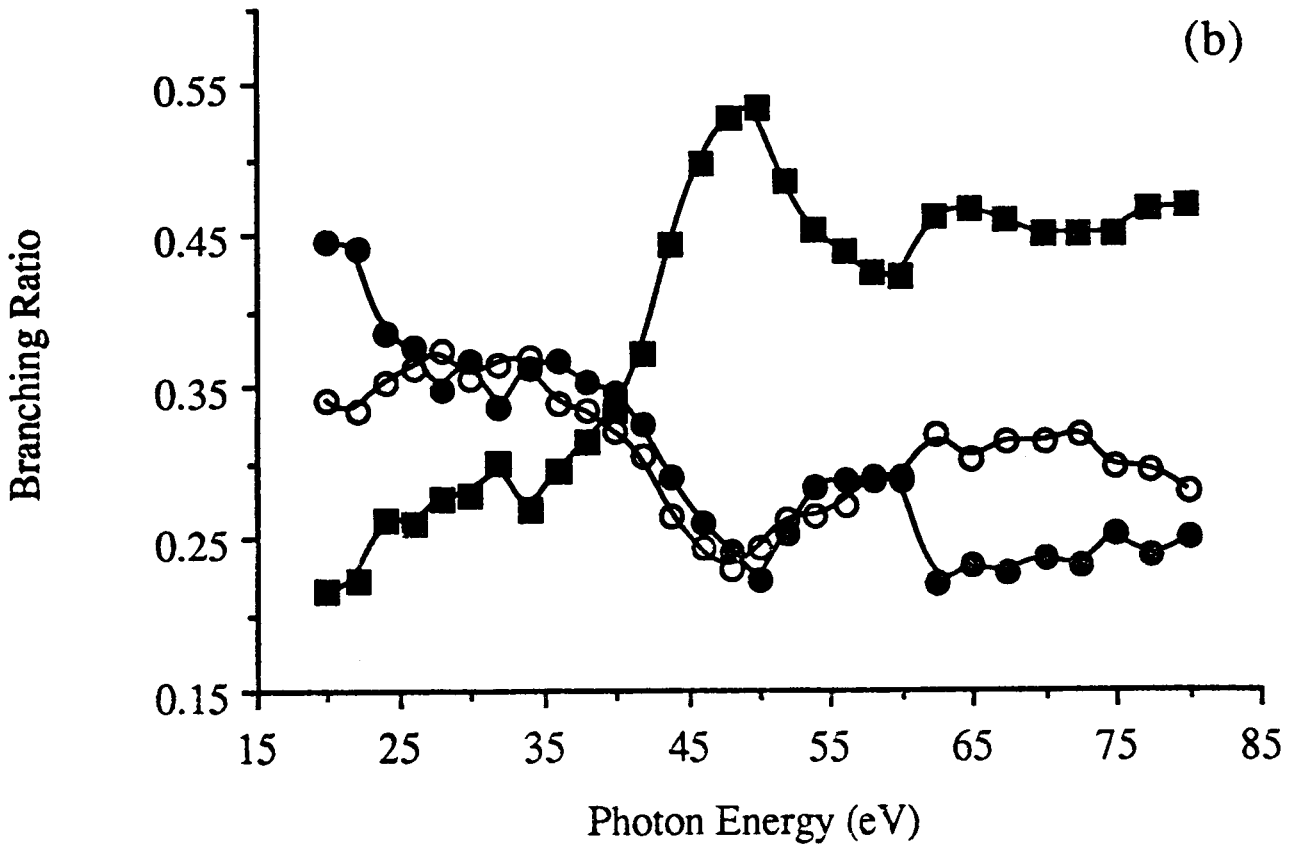

Figure 2.22 : (a) RPPICS and (b) BRs of bands A, B and C in the PE spectrum of $[Ti(\eta\text{-}C_7H_7)(\eta\text{-}C_5H_5)]$

Autoionisation

$$(3p)^5(1e_2)^4(1a_1)^1(3e_1)^0 \rightarrow (3p)^5(1e_2)^4(1a_1)^0(3e_1)^0 + e^-$$
$$(3p)^5(1e_2)^4(1a_1)^0(3e_1)^1 \rightarrow (3p)^5(1e_2)^4(1a_1)^0(3e_1)^0 + e^-$$

is possible, together with the SCK decay procesess

$$(3p)^5(1e_2)^4(1a_1)^1(3e_1)^0 \rightarrow (3p)^6(1e_2)^3(1a_1)^0(3e_1)^0 + e^-$$
$$(3p)^5(1e_2)^4(1a_1)^0(3e_1)^1 \rightarrow (3p)^6(1e_2)^3(1a_1)^0(3e_1)^0 + e^-$$

the final state of which is identical to that produced by direct photoionisation of the $1e_2$ MOs. Inter-channel coupling between these final states should result in four overlapping Fano profiles for the RPPICS of the $1e_2^{-1}$ band.

The shape of the RPPICS enhancement of band A between 38-60 eV is unlike any seen in the other [M(η-C_7H_7)(η-C_5H_5)] molecules. It is very symmetric, and if there is a shape resonance occurring, it is obscured by the p→d resonance. It proved impossible to obtain a Fano fit to the RPPICS of band A in this region, using both one and two profiles. This non-Fano enhancement may be caused by a coincident shape resonance, or may reflect the presence of four possible intermediate states in the p→d giant resonant absorption process. A qualitative inspection of Figure 2.22 (a), however, indicates that the p→d resonant enhancement of the $1e_2^{-1}$ band is large - indeed the cross section is highest in the p→d resonance region. In the absence of RPPICS data for the $1a_1^{-1}$ ionisation, it is difficult to assess precisely how significant the RPPICS enhancement of the $1e_2^{-1}$ band is. Nevertheless it would appear that there is a substantial degree of titanium 3d AO character to the $1e_2$ MOs. This suggests that the -3 formalism for the charge on the cycloheptatrienyl ring is not a good way of describing the cycloheptatrienyl-Ti bonding in this complex, as it implies a ligand-localised $1e_2$ MO.

There is no feature in the RPPICS of band A which correlates with the shape resonance seen in the cross sections of the $1a_1^{-1}$ and some of the $1e_2^{-1}$ bands of [M(η-

$C_7H_7)(\eta\text{-}C_5H_5)]$ at photon energies between 27-30 eV. Once more, the absence of a $1a_1^{-1}$ ionisation makes it difficult to draw any conclusions from this observation, in that what was quite a strong feature in the $1e_2^{-1}$ band of $[Ta(\eta\text{-}C_7H_7)(\eta\text{-}C_5H_4Me)]$ was not observed in $[Nb(\eta\text{-}C_7H_7)(\eta\text{-}C_5H_5)]$. Similarly there is no low photon energy cross section feature which equates with a delayed maximum. For atomic titanium, the delayed maximum in the 3d orbital cross section is calculated to occur at a PE KE of ca. 23 eV [21], which would place it at an incident photon energy of ca. 30 eV for band A.

The RPPICS of bands B and C are very similar to one another, with both displaying a significant enhancement in the p→d resonance region. As with band A, assessing metal d orbital character in the e_1 levels is not possible, but it is interesting that both bands should behave so similarly over the resonance. In both $[Mo(\eta\text{-}C_7H_7)(\eta\text{-}C_5H_5)]$ and $[Nb(\eta\text{-}C_7H_7)(\eta\text{-}C_5H_5)]$, the $1e_1^{-1}$ band gains in intensity relative to the $2e_1^{-1}$.

As the BR plot (Figure 2.22 (b)) shows, it is only in the high incident photon energy region (>60 eV) that the behaviour of bands B and C differ. Unfortunately this is almost certainly an artefact of the curve fitting (for a discussion of this, see Chapter 6.2.3). Above 60 eV a higher analyser pass energy is employed, which results in poorer spectral resolution, a situation which the lower light levels available from grating 1 (Chapter 6.2.1) further exacerbates. A similar problem was found with bands B and C of OsO_4 above an incident photon energy of ca. 65 eV (Chapter 4.2.2). Hence it is unlikely that the gain of band B over band C at higher photon energies is a real effect.

2.3.3 Summary of the results from the mixed ring species

In all four molecules studied, substantial RPPICS enhancements are observed in bands corresponding to ionisation from MOs with significant metal d orbital character in the region of the np subshell binding energies. This np→nd giant resonant absorption is greatest for the $1a_1^{-1}$ bands, which are due to metal-localised MOs. It is not valid to compare directly the magnitudes of resonance phenomena between complexes containing different metals, but as all of the compounds bar $[Ti(\eta\text{-}C_7H_7)(\eta\text{-}C_5H_5)]$ have their own "internal standard" (the $1a_1^{-1}$ band), it is possible to obtain a measure of the degree of metal

d orbital involvement in the other valence MOs. A comparison of relative metal d orbital content in the valence MOs of [Nb(η-C_7H_7)(η-C_5H_5)], [Mo(η-C_7H_7)(η-C_5H_5)] and [Ta(η-C_7H_7)(η-C_5H_4Me)] can then be made, but with no reference band in [Ti(η-C_7H_7)(η-C_5H_5)] an extension to this compound is not justified.

(a) *the e_1^{-1} bands* - in both [Nb(η-C_7H_7)(η-C_5H_5)] and [Mo(η-C_7H_7)(η-C_5H_5)], there is a greater degree of metal d orbital involvement in the e_1 levels of the seven-membered ring than the five. Niobium exhibits this more than does molybdenum, although the effect is not great in either system. In [Ta(η-C_7H_7)(η-C_5H_4Me)], neither e_1 level reveals a significant amount of metal d orbital character.

(b) *the e_2^{-1} bands* - strong evidence is found for substantial metal d orbital involvement with these levels in all four systems. Quantitative estimates of this effect are hampered by the existence of a molecular shape resonance, coincident in incident photon energy with the np→nd giant resonances. A qualitative comparison of the magnitudes of the RPPICS enhancements of the $1e_2^{-1}$ bands with those of the $1a_1^{-1}$, however, suggests that there is significantly more metal d orbital contribution to the $1e_2$ MOs in [Nb(η-C_7H_7)(η-C_5H_5)] and [Mo(η-C_7H_7)(η-C_5H_5)] than in [Ta(η-C_7H_7)(η-C_5H_4Me)]. These results suggest that the -3 formalism for the charge on the cycloheptatrienyl ring is a poor one, as it implies a ligand-localised set of $1e_2$ levels.

(c) *shape resonances* - evidence has been gathered to support the assertion that the occurrence and magnitude of shape resonances in these sandwich molecules is related primarily to the amount of metal d orbital content in the ionising MOs. The $1a_1$ HOMOs of [M(η-C_7H_7)(η-C_5H_5)] (M=Nb, Mo) and [Ta(η-C_7H_7)(η-C_5H_4Me)] are found to be essentially metal nd_{z^2} in character, as was the $1a_{1g}$ HOMO of [Mo(η-$C_6H_5Me)_2$]. Low incident photon energy (20-25 eV) features in the RPPICS of these $1a_1^{-1}$ bands are identified with the delayed maxima in the cross sections of the nd AOs. The maxima in the $1a_1^{-1}$ RPPICS at 27-30 eV are therefore attributed to a shape resonance. This is mirrored to some extent in the RPPICS of the mixed metal/ligand $1e_2^{-1}$ band, being visible in [Mo(η-C_7H_7)(η-C_5H_5)] and [Ta(η-C_7H_7)(η-C_5H_4Me)] but not in [Nb(η-C_7H_7)(η-C_5H_5)] (or [Ti(η-C_7H_7)(η-C_5H_5)]). As was noted for [Mo(η-$C_6H_5Me)_2$], however, the carbon 2p AO

contribution to the RPPICS of the $1e_2^{-1}$ bands at these low incident photon energies may well be obscuring the effect.

There is clear evidence to suggest that the shape resonance seen in the $1a_{1g}^{-1}$ and $1e_{2g}^{-1}$ bands of [Mo(η-$C_6H_5Me)_2$] at ca. 42 eV also occurs in the equivalent bands of [Mo(η-C_7H_7)(η-C_5H_5)] and [Nb(η-C_7H_7)(η-C_5H_5)]. That there is no such feature in the cross section of the $1e_1^{-1}$ band of either molecule is evidence that this resonance is also primarily metal d orbital content controlled, in that the $1e_{1g}^{-1}$ band of [Mo(η-$C_6H_5Me)_2$], which mirrors the shape resonance in the $1a_{1g}^{-1}$ and $1e_{2g}^{-1}$ bands, is found to have significant metal d AO character, unlike the e_1^{-1} bands of the mixed ring species. This resonance is not seen in [Ta(η-C_7H_7)(η-C_5H_4Me)] or [Ti(η-C_7H_7)(η-C_5H_5)], but may be hidden by the p→d resonance features.

2.4 Analysis of the ionisation energy data of some group V metal sandwich molecules

Following the synthesis of [Ta(η-C_7H_7)(η-C_5H_4Me)], it has become possible to obtain IE data for the series of molecules [M(η-C_7H_7)(η-C_5H_4R)] (M=V, Nb; R=H : M=Ta; R=Me). The data for the niobium and tantalum compounds are given in Table 2.5 (page 50), while those for [V(η-C_7H_7)(η-C_5H_5)] are presented in Table 2.8. The IEs listed are those obtained from a remeasurement of the spectrum by the author, while those in parentheses refer to the original work [3]. The PE spectrum of [V(η-C_7H_7)(η-C_5H_5)] is not presented here. It is very similar to the equivalent second and third row spectra, and has an analogous assignment.

Table 2.8 : assignment of the PE spectrum of [V(η-C_7H_7)(η-C_5H_5)]

Band	IE (eV) [a]	Ion state	Related MO
A	6.49 (6.42)	$^1A_1$	$1a_1$
B	6.86 (6.77)	$^3E_2$	$1e_2$
B'	7.35 (7.28)	$^1E_2$	$1e_2$
C	8.72 (8.66)		$2e_1$
C'	9.04 (8.99)		$2e_1$
D	10.40 (10.20)		$1e_1$
	>11		ligand σ and π

[a] Data in parentheses from reference [3]

Comparison of the IE data obtained for these group V complexes reveals that the $1e_1$ levels are effectively insensitive to changes in the metal. The $2e_1$ and $1e_2$ MOs also show little change as the group is descended. The 0.05 eV increase in IE of the $2e_1$ MOs as the metal is changed from vanadium to niobium, attributed to a greater metal-e_1 interaction in niobium than vanadium [26], is not continued in the third row compound, probably as a result of the methylation of the five-membered ring. This may also account for the similar trend observed in the $1e_2$ IEs. The separation of the $^3E_2$ and $^1E_2$ states (arising from ionisation of the $1e_2$ MOs) decreases as the group is descended, from 0.49 eV in [V(η-C_7H_7)(η-C_5H_5)], to 0.36 eV in [Nb(η-C_7H_7)(η-C_5H_5)] and 0.32 eV in [Ta(η-C_7H_7)(η-C_5H_4Me)]. This is as expected for a splitting stemming from an exchange interaction, and is found in the PE spectra of the bis-arene compounds [M(η-$C_6H_5R)_2$] (M=V, Nb; R=H, Me) [4] (no PE data exist for bis-arene tantalum).

The most significant effect of altering the metal atom occurs in the $1a_1$ MO, the IE of which drops 0.57 eV from [V(η-C_7H_7)(η-C_5H_5)] to [Nb(η-C_7H_7)(η-C_5H_5)] and by a further 0.38 eV from [Nb(η-C_7H_7)(η-C_5H_5)] to [Ta(η-C_7H_7)(η-C_5H_4Me)]. This orbital, which the evidence suggests is almost purely metal d_{z2}, reflects most closely the energy of the metal d electrons in the complex. The gap between the $1a_1$ and the $1e_2$ ionisations also

increases down the group, from 0.35 eV for [V(η-C_7H_7)(η-C_5H_5)] ($^3E_2$ - $^1A_1$) to 1.15 eV for [Nb(η-C_7H_7)(η-C_5H_5)] and 1.42 eV for [Ta(η-C_7H_7)(η-C_5H_4Me)]. Ligand field parameters may be established for metal sandwich compounds using the expressions given below [4, 12] in which A, B and C are the usual Racah parameters for measuring interelectronic repulsions. For d^4 cations

$$E(^1A_1) = 6A+24B+8C \qquad E(^3E_2) = 6A-8B+5C+\Delta_2 \qquad E(^1E_2) = 6A+7C+\Delta_2$$

from which it follows that

$$^3E_2 - {}^1A_1 = \Delta_2 - 44B \quad \text{and} \quad {}^1E_2 - {}^3E_2 = 16B$$

assuming that C = 4B. Using the information obtained from the PE spectra, values for Δ_2 (Figure 2.6, page 47), B and β (the nephelauxetic ratio) have been calculated, and these are given in Table 2.9, together with corresponding data for bis-arene compounds of vanadium and niobium. Similar data for both [V(η-C_7H_7)(η-C_5H_5)] and [Nb(η-C_7H_7)(η-C_5H_5)] have been presented earlier [12], based upon the original PE studies of these compounds. It should be noted, however, that the above derivations neglect spin-orbit coupling. This will be small for complexes of the first and second row metals, but may be significant for third row elements. The $1e_2$ level of [Ta(η-C_7H_7)(η-C_5H_4Me)] may be split not only by singlet-triplet interaction, but also by spin-orbit coupling. In free Ta^+, the splitting of the $5d_{3/2}$ and $5d_{5/2}$ levels is predicted as $2\zeta = 0.44$ eV [38] although delocalisation of the metal d electrons onto the cycloheptatrienyl ring will reduce the magnitude of any splitting of the $1e_2$ MOs. It has been shown (Section 2.3.2 (c)) that the tantalum 5d AO content of the $1e_2$ MOs of [Ta(η-C_7H_7)(η-C_5H_4Me)] could be as little as 14%, and hence it is unlikely that spin-orbit coupling plays any significant role in the asymmetry of band B. Therefore the errors in the values of B, β and Δ_2 for [Ta(η-C_7H_7)(η-C_5H_4Me)] arising from spin-orbit splitting are likely to be small.

Table 2.9 : ligand field analysis of some group V metal sandwich cations

Cation	Δ_2 (eV)	B (eV)	β [a]
$[V(\eta\text{-}C_7H_7)(\eta\text{-}C_5H_5)]^+$	1.72	0.031	0.43
$[Nb(\eta\text{-}C_7H_7)(\eta\text{-}C_5H_5)]^+$	2.14	0.023	0.42
$[Ta(\eta\text{-}C_7H_7)(\eta\text{-}C_5H_4Me)]^+$	2.47	0.024	0.40
$[V(\eta\text{-}C_6H_6)_2]^+$ [b]	1.91	0.047	0.63
$[V(\eta\text{-}C_6H_5Me)_2]^+$ [b]	1.87	0.046	0.63
$[V(\eta\text{-}C_6H_3Me_3)_2]^+$ [b]	1.78	0.047	0.64
$[Nb(\eta\text{-}C_6H_6)_2]^+$ [b]	2.14	0.031	0.57
$[Nb(\eta\text{-}C_6H_5Me)_2]^+$ [b]	2.01	0.035	0.57
$[Nb(\eta\text{-}C_6H_3Me_3)_2]^+$ [b]	1.95	0.035	0.66

[a] Values for $B_{free\ ion}$ from reference [38] [b] Data from reference [4]

As expected, there is a significant drop in the electron-electron repulsion parameter B on moving from vanadium to niobium and tantalum, as is also observed for the bis-arene compounds $[M(\eta\text{-}C_6H_6)_2]^+$ (M = V and Nb) [4]. The reduced B and β values obtained for the mixed ring species are in accordance with the expectation of a stronger metal-ligand interaction through the δ orbitals of the cycloheptatrienyl ring, reinforcing still further the view that there is a significant contribution from both metal and ligand orbitals in these MOs. In addition, the ligand field splitting parameter, Δ_2, increases steadily as the group is descended, as is expected for second and third vs first row metals.

In comparing Δ_2 values of $[M(\eta\text{-}C_7H_7)(\eta\text{-}C_5H_5)]^+$ with $[M(\eta\text{-}C_6H_6)_2]^+$, it is curious that Δ_2 increases on moving from $[Nb(\eta\text{-}C_6H_6)_2]^+$ to the mixed ring species whereas the opposite is true for vanadium. It may be expected that the closer energetic proximity of the metal and ring e_2 levels on moving from a six- to a seven-membered ring would result in increased Δ_2 values. The reason for the drop in the vanadium systems is not clear.

2.5 References for Chapter Two

[1] C. E. Davies, I. M. Gardiner, P. D. Grebenik, J. C. Green, M. L. H. Green, N. J. Hazel, V. S. Mtetwa and K. Prout: *J. Chem. Soc., Dalton Trans.* (1985) 669.

[2] S. Evans, J. C. Green and S. E. Jackson: *J. Chem. Soc., Faraday Trans. II* **68** (1972) 249.

[3] S. Evans, J. C. Green, S. E. Jackson and B. Higginson: *J. Chem. Soc., Dalton Trans.* (1974) 304.

[4] F. G. N. Cloke, A. N. Dix, J. C. Green, R. N. Perutz and E. A. Seddon: *Organometallics* **2** (1983) 1150.

[5] M. F. Guest, I. H. Hillier, B. R. Higginson and D. R. Lloyd: *Mol. Phys.* **29** (1975) 113.

[6] J. Weber, M. Geoffrey, A. Goursot and E. Penigault: *J. Am. Chem. Soc.* **100** (1978) 3995.

[7] G. A. Domrachev, S. Y. Ketkov and G. A. Razuvaev: *J. Organomet. Chem.* **328** (1987) 341.

[8] S. Y. Ketkov and G. A. Domrachev: *J. Organomet. Chem.* **389** (1990) 187.

[9] G. Cooper: *D. Phil. Thesis* Oxford (1987).

[10] E. Keulen and F. Jellinek: *J. Org. Chem.* **5** (1966) 490.

[11] A. Haaland: *Acta Chem. Scand.* **19** (1965) 41.

[12] K. D. Warren: *Structure and Bonding* **27** (1976) 45.

[13] K. Kimura, S. Katsumata, Y. Achiba, T. Yamazaki and S. Iwata: *Handbook of He I Photoelectron Spectra of Fundamental Organic Molecules* Japan Scientific Societies Press, Tokyo (1981).

[14] D. Briggs: *Handbook of X-ray and Ultraviolet Photoelectron Spectroscopy* Heyden, London (1977).

[15] J. L. Dehmer, A. F. Starace, U. Fano, J. Sugar and J. W. Cooper: *Phys. Rev. Lett.* **26** (1971) 1521.

[16] G. Cooper, J. C. Green and M. P. Payne: *Mol. Phys.* **63** (1988) 1031.

[17] J. G. Brennan, G. Cooper, J. C. Green, N. Kaltsoyannis, M. A. MacDonald, M. P. Payne, C. M. Redfern and K. H. Sze: *Chem. Phys.*, in press.

[18] G. Cooper, J. C. Green, M. P. Payne, B. R. Dobson and I. H. Hillier: *J. Am. Chem. Soc.* **109** (1987) 3836.

[19] U. Fano: *Phys. Rev.* **124** (1961) 1866.

[20] U. Fano and J. W. Cooper: *Phys. Rev. A* **137** (1965) 1364.

[21] J. J. Yeh and I. Lindau: *At. Data Nucl. Data Tables* **32** (1985) 1.

[22] C. M. Redfern: *D. Phil. Thesis* Oxford (1988).

[23] D. W. Clack and K. D. Warren: *J. Organomet. Chem.* **152** (1978) C60.

[24] C. J. Groenenboom, G. Sawatsky, H. J. de Liefde Meijer and F. Jellinek: *J. Organomet. Chem.* **76** (1974) C4.

[25] C. J. Groenenboom, H. J. de Liefde Meijer and F. Jellinek: *J. Organomet. Chem.* **69** (1974) 235.

[26] C. J. Groenenboom, H. J. de Liefde Meijer, F. Jellinek and A. Oskam: *J. Organomet. Chem.* **97** (1975) 73.

[27] J. C. Green, M. L. H. Green, N. Kaltsoyannis, P. Mountford, P. Scott and S. J. Simpson: *Organometallics,* in press.

[28] J. D. Zeinstra and J. L. de Boer: *J. Organomet. Chem.* **54** (1973) 207.

[29] G. Engebreston and K. E. Rundle: *J. Am. Chem. Soc.* **85** (1963) 481.

[30] F. A. Cotton: *Chemical Applications of Group Theory (3rd edition)* Wiley-Interscience, New York (1991).

[31] S. Datta, M. B. Fischer and S. S. Wreford: *J. Organomet. Chem.* **188** (1980) 353.

[32] P. Scott: *D. Phil. Thesis* Oxford (1991).

[33] F. A. Jalon, A. Otero, P. Royo, J. L. Balcazar, F. Florencio and S. Garcia-Blanco: *J. Chem. Soc., Dalton Trans.* (1989) 79.

[34] J. B. Brennan, J. C. Green and C. M. Redfern: *J. Am. Chem. Soc.* **111** (1989) 2373.

[35] M. Cukier, B. Gauthe and C. Wehnkel: *J. Phys. (Paris)* **41** (1980) 603.

[36] M. Cukier, P. Dhez, B. Gauthe, P. Jaegle, C. Wehnkel and F. Combet-Farnoux: *J. Phys. (Paris)* **39** (1978) L315.

[37] G. Wendin: *Phys. Rev. Lett.* **53** (1983) 724.

[38] J. S. Griffith: *The Theory of Transition Metal Ions* Cambridge University Press, London (1964).

CHAPTER THREE

TRIFLUOROPHOSPHINE AND NICKEL TETRAKIS(TRIFLUOROPHOSPHINE)

3.1 Introduction

The extent to which trifluorophosphine can act as a π acceptor in its complexes with transition metals has been the subject of widespread debate [1-14]. Empty, low lying PF_3 orbitals, of π character with respect to the metal-ligand bond, are cited as participating in metal→ligand back-bonding, in a manner analogous to the π^* orbitals of the carbon monoxide ligand. The nature of these orbitals has been the subject of much debate. The traditionally accepted view ascribes the π acceptor properties of PF_3 to phosphorus 3d AOs, although phosphorus 3p-3d hybrid/fluorine 2p antibonding MOs have also been suggested as possible π acceptors [12]. Evidence for the role of PF_3 as a π acid comes from the similarities in occurrence and stoichiometry of M-PF_3 and M-CO complexes [15-17]. In a recent study concerning a PE spectroscopic study of the complex $[Ni(PF_3)_4]$ [18], evidence was presented to support the existence of nickel→phosphorus back donation.

The valence electronic structure of PF_3, which has C_{3v} symmetry, is

$$(5a_1)^2(3e)^4(6a_1)^2(4e)^4(7a_1)^2(5e)^4(1a_2)^2(6e)^4(8a_1)^2$$

using the numbering scheme of Xiao et al. [12]. The $5a_1$ and 3e orbitals are predominantly fluorine 2s in character and lie very low in energy in valence orbital terms. The $6a_1$ and 4e orbitals are traditionally regarded as phosphorus-fluorine σ bonding orbitals and the $7a_1$, 5e, $1a_2$ and 6e orbitals as fluorine 2pπ orbitals. The $8a_1$ orbital is viewed as primarily a phosphorus lone pair orbital. The $6a_1$ orbital lies too low in energy to be ionised by He I radiation, although previous workers have identified the band at 22.55 eV in the He II PE spectrum of PF_3 as being due to ionisation from this orbital [19]. The earlier PE spectroscopic studies are in agreement as to the assignment of the spectrum, which is given

in Table 3.1. Both SCF-MO [10, 11] and SCF-Xα-DV [12] calculations have been performed on PF_3 to give an MO ordering differing from that inferred (on the basis of Koopmans' Theorem) from the experimentally determined ion state ordering only in reversing the $1a_2$ and 6e orbitals.

Table 3.1 : assignment of the PE spectrum of PF_3 [19]

Band	IE (eV)	Ion state	Related MO
A	12.3	$^2A_1$	$8a_1$
B	15.9	$^2E + {}^2A_2$	$6e + 1a_2$
C	17.4	^2E	5e
D	18.5	$^2A_1$	$7a_1$
E	19.4	^2E	4e
F	22.6	$^2A_1$	$6a_1$

The aims of the study of trifluorophosphine presented here were twofold; to shed further light on the MO structure of PF_3 itself, and to confirm the nickel→phosphorus back donation observed previously.

3.2 Results and discussion

3.2.1 Trifluorophosphine

The PE spectrum of PF_3 has been measured over the incident photon energy range 30-95 eV. Figure 3.1 shows the spectra obtained at 45 and 60 eV.

As discussed in Chapter One, the photoionisation cross section behaviour of MOs is to a large extent controlled by the cross section behaviour of their constituent AOs (Chapter 1.4.4). Molecular features such as shape resonances (Chapter 1.4.4 (d)) and autoionisation [20] also play their part, but over a wide photon energy range such as the 30-95 eV used here the overall trend in relative cross section will be dominated by atomic effects. For PF_3 the principal AOs involved are the phosphorus 3p and 3s orbitals and the fluorine 2p orbitals, the fluorine 2s orbitals lying too deep to be part of the valence shell. Figure 3.2 shows calculated cross section data for these three AOs [21], the most striking feature of which is that the cross section of the fluorine 2p orbital is much greater than that of the phosphorus 3s and 3p orbitals over the photon energy range employed in this investigation. If this were the case in reality, the cross section behaviour of the bands in the PE spectrum of PF_3 should be totally dominated by the fluorine 2p contribution to the ionising MOs. That this is not found to be so suggests that the absolute numerical values for the calculated AO cross sections be regarded with some suspicion, although the general trends should be more reliable. The fluorine 2p cross section falls steeply over the photon energy range 30-95 eV whereas the phosphorus 3s and 3p cross sections are less variable over this range. These features can be used to get a qualitative estimate of fluorine 2p character in the various MOs.

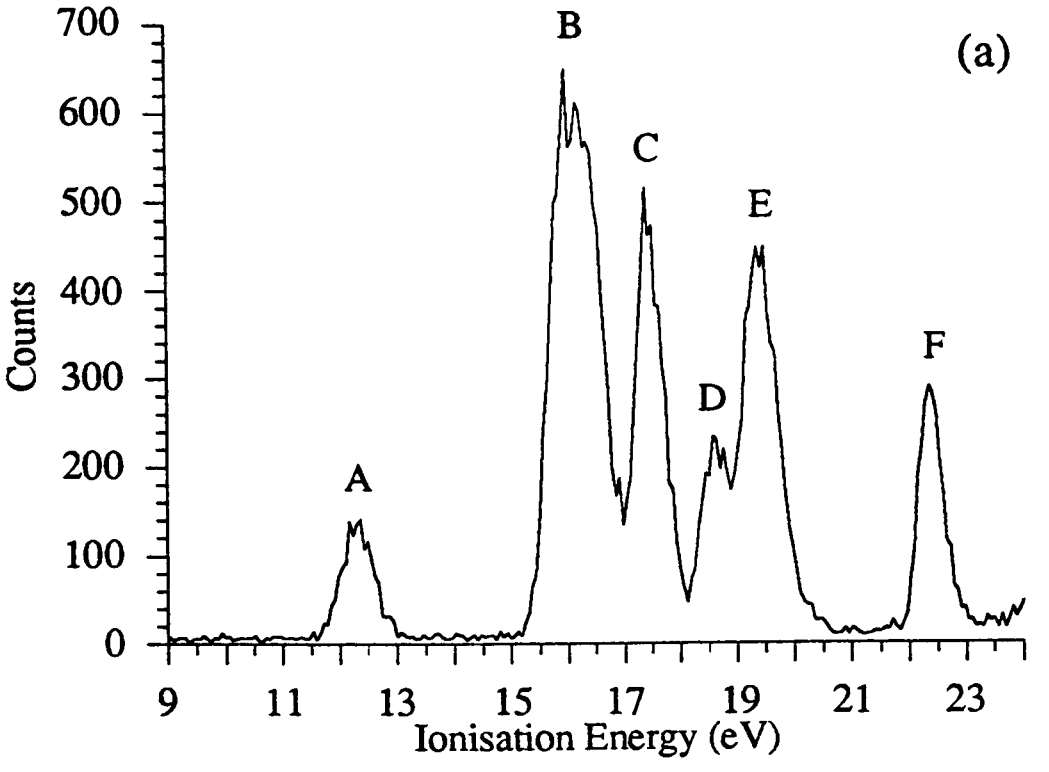

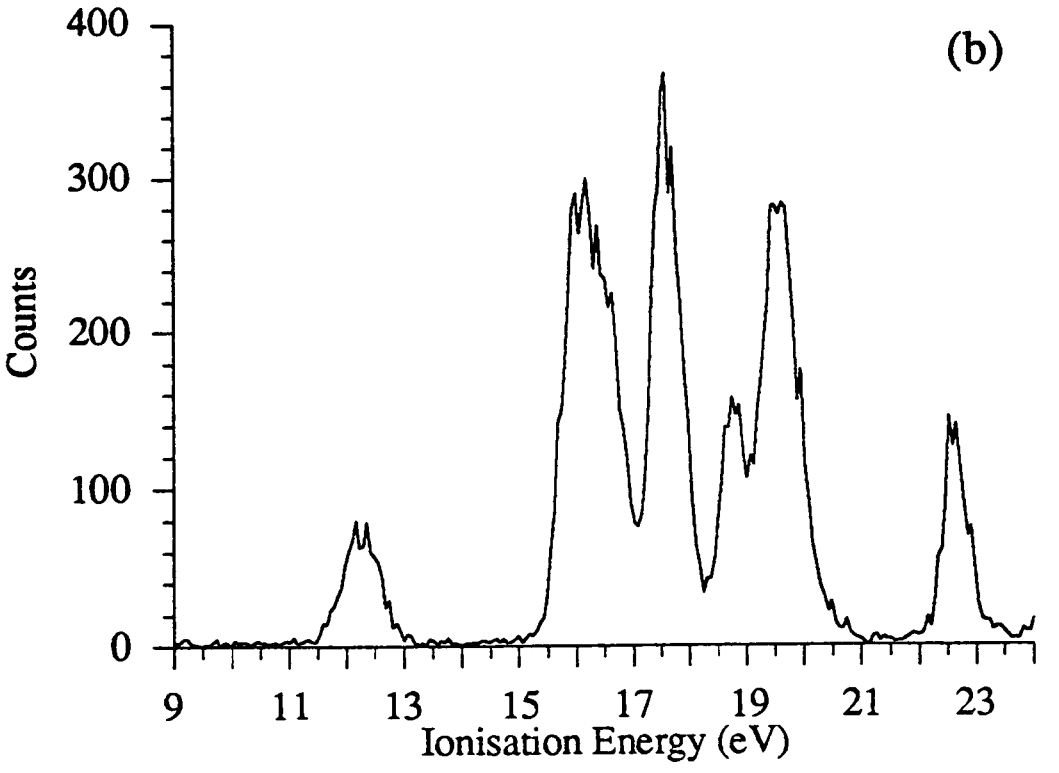

Figure 3.1 : the PE spectrum of PF_3, acquired at (a) 45 eV and (b) 60 eV

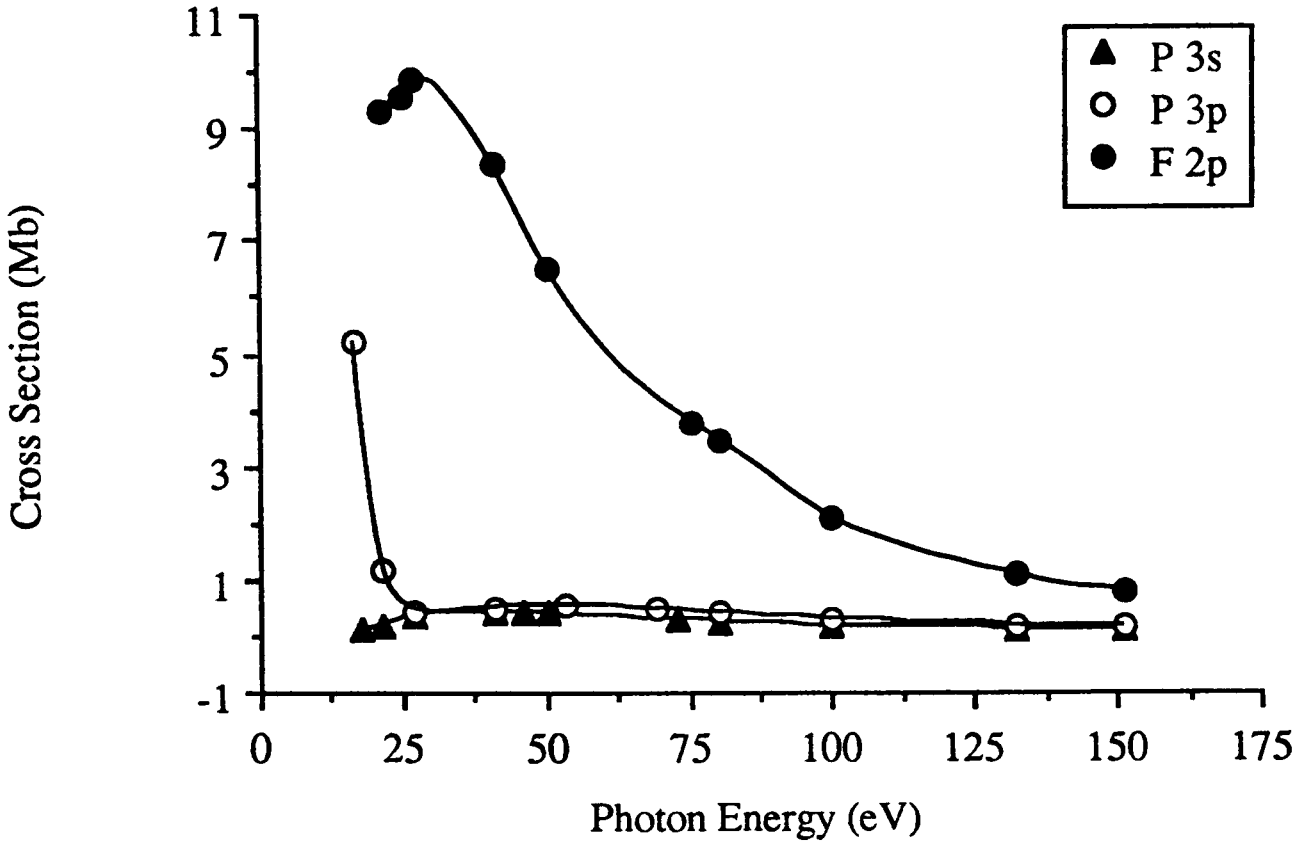

Figure 3.2 : calculated cross section data for the 3s and 3p AOs of phosphorus and the 2p AO of fluorine [21]

Figure 3.3 (a) gives RPPICS for the first six PE bands of PF_3 and Figure 3.3 (b) presents their BRs. The RPPICS plot reveals band B to have the steepest cross section fall off, followed by bands C and E and finally bands A, D and F. In relating cross section behaviour to the amount of fluorine 2p character in the MOs giving rise to a PE band, the number of orbitals ionising under that band must be taken into account. The gradient of the RPPICS plot of a band due to ionisation from three MOs will be three times as great as that from a band arising from only one MO if all of the MOs have similar AO constituents. Band B arises from ionisation of three orbitals ($6e + 1a_2$), bands C and E from ionisation of doubly degenerate orbitals (5e and 4e respectively) and bands A, D and F from singly degenerate orbitals ($8a_1$, $7a_1$ and $6a_1$). At 30 eV, for example, the BR per orbital is ca. 0.14 for band B, 0.1 for bands C and E, 0.08 for band D and 0.05 for bands A and F. As the photon energy is increased, the BR ordering remains largely unaltered, although the differentiation between them becomes smaller. The major movement in the BR plot is

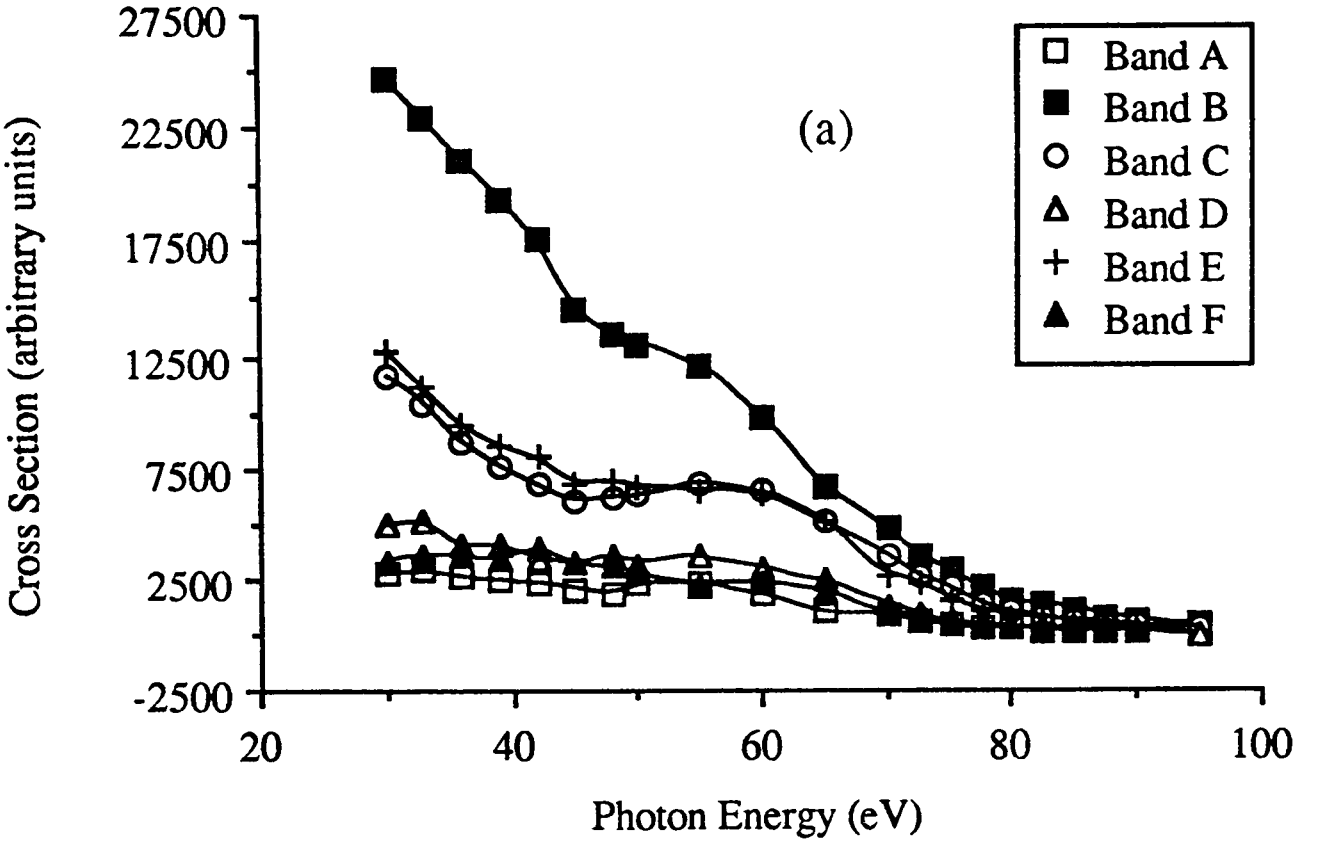

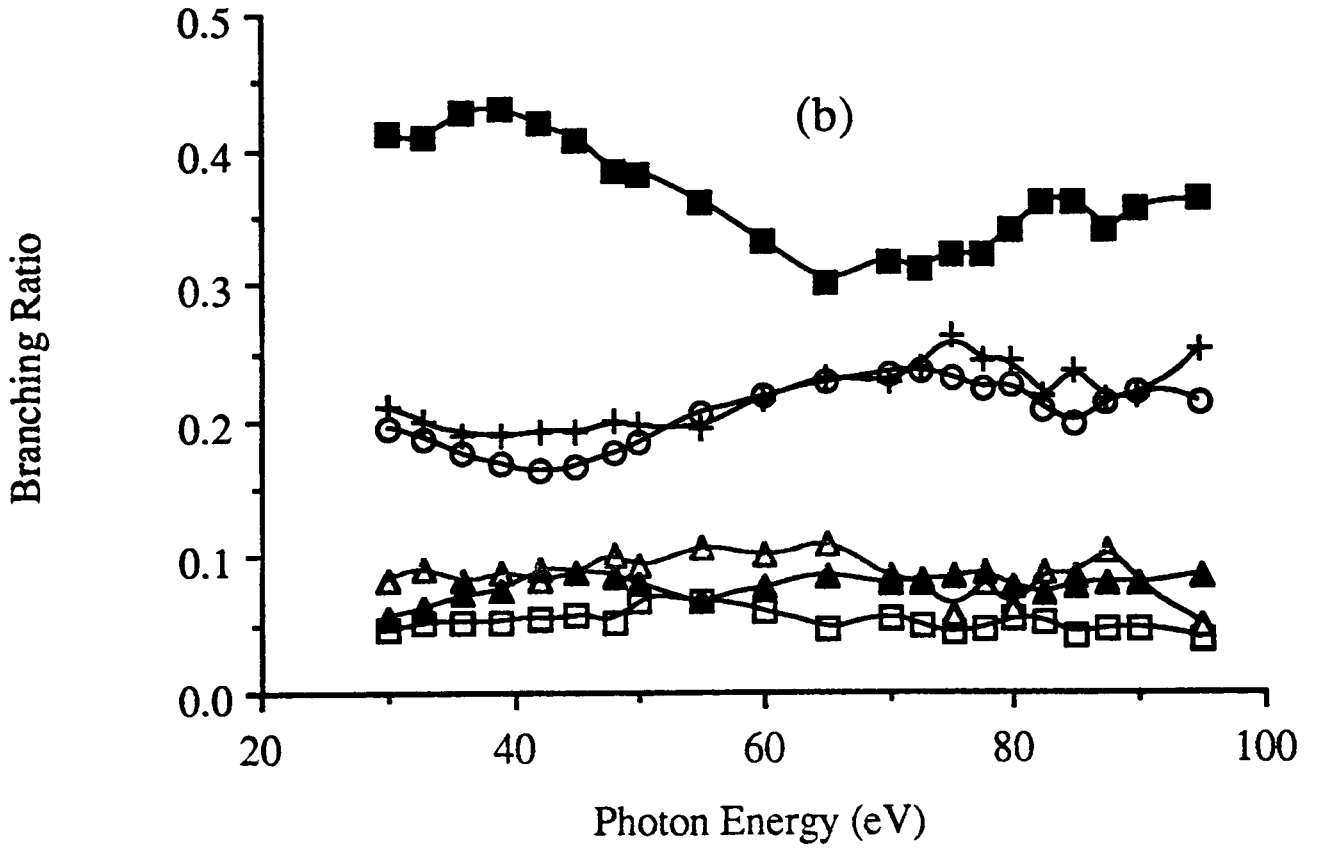

Figure 3.3 : (a) RPPICS and (b) BRs of the first six bands in the PE spectrum of PF_3

between bands B, C and E, in which C and E are seen to increase relative to B. This results from the differing rates of cross section fall off of the bands and it may be concluded that the fluorine 2p AO contribution to the $1a_2$ and 6e MOs is greater than that to the 4e and 5e, which are similar to one another. The fluorine content of the a_1 symmetry MOs appears to be approximately similar, in that there is little change in their BRs as the photon energy is increased.

Table 3.2 : Ground state valence orbitals of PF_3 calculated by the SCF-Xα-DV method [12]

	Atomic composition						
	Phosphorus			Fluorine			
Orbital	3s	3p	3d	2s	3s	2p	3p
$6a_1$	0.35			0.23	0.01	0.40	0.01
4e		0.16	0.01	0.06	0.01	0.76	
$7a_1$	0.06	0.14	0.02	0.01		0.77	
5e			0.02			0.97	
6e			0.01			0.99	
$1a_2$						0.99	
$8a_1$	0.29	0.32	0.01		0.01	0.36	

The percentage atomic characters of the various MOs calculated by Xiao et al. [12] are given in Table 3.2. From these it can be seen that the experimental results presented here differ from the calculation with regard to the fluorine 2p content of the 5e MO. Xiao suggests that the $1a_2$, 6e and 5e MOs are almost pure fluorine 2p, whereas the behaviour of band C on both the RPPICS and BR plots indicates a fluorine 2p content more in line with that of the 4e MO. The fluorine contribution to the 5e MO is therefore found to be smaller than that predicted by the calculation.

Figure 3.4 presents the RPPICS of each of the six valence bands, plotted against the KE of the PE rather than against the incident photon energy (as in Figure 3.3 (a)). This method is useful for directly comparing MO cross section features with those of AOs, in that it eliminates difficulties that may arise from the shift in IE between atom and molecule. Several of the bands show a feature in their RPPICS between KEs of 30 and 50 eV, which in some cases corresponds to a distinct maximum (bands A, C and F) and in others to a change in gradient or "shoulder" (bands D, E and, to a lesser extent band B). As the strength of the feature seems to correlate inversely with fluorine content, it may well be associated with the phosphorus content of the related MO. The Cooper minimum (Chapter 1.4.3 (a)) of the phosphorus 3p AO is calculated to occur at a PE KE of ca. 18 eV [21]. The AO cross section then passes through a maximum at a KE of 45 eV, and it is this feature that may be giving rise to the MO cross section maxima in the KE range 30-50 eV. The possibility that these maxima may be due to a shape resonance should also be considered.

Bands A and F (the $8a_1$ and $6a_1$ MOs respectively) have similar cross section behaviour. Both have the distinct maximum at a KE of ca. 40 eV, which is stronger in band A, and there is another maximum in both cross sections at low PE KEs (20.70 and 13.40 eV), which is more pronounced in band F. This can be attributed to the maximum in the phosphorus 3s AO cross section which is calculated to occur at a KE of 24 eV. The magnitude of the maxima suggests that the $8a_1$ MO has a larger phosphorus 3p contribution than 3s, and that the $6a_1$ MO has more 3s than 3p. The sharp feature in the cross section of band F at a KE of 19.40 eV cannot be readily explained on AO grounds, and is attributed to a molecular shape resonance. The cross section data support the calculation in revealing a phosphorus 3s contribution to the $8a_1$ and $6a_1$ MOs, and in suggesting that this is greater in the $6a_1$ MO. Calculation and experiment differ, however, in that the $6a_1$ MO is predicted to have no phosphorus 3p character whatsoever; this is inconsistent with the experimental evidence.

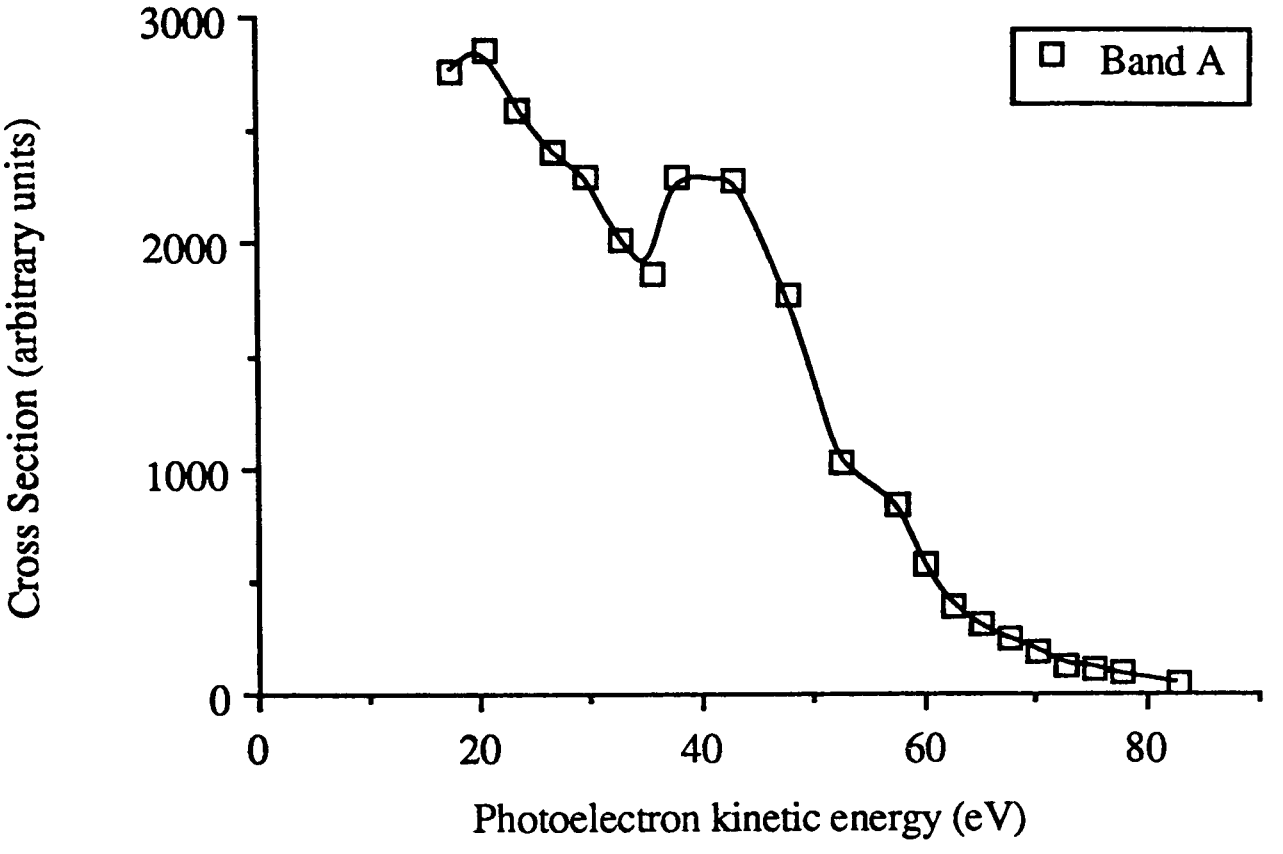

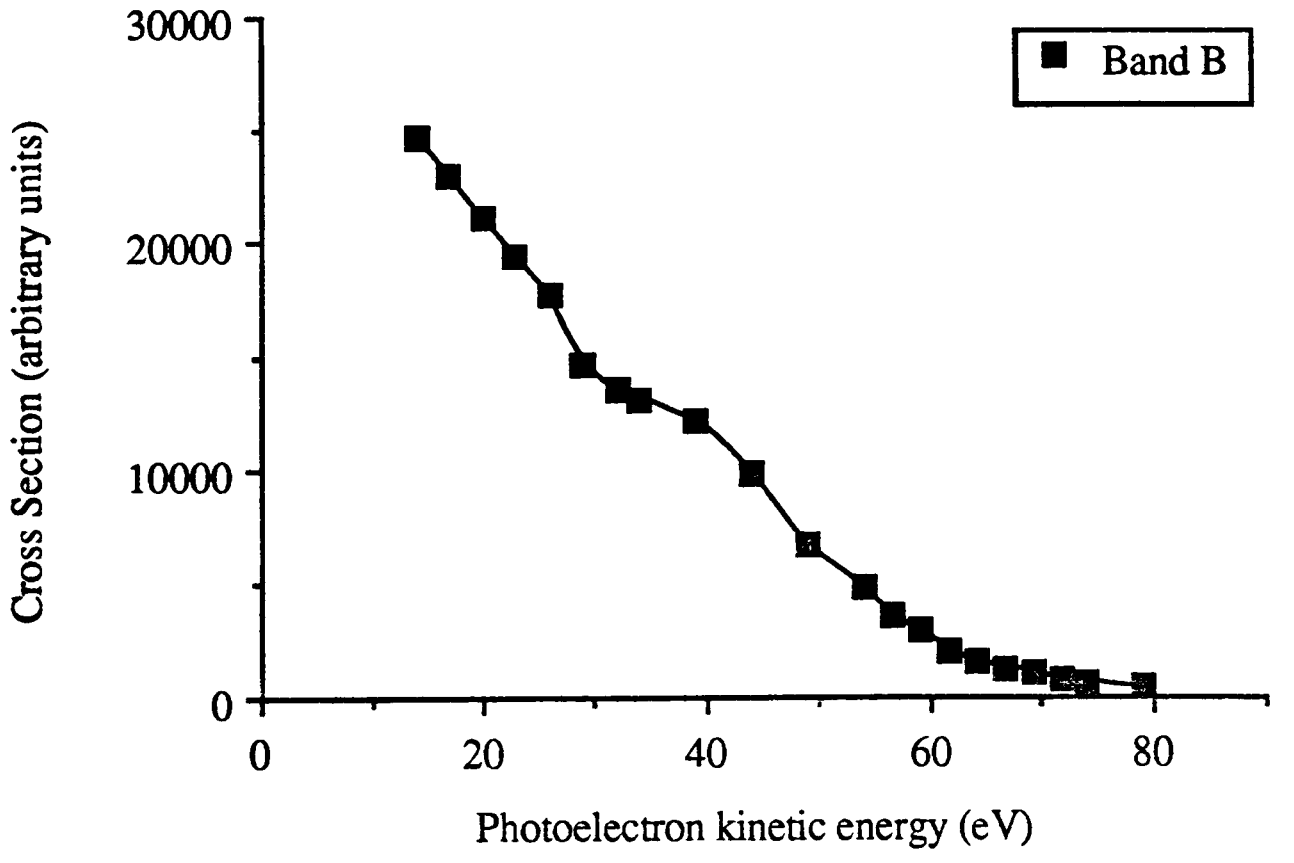

Figure 3.4 : RPPICS of the six valence bands in the PE spectrum of PF_3, plotted as a function of PE KE

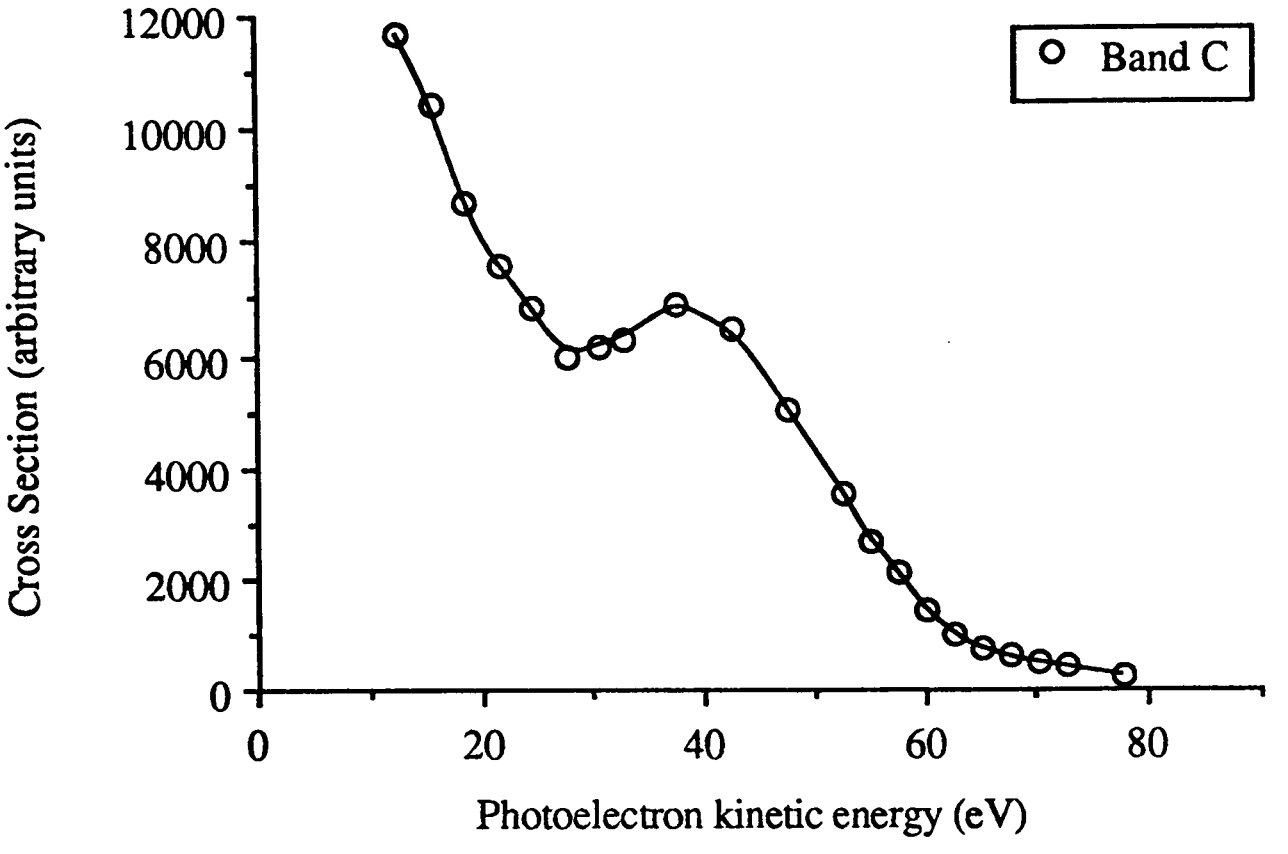

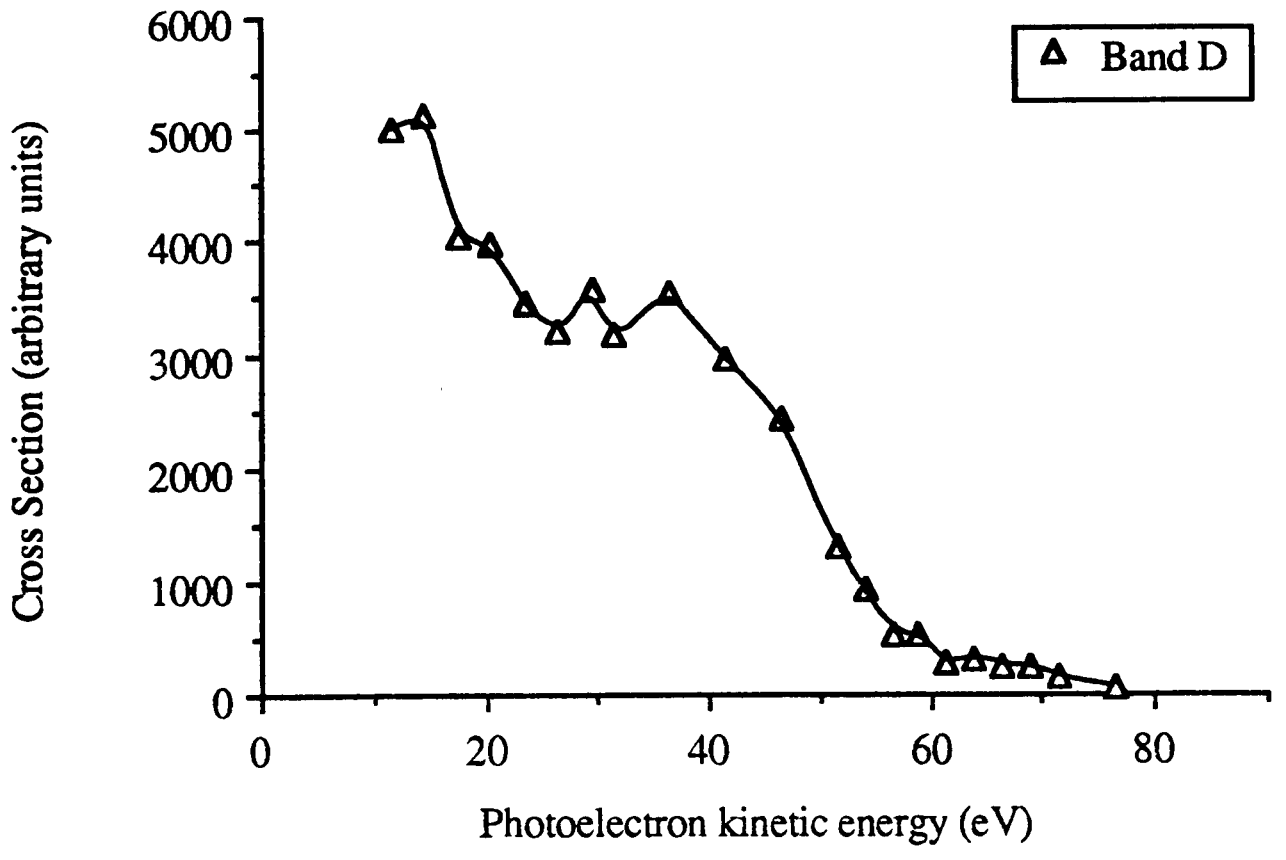

Figure 3.4 : RPPICS of the six valence bands in the PE spectrum of PF_3, plotted as a function of PE KE (continued)

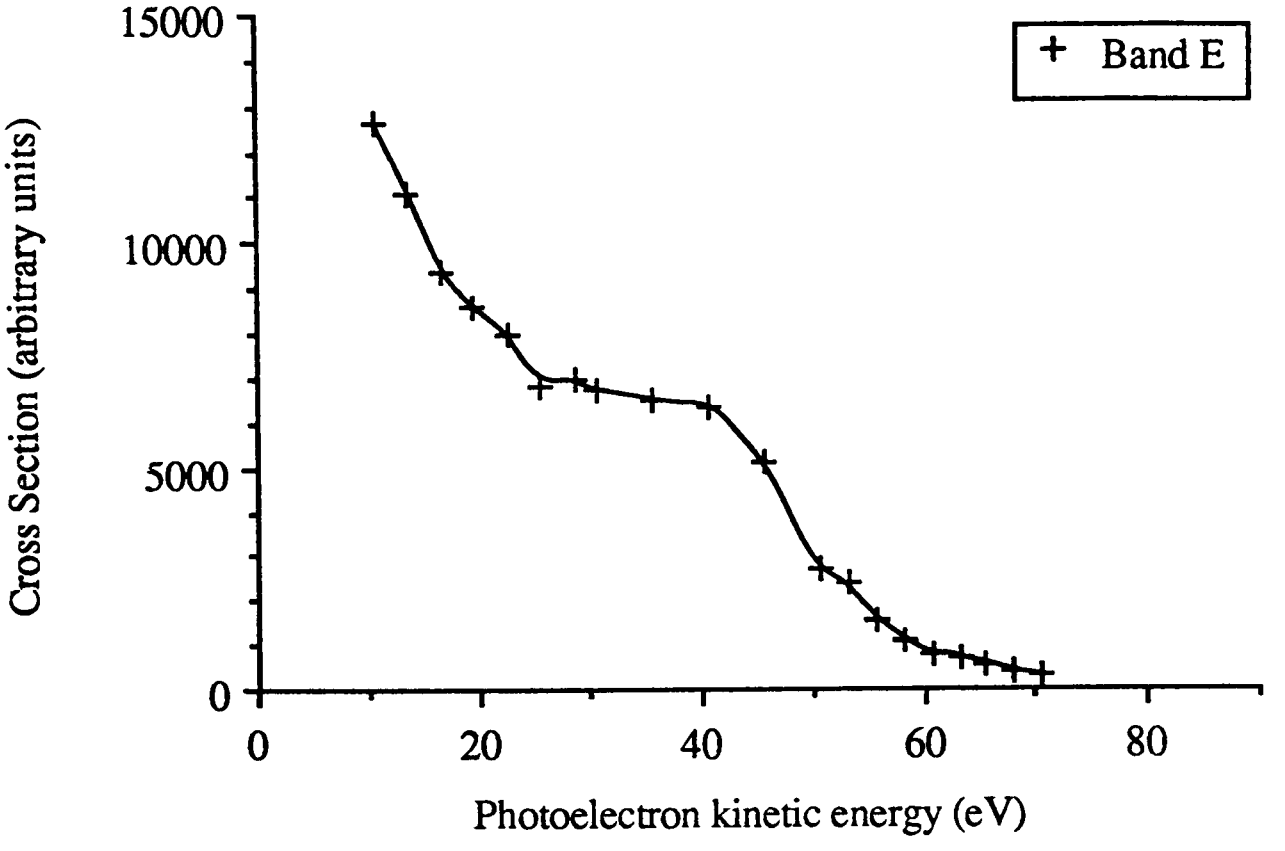

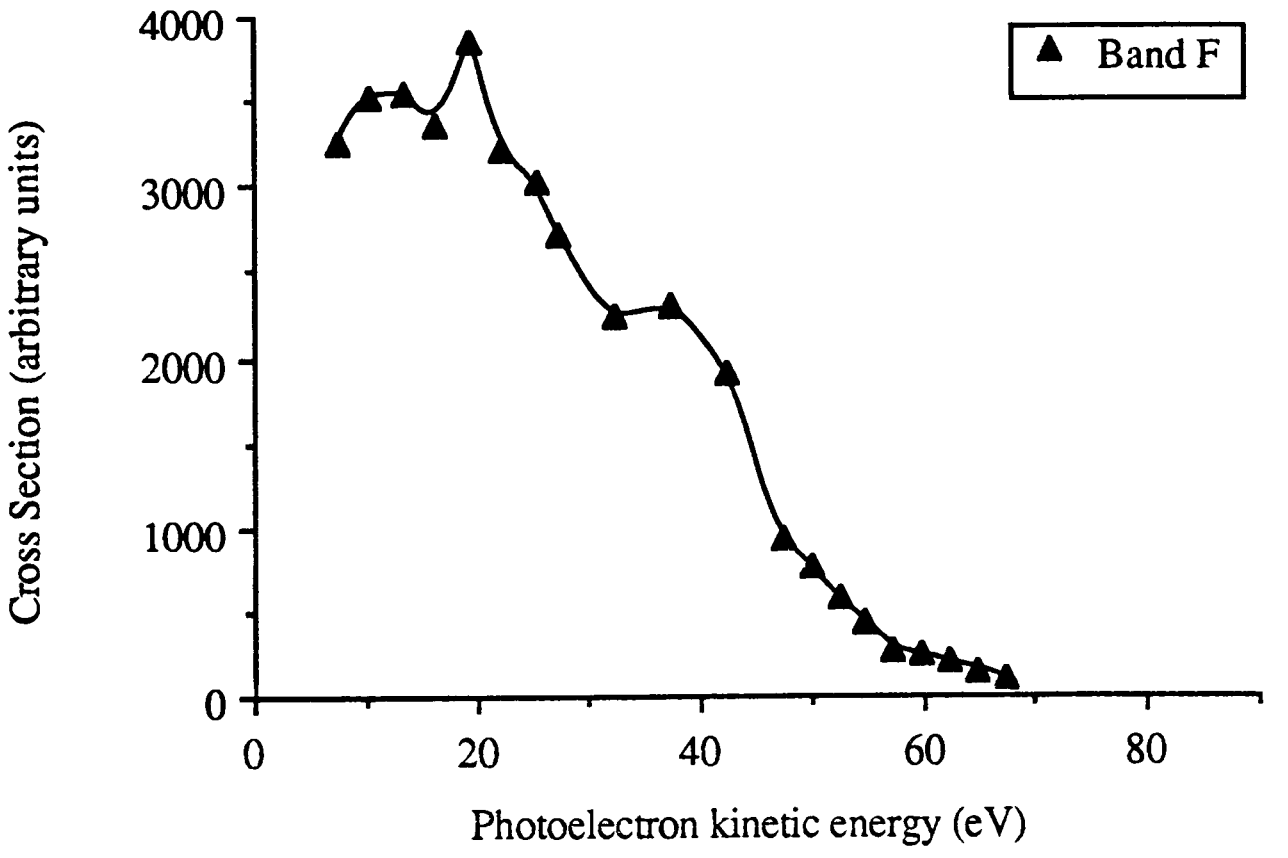

Figure 3.4 : RPPICS of the six valence bands in the PE spectrum of PF_3, plotted as a function of PE KE (continued)

As stated above, the 6e and $1a_2$ (band B) and the 5e MOs (band C) are calculated to be pure fluorine 2p. However, the RPPICS results for band C indicate significant phosphorus 3p AO character to the MO in that its cross section profile is reminiscent of that of an AO passing through its Cooper minimum, which the fluorine 2p cannot have as it does not possess a radial node. The behaviour of band B suggests that the 6e and $1a_2$ MOs are in closer agreement with the results of the calculation. The cross section data for the three bands arising from ionisation of e type MOs indicate that the 5e have the greatest phosphorus 3p AO contribution. Very little phosphorus character is found for the 6e MO, with the 4e intermediate between the two.

The $7a_1$ (band D) and 4e (band E) MOs are calculated by Xiao et al. to be predominantly fluorine 2p (~75%), although a phosphorus 3p contribution (~15%) is predicted. The cross section profiles of bands D and E are very similar, although the data for band D is somewhat erratic between KEs of 26 and 41 eV. Both have an initial fall (~11 - ~26 eV), a region in which the cross section decrease is halted (~26 - ~41 eV) and another subsequent fall. This suggests that these two MOs have very similar AO constituents, in proportions consistent with the Xα calculation.

It is therefore possible to explain the experimentally determined MO cross sections adequately in terms of AO cross section behaviour. The results indicate that the degree of phosphorus 3p - fluorine 2p AO mixing in the valence orbitals of PF_3, notably the 5e orbital, is greater than that predicted by calculation.

3.2.2 Nickel tetrakis(trifluorophosphine)

One of the aims in carrying out this study of PF_3 was to compare the results with those obtained on $[Ni(PF_3)_4]$. The spectrum of $[Ni(PF_3)_4]$, acquired at a photon energy of 45 eV, is given for comparison in Figure 3.5 [18]. Table 3.3 gives the assignment of the spectrum, the details of which have been discussed elsewhere [18, 22]. Bands A and B are due to ionisations from the nickel 3d-based t_2 and e MOs, while bands C and D are assigned to the orbitals responsible for binding the PF_3 units to the metal (t_2 and a_1). Above an IE of 15.5 eV, the PE spectra of $[Ni(PF_3)_4]$ and PF_3 are very similar, and the three E bands correlate directly with features in the PE spectrum of PF_3. The E1 band arises from ionisation of MOs derived from the PF_3 6e and $1a_2$ MOs (band B), the E2 from the 5e (band C) and the E3 band from the $7a_1$ and the 4e PF_3 MOs (bands D + E).

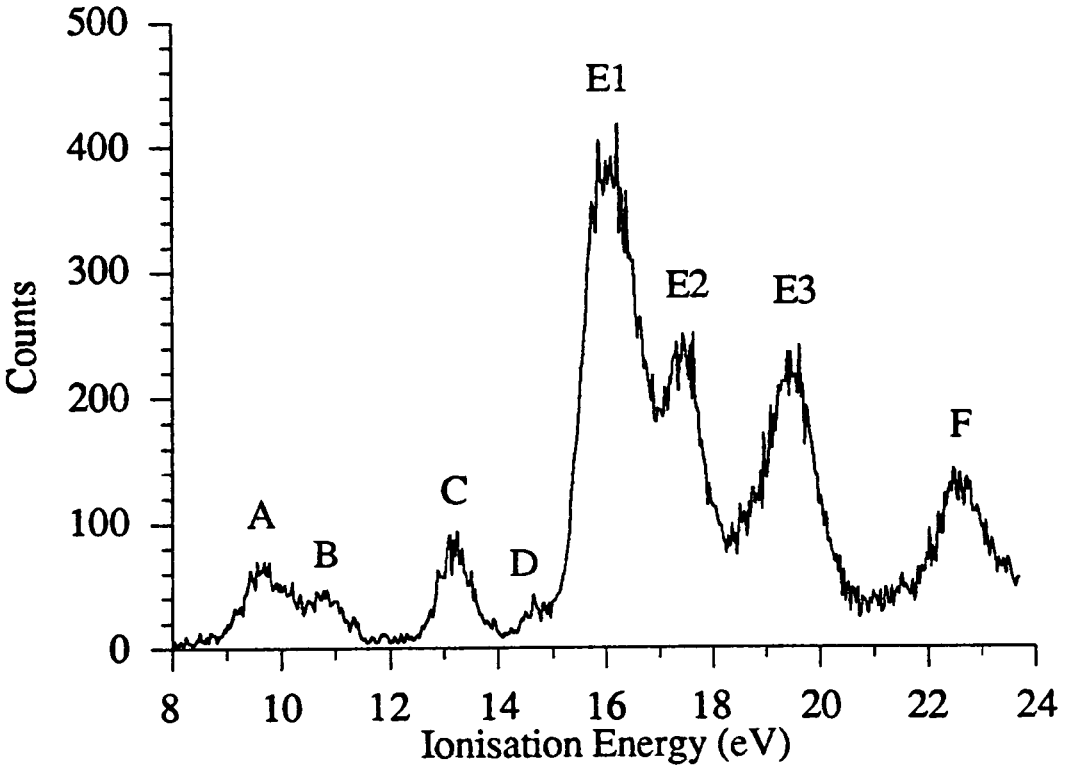

Figure 3.5 : the PE spectrum of $[Ni(PF_3)_4]$, acquired at an incident photon energy of 45 eV [18]

Table 3.3 : assignment of the PE spectrum of $[Ni(PF_3)_4]$ [18, 22]

Band	IE (eV)	Assignment	PF_3 parent orbital
A	9.69	t_2 (Ni 3d)	
B	10.74	e (Ni 3d)	
C	13.17	t_2 (M-P)	$8a_1$
D	14.65	a_1 (M-P)	$8a_1$
E1	15.97	F lone pair	6e, $1a_2$
E2	17.48	M-P-F bonding*	5e
E3	19.42	P-F bonding	4e, $7a_1$
F	22.40	P-F bonding	$6a_1$

*original assignment (to fluorine lone pair) in reference [22] altered following the work reported in reference [18]

Figure 3.6 shows the renormalised BRs of the E bands in $[Ni(PF_3)_4]$, and those of the corresponding bands in PF_3. It is immediately clear that the PF_3 5e band is of lower relative intensity than the E2 band in $[Ni(PF_3)_4]$. In addition, the marked BR behaviour of the E2 band in the photon energy range 70-90 eV is not observed for band C in the PE spectrum of PF_3. The behaviour of the E2 band in this region may be explained by assuming some nickel 3d character to the MOs from which ionisation is occurring. The cross section of PE bands with nickel 3d character may be enhanced in the region of the nickel 3p subshell IEs ($^2P_{3/2}$ = 73 eV, $^2P_{1/2}$ = 75 eV [23]) on account of the p→d giant resonance effect (Chapter 1.4.3 (c)). That the E2 band's BR behaviour in the photon energy region 70-90 eV is not mirrored by that of band C in PF_3, together with the fact that the E2 band has a higher relative intensity at all photon energies is strong evidence to support a nickel 3d contribution to the MOs giving rise to the E2 band.

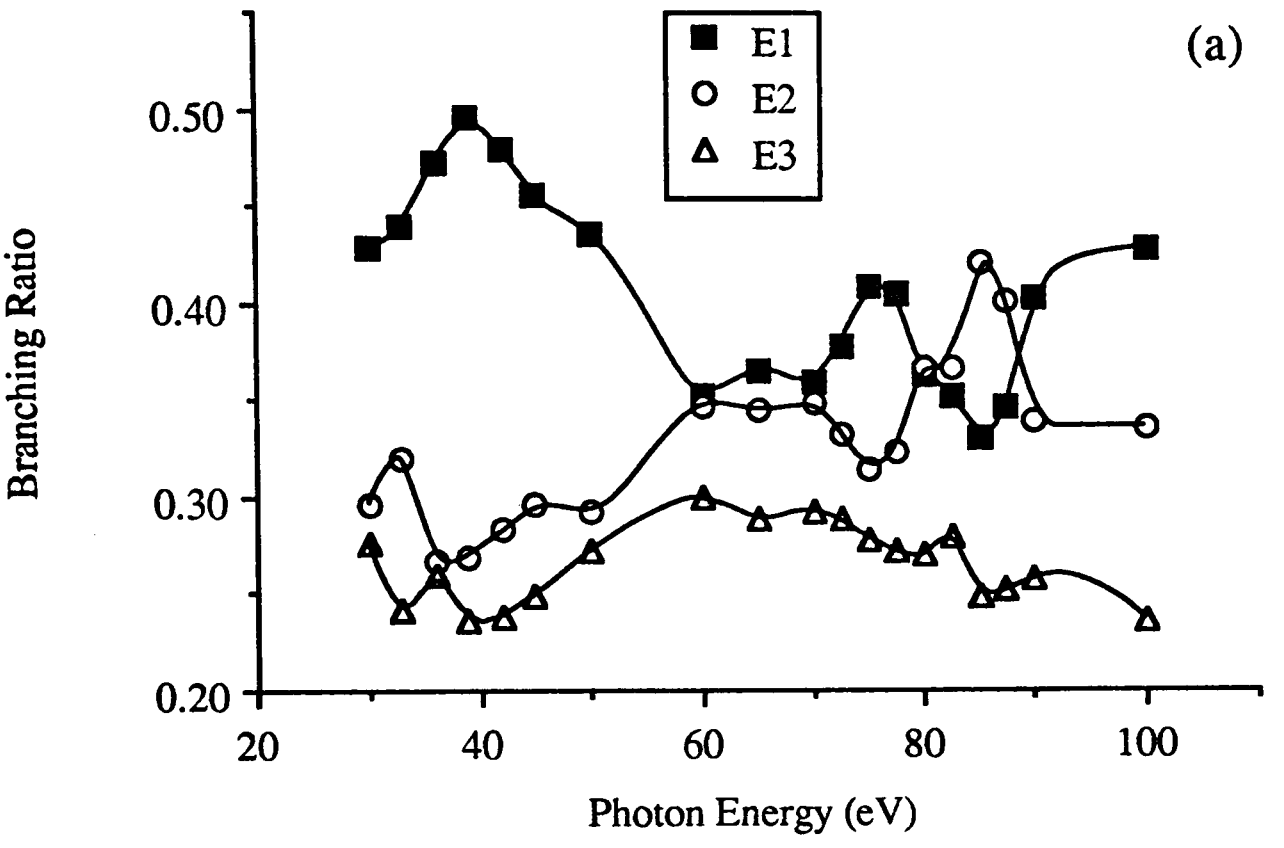

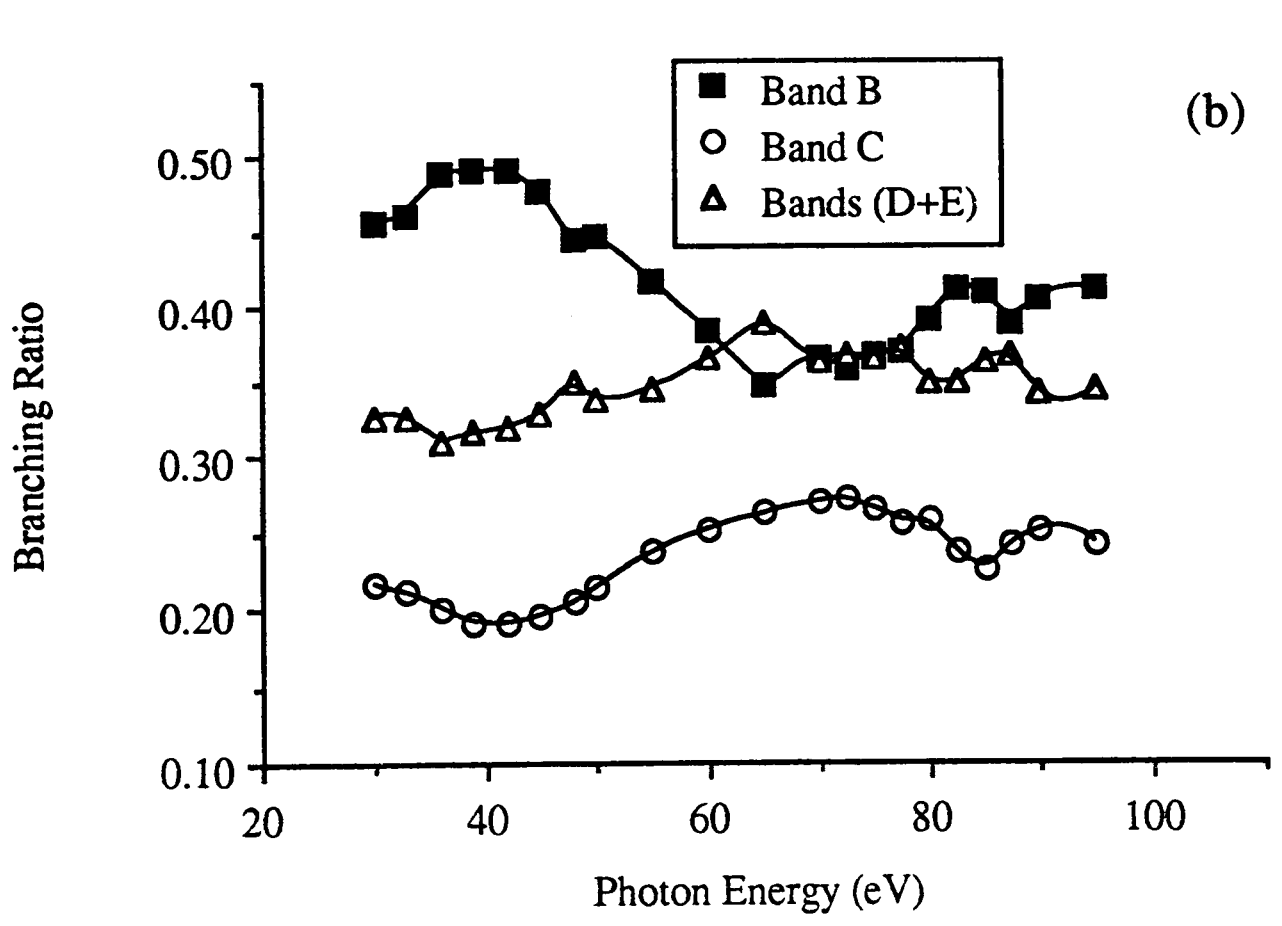

Figure 3.6 : renormalised BRs of (a) the E bands in the PE spectrum of $[Ni(PF_3)_4]$ [18] and (b) bands B, C and (D+E) in the PE spectrum of PF_3

3.2.2 (a) On the nature of nickel→PF_3 back donation

The 7e LUMO of PF_3 is believed to be the main orbital involved in metal→PF_3 back donation, but the studies of $[Ni(PF_3)_4]$ and PF_3 described above suggest that the levels derived from the PF_3 5e MOs also participate in the metal-ligand π bonding process. It would appear that the PF_3 5e and 7e MOs mix with the metal d orbitals of e symmetry to produce a three-level system in which the different MOs contain very different amounts of phosphorus, fluorine and nickel character. To represent this type of interaction it is first necessary to decide upon the nature of the e symmetry orbitals of PF_3. As mentioned in Section 3.1, this is by no means clear for the 7e MO, and the cross section data presented for the 5e MO suggest that it has significant phosphorus 3p AO character, in contrast to its previous description as a fluorine lone pair MO. Xiao et al. [12] calculate the 7e MO to be a hybrid of 44% phosphorus 3p, 23% phosphorus 3d and 26% fluorine 2p AO composition. A schematic representation of this MO is shown below, viewed in the plane of one of the phosphorus-fluorine bonds. The effect of the phosphorus 3p-3d hybridisation is to direct the empty π orbital along the principal axis, i.e. in the direction of a metal atom in a complex of PF_3.

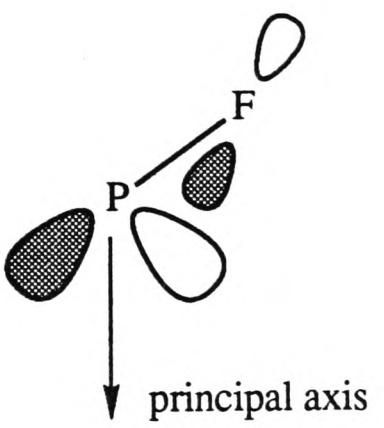

Figure 3.7 shows a schematic representation of the three-level system, and illustrates how a small but significant nickel 3d AO contribution to the complex MOs derived mainly from the PF_3 5e MOs can arise. The energy of the 5e MO is not greatly perturbed by the process, as the IEs of band C of PF_3 (17.4 eV) and the E2 band of $[Ni(PF_3)_4]$ (17.48 eV) indicate. The RPPICS results, however, suggest that their composition is affected on complexation to the metal centre, with a nickel 3d AO

contribution being introduced. The discovery of a significant phosphorus 3p AO contribution to the 5e MO of PF_3 is entirely consistent with this description. Any largely ligand-based MO in $[Ni(PF_3)_4]$ that exhibits nickel 3d AO character must have some phosphorus 3p contribution, as direct nickel-fluorine overlap will be small.

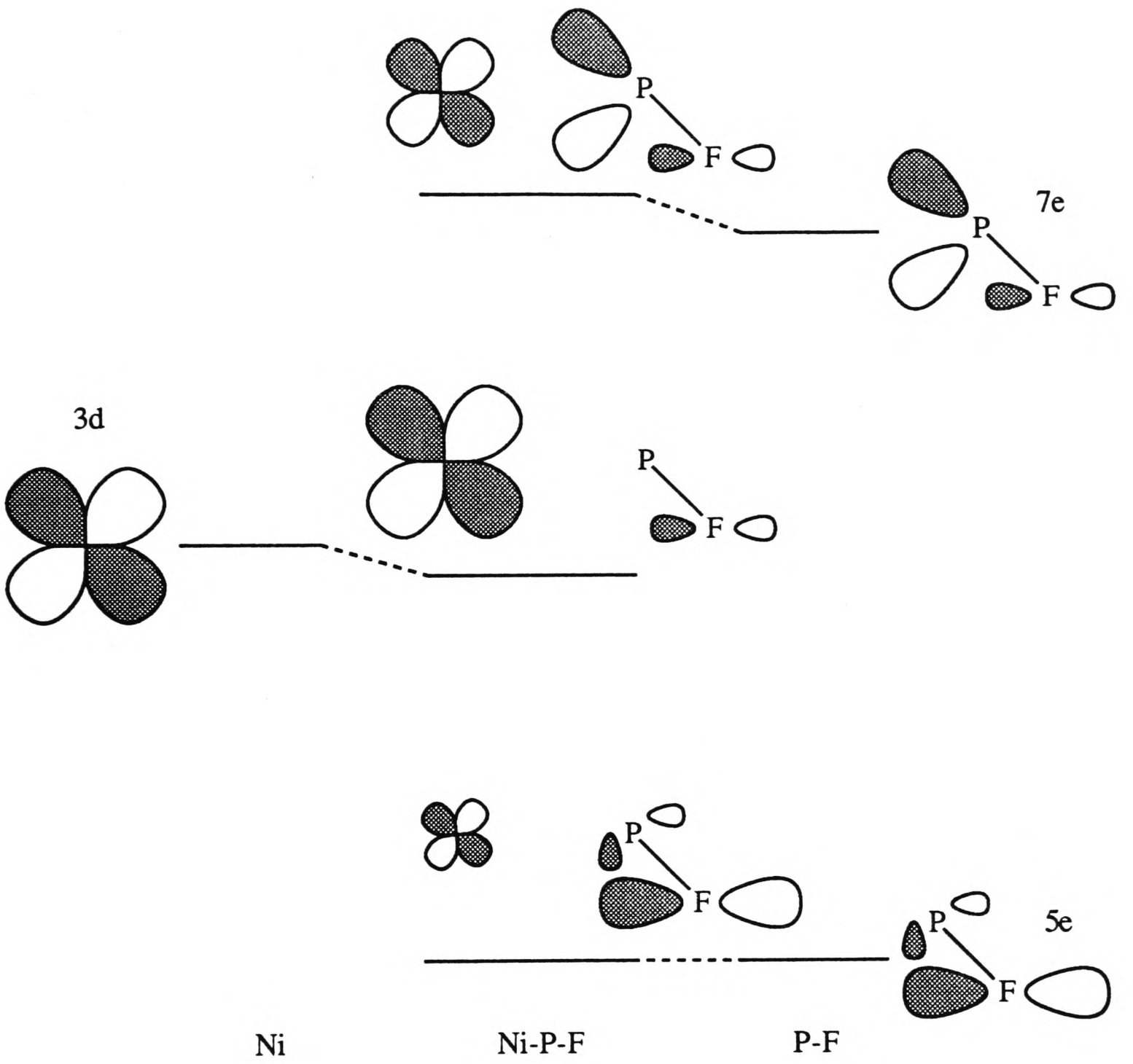

Figure 3.7 : schematic representation of the interaction of the 5e and 7e MOs of PF_3 with the e symmetry nickel d orbitals. The MOs are viewed through a plane containing the metal, phosphorus and one of the fluorine atoms. The approximate magnitudes of the atomic contributions to the MOs are represented by the sizes of the lobes

3.3 Conclusions

RPPICS of the valence bands of PF_3 show contributions from phosphorus AOs, not only to the $8a_1$ (lone pair) orbital and the 4e and $6a_1$ σ bonding orbitals, but also to the 5e and $7a_1$ orbitals which may be regarded as π bonding.

A comparison of BRs for ionisations from corresponding bands in the spectra of PF_3 and $[Ni(PF_3)_4]$ demonstrate a nickel 3d AO contribution to the orbitals in $[Ni(PF_3)_4]$ derived from the 5e orbital of PF_3. Thus the π back donation which is proposed to occur between the nickel 3d orbitals and the 7e LUMO of PF_3 is also seen to affect the composition of the 5e derived orbitals.

3.4 References for Chapter Three

[1] R. J. Angelici and C. M. Ingemanson: *Inorg. Chem.* **8** (1969) 83.

[2] W. A. G. Graham: *Inorg. Chem.* **7** (1968) 315.

[3] R. Mason and D. W. Meek: *Angew. Chem., Int. Ed. Engl.* **17** (1978) 183.

[4] B. B. Wayland and M. E. Abn-Elmageed: *J. Am. Chem. Soc.* **96** (1974) 4809.

[5] R. R. Corederman and J. L. Beauchamp: *Inorg. Chem.* **16** (1977) 3135.

[6] J. M. Savariault and J. F. Labarre: *Theor. Chim. Acta* **42** (1976) 207.

[7] J. M. Savariault, A. Serafini, M. Pelissier and P. Cassoux: *Theor. Chim. Acta* **42** (1976) 155.

[8] G. Wilkinson: *J. Am. Chem. Soc.* **73** (1951) 5501.

[9] J. Chatt: *Nature (London)* **165** (1950) 637.

[10] I. H. Hillier and V. R. Saunders: *Trans. Faraday Soc.* **66** (1970) 2401.

[11] M. F. Guest, I. H. Hillier and V. R. Saunders: *J. Chem. Soc., Faraday Trans. II* (1972) 867.

[12] S. X. Xiao, W. C. Trogler, D. E. Elliss and Z. Berkovitch Yellin: *J. Am. Chem. Soc.* **105** (1983) 7033.

[13] D. Marynick: *J. Am. Chem. Soc.* **106** (1984) 4064.

[14] A. G. Orpen and N. G. Connelly: *J. Chem. Soc., Chem. Commun.* (1985) 1310.

[15] T. Kruck: *Angew. Chem., Int. Ed. Engl.* **6** (1967) 53.

[16] J. F. Nixon: *Adv. Inorg. Chem. Radiochem.* **13** (1970) 363.

[17] J. F. Nixon: *Endeavour* **19** (1973) 32.

[18] J. B. Brennan, J. C. Green, C. M. Redfern and M. A. MacDonald: *J. Chem. Soc., Dalton Trans.* (1990) 1907.

[19] J. P. Maier and D. W. Turner: *J. Chem. Soc., Faraday Trans. II* (1972) 711.

[20] J. Berkowitz: *Photoabsorption, Photoionisation and Photoelectron Spectroscopy* Academic Press, New York (1979).

[21] J. J. Yeh and I. Lindau: *At. Data Nucl. Data Tables* **32** (1985) 1.

[22] P. J. Bassett, B. R. Higginson, D. R. Lloyd, N. Lynaugh and P. J. Roberts: *J. Chem. Soc., Dalton Trans.* (1974) 2316.

[23] D. Briggs: *Handbook of X-ray and Ultraviolet Photoelectron Spectroscopy* Heyden, London (1977).

CHAPTER FOUR

TETRAHEDRAL CO-ORDINATION IN FORMALLY d^0 TRANSITION METAL COMPLEXES - OsO_4, THE GROUP IVA TETRAHALIDES $TiCl_4$, $TiBr_4$ AND $ZrBr_4$, $[(CH_3)ReO_3]$ AND ReO_3Cl

4.1 Introduction

Tetrahedral co-ordination is one of the geometries central to inorganic chemistry. A thorough knowledge of the electronic structures of tetrahedral molecules is therefore of key importance in understanding a wide range of chemical systems. A series of formally d^0 tetrahedral or pseudo-tetrahedral molecules MX_4 (M=Ti, Zr, Hf; X=Cl, Br, I), $VOCl_3$, CrO_2Cl_2, ReO_3Cl and OsO_4 was targeted for a synchrotron radiation-based PE spectroscopic investigation, with the dual aims of unequivocally assigning their PE spectra and of providing detailed information on the nature of the metal-ligand interactions as the halogens are gradually replaced by oxygen atoms. Unfortunately, experimental difficulties with the spectrometer in Daresbury prevented study of all but a few of the chosen compounds,¶ and this Chapter describes the variable photon energy results obtained upon OsO_4 and the group IVA tetrahalides $TiCl_4$, $TiBr_4$ and $ZrBr_4$. The structural simplicity and high symmetry of these complexes belie PE spectra over which there is still no general agreement as to assignment, despite numerous measurements using helium discharge lamp PES (OsO_4 [1-5]; $TiCl_4$ [4, 6-10]; $TiBr_4$ and $ZrBr_4$ [5, 8, 9]).

A detailed investigation of the photon energy dependence of the valence MO cross sections of CCl_4, CF_4 and $SiCl_4$ has been performed [11-13]. The tetrahalides discussed in this Chapter therefore stand apart from the rest of the Thesis in having a significant body of data on closely related molecules with which to compare and contrast the results. It is particularly valuable to have the opportunity of comparing transition metal and main group

¶ For a discussion of this, see Chapter 6.2.1.

tetrahalides, in that halogen- and central atom-derived effects may be distinguished more easily. Furthermore, $TiCl_4$ was itself the subject of a recent investigation by PES using synchrotron radiation [14], with which comparison is made.

The PE spectroscopic investigation of OsO_4 described in this Chapter forms part of a combined experimental and theoretical re-evaluation of the electronic structure of this molecule. As the results from these other techniques are central to the arguments employed in assessing the electronic strucutre of OsO_4, they are presented in the appropriate Sections. OsO_4 is discussed first, followed by the three tetrahalide title molecules, before a study of $[(CH_3)ReO_3]$ and ReO_3Cl is given to conclude the Chapter.

4.2 Osmium tetroxide

The volatility and classic character of OsO_4 led to both this molecule and the closely related RuO_4 being early targets in the application of gas phase PES to the study of bonding in transition metal complexes [1-5]. RuO_4 proved a difficult candidate for investigation as both CO_2 and H_2O accompanied the spectrum in the early stages of measurement and the electron multipliers were attacked leading to poor instrumental performance [1-4]. Once the ambiguities, due to impurities, in the number of spectral bands were resolved there was general agreement on the correlation of bands between the two compounds. Subsequently, two theoretical papers concurred [15, 16] in revising the assignment of the PE spectrum of OsO_4. It therefore seemed appropriate to study the PE spectrum of OsO_4 over a wide range of photon energies using synchrotron radiation in order to clarify the spectral assignment and to obtain further information on the bonding in this prototypical molecule. As RuO_4 had had a deleterious effect on electron detectors, it was not considered a suitable candidate for study, as the channel plates in the spectrometer used in Daresbury appear to be particularly sensitive to chemical attack.

The discrepancy between the generally accepted experimental assignment of the valence ionisations and the theoretical predictions suggested that a theoretical reinvestigation might also be enlightening. Pseudopotential calculations on OsO_4 have been

carried out by Stephen Jarrett-Sprague and Ian Hillier at the University of Manchester, and IEs obtained by use of an ab initio many-body Green's function formalism [17, 18].

4.2.1 Bonding and interpretation of the photoelectron spectrum

The valence electronic structures of the d^0 tetrahedral MO_4 species are of the form

$$1a_1^2 1t_2^6 2t_2^6 1e^4 2a_1^2 3t_2^6 1t_1^6$$

(where the numbering scheme ignores orbitals correlating with the core orbitals of the constituent atoms). A schematic MO diagram showing the possible atomic contributions to the various MOs is given in Figure 4.1. The $1a_1$ and $1t_2$ are essentially core oxygen 2s orbitals. Of the other occupied levels the $2t_2$ and $2a_1$ are traditionally associated with M-O σ bonding and the 1e and $3t_2$ with M-O π bonding, though there is strictly no σ/π separability among the t_2 set of MOs. The $1t_1$ orbital, in the absence of any effective f orbital contribution from the central atom, is non-bonding. For a d^0 tetrahedral molecule, such as OsO_4, five primary ion states are expected to occur in the ionisation region studied, namely a $^2A_1$, a ^2E, a $^2T_1$ and two $^2T_2$ states. However, more than five bands may well be observed as the orbitally degenerate states may be subject to Jahn-Teller distortion or spin-orbit splitting. Figure 4.2 shows the PE spectrum of OsO_4, obtained at high resolution with He I radiation by Burroughs et al. [4] and at lower resolution with synchrotron radiation at 39, 52.5 and 66 eV. IE data and the various proposed band assignments are summarised in Table 4.1. A detailed discussion of these assignments is deferred until after the presentation of the RPPICS results.

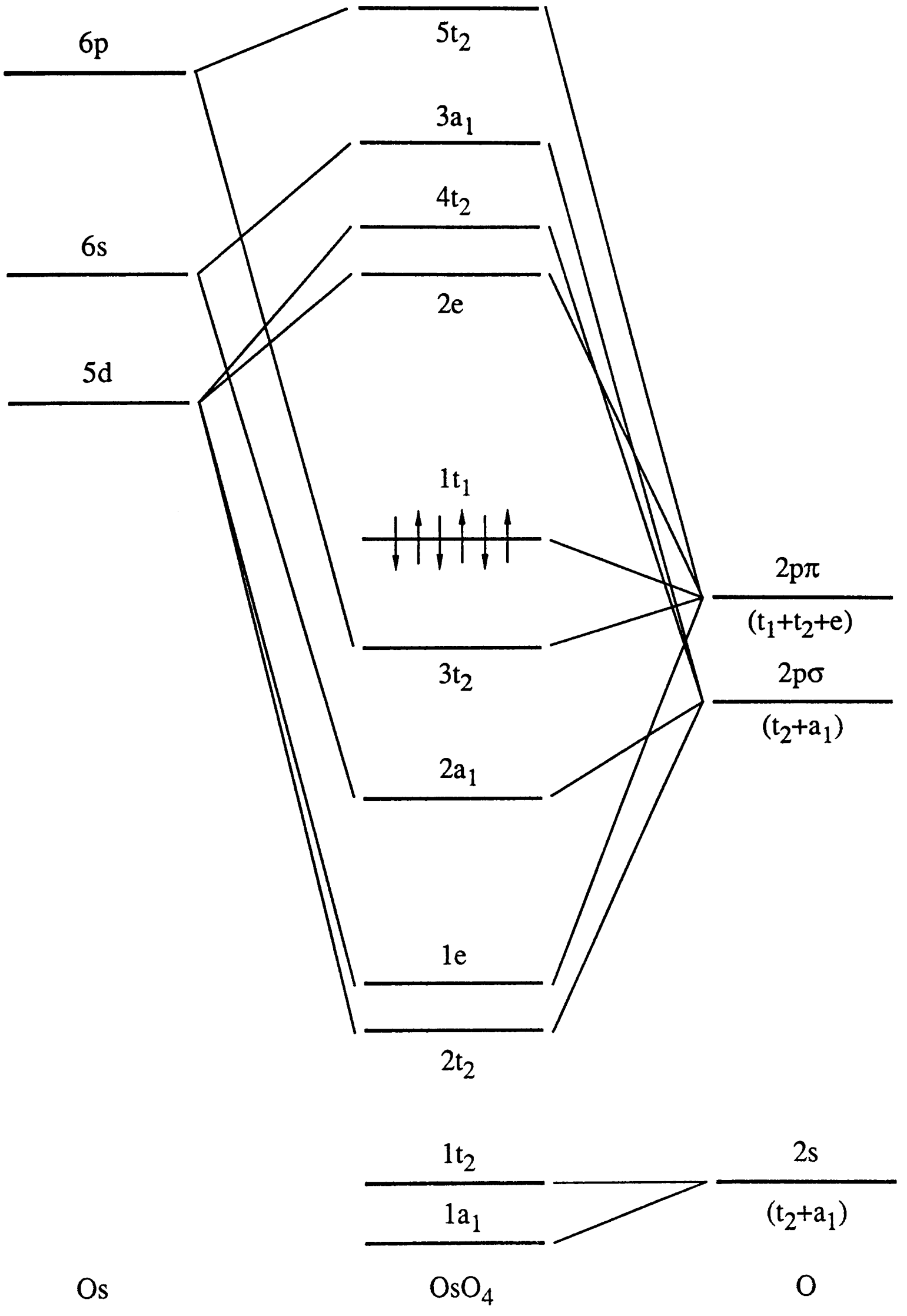

Figure 4.1 : qualitative MO diagram for OsO_4 (labels in parentheses indicate the symmetries of the MOs of the O_4 tetrahedron)

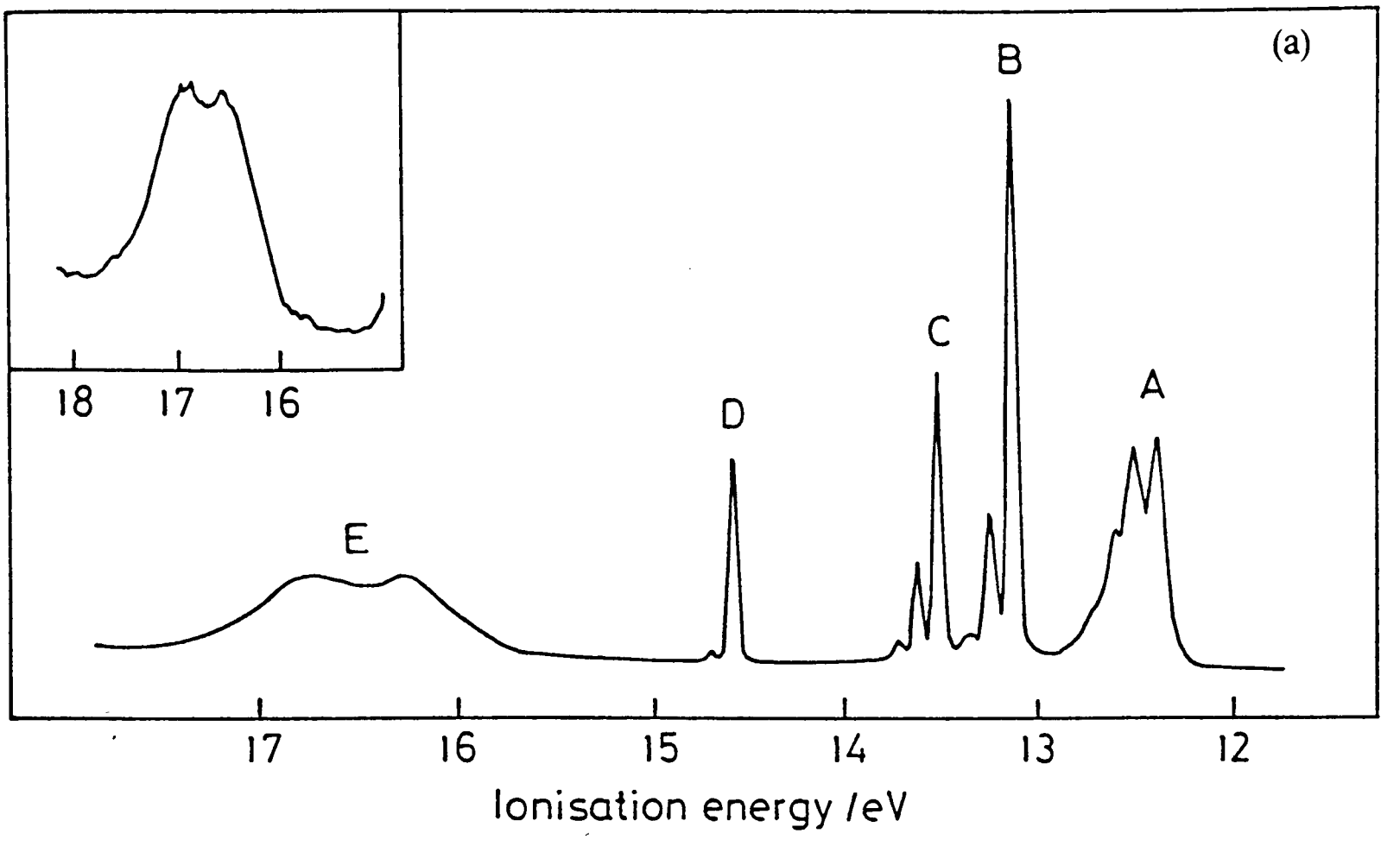

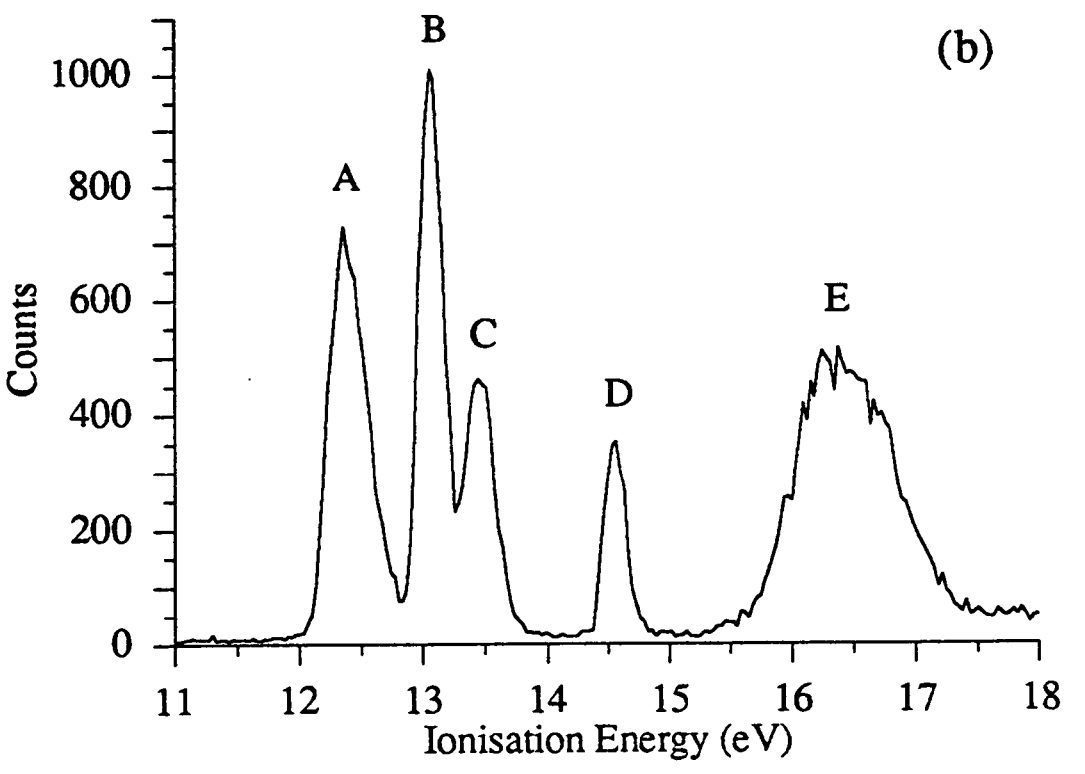

Figure 4.2 : the PE spectrum of OsO_4, acquired at (a) 21.22 (He I - spectrum from reference [4]) and (b) 39 eV

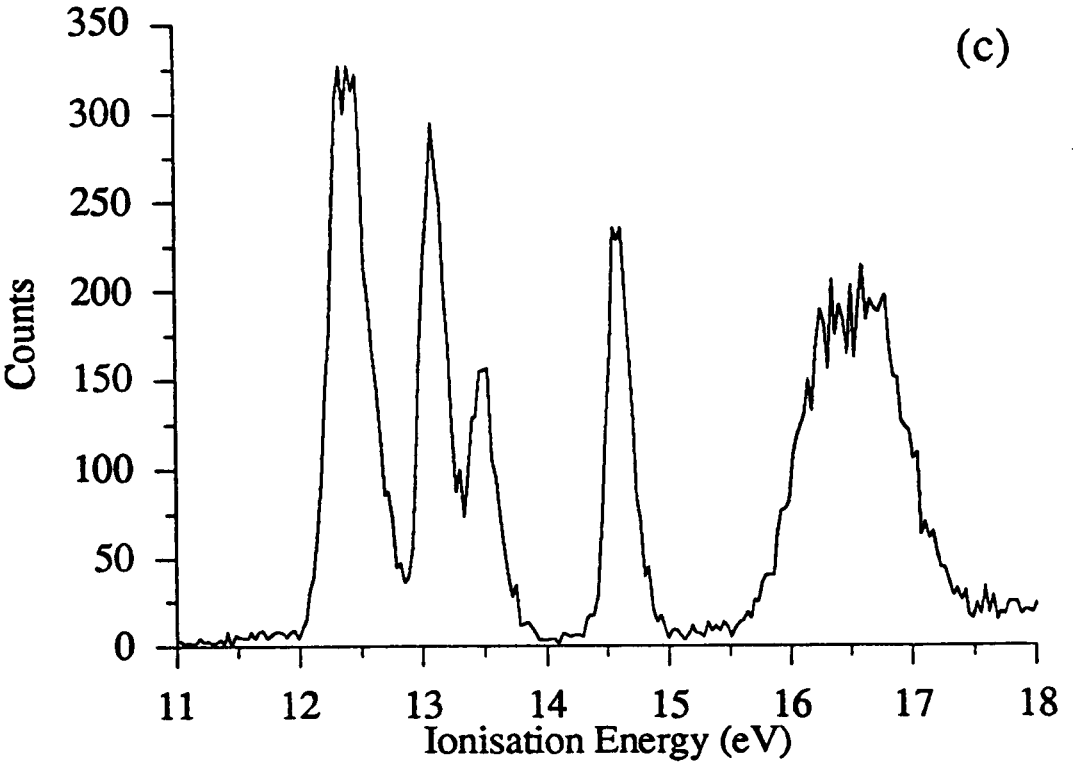

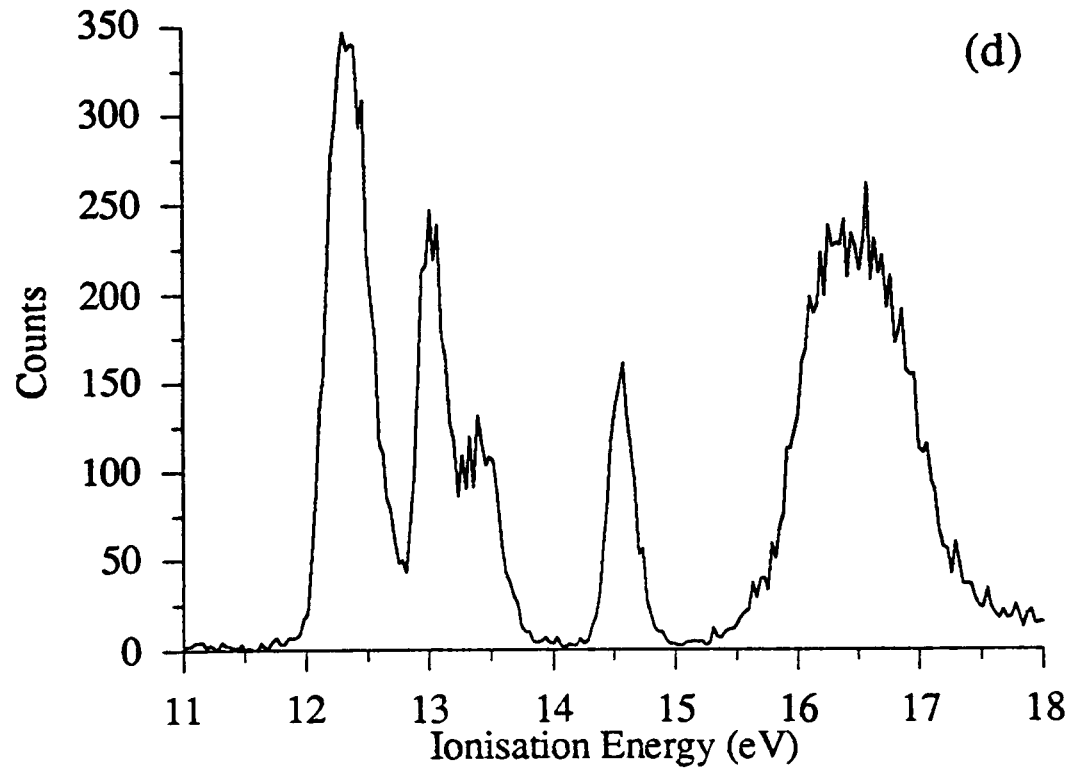

Figure 4.2 (continued) : the PE spectrum of OsO_4, acquired at (c) 52.5 and (d) 66 eV

Table 4.1 : IEs and assignments of the PE spectrum of OsO_4

Band	IE (eV)[a]	Reference				
		[1][b]	[2]	[3, 4]	[15]	[16]
A	12.35	$^2T_1$	$^2T_2$	$^2T_1$	$^2T_1$	$^2T_1$
B	13.11	$^2T_2$ (U')	$^2T_1$	$^2T_2$	$^2T_2$	$^2T_2$
C	13.54	$^2T_2$ (E")	$^2A_1$	^2E	$^2A_1$	$^2A_1$
D	14.66	^2E	^2E	$^2A_1$	^2E	^2E
E	16.4,16.8	$^2T_2$	$^2T_2$	$^2T_2$	$^2T_2$	$^2T_2$

[a] IE values taken from references [3] and [4], where IEs for the observed vibrational fine structure are also given

[b] Diemann and Müller assigned the $^2A_1$ ion state to a band at 15.58 eV which was subsequently shown to be from an impurity

4.2.2 RPPICS results

The PE spectrum of OsO_4 has been obtained using synchrotron radiation over the incident photon energy range 24-115 eV. As is clear from Figure 4.2, no attempt was made to resolve the vibrational fine structure seen in the early studies when measuring OsO_4 with synchrotron radiation. Consequently the bands had an asymmetric shape and it proved necessary to use asymmetric Gaussian functions to fit the peaks, and thus obtain the band areas used in the RPPICS calculations. The RPPICS for bands A-E in the PE spectrum of OsO_4 are given in Figure 4.3, and expanded plots of each band are presented in Figure 4.4.

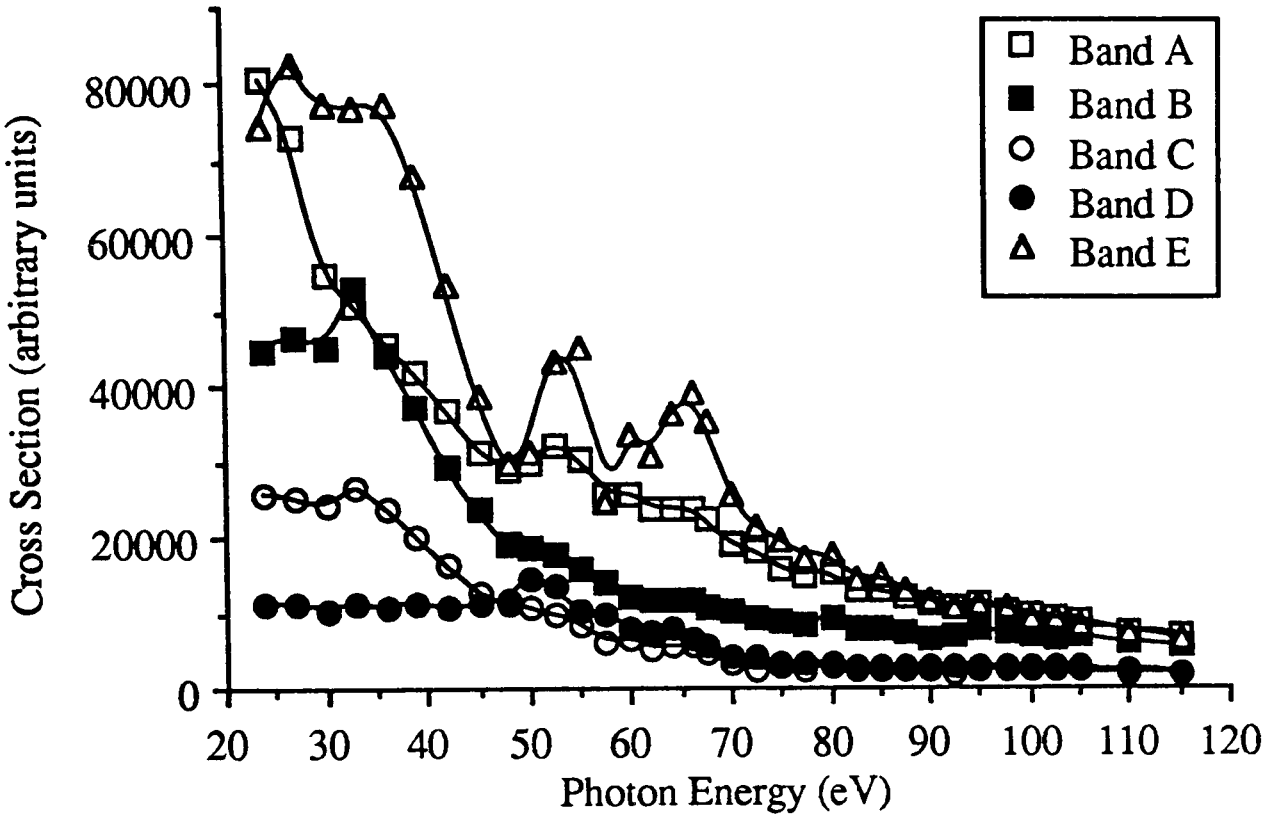

Figure 4.3 : RPPICS of bands A-E in the PE spectrum of OsO_4

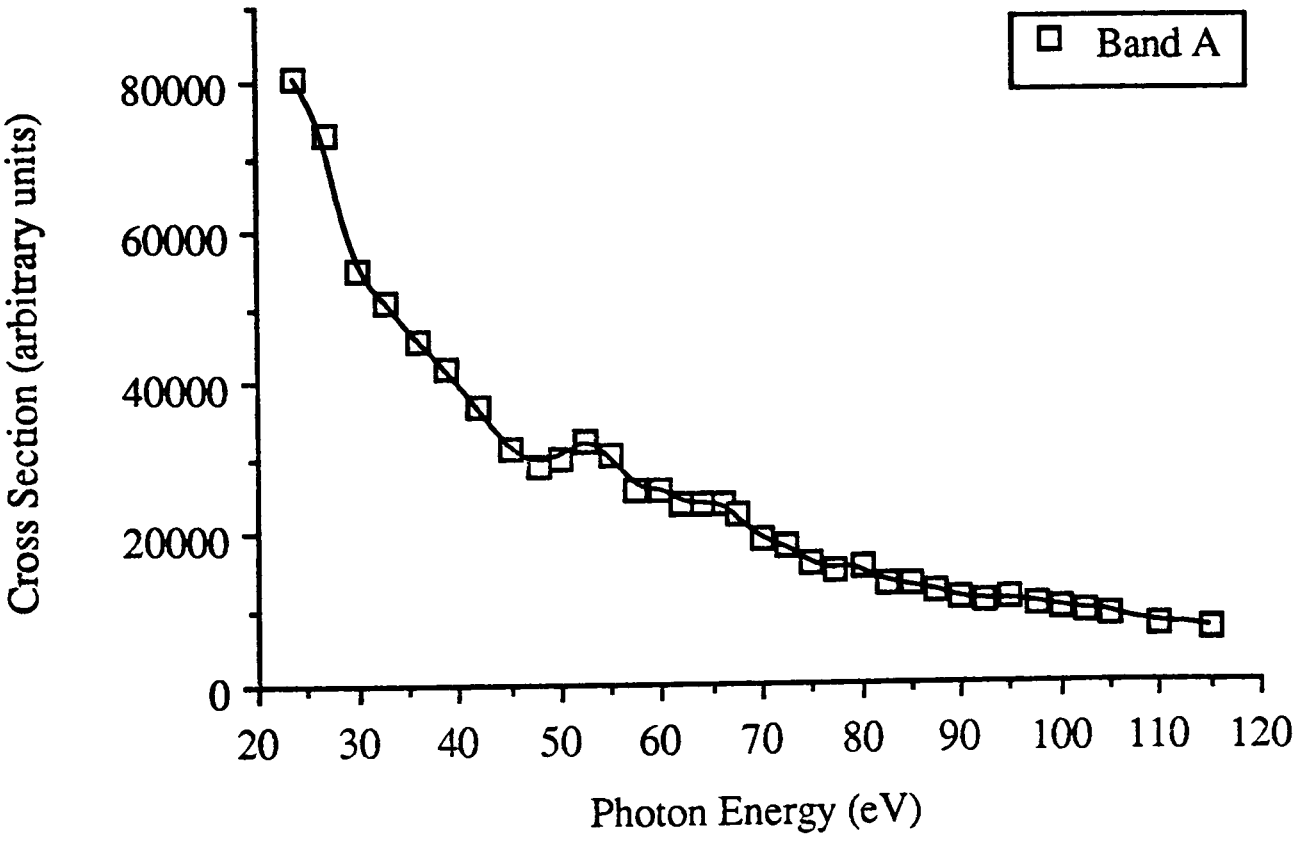

Figure 4.4 : individual RPPICS of bands A-E in the PE spectrum of OsO_4

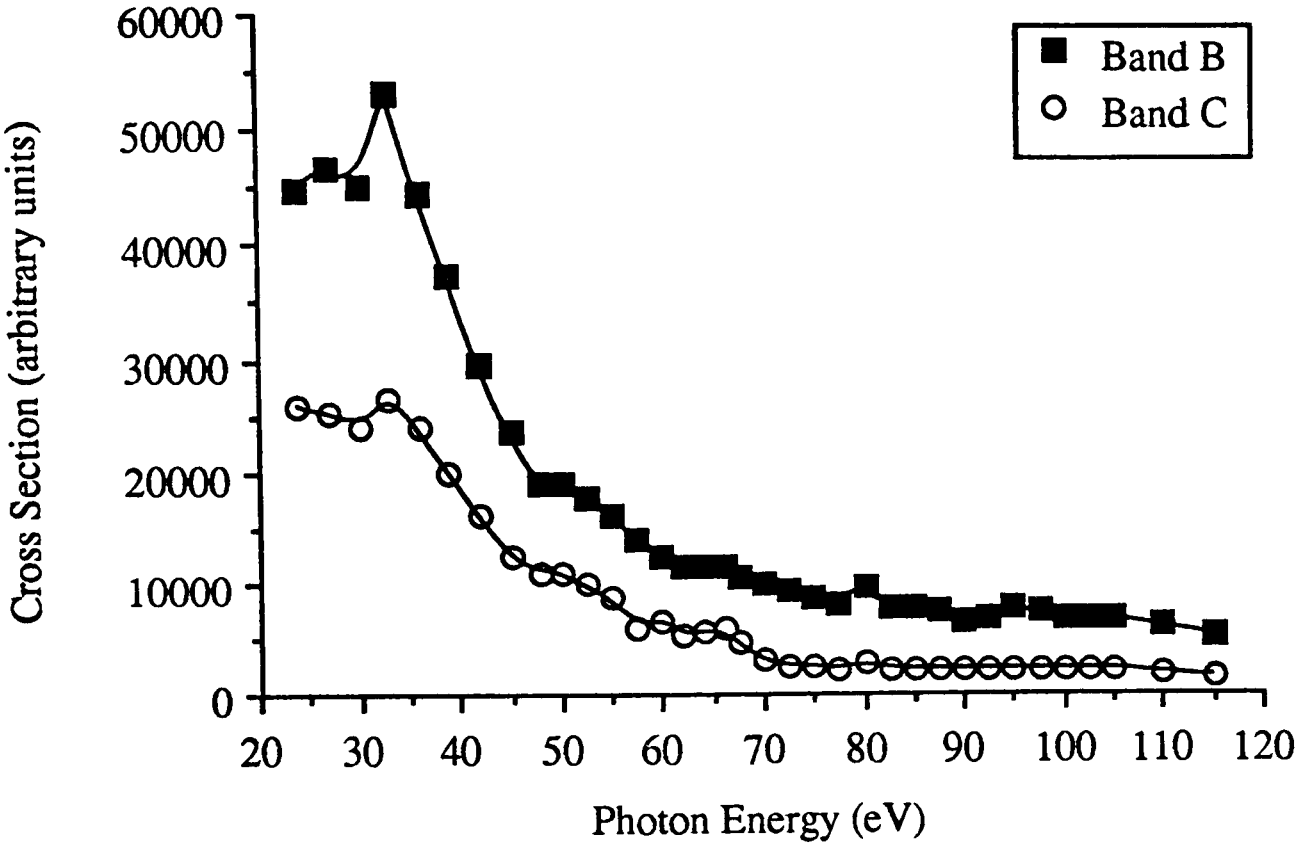

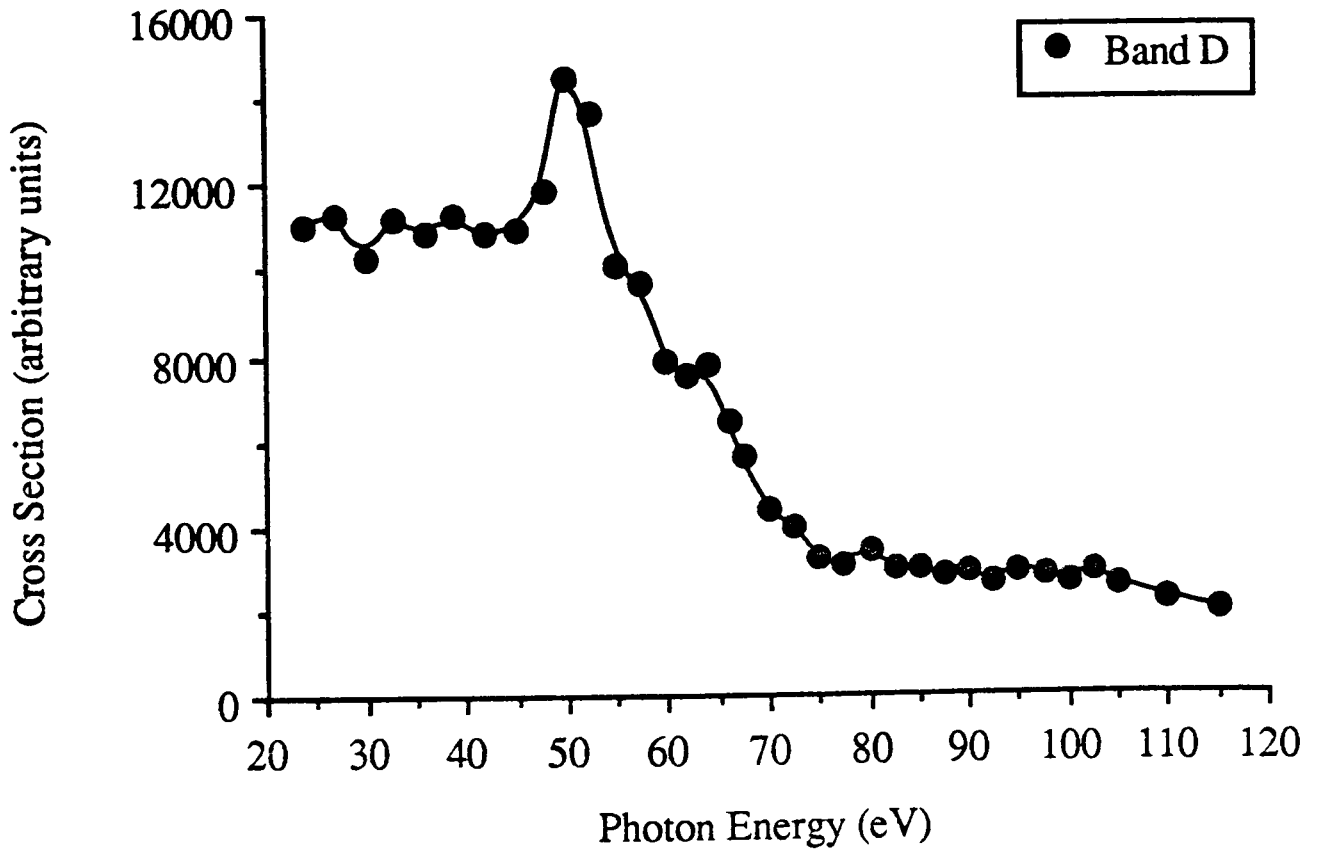

Figure 4.4 : individual RPPICS of bands A-E in the PE spectrum of OsO_4 (continued)

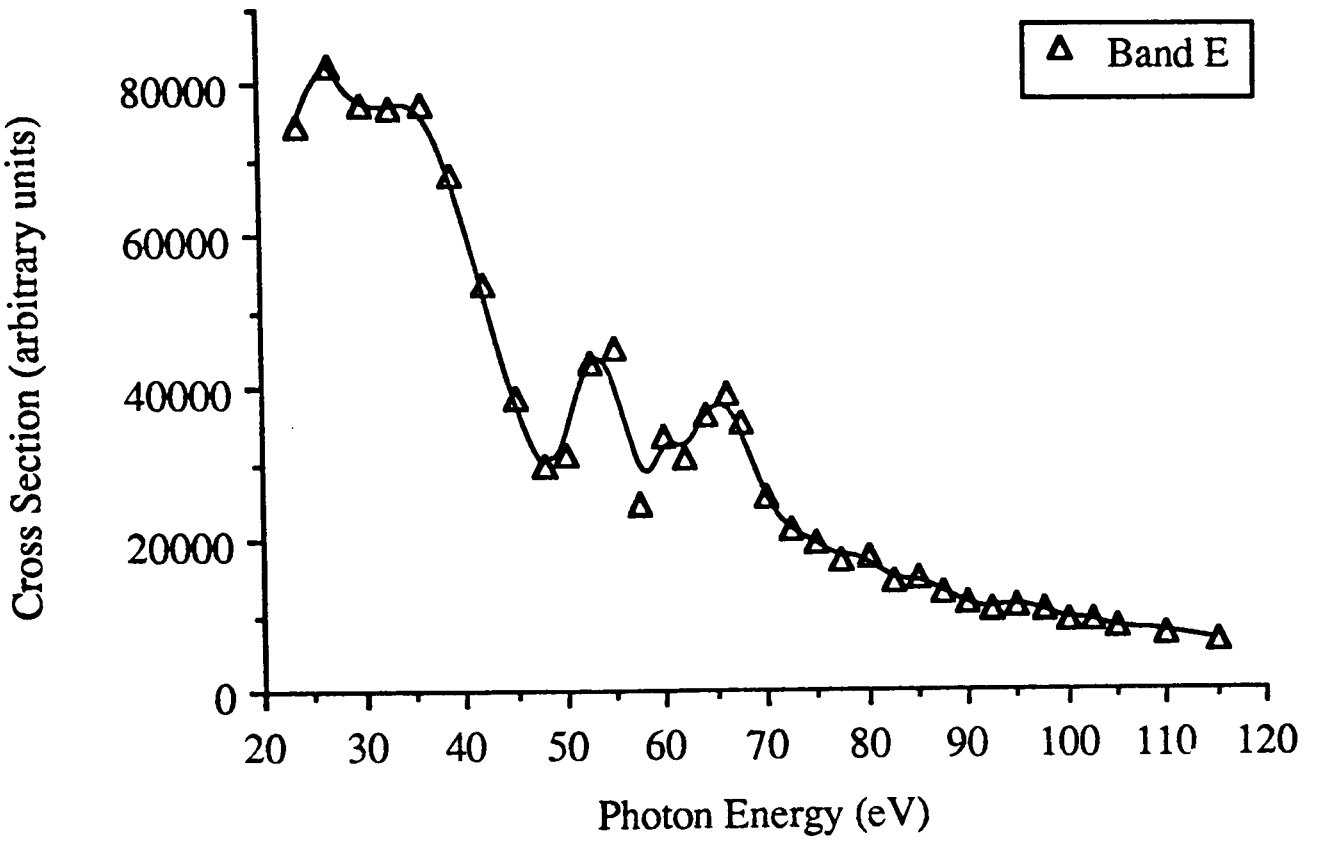

Figure 4.4 : individual RPPICS of bands A-E in the PE spectrum of OsO_4 (continued)

The most pronounced feature is the "double hump" profile of the cross section data for band E in the region 50-70 eV. This is a clear indication of a p→d giant resonant enhancement (Chapter 1.4.3 (c)) of the cross section of this band, coinciding with the osmium 5p subshell ionisation potentials ($^2P_{3/2}$ = 49 eV, $^2P_{1/2}$ = 61 eV [19]). As with [Ta(η-C_7H_7)(η-C_5H_4Me)] (Chapter 2.3.2 (c)), a group theoretical treatment of the p→d resonance in a third row transition metal complex is not valid in the LS coupling scheme, as the magnitude of exchange and spin-orbit splittings are similar. Unlike [Ta(η-C_7H_7)(η-C_5H_4Me)], however, discussing the p→d resonance in band E of OsO_4 in terms of double groups will not be complicated by the presence of a coincident shape resonance, and there will not be the possibility of more than two open shells in the intermediate to which absorption occurs. Furthermore, no approximations are made as to the point group of OsO_4, in contrast to [Ta(η-C_7H_7)(η-C_5H_4Me)].

5p→5d giant resonant absortion in OsO_4 is represented by the equations

$$5p^62t_2^62a_1^21e^43t_2^61t_1^62e^04t_2^0 + h\nu \rightarrow 5p^52t_2^62a_1^21e^43t_2^61t_1^62e^14t_2^0$$

and

$$5p^62t_2^62a_1^21e^43t_2^61t_1^62e^04t_2^0 + h\nu \rightarrow 5p^52t_2^62a_1^21e^43t_2^61t_1^62e^04t_2^1$$

Using T_d^* double group symmetry labels, in the j-j coupling limit, the irreducible representations of the 5p, 2e and $4t_2$ MOs (T_2, E and T_2 respectively) must be multiplied by the electron spin representation (E') before their direct product is taken to determine the states arising from the $5p^52t_2^62a_1^21e^43t_2^61t_1^62e^14t_2^0$ and $5p^52t_2^62a_1^21e^43t_2^61t_1^62e^04t_2^1$ configurations. For absorption to the 2e MOs

$$T_2 \times E' = E'' + U' \qquad E \times E' = U'$$

$$(E'' + U') \times U' = \{E + T_1 + T_2\} + A_1 + E + T_2 + A_2 + 2T_1 + T_2 \text{ (each singlet and triplet)}$$

(4.1)

If we now apply the electric dipole selection rule, we find that only T_2 symmetry excited states can be reached by photoabsorption. If we also invoke the $\Delta S = 0$ selection rule, only singlet states are possible intermediates. Since the E'' and U' states arising from the direct product $T_2 \times E'$ correspond to the different spin-orbit states of the $5p^5$ (transforming as t_2^5 in T_d symmetry) configuration (with U' lying at lower binding energy than E'' for spin-orbit coupling in a t_2^5 configuration derived from p AOs (Table 4.4, page 124)) the two T_2 states on the right hand side of equation (4.1) are of lower energy than the single T_2 in { } brackets. Therefore two p→d absorption, and so two photoionisation resonance peaks, are expected with an intensity ratio, lower energy : higher energy = 2 : 1, in any band corresponding to ionisation of MOs with appreciable metal d orbital character. Similar treatment of absorption to the $4t_2$ MOs yields the following direct products

$$T_2 \times E' = E'' + U' \qquad T_2 \times E' = E'' + U'$$

$$(E'' + U') \times (E'' + U') = \{A_1 + T_1 + E + T_1 + T_2\} + E + T_1 + T_2 + A_1 + E + T_2 + A_2 + 2T_1 + T_2 \text{ (each singlet and triplet)}$$

from which it can be seen that there should be two photoionisation peaks with an expected intensity ratio, lower energy : higher energy = 3 : 1. Figures 4.3 and 4.4 reveal that this expected intensity ratio is not found in practice, with the second resonance peak being at least of similar area to the first. This is as found in [Ta(η-C_7H_7)(η-C_5H_4Me)] and in the other third row systems discussed in Chapter 2.3.3 (c), providing further evidence that neither the LS nor the j-j coupling schemes are appropriate when exchange and spin-orbit effects are of comparable magnitude.

Interchannel coupling between the final states derived from ionisation via the resonance intermediate T_2 states and those from direct photoionisation should lead to five overlapping Fano profiles for the first RPPICS enhancement of band E (at 55 eV) and two for the second maximum (at 66 eV). It proved impossible to obtain a good Fano fit (using equation (1.9)) to the RPPICS of band E in the p→d resonance region. However the equation employs only two resonance energies and therefore can only attempt to model the cruder splitting of the RPPICS maxima due to the spin-orbit states of the osmium 5p subshell and not the finer details of the number of T_2 states in the resonance intermediate.

Between 24 and 37 eV incident photon energy, the cross section of band E passes through a maximum, which can be identified with the delayed maximum (Chapter 1.4.3 (b)) in the cross section of the 5d AO of osmium, calculated to occur at a PE KE of 15.1 eV [20]. This compares favourably with the ca. 14 eV found from experiment.

The RPPICS of band D maintains a fairly constant level between incident photon energies of 24 to 44 eV. Between 44 and 55 eV there is a strong intensity rise and fall with a maximum at ca. 50 eV. Though this coincides with the region of the 5p $^2P_{3/2}$ ionisation, the absence of a second maximum between 55 and 70 eV suggests that a p→d resonance is not the correct explanation of this feature. At higher photon energies the cross section falls off sharply. Overall the very different cross section behaviour of band D in comparison

with bands A to C supports the assignment of this band to the $2a_1^{-1}$ ionisation. Sharp a_1^{-1} ionisation bands which show relative intensity increases in He II over He I spectra are found in the PE spectra of transition metal tetrahalides [9], a theme which will be expanded on later in this Chapter. The cross section features of band D may well reflect a significant osmium 6s contribution to the $2a_1$ MO, in that the 6s AO is calculated to have a strong Cooper minimum at an incident photon energy of ca. 15 eV, which is followed by a substantial maximum at ca. 40 eV [20]. Alternatively the maximum at ca. 50 eV could be due to a molecular shape resonance.

The cross section behaviour of band A is rather different from that of bands B and C whose RPPICS resemble one another. The renormalised BRs of bands B and C are presented in Figure 4.5, and are very close to 2:1 in the spectra acquired with photon energies below 70 eV. Above this photon energy the ratio increases to a value of ~3.5:1 but this change may well be an artefact of the fitting; above 70 eV a higher pass energy is used for the electron analysis and the resolution deteriorates. All three bands show small intensity fluctuations between 55 and 70 eV in the same region as band E, though the features are much weaker. Within the three bands the maxima are most pronounced for band A. Inter-channel coupling (Chapter 1.4.3 (c)) has been observed to produce such an effect on ionisation bands from MOs which, by symmetry, may have no metal d character [21], but these RPPICS features are normally weaker than those associated with orbitals in which d character is symmetry allowed.

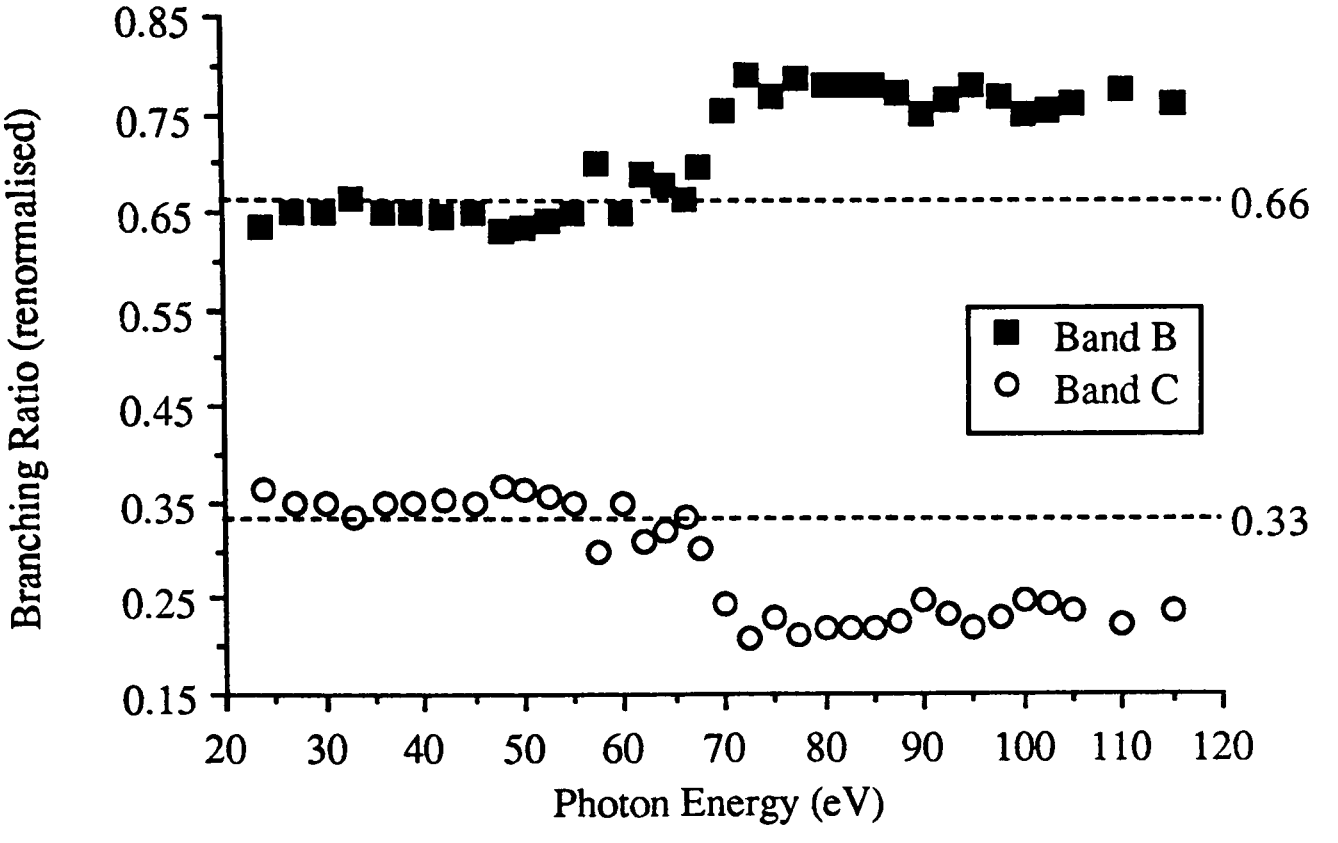

Figure 4.5 : renormalised BRs of bands B and C in the PE spectrum of OsO_4

4.2.3 Assignment of the photoelectron spectrum of OsO_4

As part of a joint project to reinvestigate the PE spectrum of OsO_4, the IEs of the valence MOs have been calculated by Stephen Jarrett-Sprague and Ian Hillier at the University of Manchester, employing both Green's function and ΔSCF-CI approaches (Chapter 1.3.1). They are presented in Table 4.2, and Table 4.3 gives the orbital characteristics of the valence MOs. For further details of these calculations, the reader is directed to references [17] and [18], and only the most salient results are discussed here. These form an integral part of a multi-faceted argument, employing both experimental and theoretical approaches, which is presented below.

Table 4.2 : calculated IEs of OsO_4

MO	Calculated IE (eV)		Band assignment
	Green's function	ΔSCF-CI	
$1t_1$	12.4	11.7	A
$3t_2$	13.6	13.2	B, C
$2a_1$	14.7	14.4	D
$2t_2$	17.6	a	E
1e	18.0	18.2	E

[a] the SCF method can obtain only the lowest state of a particular symmetry

Table 4.3 : orbital characteristics (Mulliken population analysis) of OsO_4

MO	Osmium			Oxygen	
	6s	5p	5d	2s	2p
$1t_1$	0.000	0.000	0.000	0.000	0.250
$3t_2$	0.000	0.046	0.014	0.003	0.232
$2a_1$	0.172	0.000	0.000	0.013	0.194
$2t_2$	0.000	0.000	0.492	0.000	0.130
1e	0.000	0.023	0.432	0.023	0.133

In the PE spectrum of OsO_4, bands A-D all show resolved vibrational structure (Figure 4.2 (a)). This is most complex in A where the band system is dominated by a progression of mean interval ca. 900±80 cm^{-1}, which is assigned to the a_1 stretch, and which has a frequency of 965 cm^{-1} in the ground state of OsO_4 [22]. Furthermore, there is a second progression of interval ca. 300±80 cm^{-1} representing excitation of either a t_2 [4] or e mode [1] (323 cm^{-1} and 333 cm^{-1} respectively for OsO_4 [22]). Bands B, C and D exhibit fine structure due to an a_1 mode with intervals of 900-950 cm^{-1}, just less than that

of neutral OsO_4. The similarity of the vibrational fine structure of bands B and C is particularly striking.

Band E is broad with no resolvable fine structure, but has two distinct maxima about 0.4 eV apart. As this splitting is too great for a simple vibrational progression, three alternative interpretations are possible. Either band E correlates with two primary ion states, or it is a ^2T state split by either Jahn-Teller or spin-orbit coupling. If either of the latter two explanations is adopted, the conclusion must be that there is very little π bonding in OsO_4, as bands B and C, which are then assigned to $^2T_2$ and ^2E ion states respectively and which arise from the π type orbitals, show negligible d character in their RPPICS. The results of the calculations reported here strongly suggest that band E must be assigned to both $^2T_2$ and ^2E ion states, which restores the picture of strong π bonding as the 1e orbital is shown to be both strongly bound and to have a high d content (Table 4.3).

If band E does arise from two separate states then two of the bands A-D must also arise from the same state with the degeneracy lifted by one of the possible mechanisms. Only band A shows a Jahn-Teller active vibrational mode, bands B, C and D showing a progression due to an a_1 stretch. Furthermore, Jahn-Teller splittings of degenerate ion states of the magnitude found for the separations of bands A, B, C and D are acccompanied by much more extensive vibronic structure than is found here. Methane, for example, where the t_2 orbitals are strongly bonding, has a $^2T_2$ ionisation band with maxima separated by ca. 0.8 eV and extensive structure [23], whereas the U' component of the non-bonding t_1 ionisation of CBr_4 shows a splitting of 0.09 eV and no extensive vibronic structure [8]. None of the MOs giving rise to bands A-D is strongly bonding. The spectral appearance is therefore inconsistent with the production of four well separated bands from three primary ion states by a Jahn-Teller mechanism.

The most likely candidate for a spin-orbit split pair of bands are B and C. They have identical vibrational fine structure and show a constant 2:1 BR over the photon energy range where the bands are well resolved (20-70 eV). Furthermore, the separation of bands B and C is 0.4 eV in OsO_4 and 0.09 eV in the closely related RuO_4 [3, 4], consistent with an increase in spin-orbit splitting with atomic number of the central atom. No other pair of

bands fulfils these necessary conditions. Orchard et al. [3, 4] rule out the possibility of B and C being spin-orbit components arising from an osmium 5d contribution to the $3t_2$ MO, as a t_2 hole state gives rise to the sequence of multiplet states E'' < U' [8, 24] (as is found for example in the d band ionisation of $[W(CO)_6]$ [25]). But band B is twice as intense as band C giving a multiplet ordering which is qualitatively incorrect. Also the RPPICS data determined here show minimal 5d character in the orbitals giving rise to bands B and C, and the calculation predicts only 1.4% d character (Table 4.3).

The ordering of spin-orbit multiplets for $^2T_2$ states is given in Table 4.4. Spin-orbit splitting could also originate from an osmium 6p contribution to the $3t_2$ MO. For a hole in a p shell (p^5 configuration), the spin-orbit multiplet ordering is U' < E'' (as is found for the 5p ionisations of xenon with $^2P_{3/2} < {}^2P_{1/2}$).

Table 4.4 : energy ordering of spin-orbit multiplets for $^2T_2$ states in MO_4^+ ions arising from metal-derived spin-orbit coupling

		Configuration	
		t_2^1	t_2^5
Orbital origin of splitting	p	E'' < U'	U' < E''
	d	U' < E''	E'' < U'

The multiplet splitting should be

$$\frac{3}{2}c^2\zeta_{6p}$$

where c is the coefficient of the osmium 6p orbital in the $3t_2$ MO and ζ_{6p} is the 6p spin-orbit coupling constant. The calculation (Table 4.3) predicts a 5% 6p contribution to the $3t_2$ MO of OsO_4. Estimates of ζ_{6p} for osmium in various configurations have been calculated by Norman Edelstein of the Lawrence Berkeley Laboratory using Cowan's procedure [26]. The results are given in Table 4.5. Mulliken population analysis suggests a configuration between d^4 and d^5 for osmium in OsO_4 (Table 4.3). The rough prediction of the U' - E''

splitting is therefore 0.064 eV. This is considerably less than the observed value of 0.4 eV but the theoretical estimates are somewhat crude, a higher charge on the osmium together with a higher 6p contribution to the $3t_2$ MO could increase the estimate significantly, but it would need say 18% 6p character and a d^2 configuration to produce the observed splitting of 0.4 eV.

The $3t_2$ σ bonding level of $[Pb(CH_3)_4]$ shows a multiplet splitting of 0.91 eV. Given a value of ζ_{6p} for lead of 1.16 eV, a 52% contribution from the lead 6p orbital to the $3t_2$ MO can be estimated [28]. In this case the band is broad, suggesting unresolved vibrational structure consistent with significant bonding character implied by such a high lead contribution.

Table 4.5 : calculation of spin-orbit constants for osmium 6p [27]

Ion	Configuration	ζ_{6p} (eV)	
		Blume-Watson[a]	R*VI[b]
Os	$[Xe]4f^{14}5d^{6}6s^{1}6p^{1}$	0.294	0.298
Os^{+}	$[Xe]4f^{14}5d^{6}6p^{1}$	0.456	0.462
Os^{2+}	$[Xe]4f^{14}5d^{5}6p^{1}$	0.715	0.725
Os^{3+}	$[Xe]4f^{14}5d^{4}6p^{1}$	0.979	0.992
Os^{4+}	$[Xe]4f^{14}5d^{3}6p^{1}$	1.237	1.255
Os^{5+}	$[Xe]4f^{14}5d^{2}6p^{1}$	1.500	1.521
Os^{6+}	$[Xe]4f^{14}5d^{1}6p^{1}$	1.765	1.789
Os^{7+}	$[Xe]4f^{14}6p^{1}$	2.032	2.060

[a] ζ_{6p} calculated by the Blume-Watson method, see reference [26] p. 94

[b] ζ_{6p} calculated with equation 8.2 reference [26]

An alternative conceivable source of spin-orbit coupling is the osmium core 5p orbitals mixing with the $3t_2$ level. This is not without precedent, in that recent relativistic Hartree-Fock-Slater calculations of the IEs of UF_4, UCl_4, ThF_4 and $ThCl_4$ [29] have suggested a reassignment of the valence PE spectra [30, 31]. The formerly $4t_2^{-1}$ band of the chlorides has been reassigned to the U' component of the associated $^2T_2$ primary ion state, the E" ionisation being placed coincident with the $1t_1^{-1}$ band. The mechanism for this is believed to be a significant metal 6p AO admixture in the valence t_2 bands, and agreement between calculation and experiment is impressive for the chlorides, though less so for the fluorides. Recent HF pseudopotential calculations by Pyykkö and Li at the University of Helsinki suggest that there could indeed be sufficient osmium 5p AO character to the $3t_2$ MO to produce the observed splitting [32]. In the light of this work, core mixing cannot be discounted as the origin of the splitting of bands B and C.

One consequence of assigning bands B and C to a $^2T_2$ state is that band A must arise from the $^2T_1$ ion state. The very small p→d resonance in this band results from inter-channel coupling as there can be no d orbital contribution to the $1t_1$ MO.

Although the situation regarding the magnitude of the spin-orbit splitting is not entirely satisfactory, the following assignment

Band	A	B	C	D	E
State	$^2T_1$	U' ($^2T_2$)	E" ($^2T_2$)	$^2A_1$	^2E, $^2T_2$

seems the most plausible. The arguments in favour of this choice are the weight of the ion state calculations, the consistency between the experimental evidence of the osmium 5d AO contribution to the orbitals associated with band E and that predicted by the theory for the $2t_2$ and 1e MOs, and the large body of evidence for multiple bonding, and hence π bonding, in OsO_4.

4.3 Titanium tetrachloride

$TiCl_4$ occupies a position at least as fundamental as OsO_4 in terms of electronic structure determination, and has received considerable attention from both experiment and theory. Yet despite several reports and discussions of both the He I and He II PE spectra [4, 6-10] and numerous calculations of the MO structure [4, 10, 33-43], there is still no general agreement as to the assignment of the PE spectrum. An extension of the PES experiment to synchrotron radiation was the obvious solution, and indeed had already been performed [14]. The results of these two variable photon energy investigations are discussed simultaneously where appropriate.

4.3.1 Bonding and interpretation of the photoelectron spectrum

The valence electronic structures of the d^0 tetrahedral MCl_4 species are closely related to those of the MO_4 systems described in Section 4.2.1. The $1a_1$ and $1t_2$ MOs are again essentially ligand s orbital-based, and the five primary ion states identified in OsO_4 are once more expected to occur in the ionisation region studied. The ordering of these ion states may well be different, however, on account of the differing relative energies and overlaps of metal and ligand valence AOs.

The PE spectrum of $TiCl_4$, obtained with synchrotron radiation at 24 and 40 eV, is shown in Figure 4.6. IEs and band assignments are collected in Table 4.6, from which it can be seen that there are essentially two different assignments proposed for the valence bands. The discussion centres chiefly on the ordering of the $2a_1$ and $2t_2$ MOs. The only PES experiment to favour the assignment of band E to the $2t_2$ MO is that of Bancroft et al. [10], in which He II/He I intensity changes are cited as a central piece of evidence, providing further impetus for a synchrotron radiation-based study.

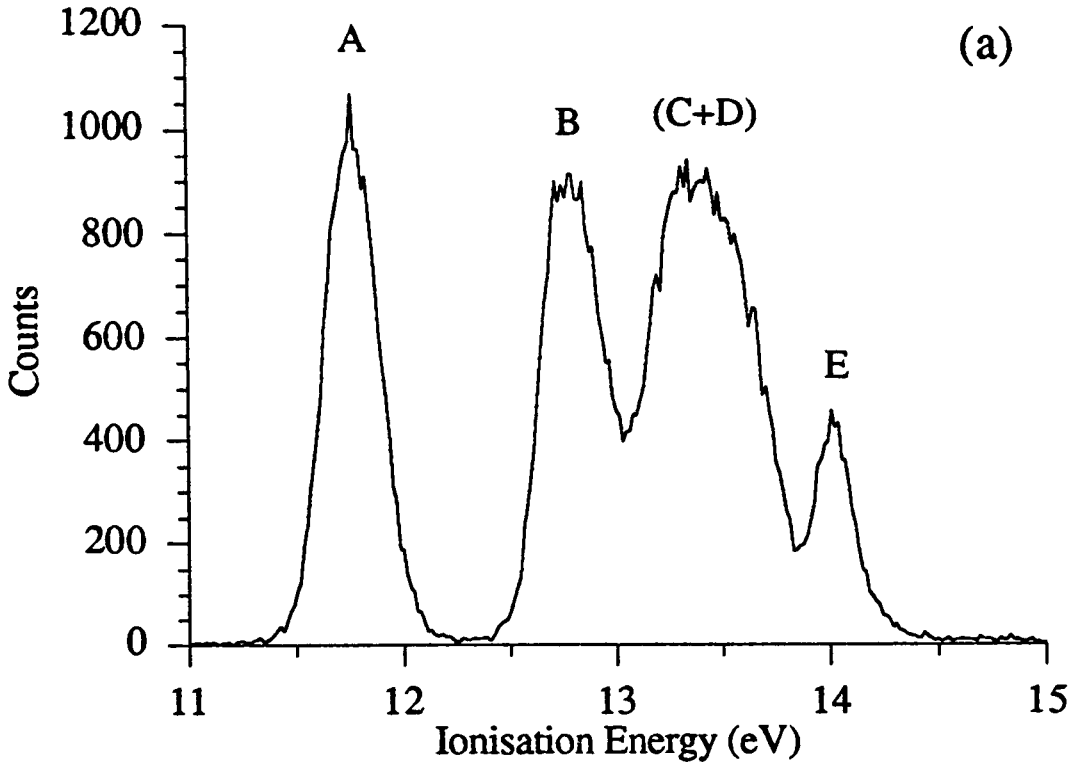

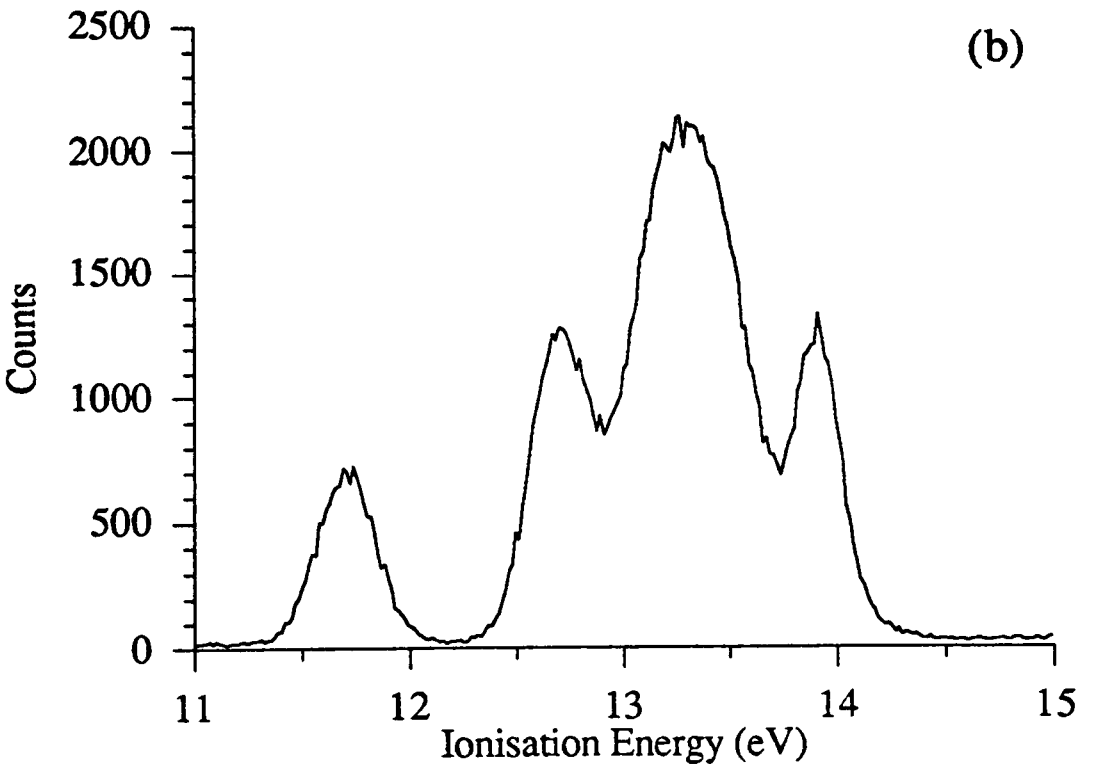

Figure 4.6 : the PE spectrum of $TiCl_4$, acquired at (a) 24 and (b) 40 eV

Table 4.6 : IEs and assignments in the PE spectrum of $TiCl_4$

Band	IE (eV)[a]	Reference/Assignment	
		[4, 6-9, 14, 33-35, 38, 39, 42, 43]	[10, 36, 37, 40, 41]
A	11.69	$^2T_1$	$^2T_1$
B	12.67	$^2T_2$	$^2T_2$
(C+D)	13.17, 13.46	$^2T_2$, ^2E	^2E, $^2A_1$
E	13.91	$^2A_1$	$^2T_2$

[a] data from reference [10]

4.3.2 RPPICS results and discussion

The valence PE spectrum of $TiCl_4$ has been measured over the incident photon energy range 17-69 eV and RPPICS have been determined for four bands, labelled A, B, (C+D) and E for consistency with previous workers. The cross sections are presented in Figure 4.7, and plotted individually in Figure 4.8.

The cross section of band A shows a rapid fall off at low incident photon energies, with a shallow minimum at 46 eV and a subsequent small maximum at 64 eV. The generally accepted assignment of this band to the $1t_1$ MOs indicates that the only AO contributions to this MO come from the chlorine atoms, as none of the valence AOs of titanium transforms as t_1 in T_d symmetry. Thus the cross section behaviour of this band should be very similar to that of the equivalent bands in the PE spectra of CCl_4 and $SiCl_4$, i.e. independent of the central atom.

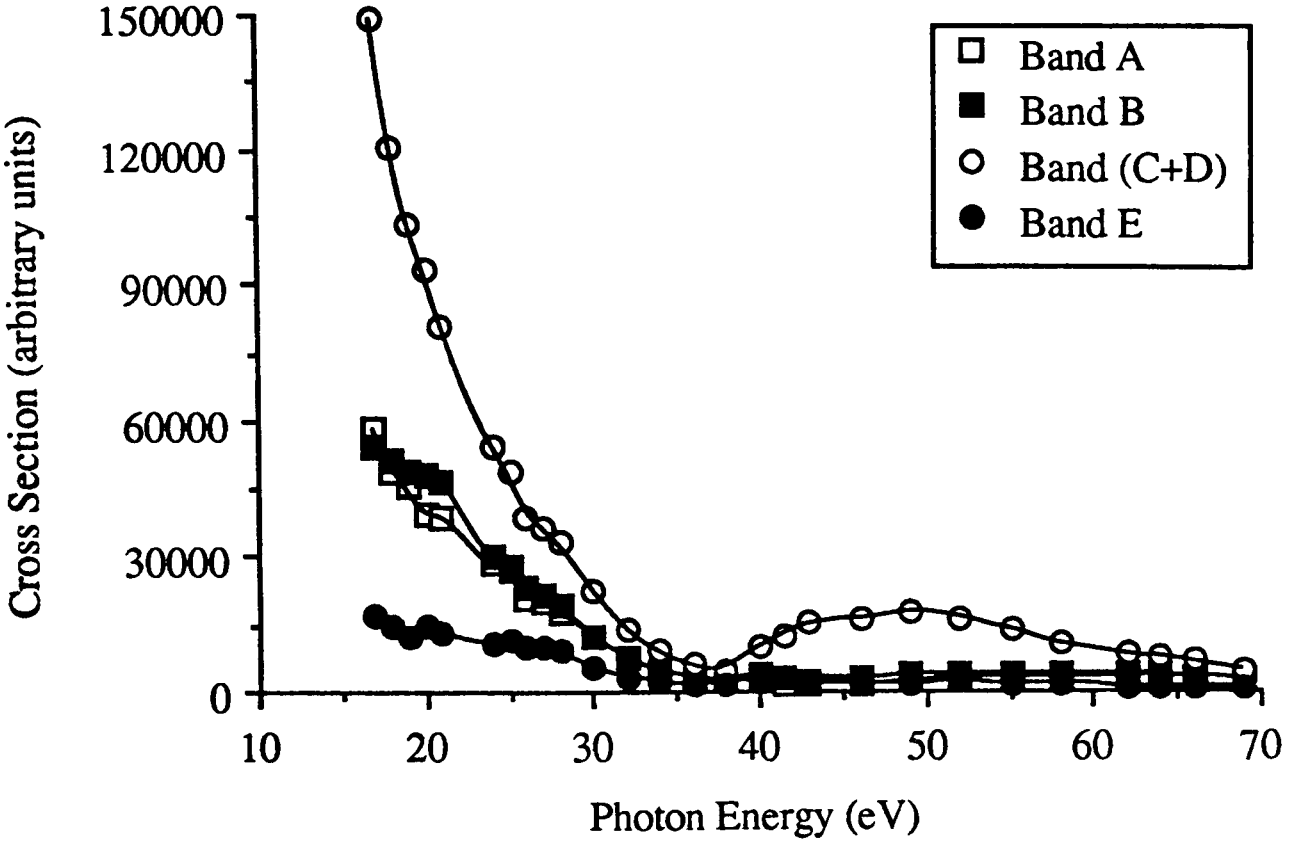

Figure 4.7 : RPPICS of bands A-E in the PE spectrum of $TiCl_4$

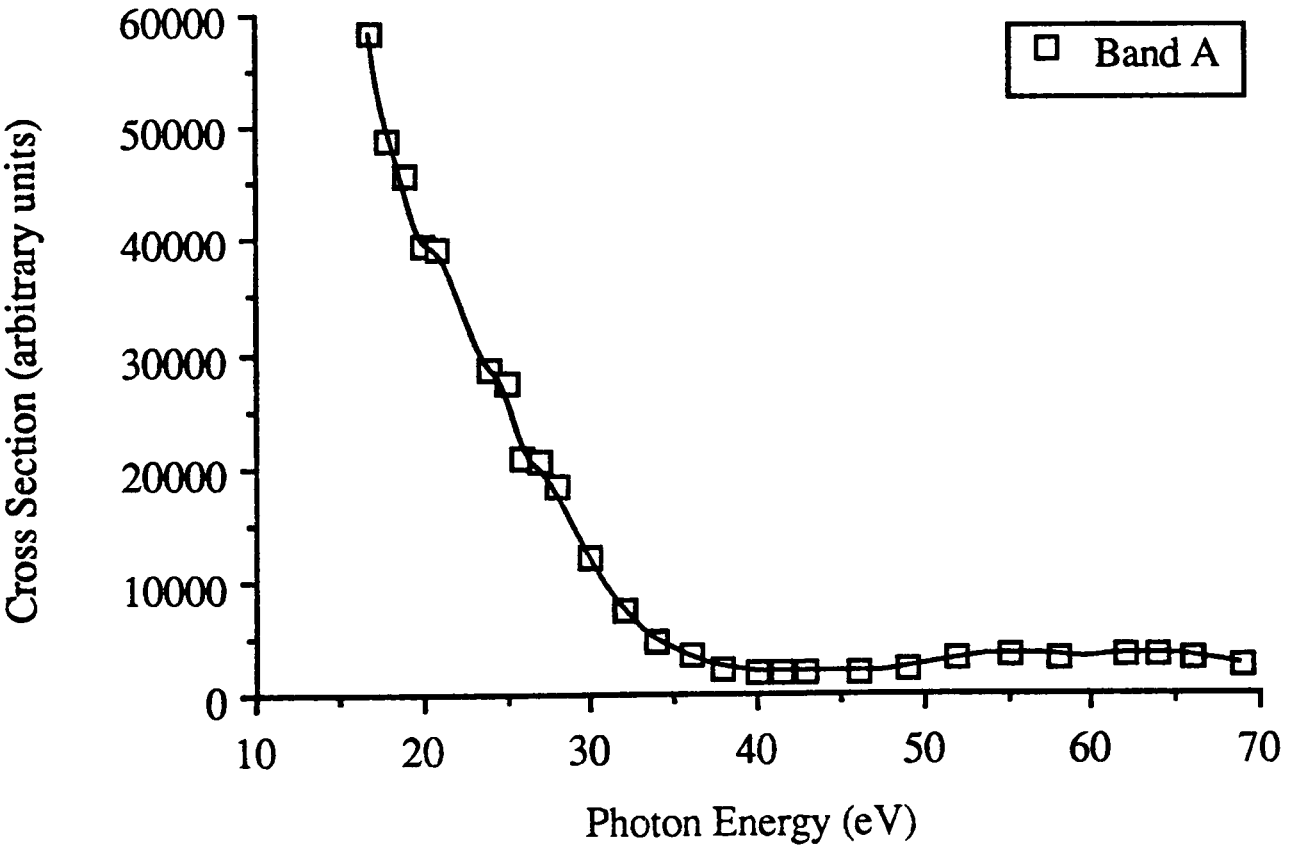

Figure 4.8 : individual RPPICS of bands A-E in the PE spectrum of $TiCl_4$

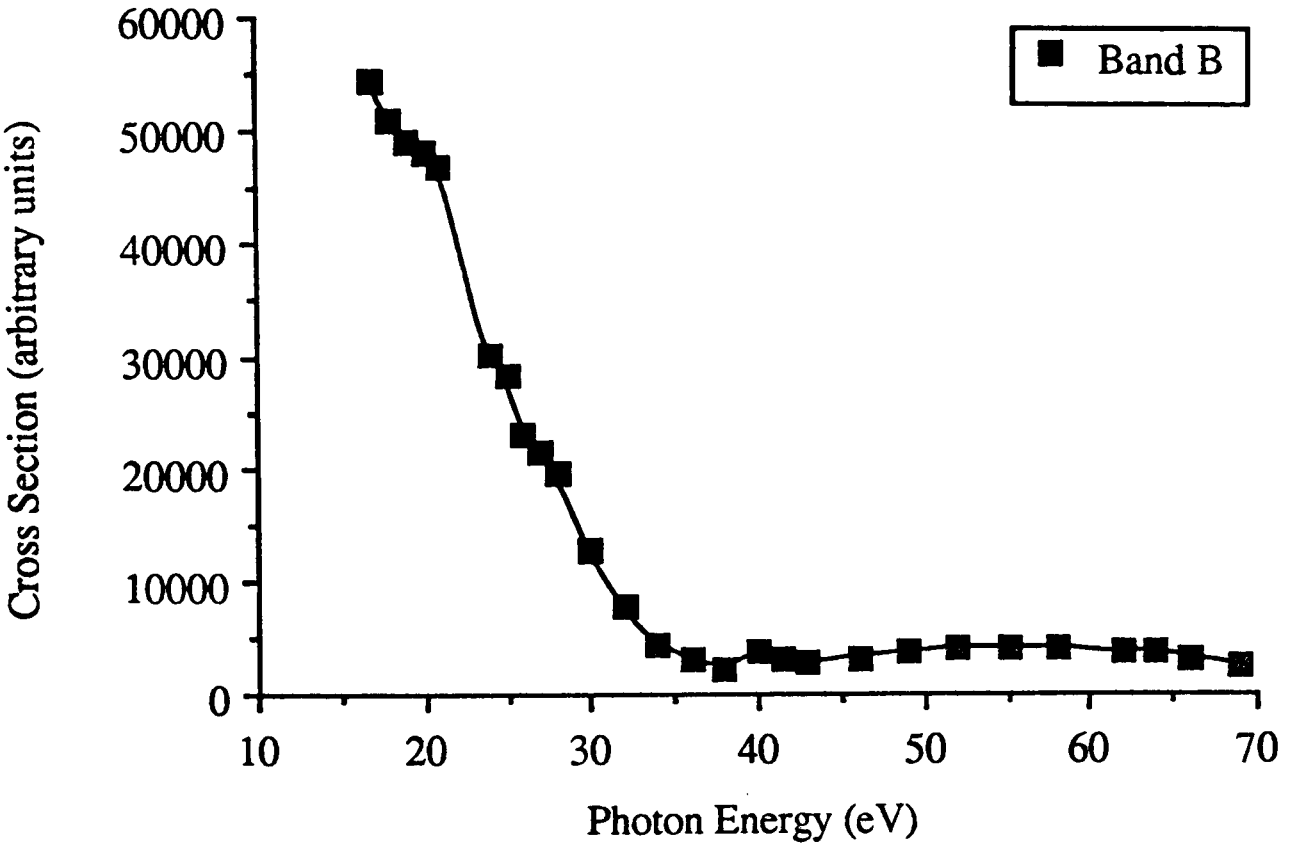

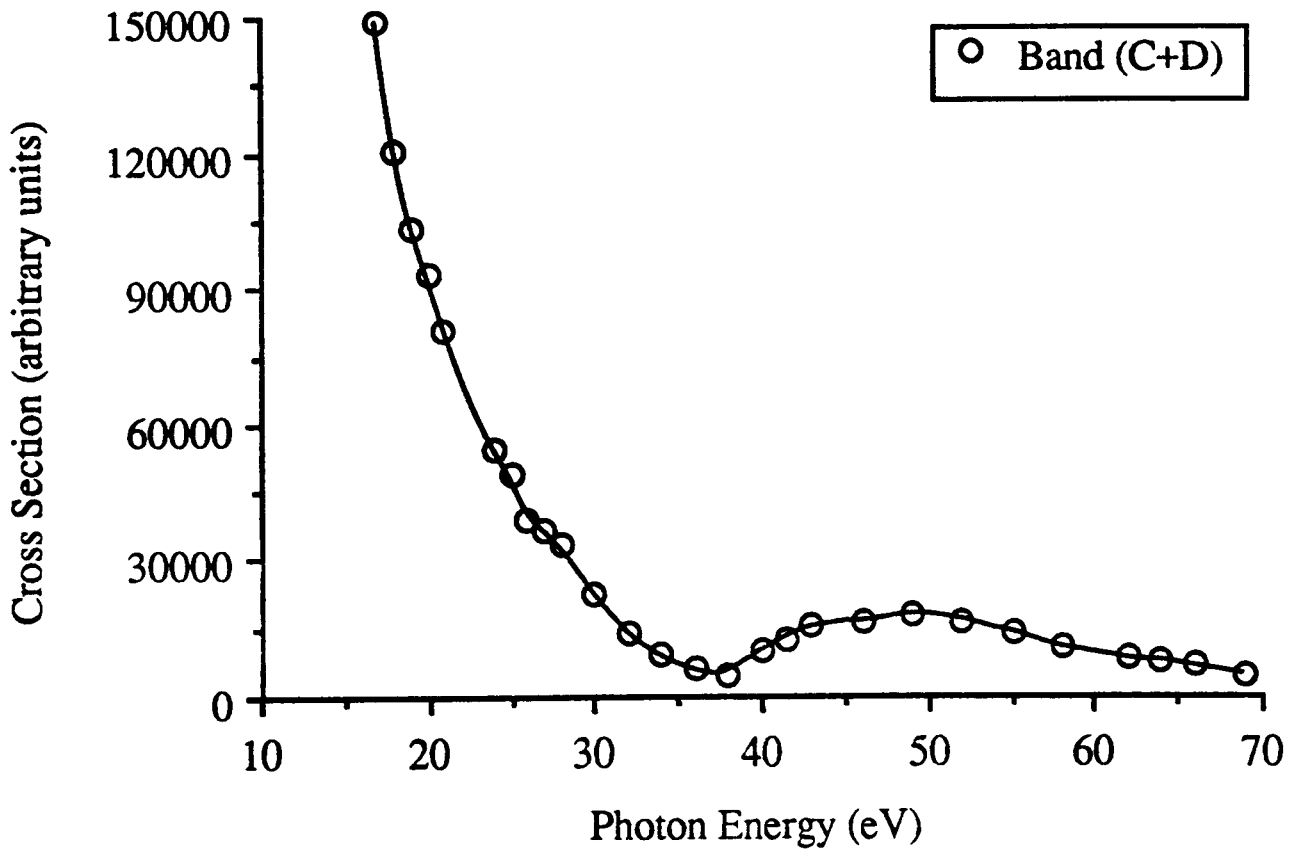

Figure 4.8 : individual RPPICS of bands A-E in the PE spectrum of $TiCl_4$ (continued)

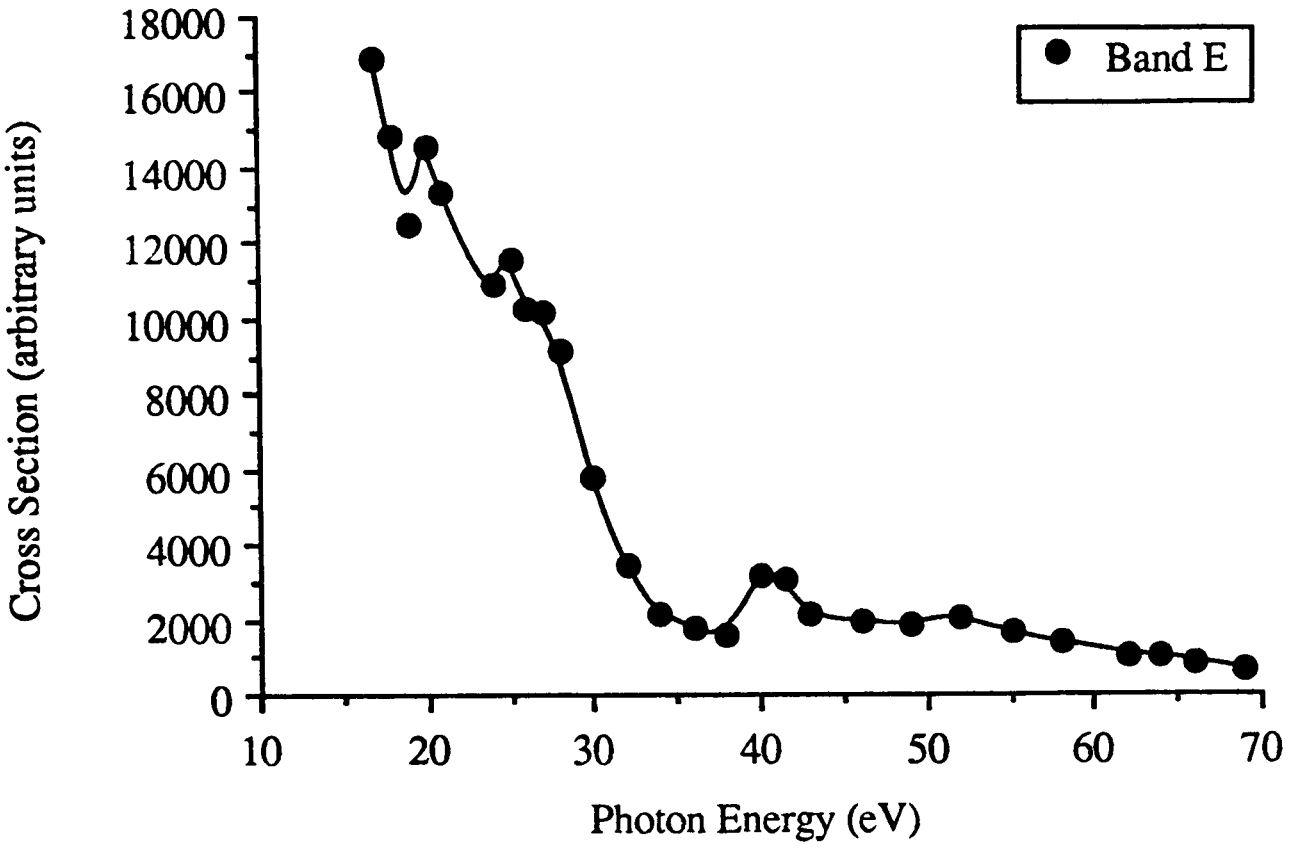

Figure 4.8 : individual RPPICS of bands A-E in the PE spectrum of $TiCl_4$ (continued)

In their work on CCl_4 and $SiCl_4$, Carlson et al. discuss the Cooper minimum in molecules [11, 13] (Chapter 1.4.3 (a) and 1.4.4 (a)). The cross section behaviour of the $1t_1^{-1}$ bands in both main group molecules is very similar to that of band A in $TiCl_4$, with a shallow minimum at 43 eV (CCl_4) and 42 eV ($SiCl_4$) incident photon energy. This is equated with the Cooper minimum in the 3p AO of chlorine, which has subsequently been calculated to occur at a PE KE of ca. 30 eV [20]. This compares with 31.4 eV for CCl_4, 30.0 eV for $SiCl_4$ and 34.2 eV for $TiCl_4$. There is therefore little doubt that the RPPICS of band A can be adequately explained in terms of an MO strongly localised on the chlorine atoms. Indeed, Hillier and Kendrick have calculated this MO to contain 98% chlorine 3p character [42]. As the cross section variations of band A are very similar to those found for the $1t_1^{-1}$ band in the previous synchrotron study of $TiCl_4$ [14], all of the variable photon energy studies are in agreement as to the assignment and cross section behaviour of the first ionisation band of these tetrachlorides.

The $3t_2$ MO is also calculated to be over 90% chlorine 3p in character [42] and band B is therefore expected to show RPPICS similar to those of band A. This is indeed found to be the case, with two minor differences. There is a slight shoulder to the RPPICS fall off at 21 eV photon energy, and a small maximum at 40 eV, neither of which is seen in the cross sections of the equivalent bands of CCl_4 and $SiCl_4$. The data for the $3t_2^{-1}$ band from the previous synchrotron study of $TiCl_4$ does not begin at a low enough incident photon energy to distinguish the cross section shoulder, but does find a small maximum at 40 eV. The most likely explanation for this feature is a molecular shape resonance (Chapter 1.4.4 (d)), as there is no feature in the cross section of the 3p AO of chlorine (or indeed any other possible AO contributor to the $3t_2$ MO) that can explain it. A similar explanation for the low incident photon energy shoulder is also favoured, and this is discussed later in relation to band E.

The assignment of bands A and B has not been the subject of debate, unlike that of bands (C+D) and E. Either band (C+D) contains the 1e and $2t_2$ MOs, with the $2a_1$ assigned to band E, or the $2t_2$ and $2a_1$ MO ordering is reversed. The analysis of the RPPICS of these two bands attempts to resolve this dilemma.

The cross section behaviour of band (C+D) is different from that of bands A and B in having a much more pronounced maximum following the initial fall off. The MOs ionising under band (C+D), whatever their assignment, will be predominantly chlorine 3p in character, and it is therefore difficult to explain the much larger cross section maximum in terms of the recovery of the cross section following the Cooper minimum seen in bands A and B. The other effect which can explain the feature is that of a p→d giant resonant enhancement. Although they are not metal d orbital-localised, a d orbital contribution to the MOs ionising under band (C+D) should manifest itself in a RPPICS enhancement in the region of the titanium 3p AO IEs ($^2P_{3/2}$ = 38 eV, $^2P_{1/2}$ = 39 eV [19]).

For $TiCl_4$, 3p→3d giant resonant absorption is represented by the equations

$$3p^6 2a_1^2 1e^4 2t_2^6 3t_2^6 1t_1^6 2e^0 4t_2^0 + h\nu \rightarrow 3p^5 2a_1^2 1e^4 2t_2^6 3t_2^6 1t_1^6 2e^1 4t_2^0$$

and

$$3p^6 2a_1^2 1e^4 2t_2^6 3t_2^6 1t_1^6 2e^0 4t_2^0 + h\nu \rightarrow 3p^5 2a_1^2 1e^4 2t_2^6 3t_2^6 1t_1^6 2e^0 4t_2^1$$

The irreducible representations of the $3p^5$ configuration transform as T_2 in T_d symmetry, so that the states arising from the $3p^5 2a_1^2 1e^4 2t_2^6 3t_2^6 1t_1^6 2e^1 4t_2^0$ configuration are given by the direct product

$$T_2 \times E = {}^1T_1 + {}^1T_2 + {}^3T_1 + {}^3T_2$$

and those from the $3p^5 2a_1^2 1e^4 2t_2^6 3t_2^6 1t_1^6 2e^0 4t_2^1$ configuration by the direct product

$$T_2 \times T_2 = {}^1A_1 + {}^1E + {}^1T_1 + {}^1T_2 + {}^3A_1 + {}^3E + {}^3T_1 + {}^3T_2$$

The electric dipole selection rule permits transitions only to T_2 excited states which, together with the $\Delta S = 0$ rule, gives the allowed final states as ${}^1T_2$. Autoionisation

$$3p^5 2a_1^2 1e^4 2t_2^6 3t_2^6 1t_1^6 2e^1 4t_2^0 \rightarrow 3p^5 2a_1^2 1e^4 2t_2^6 3t_2^6 1t_1^6 2e^0 4t_2^0 + e^- \quad (4.2\ (a))$$

$$3p^5 2a_1^2 1e^4 2t_2^6 3t_2^6 1t_1^6 2e^0 4t_2^1 \rightarrow 3p^5 2a_1^2 1e^4 2t_2^6 3t_2^6 1t_1^6 2e^0 4t_2^0 + e^- \quad (4.2\ (b))$$

is possible, together with the SCK decay processes

$$\begin{aligned} & & & 3p^6 2a_1^2 1e^4 2t_2^6 3t_2^6 1t_1^5 2e^0 4t_2^0 + e^- \\ & & & 3p^6 2a_1^2 1e^4 2t_2^6 3t_2^5 1t_1^6 2e^0 4t_2^0 + e^- \\ & 3p^5 2a_1^2 1e^4 2t_2^6 3t_2^6 1t_1^6 2e^1 4t_2^0 \rightarrow & & 3p^6 2a_1^2 1e^4 2t_2^5 3t_2^6 1t_1^6 2e^0 4t_2^0 + e^- \quad (4.3\ (a)) \\ & & & 3p^6 2a_1^2 1e^3 2t_2^6 3t_2^6 1t_1^6 2e^0 4t_2^0 + e^- \\ & & & 3p^6 2a_1^1 1e^4 2t_2^6 3t_2^6 1t_1^6 2e^0 4t_2^0 + e^- \end{aligned}$$

and

$$3p^62a_1^21e^42t_2^63t_2^61t_1^52e^04t_2^0 + e^-$$

$$3p^62a_1^21e^42t_2^63t_2^51t_1^62e^04t_2^0 + e^-$$

$$3p^52a_1^21e^42t_2^63t_2^61t_1^62e^04t_2^1 \rightarrow 3p^62a_1^21e^42t_2^53t_2^61t_1^62e^04t_2^0 + e^- \quad (4.3\ (b))$$

$$3p^62a_1^21e^32t_2^63t_2^61t_1^62e^04t_2^0 + e^-$$

$$3p^62a_1^11e^42t_2^63t_2^61t_1^62e^04t_2^0 + e^-$$

Inter-channel coupling between the final states reached in equations (4.3 (a)) and (4.3 (b)) and those produced by direct photoionisation

$$3p^62a_1^21e^42t_2^63t_2^61t_1^52e^04t_2^0 + e^-$$

$$3p^62a_1^21e^42t_2^63t_2^51t_1^62e^04t_2^0 + e^-$$

$$3p^62a_1^21e^42t_2^63t_2^61t_1^62e^04t_2^0 + h\nu \rightarrow 3p^62a_1^21e^42t_2^53t_2^61t_1^62e^04t_2^0 + e^-$$

$$3p^62a_1^21e^32t_2^63t_2^61t_1^62e^04t_2^0 + e^-$$

$$3p^62a_1^11e^42t_2^63t_2^61t_1^62e^04t_2^0 + e^-$$

should lead to two overlapping Fano profiles, resulting from absorption to the two $^1T_2$ excited states, for the RPPICS of any band corresponding to ionisation from MOs with appreciable metal d orbital character.

A Fano resonance profile with a sloping background cross section was fitted to the experimentally determined RPPICS of band (C+D) using equation (1.9). The values of the Fano parameters obtained are given in Table 4.7. A satisfactory fit was obtained only when two profiles were used; attempts to fit one profile resulted in a significant deterioration in the quality of the fit. This may well reflect the presence of two T_2 states accessible in the intermediate, one from absorption to the 2e MO and one to the $4t_2$.

Table 4.7 : Fano parameters obtained from the RPPICS of band (C+D) in the PE spectrum of $TiCl_4$

q	E_r (eV)	σ_0	Γ	X	hν range (eV)
1.73	40.4	35256	9.87	0.020	38 - 69
	47.8		14.07		

The $2a_1$ MO can have no metal d orbital contribution by symmetry, and Hillier and Kendrick have calculated the 1e MO to have 16% titanium 3d AO character and the $2t_2$ 25% [42]. Hence any p→d resonant enhancement in the cross section of the $2a^{-1}$ ionisation must arise through inter-channel coupling (as for the $1t_1^{-1}$ ionisation of OsO_4) and is therefore expected to be much weaker than that in the $1e^{-1}$ and $2t_2^{-1}$ bands.

The cross section behaviour of band E is different from that of any of the other bands, with more features superimposed upon the general fall off. A sharp maximum at 20 eV is followed by another at 25 eV, and the cross section reaches a minimum at 38 eV before undergoing a broad gentle enhancement with a somewhat sharper maximum at 40 eV. The recovery of the cross section after the minimum at 38 eV is more reminiscent of bands A and B than (C+D).

The overall RPPICS profile of band E strongly suggests its assignment to the $2a_1$ MO. The alternative assignment - to the $2t_2$ - would appear to be ruled out by the lack of substantial enhancement in the p→d resonance region. Furthermore, the feature at 25 eV photon energy may well reflect the maximum in the cross section of the 4s AO of titanium, which is calculated to occur at a PE KE of ca. 15 eV [20] and is found here at 11 eV. (The most likely cause of this maximum is as the recovery of the cross section following a below-threshold Cooper minimum; one of the three possible Cooper minima of a 4s AO). This suggestion is favoured by Wetzel in his synchrotron study, which finds cross section behaviour for bands (C+D) and E similar to that presented in Figures 4.7 and 4.8. The $2t_2$ MO can have no titanium 4s character and one would therefore have to invoke a shape resonance to explain the feature, if this were the assignment.

The $1t_1$ MO is chlorine 3p-based and contains six electrons. Figure 4.9 presents the renormalised BRs of bands A and (C+D). If (C+D) arises from the 1e and $2t_2$ MOs, there should be ten electrons ionising under this band, which would produce a 10 : 6 (0.625 : 0.375) intensity ratio of band (C+D) to band A if all the MOs had similar localisation properties. Over the p→d resonance, the BRs diverge significantly, but outside of this region the relative areas are very close to the predicted value. A similar plot for band A vs band E (Figure 4.10) shows more variable behaviour, which is not surprising given the RPPICS features of band E. Nevertheless it is very difficult to reconcile Figure 4.10 with there being six electrons under both band A and E, as the relative intensity of band A is significantly greater than that of band E over the majority of the photon energy range employed.

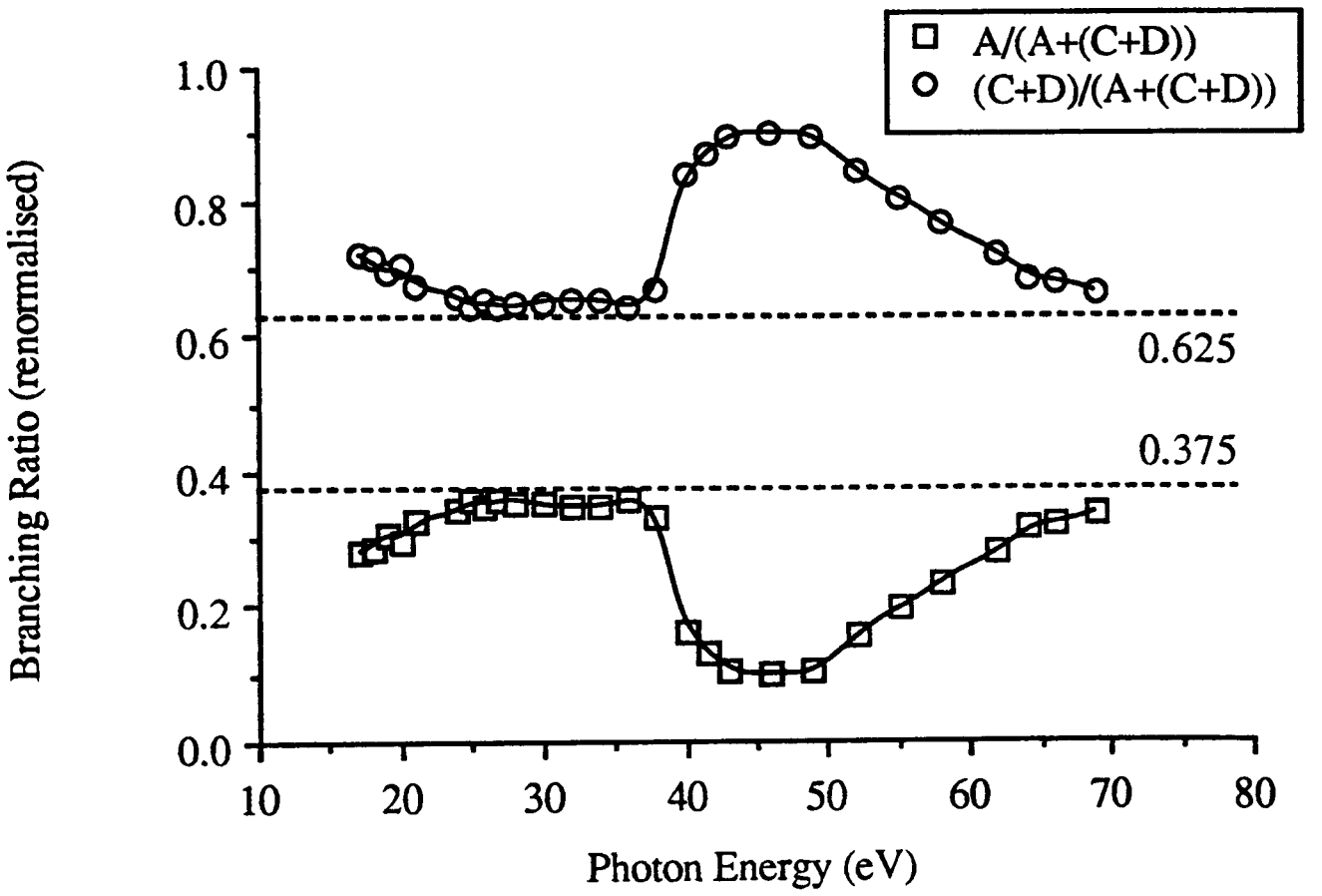

Figure 4.9 : renormalised BRs of bands A and (C+D) in the PE spectrum of $TiCl_4$

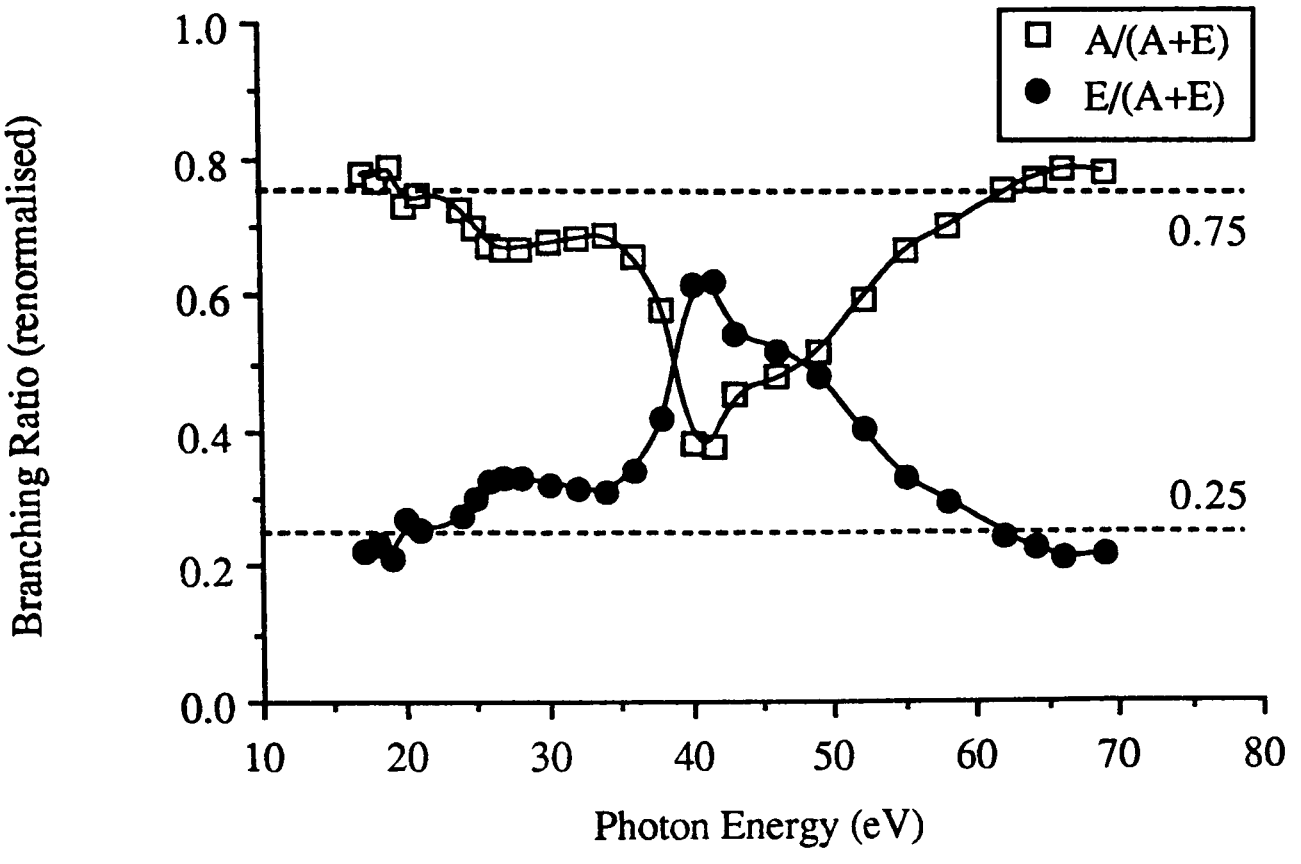

Figure 4.10 : renormalised BRs of bands A and E in the PE spectrum of $TiCl_4$

Taken together, the p→d giant resonant enhancement of band (C+D) but not E, the relative areas of the two bands with respect to band A and the possible titanium 4s AO-derived maximum in band E leave little doubt that the assignment of Bancroft et al. [10] is incorrect. Indeed one of the main pieces of evidence that they cite is the relative intensity increase of band E as the ionising radiation is changed from He I to He II. Figure 4.8 clearly shows this enhancement to arise not from the wider p→d resonance, but from a sharper feature coinicident with He II photon energy. This maximum in band E was also found by Wetzel, and was attributed to a shape resonance, providing another elegant illustration of the potential pitfalls of He II/He I intensity changes. It is likely that the feature at 20 eV in band E is also due to a shape effect, and it therefore appears that there are two shape resonances - at 20 and 40 eV photon energy - in bands B and E, both of which are stronger in the $2a_1^{-1}$ ionisation.

A shape resonance was suggested as a possible explanation of the sharp maximum in the RPPICS of the $2a_1^{-1}$ ionisation of OsO_4 at 50 eV (Figure 4.4) The RPPICS of band

E of $TiCl_4$ looks rather different from the equivalent band in OsO_4, in that the almost constant cross section between 24 - 45 eV in OsO_4 is replaced with a steep fall off in $TiCl_4$. This is readily explained in terms of the cross section of the AO contributors to the two $2a_1$ MOs. The oxygen 2p AO has no radial node and therefore no Cooper minimum in its cross section, in contrast to the 3p AO of chlorine. Following the different low photon energy RPPICS behaviour, both ionisations reveal a cross section maximum, which occurs 10 eV lower in incident photon energy in $TiCl_4$. If the origin of this feature in both molecules is as a shape resonance, it may well be characteristic of a_1^{-1} ionisations, the difference in position presumably being due to the difference in the molecular potential fields generated by tetrahalides and tetroxides. It should be noted, however, that no similar feature was seen in the equivalent ionisation of CCl_4 [11], and the quality of the data prevented the dip in the value of β for the $7a_1^{-1}$ band of $SiCl_4$ at 60 eV being assigned to a shape effect with any confidence [13].

The experimental data presented here strongly favour the assignment

Band	A	B	(C+D)	E
State	$^2T_1$	$^2T_2$	^2E, $^2T_2$	$^2A_1$

The only significant p→d resonance feature occurs in band (C+D), and the relative intensity increase of band E in the He II spectrum has been shown to arise from a shape resonance coincident with the energy of He II photons.

A comparison of the assignments of the spectra of OsO_4 and $TiCl_4$ reveals that in both molecules the ^2E and higher IE $^2T_2$ bands are very close together in binding energy. The $^2A_1$ ionisation inverts its position relative to the (^2E+$^2T_2$) band on moving from OsO_4 to $TiCl_4$, to the extent that it is the most stabilised of the valence ionisations in the tetrachloride.

4.4 Titanium tetrabromide and zirconium tetrabromide

The tetrabromides of titanium and zirconium have received much less attention than OsO_4 and $TiCl_4$. The He I and He II PE spectra of both molecules have been measured [5, 8, 9] and an INDO-MO calculation of $TiBr_4$ has been performed [36], but there is no debate in the literature comparable with that on OsO_4 and $TiCl_4$. Nevertheless it was decided to undertake a variable photon energy PES study of these tetrabromides in order to investigate the previous assignments in more detail and to provide a comparison with $TiCl_4$.

4.4.1 Bonding and interpretation of the photoelectron spectra

The valence electronic structures of $TiBr_4$ and $ZrBr_4$ are as for $TiCl_4$, i.e.

$$1a_1^2 1t_2^6 2a_1^2 2t_2^6 1e^4 3t_2^6 1t_1^6$$

with only the top five MOs featuring in the IE region measured in this investigation. The PE spectra of these molecules are given in Figure 4.11, from which it can be seen that the tetrabromide spectra are significantly more complicated than that of $TiCl_4$. This increased complexity is due mainly to the effects of bromine-centred spin-orbit coupling [5, 9].

Halogen-derived spin-orbit coupling in MX_4^+ ions has been discussed before [5, 8, 9], in which it is found that $^2T_2$ and $^2T_1$ terms are split to give U' (four-fold degenerate) and E' or E" (two-fold degenerate) states in the T_d^* double group (c.f. Sections 4.2.2 and 4.2.3). To a first order the splittings are given by $(3/2)\zeta_t$, where ζ_t is the spin-orbit coupling constant for the particular t molecular subshell. Table 4.8 gives the energy ordering of the spin-orbit components of the ^2T states. In addition to the U' and E" ordering being opposite for $t_2(\pi)$ and $t_2(\sigma)$ subshells, the splitting in $t_2(\pi)$ levels is predicted to be about twice that in $t_2(\sigma)$ [5, 8, 9], neglecting contributions from admixed $d(t_2)$ orbitals. It is important to stress, however, the absence of σ/π separability in the t_2 MOs, an issue which is of increased significance in the tetrabromides. In $TiCl_4$, the splitting of the $^2T_2$ ion states is approximately 0.5 eV. The $2t_2$ MOs have been shown to possess significant metal d orbital character, while the $3t_2$ MOs are essentially chlorine-localised. In as much as it is a valid approach, the $2t_2$ MOs may be regarded as the metal-ligand σ

bonding levels in $TiCl_4$, with the $3t_2$ being of greater π character. In $TiBr_4$ and $ZrBr_4$, however, the magnitude of the spin-orbit perturbation of the t_2 levels is comparable with any σ/π splitting, with the consequence that any real justification in retaining σ/π notation for the t_2 levels is lost. For this reason no distinction is made in the σ/π nature of the bands arising from ionisation of the $2t_2$ and $3t_2$ MOs of the tetrabromides.

Table 4.8 : energy ordering of spin-orbit multiplets of ^2T states in MX_4^+ ions arising from halogen-derived spin-orbit coupling [5, 8, 9]

molecular t subshell	multiplet splitting
t_1 (π)	U' < E'
t_2 (π)	U' < E''
t_2 (σ)	E'' < U'

The E and A states of the T_d point group are not split on moving to T_d^* symmetry, and transform as U' and E' respectively in the double group. This opens up the possibility of mixing between states derived from different parent MOs in T_d symmetry, through the mechanism of spin-orbit coupling (e.g. U' states in T_d^* can arise from T_2, T_1 and E states in T_d symmetry).

Table 4.9 provides IE data and band assignments for $TiBr_4$, while those for $ZrBr_4$ are given in Table 4.10. The assignments are the same as those given by Egdell (which are based on an extensive comparison of the He I and He II spectra of the complete MX_4 series, M=Ti, Zr, Hf; X= Cl, Br, I [5, 9]) and the RPPICS data supporting them are discussed below. A diagram showing the potential splitting of the five primary ion states under the influence of spin-orbit coupling is given in Figure 4.12. The band labels correspond to the PE spectrum of $TiBr_4$. $ZrBr_4$ is similar except that the region described by bands D and E in $TiBr_4$ is further split into three bands via a Jahn-Teller mechanism. This is discussed more fully later (page 160).

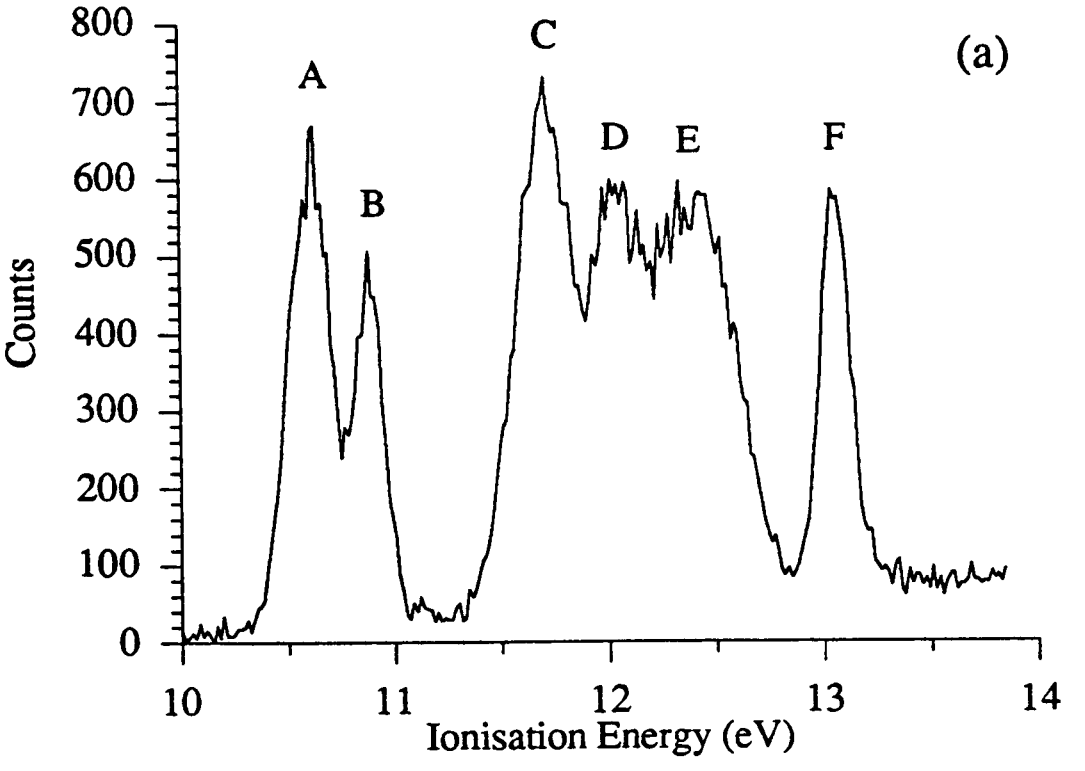

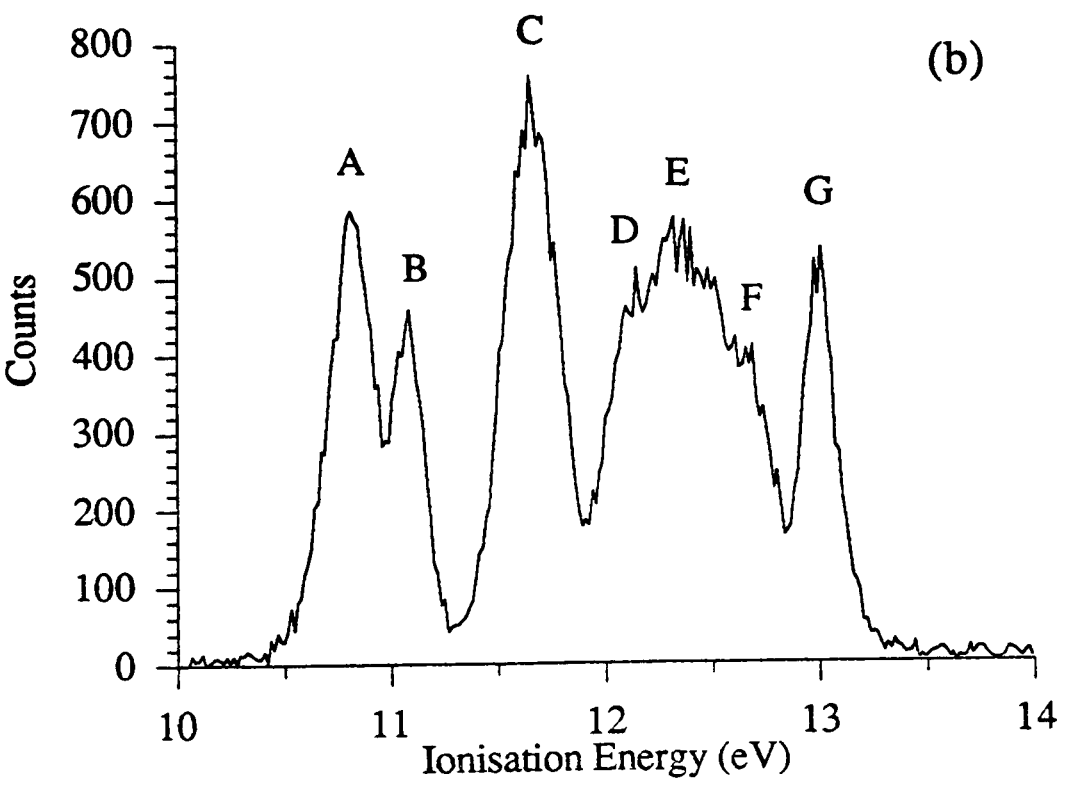

Figure 4.11 : the PE spectra of (a) $TiBr_4$ (acquired at 30 eV) and (b) $ZrBr_4$ (26 eV)

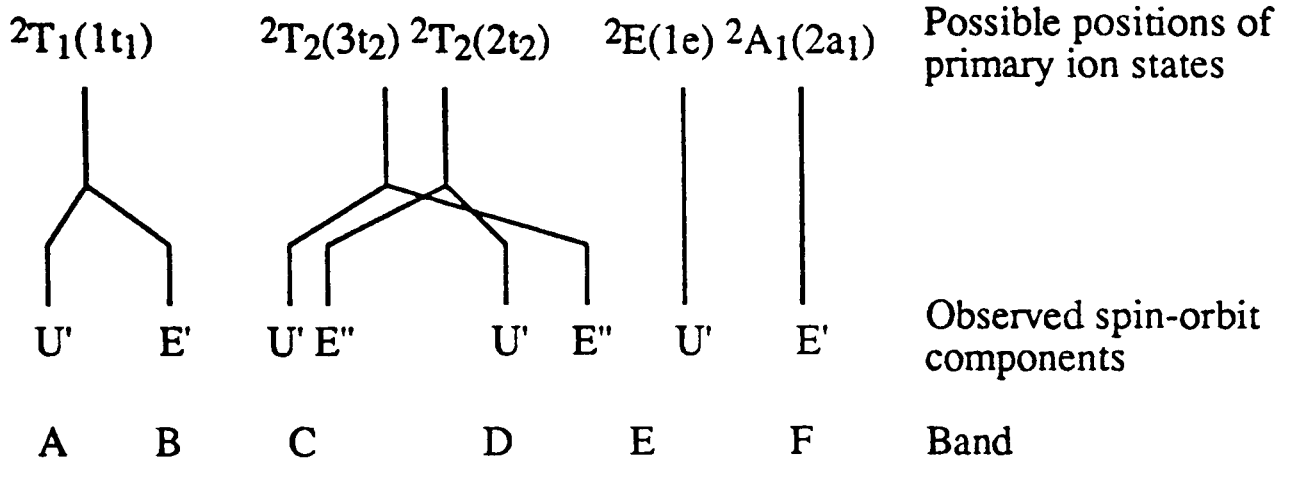

Figure 4.12 : the relationship of the PE bands to the spin-orbit components of the primary ion states of $TiBr_4$

Table 4.9 : IEs and band assignments of the PE spectrum of $TiBr_4$

Band	IE (eV) [a]	Assignment [b]
A	10.60	U' ($1t_1(\pi)$)
B	10.86	E' ($1t_1(\pi)$)
C	11.68	U' ($3t_2$), E" ($2t_2$)
D	12.00	U' ($2t_2$)
E	12.31, 12.42	E" ($3t_2$), U' ($1e(\pi)$)
F	13.04	E' ($2a_1(\sigma)$)

[a] IE data from reference [5] [b] assignments given in terms of the symmetry of the final state and the parent MO

Table 4.10 : IEs and band assignments of the PE spectrum of $ZrBr_4$

Band	IE (eV) [a]	Assignment [b]
A	10.86	U' ($1t_1(\pi)$)
B	11.09	E' ($1t_1(\pi)$)
C	11.64	U' ($3t_2$), E" ($2t_2$)
D	12.08	U' ($2t_2$) [c]
E	12.34, 12.51	E" ($3t_2$), U' ($1e(\pi)$) [c], U' ($2t_2$) [c]
F	12.71	U' ($1e(\pi)$) [c]
G	12.99	E' ($2a_1(\sigma)$)

[a] IE data from reference [5] [b] assignments given in terms of the symmetry of the final state and the parent MO [c] U' states split by Jahn-Teller distortion (page 160)

4.4.2 RPPICS results and discussion

The valence PE spectra of $TiBr_4$ and $ZrBr_4$ have been measured over the incident photon energy ranges 20-60 and 20-80 eV respectively, and RPPICS have been determined for 6 ($TiBr_4$) and 7 ($ZrBr_4$) bands.

4.4.2 (a) $TiBr_4$

Figure 4.13 gives the RPPICS of bands A-F of $TiBr_4$, while Figure 4.14 presents them individually for clarity.

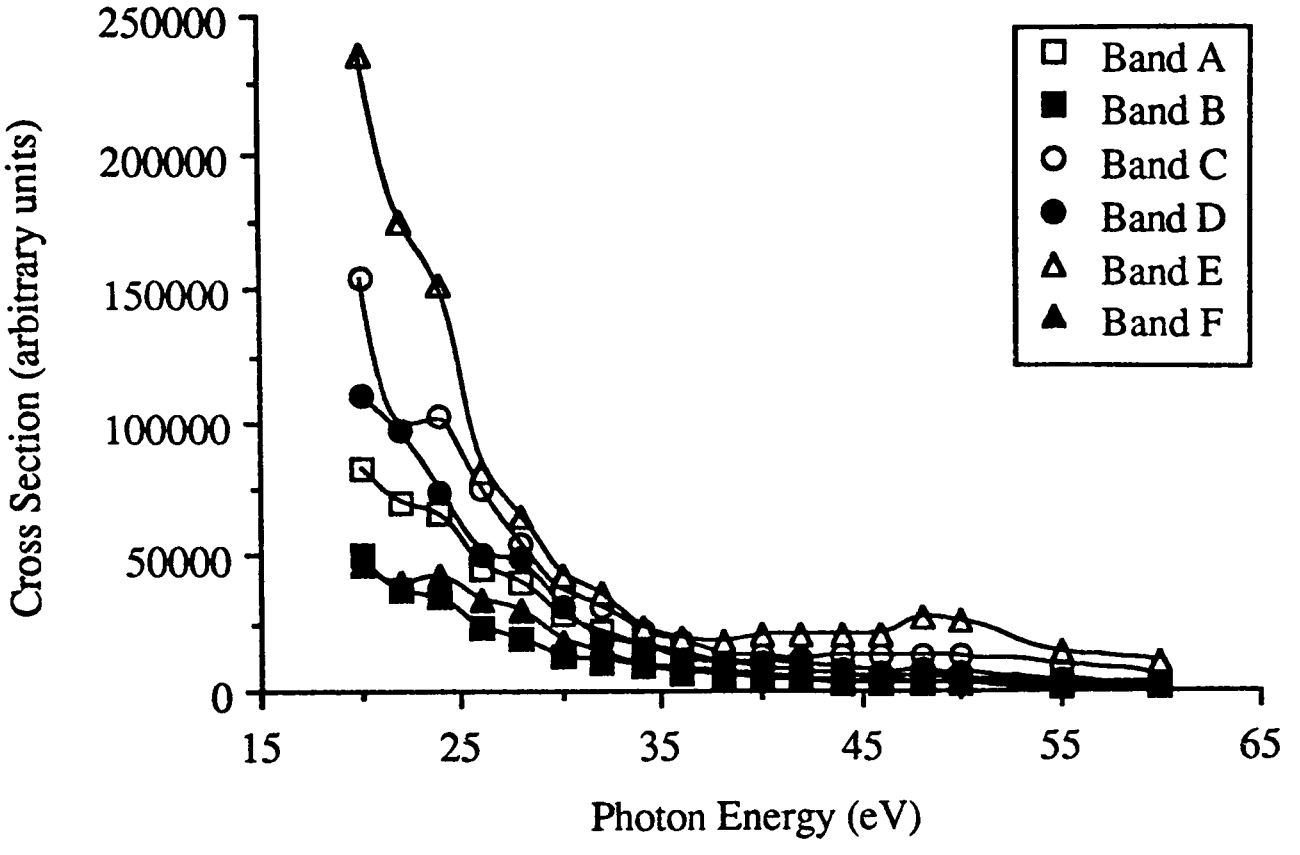

Figure 4.13 : RPPICS of bands A-F in the PE spectrum of $TiBr_4$

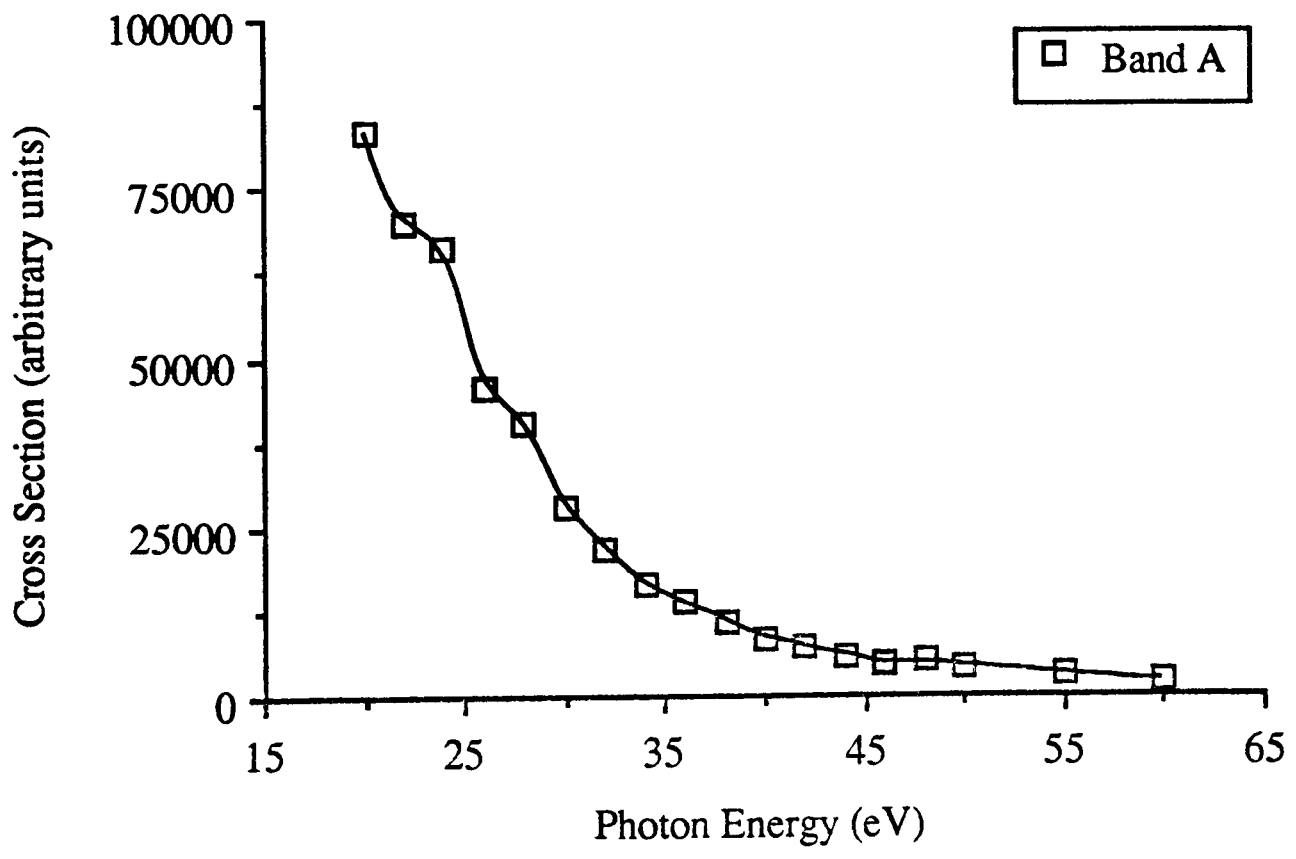

Figure 4.14 : individual RPPICS of bands A-F in the PE spectrum of $TiBr_4$

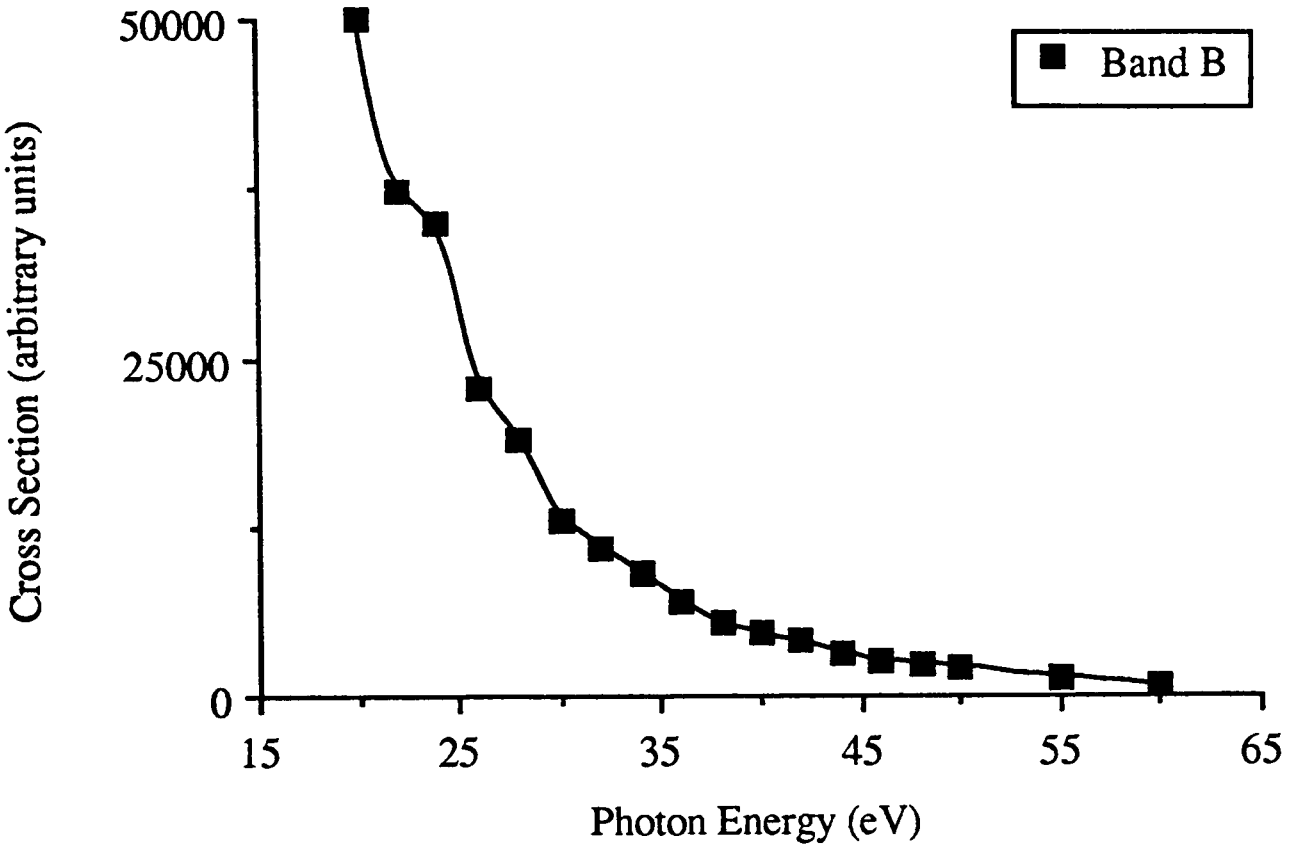

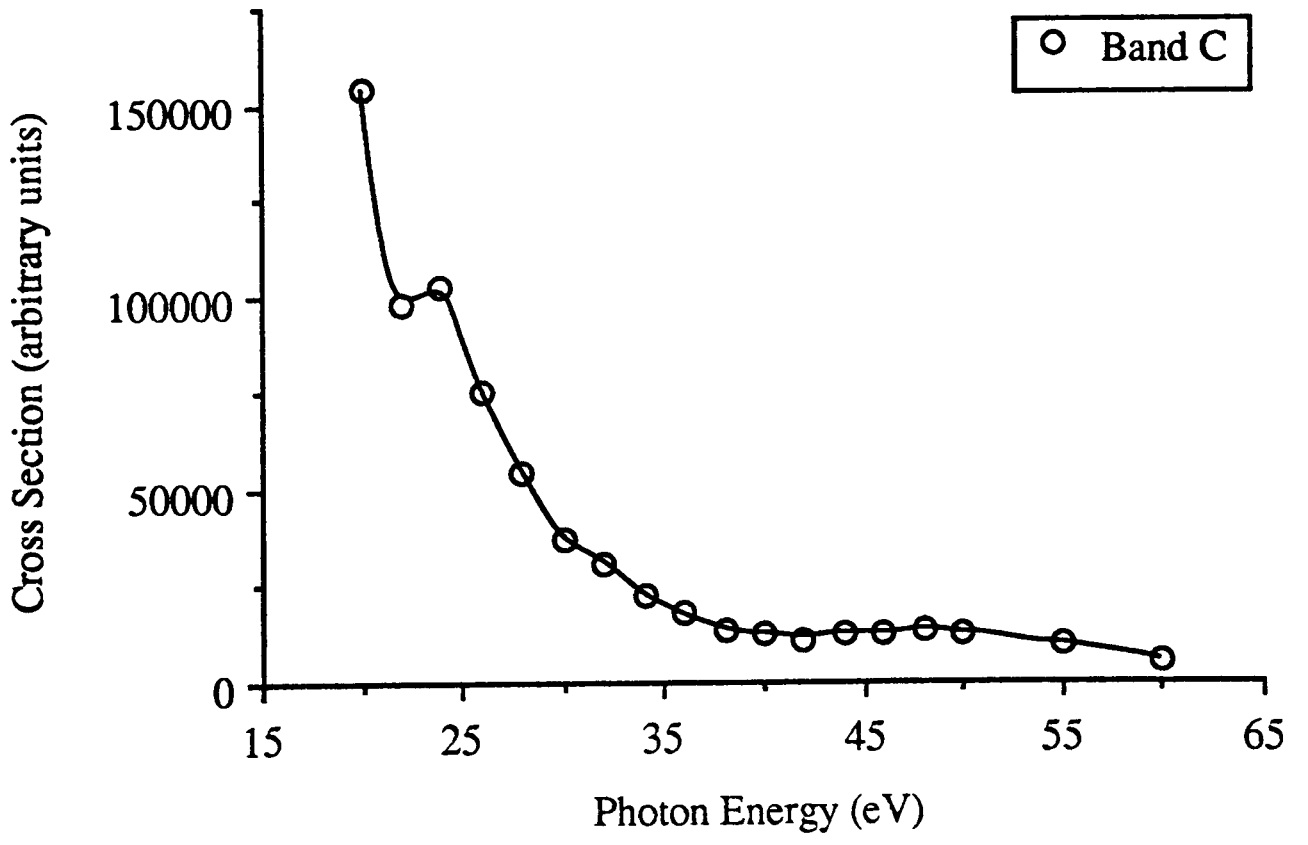

Figure 4.14 : individual RPPICS of bands A-F in the PE spectrum of $TiBr_4$ (continued)

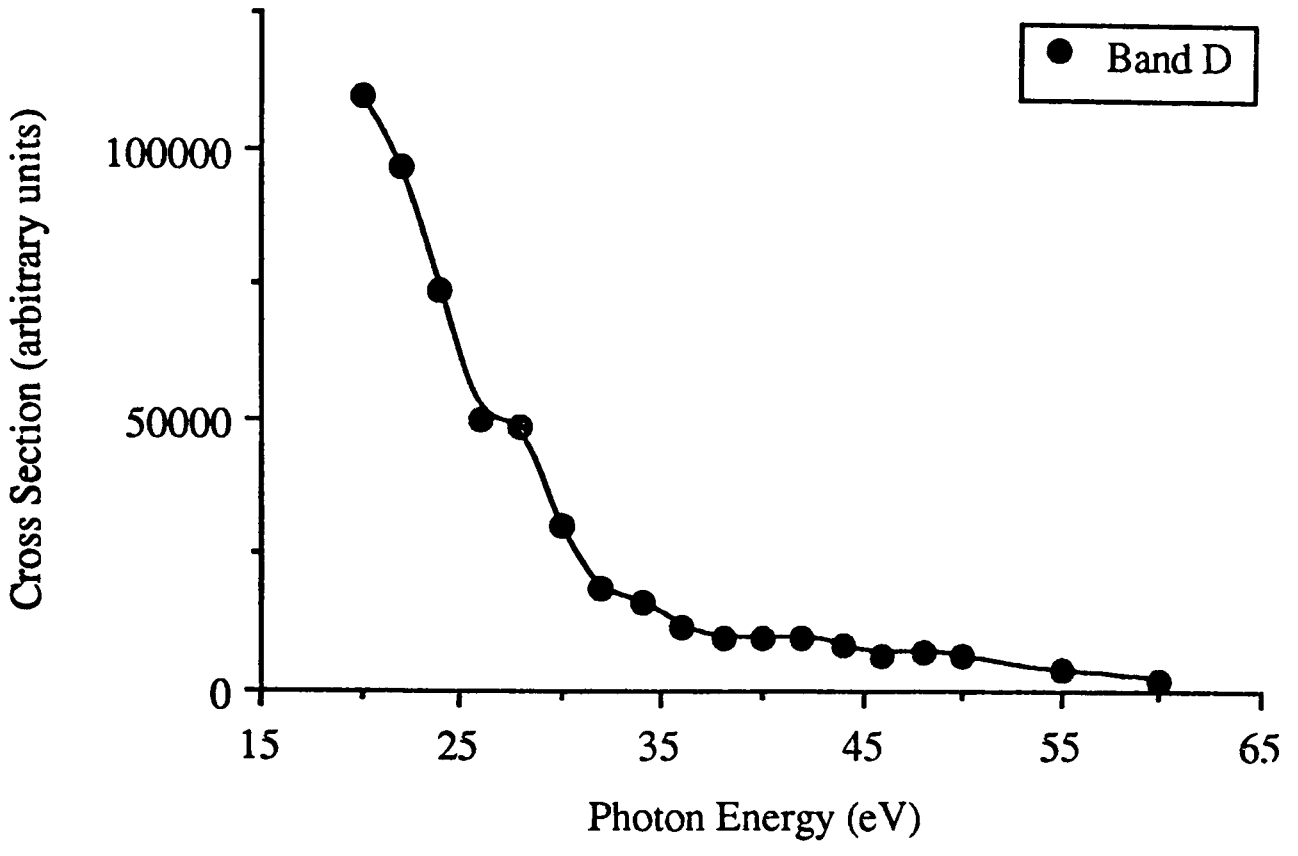

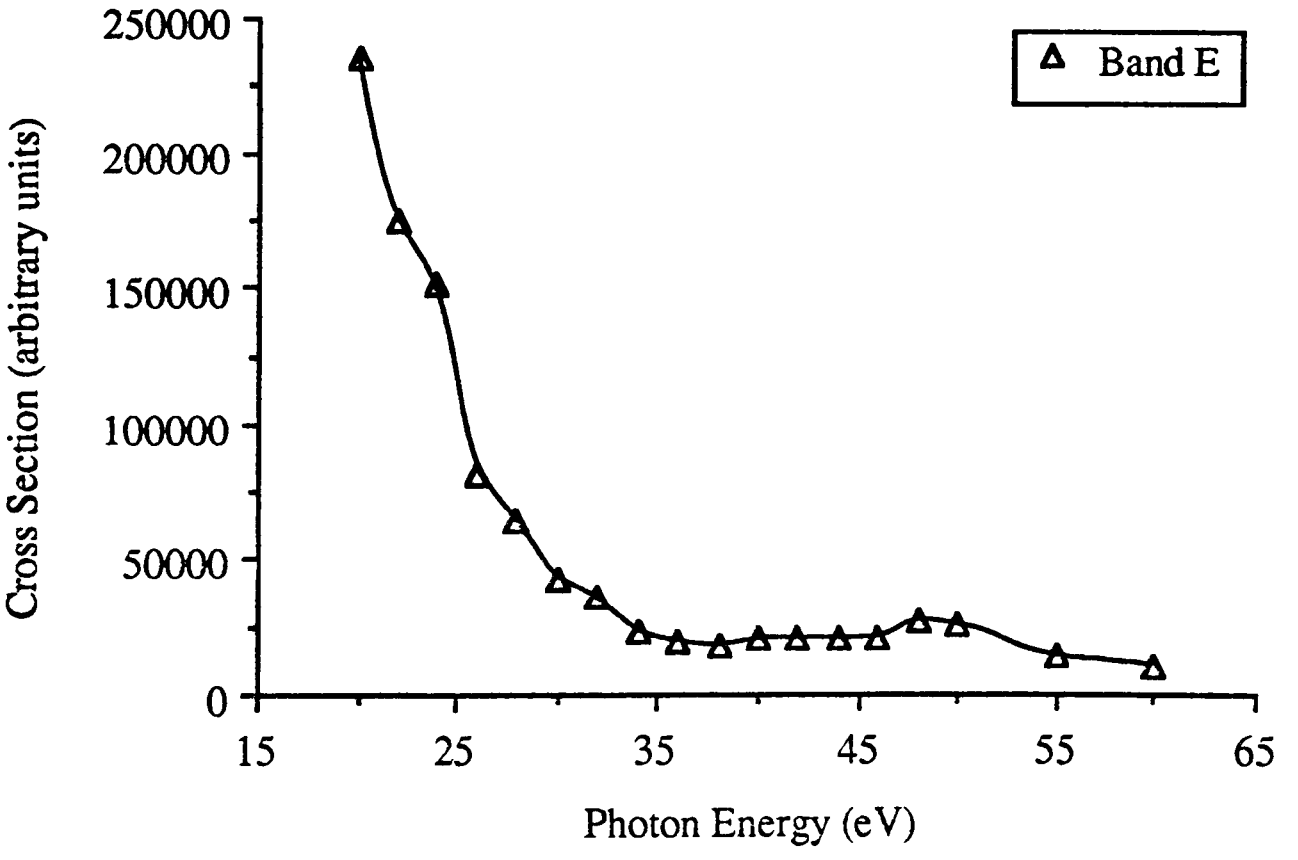

Figure 4.14 : individual RPPICS of bands A-F in the PE spectrum of $TiBr_4$ (continued)

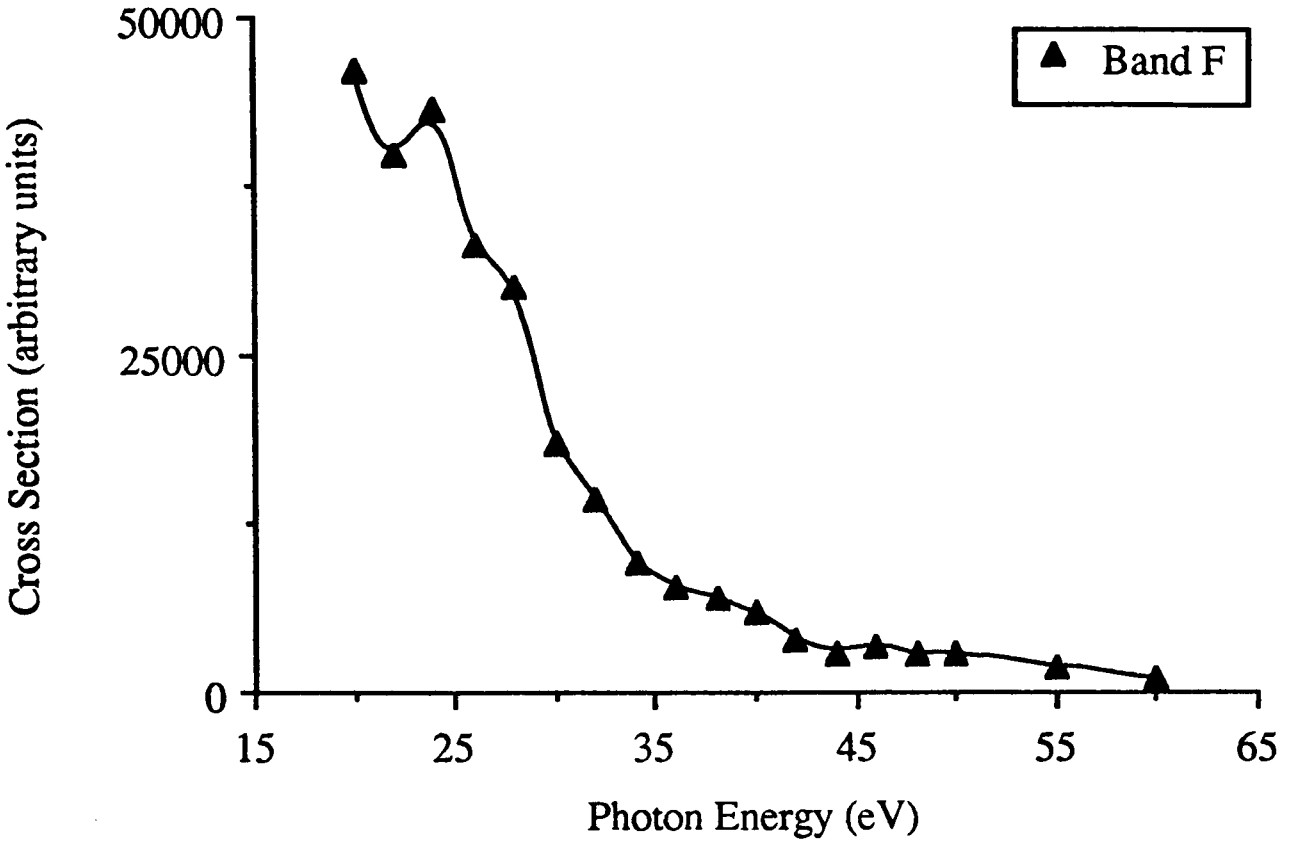

Figure 4.14 : individual RPPICS of bands A-F in the PE spectrum of $TiBr_4$ (continued)

The cross sections of all of the valence bands of $TiBr_4$ are rather featureless in comparison with those of the tetrachloride. Bands A and B have essentially monotonic fall offs in cross section, interrupted by a slight shoulder at 24 eV photon energy and a small levelling off between 40-50 eV. The assignment of bands A and B is to the spin-orbit split components of the $^2T_1$ primary ion state. Hence both bands are expected to show cross section behaviour which is essentially bromine 4p AO in character.‡ Yeh and Lindau calculate that there is no distinct Cooper minimum in the cross section of the 4p AO of bromine, unlike the 3p AO of chlorine [20]. Instead a reduction in the rate of cross section fall off is predicted at ca. 50 eV photon energy. This correlates well with the observed behaviour of the U' and E' components of the $^2T_1$ primary ion state. As the AO nature of the electrons ionising under bands A and B is the same, the renormalised BRs of A vs B

‡ This treatment assumes that no significant metal d orbital character is introduced into the U' MO via spin-orbit coupling. The E' MO can have no metal d contribution by symmetry.

should be in 2 : 1 ratio over all of the incident photon energy range employed. Figure 4.15 reveals this to be the case, further supporting the initial assignment.

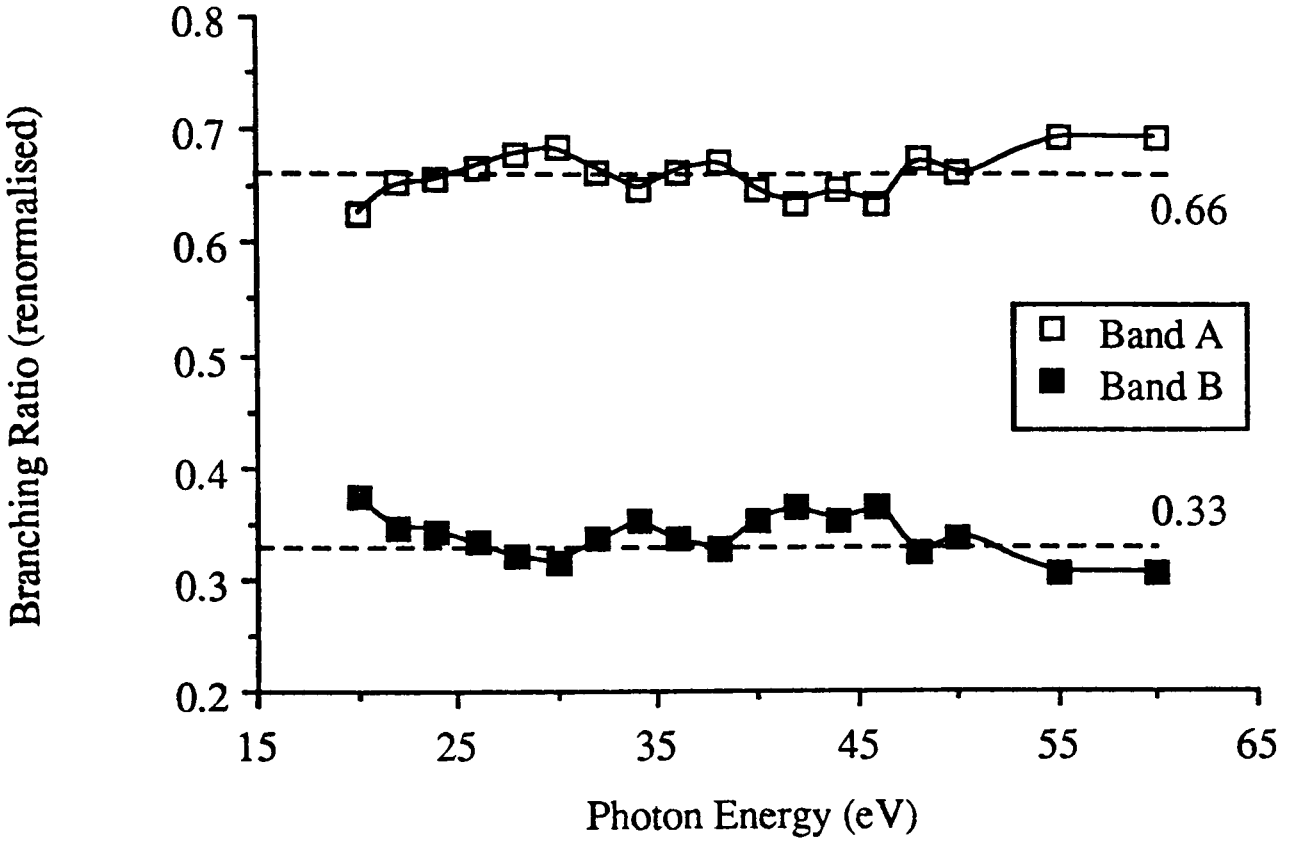

Figure 4.15 : renormalised BRs of bands A and B in the PE spectrum of $TiBr_4$

The cross section behaviour of band F is in some ways similar to that of band E in the PE spectrum of $TiCl_4$. The fall off from 20-22 eV is interrupted by a sharp maximum at 24 eV, before continuing to 36 eV. There is a subsequent reduction in the rate of fall off and another very small maximum at 46 eV. The sharp maximum in the $2a_1^{-1}$ ionisation of $TiCl_4$ at 25 eV was attributed to a maximum in the titanium 4s AO cross section (page 136), and was found to occur at a PE KE of 11 eV compared with the calculated value of 15 eV. If this is indeed the cause of the corresponding maximum of band F of $TiBr_4$, then it also occurs at a PE KE of 11 eV, consistent with an effect derived from an AO on the metal atom. Figure 4.16 presents the renormalised BRs of bands (A+B) (which between them contain six electrons) and band F, from which it can be seen that the relative areas are

slightly different from the expected 3 : 1 statistical ratio. There can be little doubt, however, that band F is the $2a_1^{-1}$ band, supporting further the assignment presented for $TiCl_4$.

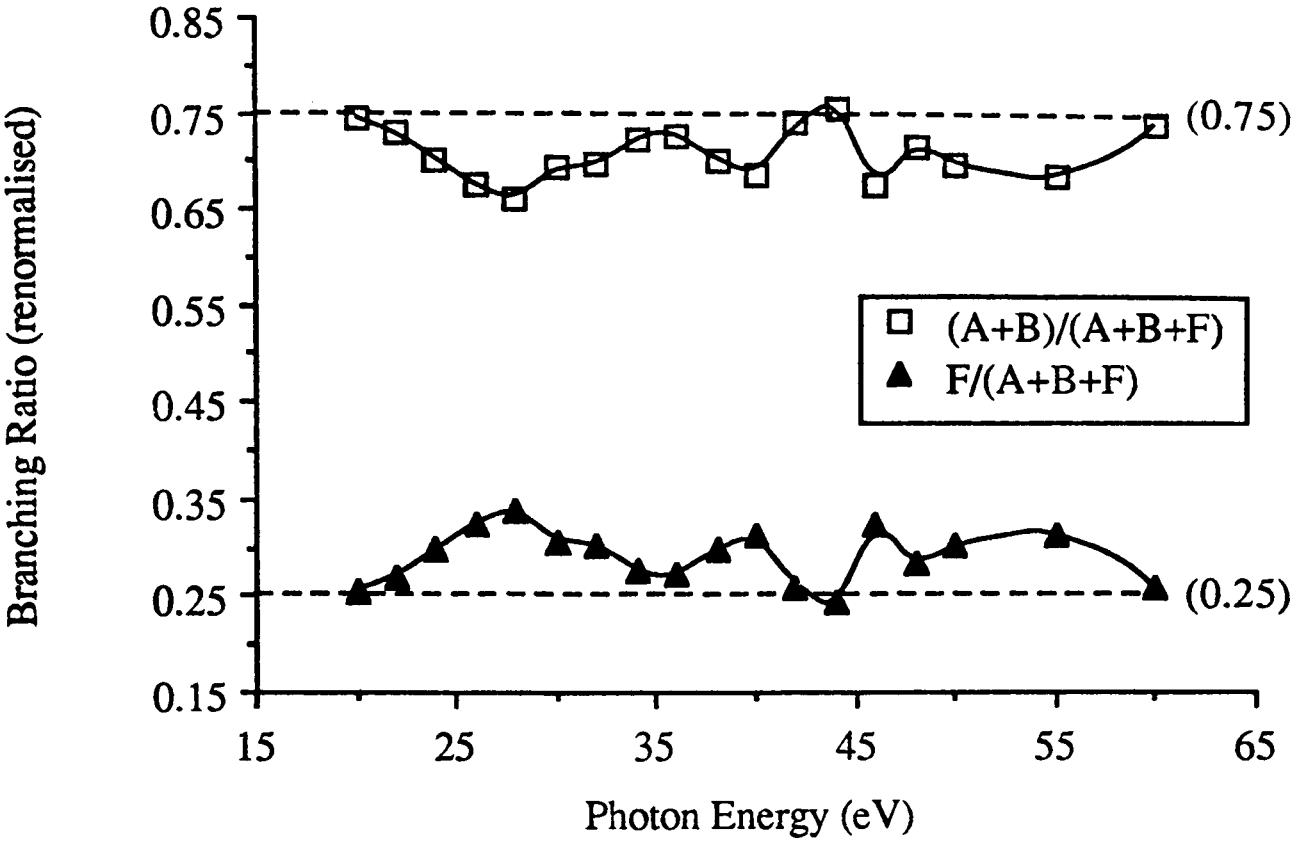

Figure 4.16 : renormalised BRs of bands (A+B) and F in the PE spectrum of $TiBr_4$

The major difference between the cross section variation of the two $2a_1^{-1}$ ionisation bands lies in their behaviour in the region of He II photon energy. Band E in the PE spectrum of $TiCl_4$ undergoes a significant enhancement between 38-44 eV photon energy, whereas band F of $TiBr_4$ has only a small reduction in the rate of cross section fall off. This is reflected in the relative intensities of the bands in the He II spectra of the two tetrahalides [6, 9]. It would thus appear that the shape resonance believed to give rise to this enhancement is more muted in the tetrabromide than the tetrachloride.

The assignment of bands A and B to the $^2T_1$ primary ion state and band F to the $^2A_1$ requires that bands C, D and E be assigned to the $^2T_2$, ^2E and $^2T_2$ primary ion states arising from the $3t_2$, 1e and $2t_2$ MOs respectively. The $^2T_2$ states may of course be split by spin-orbit coupling. The most notable feature of the RPPICS of bands C, D and E is the

lack of any significant enhancement in the incident photon energy region of the titanium 3p→3d giant resonance. It was noted by Egdell that He I/He II intensity changes are less dramatic for $TiBr_4$ than $TiCl_4$ [6, 9], a point which is bourne out by the data presented in Figures 4.13 and 4.14. Firm conclusions, however, cannot be drawn as to the relative amounts of metal d orbital character to these MOs in $TiBr_4$ and $TiCl_4$. The RPPICS behaviour of the metal-localised ionisations of $[M(\eta\text{-}C_5H_5)_2]$ (M=Fe, Ru, Os) [21, 44] over the incident photon energy range of the metal np subshell binding energies is somewhat subdued in the iron and osmium cases, whereas the ruthenium cross section undergoes a substantial increase. It may well be that the direct ionisation channel dominates the resonant pathway to a greater degree in the bromide than in $TiCl_4$.

Of the three bands, band E undergoes the greatest RPPICS enhancement in the region 40-55 eV. While this behaviour is no more pronounced than that of, say, band A ($^2T_1$) of $TiCl_4$ passing through its Cooper minimum, the lack of such a minimum in the bromine 4p AO (and in bands A and B) suggests that the enhancement may be ascribed to a p→d resonance, albeit a small one. The p→d giant resonant absorption process for $TiBr_4$ is represented by the same equations as $TiCl_4$, detailed on pages 134-135, and the subsequent group theoretical treatment is also the same (as the process is essentially metal-localised, it unlikely that increased spin-orbit coupling on the halogen atoms will greatly affect this treatment). The RPPICS of any band with appreciable metal d character should undergo an enhancement which is described by two overlapping Fano profiles resulting from absorption to the two permitted $^1T_2$ excited states. However, none of the bands C-E fitted well to Fano profiles using either one or two functions.

It was noted by Egdell that the relative intensity of band C in the He I spectrum suggested its assignment to three Kramers doublet final states, i.e. that six electrons are giving rise to this band. Figure 4.17 shows that in the incident photon energy range 20-42 eV the relative areas of bands (A+B) and C are very similar to one another, indicating that the original suggestion is correct. From 44-60 eV band C gains in relative intensity, presumably due to a degree of titanium 3d AO character in the MOs giving rise to it.

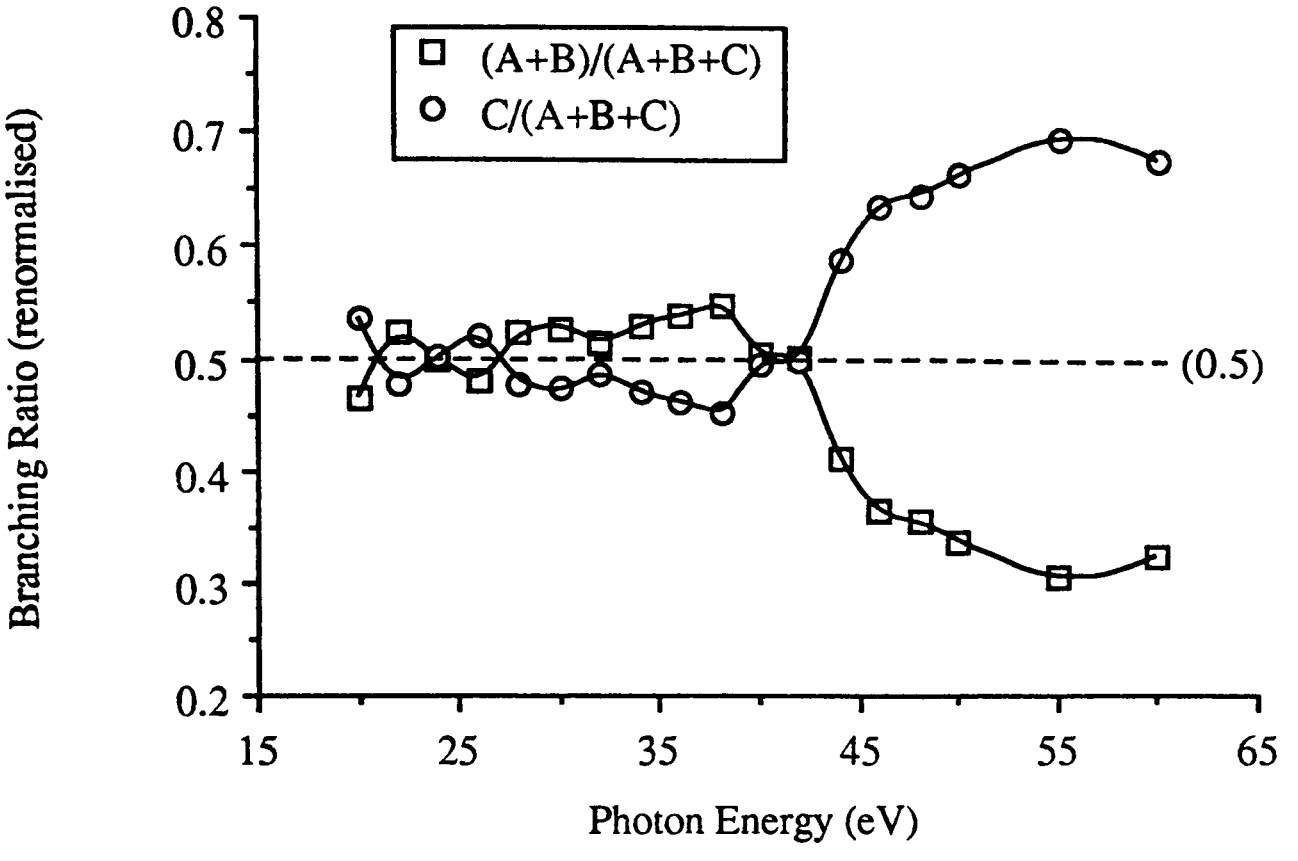

Figure 4.17 : renormalised BRs of bands (A+B) and C in the PE spectrum of $TiBr_4$

If the primary ion state ordering of $TiCl_4$ is preserved in $TiBr_4$, then band C must be due in part to electrons ionising from the $3t_2$ MO. The resulting $^2T_2$ primary ion state will split into U' and E" components. In order that the relative areas of bands (A+B) and C be equal, band C must also contain an E" ionisation. It is likely that the splitting of the U' and E" components of the $^2T_2(3t_2)$ state will be too great for them to ionise under a single PE band, and hence that band C contains the E" component of the $^2T_2(2t_2)$ primary ion state. Furthermore, band C has a distinct high IE shoulder to it in the He I spectrum [6], lending support to its origin as two separate ionisation processes.

If the assignment of band C is correct, bands D and E must contain two U' (from the $^2T_2(2t_2)$ and $^2E(1e)$ primary ion states) and the remaining E" ($^2T_2(3t_2)$) ionisations. Figure 4.18 presents the renormalised BRs of bands C, D and E, from which it can be seen that band E gains in relative intensity above an incident photon energy of 35 eV, mainly at the expense of band C. A comparison of relative areas is hampered by deterioration of spectral resolution above ca. 35 eV, and the resulting increased dependence of band areas

upon the curve fitting program. Nevertheless it is clear that band D is the least intense of all three bands over the entire photon energy range employed, suggesting that it arises from ionisations involving two Kramers doublets final states, with band E arising from ionisation of six electrons. The most logical assignment is therefore to place the U'($^2T_2(2t_2)$) MO under band D, leaving the E''($^2T_2(3t_2)$) and U'($^2E(1e)$) to band E. In $TiCl_4$, the ^2E and $^2T_2(2t_2)$ ionisations are virtually coincident in energy. If the proposed assignment of bands D and E of $TiBr_4$ is correct, the lifting of the degeneracy of the $^2T_2$ ion states through spin-orbit coupling has resulted in a separation of the formerly ^2E and $^2T_2$ ionisations, via mixing of the U' levels derived from them.

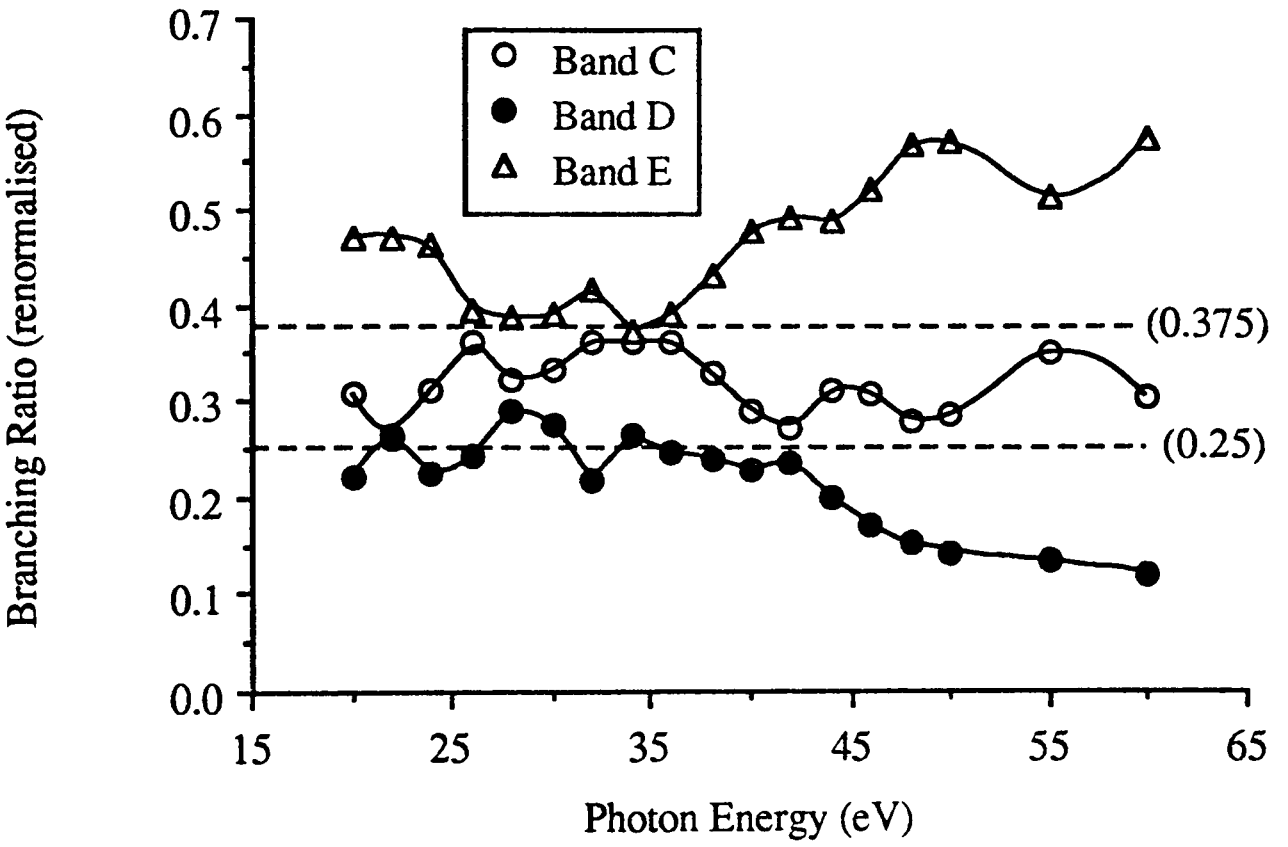

Figure 4.18 : renormalised BRs of bands C, D and E in the PE spectrum of $TiBr_4$

The sharp maximum in the RPPICS of band F at 24 eV, attributed to a maximum in the cross section of the 4s AO of titanium, is also present in band C and appears as a slight shoulder in bands A, B and E. The $2a_1$ MO transforms as E' in T_d^*, as does the higher IE component of the $1t_1$ MO (band B) (and also the 4s AO of titanium). Hence it is not

difficult to see how a cross section enhancement of band B could arise, but it is necessary to invoke inter-channel coupling (Chapter 1.4.3 (c)) to explain the effects in the other bands. The small RPPICS enhancement of band A of OsO_4 in the region of the osmium p→d resonance (page 126) was explained in a similar manner.

Band D has a shoulder at 28 eV photon energy which has no counterpart in the cross sections of any of the other bands. It is most likely that a shape resonance is the cause of this feature, as there are no atomic effects which readily explain it.

4.4.2 (b) $ZrBr_4$

Figure 4.19 presents the RPPICS of bands A-G in the PE spectrum of $ZrBr_4$, and these are plotted individually in Figure 4.20.

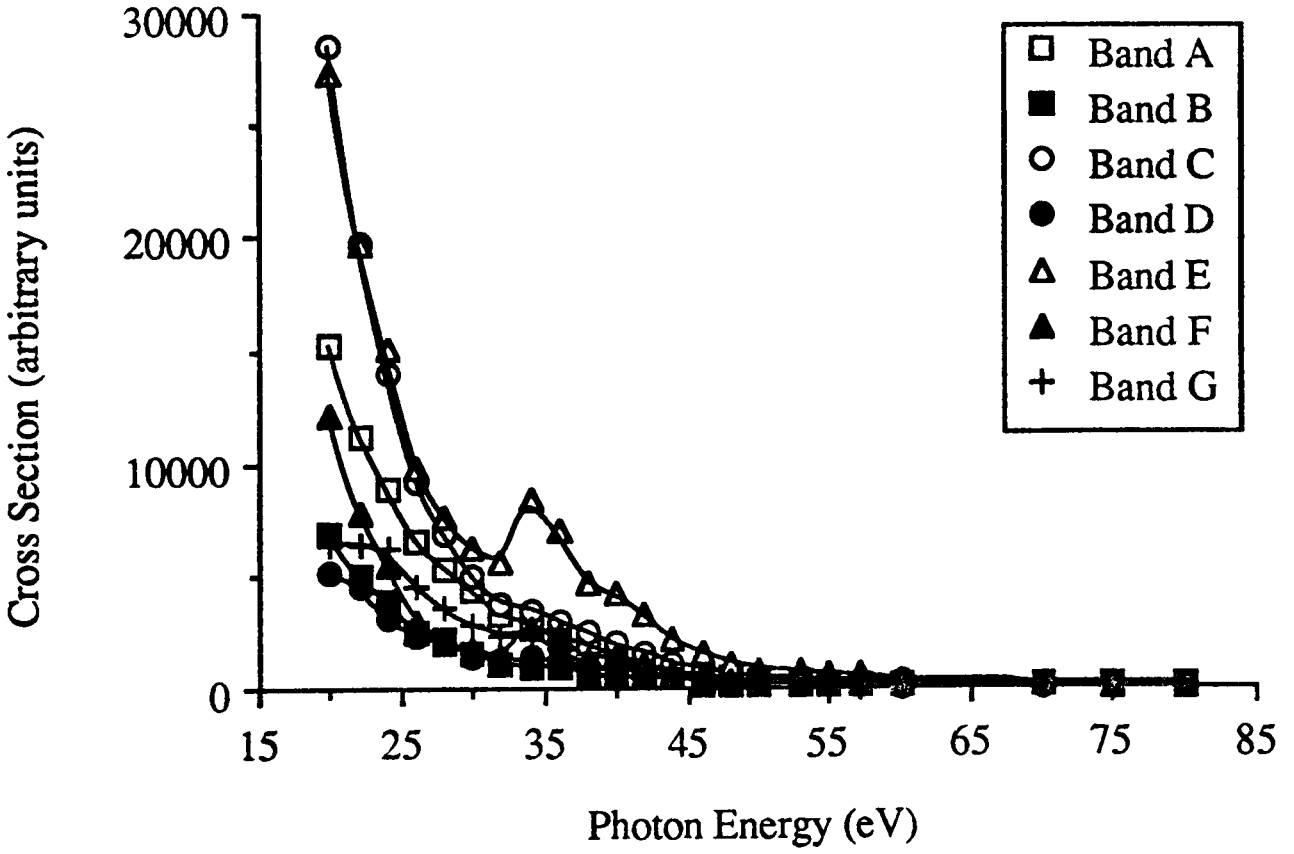

Figure 4.19 : RPPICS of bands A-G in the PE spectrum of $ZrBr_4$

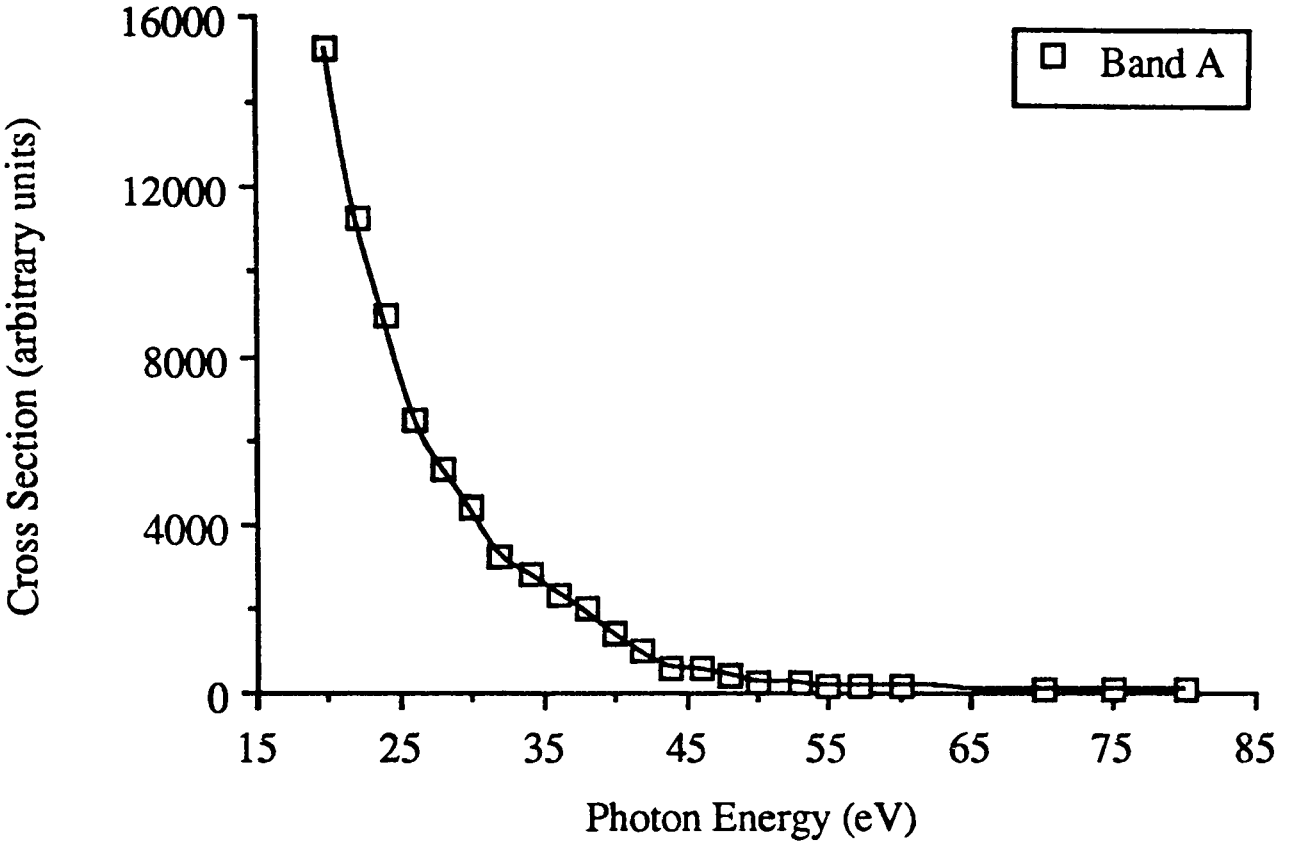

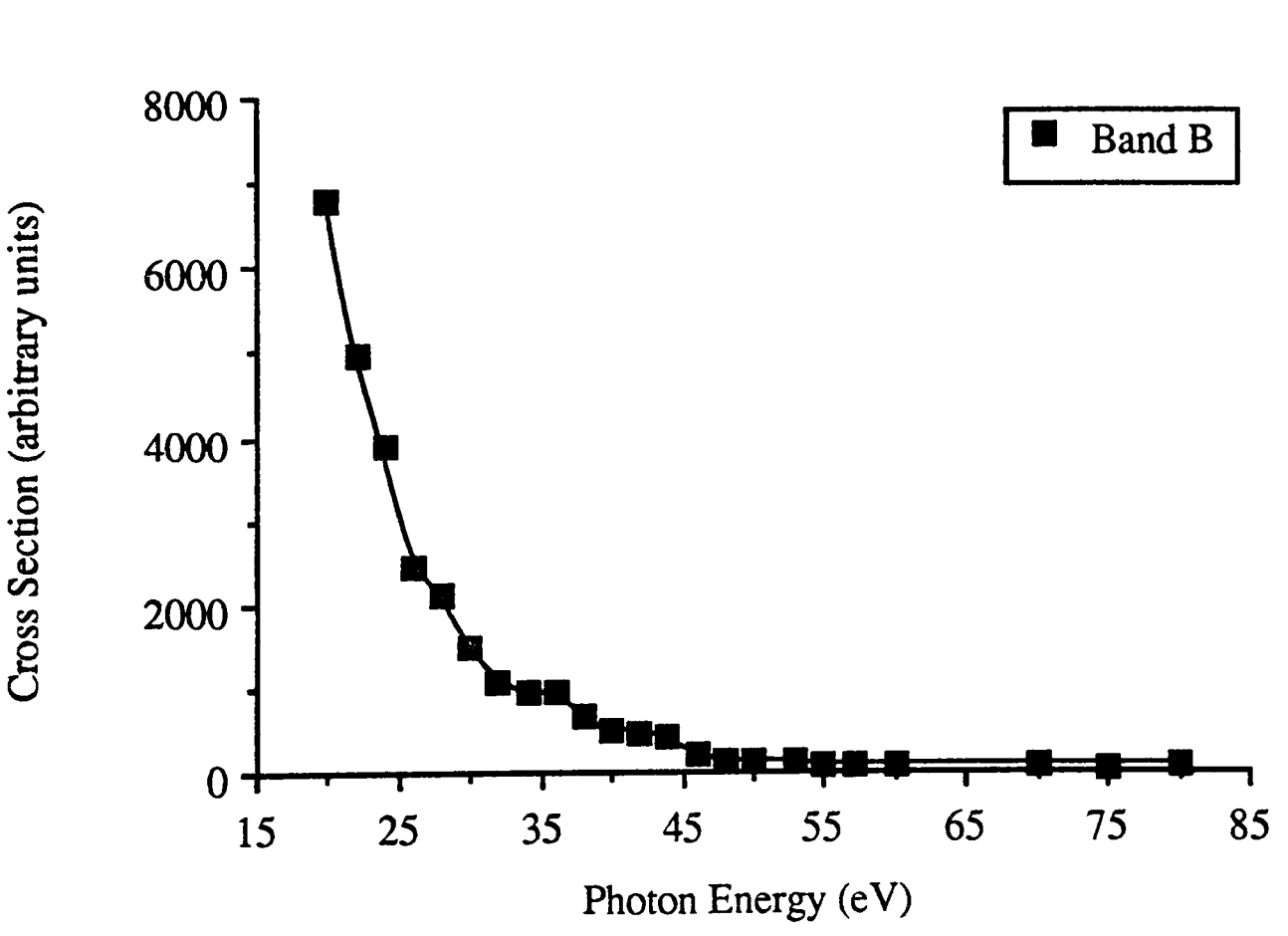

Figure 4.20 : individual RPPICS of bands A-G in the PE spectrum of $ZrBr_4$

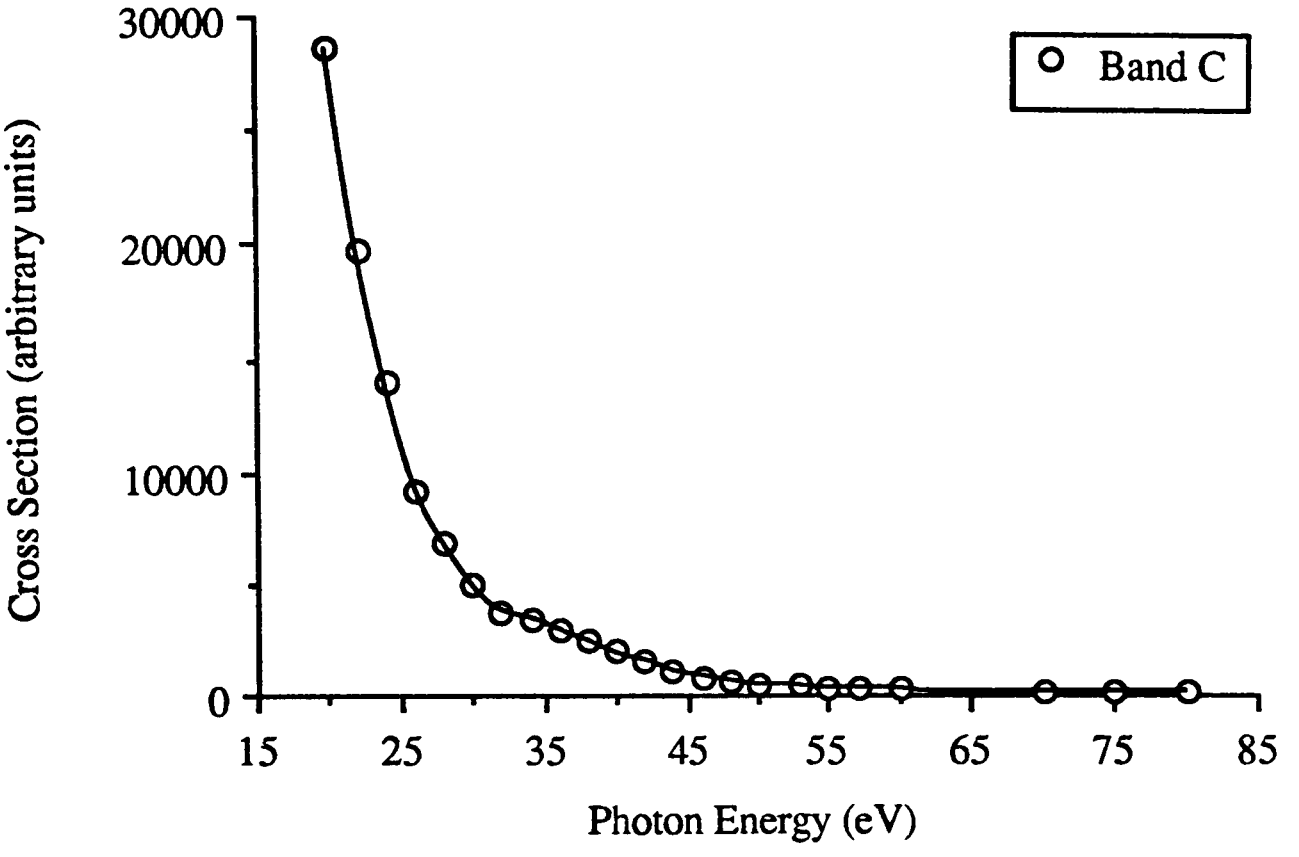

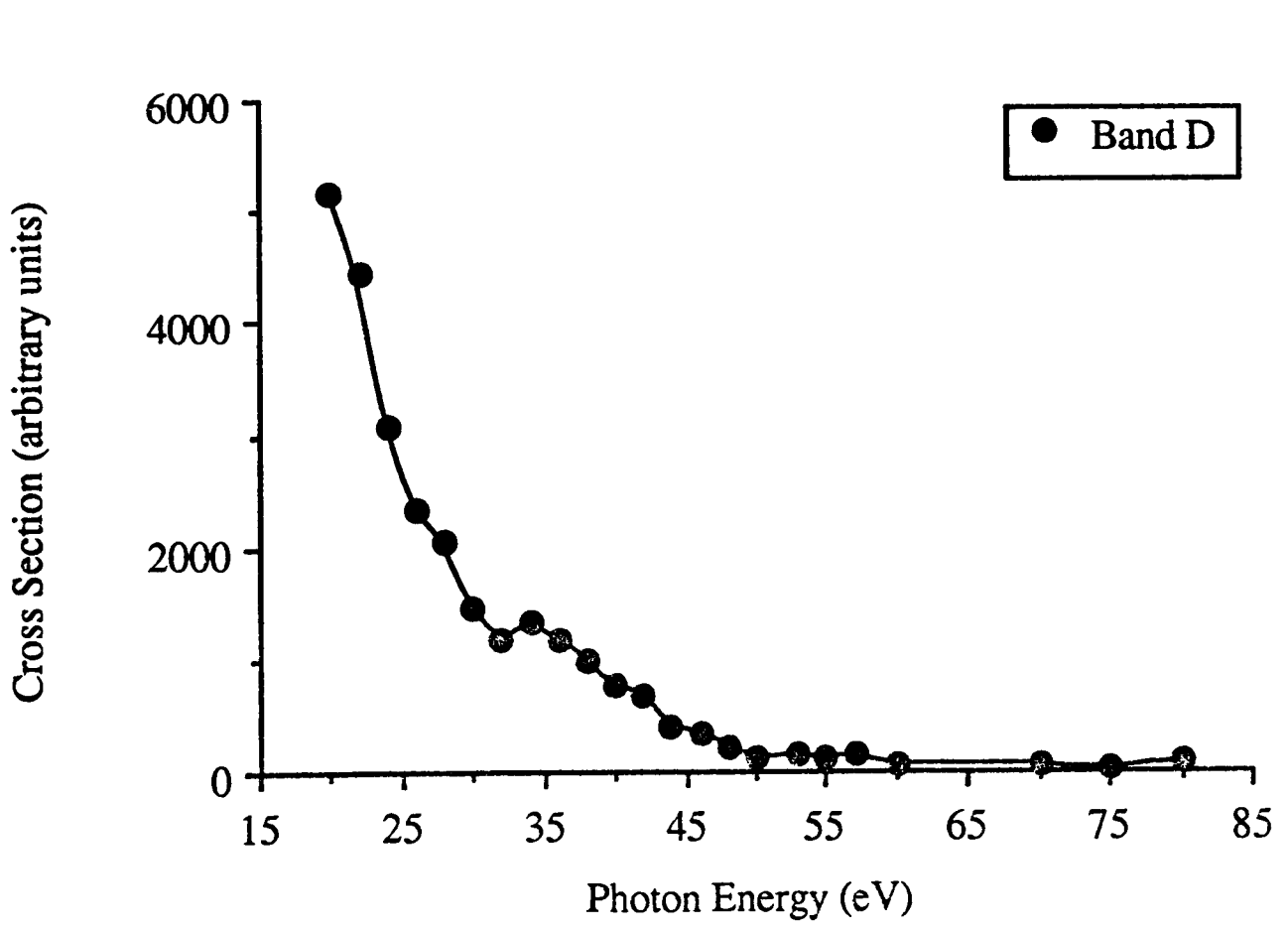

Figure 4.20 : individual RPPICS of bands A-G in the PE spectrum of $ZrBr_4$ (continued)

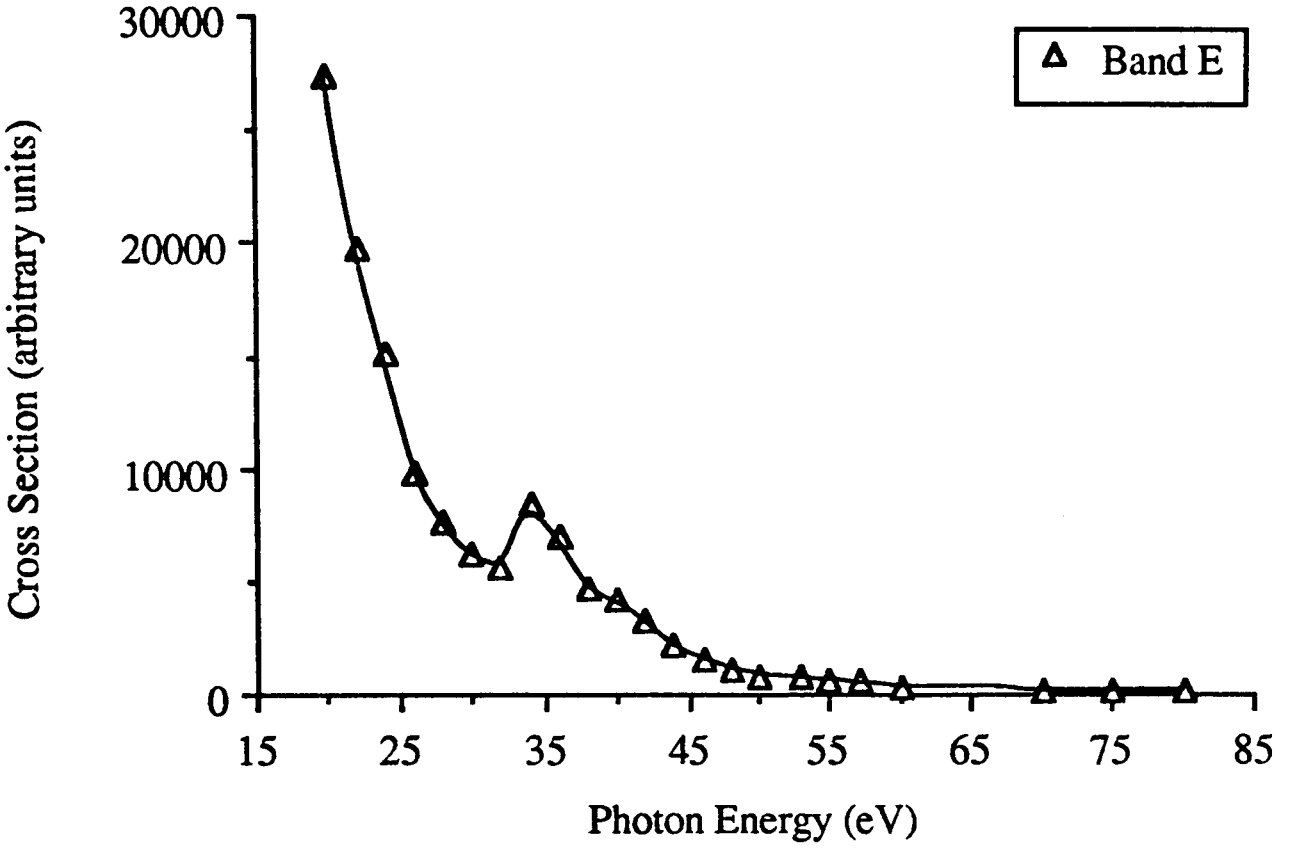

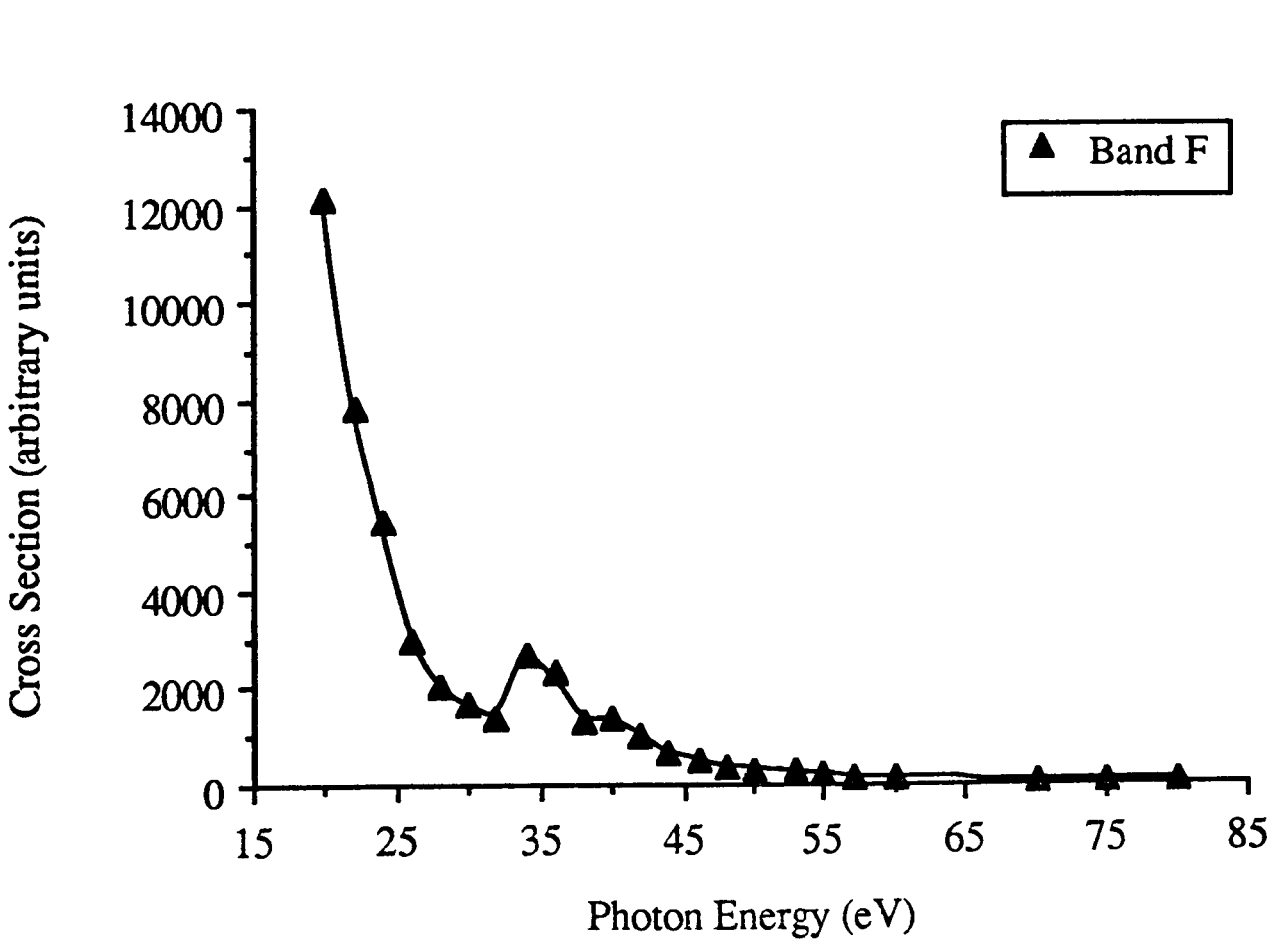

Figure 4.20 : individual RPPICS of bands A-G in the PE spectrum of $ZrBr_4$ (continued)

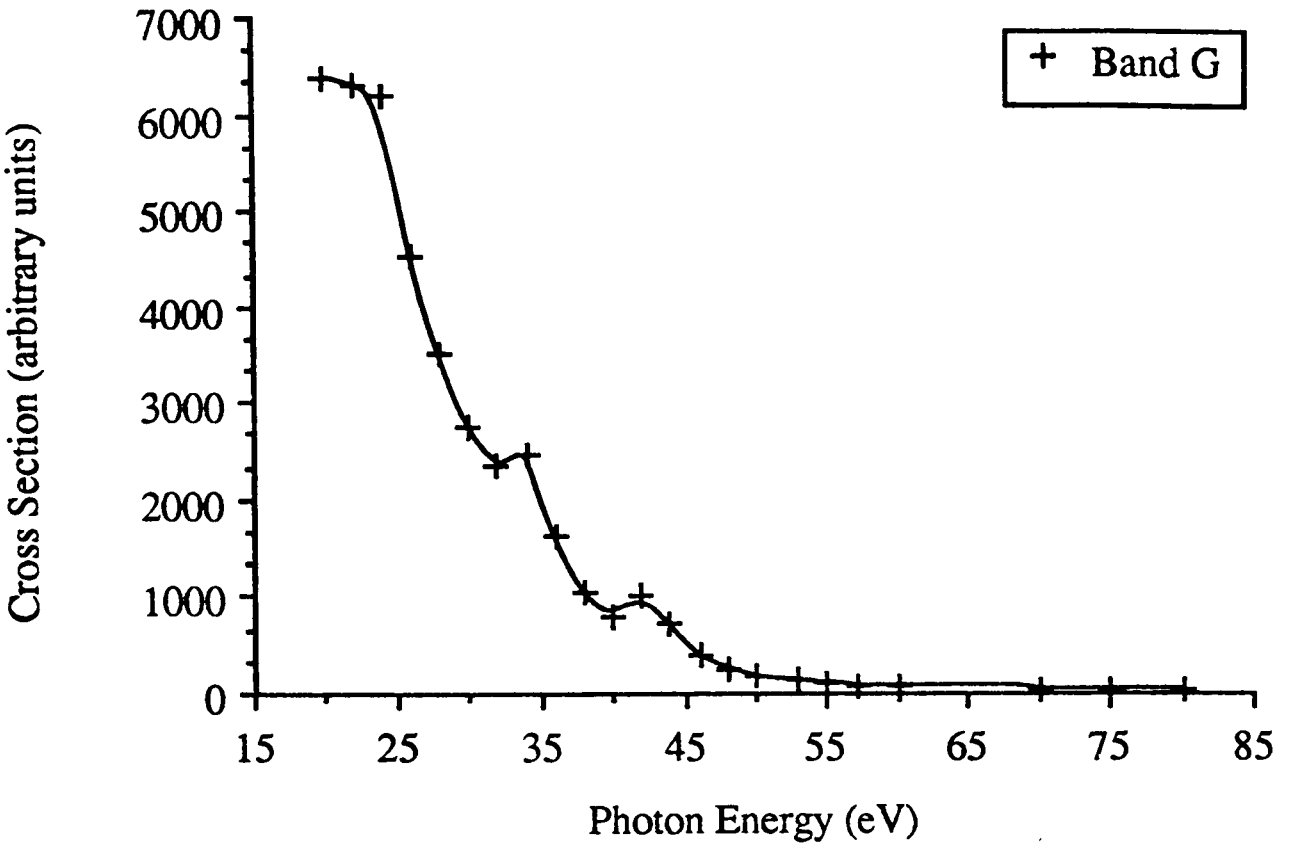

Figure 4.20 : individual RPPICS of bands A-G in the PE spectrum of $ZrBr_4$ (continued)

The cross section behaviour of band A is very similar to the equivalent band of $TiBr_4$, and is consistent with its assignment to the U' component of the essentially bromine 4p-localised $1t_1$ MO. It is curious that band B has a somewhat different cross section variation, in that the general fall off is interrupted by a small maximum at 36 and a shoulder at 44 eV. This is surprising as this band is assigned to the E' component of the $^2T_1$ primary ion state and would therefore be expected to show behaviour similar to that of band A. It would be less surprising were band A to show behaviour other than a monotonic fall off, in that the U' MO may acquire some metal d orbital character whereas the E' cannot. As the results on bands D-F suggest (pages 159-162), there is a significant degree of metal d orbital character in the MOs ionising under these bands. It would therefore appear from the RPPICS of band A that the distribution of zirconium 4d AO admixture over the relativistic subshells is confined to those which arise from the $^2T_2(2t_2)$ and $^2E(1e)$ primary ion states, supporting the observations of Egdell [6].

Band C has RPPICS very similar to that of band A, with a sharp initial fall off modified slightly above 32 eV. This behaviour is again characteristic of a predominantly bromine 4p-localised ionisation and is reminiscent of that of band C of $TiBr_4$ (Figure 4.14) with the exception of the maximum at 24 eV and the more gentle fall off between 34-44 eV. It may be assigned in an analogous manner, to the U'($^2T_2(3t_2)$) and E''($^2T_2(2t_2)$) ionisations.

The cross section variation of band G has three principal features superimposed upon the general fall off. The shoulder at 24 eV equates with similar features in the $2a_1^{-1}$ ionisations of $TiCl_4$ and $TiBr_4$, which were attributed to a maximum in the cross section of the 4s AO of titanium. A similar maximum is calculated to occur in the cross section of the 5s AO of zirconium at a PE KE of ca. 19 eV [20], in comparison with the 11 eV found by experiment. The maximum at 42 eV is reminiscent of that of the $2a_1^{-1}$ band of $TiCl_4$, which was attributed to a shape resonance and believed to be responsible for the relative intensity increases of the a_1^{-1} bands in He II spectra. It is interesting that this effect is not so pronounced in band F of $TiBr_4$, but comes through more in the second row system.

Bands D, E and F all show enhancements in their RPPICS in the region of the zirconium 4p subshell IEs ($^2P_{3/2}$ = 33 eV, $^2P_{1/2}$ = 35 eV [19]). As these bands are the equivalent of band (C+D) in $TiCl_4$ - i.e. are derived principally from the $^2T_2(2t_2)$ and $^2E(1e)$ primary ion states - they are the ones which should have the most zirconium 4d AO contribution. Unlike $TiBr_4$, the RPPICS enhancements of band D, E and F are quite substantial, although direct comparisons of the magnitudes of resonance phenomena between metals are not valid.

The p→d giant resonant absorption process for $ZrBr_4$ is represented by the same equations as that for $TiCl_4$ (pages 134-135), with the obvious exception that the inner subshell is the 4p and not the 3p AO. As with $TiBr_4$, the magnitude of metal derived spin-orbit coupling effects will be so small as to permit the treatment in the T_d point group. The group theoretical analysis gives two possible $^1T_2$ states as intermediates to which absorption can occur. To attempt to gauge the magnitude of the resonance ionisation channel, Fano profiles (using equation (1.9)) were fitted to the RPPICS of bands D, E and

F over the photon energy range 32-44 eV. Unlike $TiCl_4$, the cross section enhancements of bands D and E fitted well to one Fano profile. That of band F was not so good, but it was decided to persevere with one profile to enable a comparison with bands D and E to be made more readily. The values obtained from the Fano fits are given in Table 4.11.

Table 4.11 : Fano parameters obtained on bands D, E and F in the PE spectrum of $ZrBr_4$, over the incident photon energy range 32-44 eV

	σ_0	X	q	E_r (eV)	Γ (eV)
Band D	1589	0.061	0.008	30.71	1.53
Band E	4171	0.051	1.11	31.90	4.61
Band F	1018	0.045	1.39	32.48	4.46

The line profile index measures the relative contribution of the direct and resonant ionisation channels; the bigger the q value, the more significant the resonant channel. The q values listed in Table 4.11 rather confirm what may be deduced by inspection of Figure 4.20, that the resonance is weakest in band D and strongest in band F. It would also seem that the two $^1T_2$ intermediate states lie closer together in $ZrBr_4$ than $TiCl_4$, as only one Fano profile is required to fit the RPPICS enhancement.

Both the He I spectra and those obtained with synchrotron radiation indicate that there are more bands in the spectrum of $ZrBr_4$ than $TiBr_4$. In order to explain this, it is necessary to assume that at least one of the U' levels is subject to a significant Jahn-Teller distortion. This may well reflect greater M-X covalent bonding in the second row system. One possible assignment which retains the MO ordering presented for $TiBr_4$ is to have one Jahn-Teller component of the U'($^2T_2(2t_2)$) ionisation under band D, one Jahn-Teller component of the U'($^2E(1e)$) ionisation under band F, leaving the two remaining U' Jahn-Teller components together with the E''($^2T_2(3t_2)$) ionisation assigned to band E (Table 4.10, page 144). If this were true, bands D and F would arise from ionisations involving only one Kramers doublet final state, with three responsible for band E. Figure 4.21

presents the renormalised BRs of bands D, E and F, from which it can be seen that the above suggestion is not unreasonable. The fact that the three bands overlap to such a significant extent means that reliable deconvolution is not always certain, especially in the spectra acquired at higher incident photon energy. Nevertheless, a 6 : 4 ratio of bands E : (D+F) suggests itself from Figure 4.21.

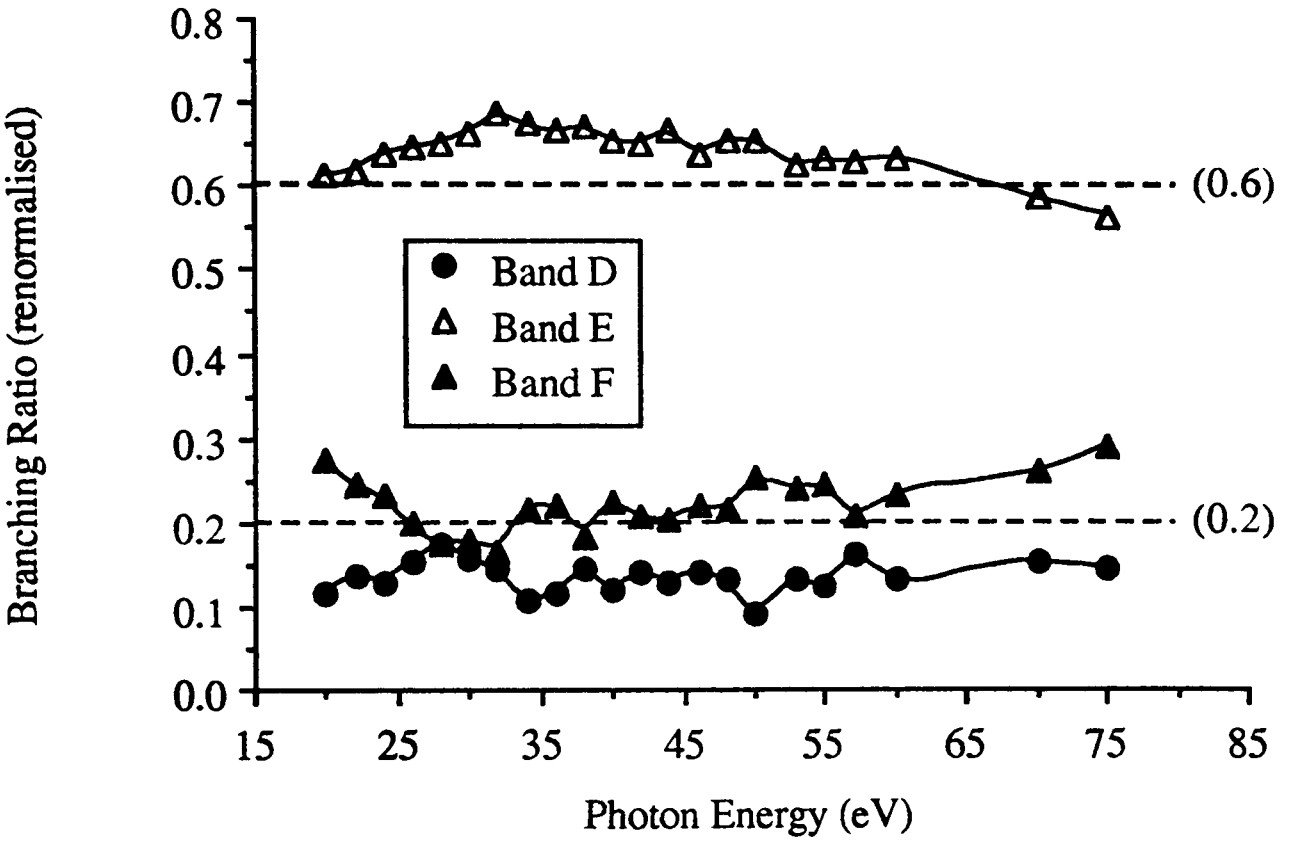

Figure 4.21 : renormalised BRs of bands D, E and F in the PE spectrum of $ZrBr_4$

There is a maximum in the RPPICS of band G at 34 eV, the same photon energy as the enhancements of bands D-F which were attributed to the zirconium p→d resonance. It is unlikely that there is any direct p→d resonance effect on the RPPICS of band G, in that the $2a_1$ (E') MO can have no zirconium 4d AO contribution (in either the T_d or T_d^* point groups). The two possible explanations for this feature are that it arises as a result of inter-channel coupling, or that it is a shape resonance. It is worth noting that there are slight modifications to the RPPICS of band B at 34 and 44 eV, which may be weaker

counterparts of those of band G. The two bands are the only ones to arise from MOs of E' symmetry.

4.4.3 Summary of the results from $TiBr_4$ and $ZrBr_4$

The cross section data obtained on the tetrabromides support the previous assignment of their spectra. A consistent pattern emerges which allows $TiCl_4$, $TiBr_4$ and $ZrBr_4$ to be discussed within the same primary ion state ordering. The highest IE band shows behaviour which, in all cases, is appreciably different from that of the other bands, and which allows its assignment to the $2a_1$ MO to be made with some confidence. Metal d AO contributions are found exclusively in bands arising from the t_2 and e MOs, although the evidence for appreciable titanium 3d AO character to any of the ionisation bands of $TiBr_4$ is not strong. At lowest IE come bands which are confidently assigned to the halogen p lone pair MOs.

4.5 $[(CH_3)ReO_3]$ and ReO_3Cl

4.5.1 $[(CH_3)ReO_3]$

The relationship of $[(CH_3)ReO_3]$ to the tetrahedral molecules discussed thus far in this Chapter is clear; furthermore it occupies a position of some importance in terms of bonding in organometallic compounds in possessing a single metal-carbon σ bond. Its He I PE spectrum was recently published [45] and an assignment was presented based largely on the results of an accompanying Fenske-Hall Xα calculation. As no He II spectrum was available and no attempt was made to assign the spectrum using empirical arguments, it was decided to investigate $[(CH_3)ReO_3]$ more closely.

The He I and He II spectra are presented in Figure 4.22, and IEs, band assignments and $R_{II/I}$ values (relative areas in the He II spectrum divided by those in the He I) are given in Table 4.12. The He I spectrum is identical to that presented by Herrmann et al., and is rather different from those of the tetrahalides and OsO_4. In order to aid spectral assignment, an Extended Hückel Molecular Orbital (EHMO) calculation was performed on $[(CH_3)ReO_3]$, the input parameters for which are given in Appendix One. An EHMO

calculation was also performed by Herrmann et al., although little use was made of it in assigning the spectrum. Table 4.13 presents the results of this calculation, and contour plots of some of the valence MOs are shown in Figure 4.23.

Table 4.12 : IEs and band assignments of the PE spectrum of $[(CH_3)ReO_3]$

Band	IE (ev) [a]	Assignment [b]	$R_{II/I}$
A (adiabatic)	11.46		
A (vertical)	11.63 (11.80)	$5a_1$ ($^2T_2(2t_2)$)	1.64
B	11.94 (11.95)	5e ($^2T_1(1t_1)$)	0.88
C	12.27 (12.35)	$1a_2$ ($^2T_1(1t_1)$)	0.69
C'	12.44		
C''	12.62		
D	13.08 (13.2)	$4a_1$ ($^2T_2(3t_2)$)	0.97
E	13.83 (13.8)	4e ($^2T_2(3t_2)$)	0.79
E'	14.08		
F	14.54 (14.6)	$3a_1$ ($^2A_1(2a_1)$)	1.07
G	15.26 (15.3)	3e, 2e ($^2T_2(2t_2)$+$^2E(1e)$)	1.01

[a] Values in parentheses from reference [45]

[b] Assignment given in terms of MO from which ionisation is occurring (using the numbering scheme of Herrmann et al.) and related primary ion state of OsO_4

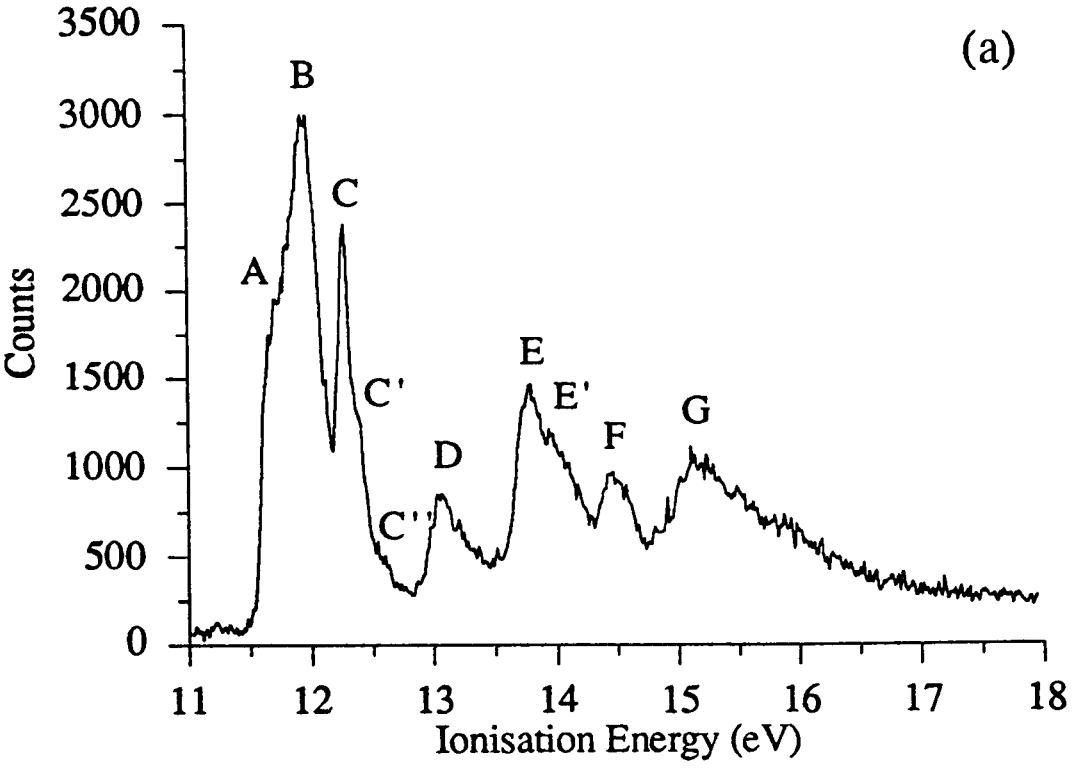

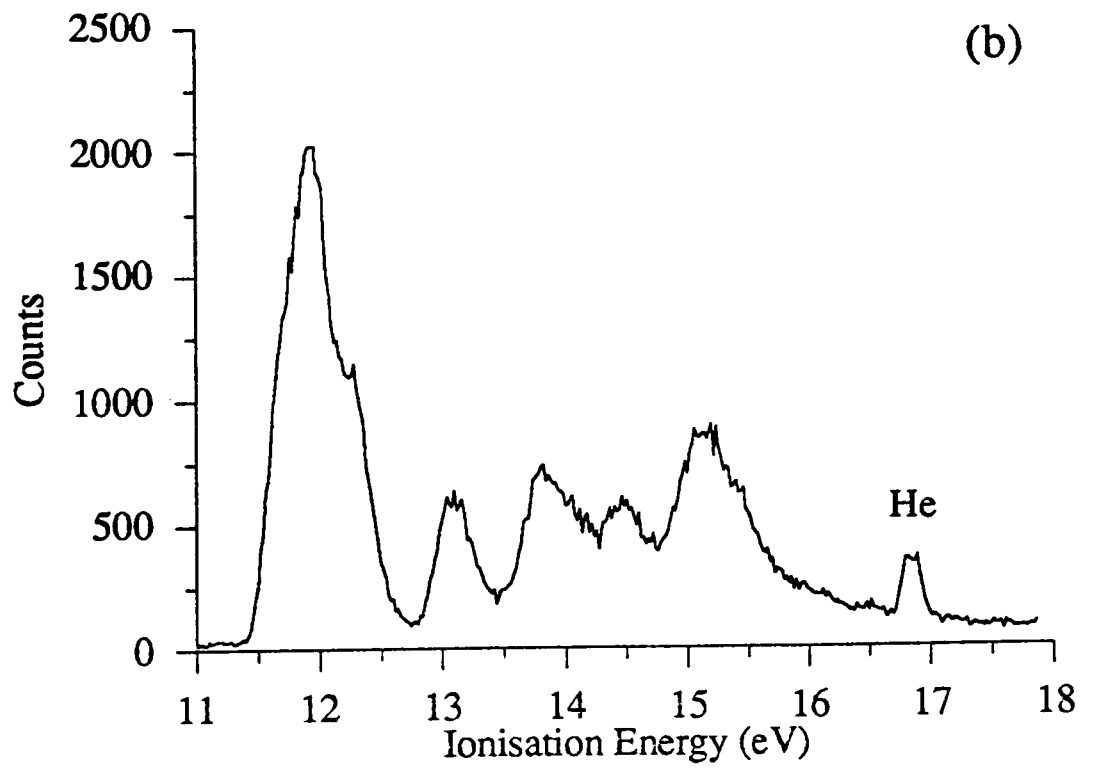

Figure 4.22 : the (a) He I and (b) He II PE spectrum of $[(CH_3)ReO_3]$

Table 4.13 : results of the EHMO calculation of $[(CH_3)ReO_3]$

MO Number/ Symmetry		Energy (eV)	AO character (%) Re	O	C	H	Principal bonding characteristics
13	$5a_1$	-13.94	32.21	6.19	52.24	8.34	Re-C σ bonding
14	$1a_2$	-14.74	0.00	100.00	0.00	0.00	O p lone pair
15,16	5e	-14.91	2.53	93.20	1.87	2.40	O p lone pair
17	$4a_1$	-15.10	4.38	95.10	0.44	0.09	O p lone pair
18,19	4e	-15.22	6.27	63.80	13.96	15.95	O p lone pair + C-H σ bonding
20	$3a_1$	-15.41	17.99	81.56	3.65	0.09	Re-O σ/π bonding
21,22	3e	-15.67	15.73	45.88	18.75	19.65	Re-O σ/π+ C-H σ bonding
23,24	2e	-15.88	24.24	51.28	12.71	11.77	Re-O σ/π+ C-H σ bonding

$[(CH_3)ReO_3]$ belongs to the C_{3v} point group, and descending in symmetry from T_d to C_{3v} lifts the threefold degeneracy of the T type orbitals, as indicated in Table 4.14. This is certainly one of the main reasons for the increased complexity of the PE spectrum of $[(CH_3)ReO_3]$ over the T_d systems. It is not unreasonable to attempt an assignment in which the gross ordering of the five primary ion states of OsO_4 is maintained in $[(CH_3)ReO_3]$. If this approach is brought to the EHMO calculation results, the ordering of MOs 13-24 (the valence MOs) can be understood in terms of the lowering of symmetry from T_d to C_{3v}, with the exception of MO 13 which, being of a_1 symmetry, cannot have been produced from the formerly $^2T_1$ primary ion state. As is clear from Figure 4.23 (a), this MO is principally of rhenium-carbon σ bond character, and thus the EHMO calculation suggests that a strongly bonding MO is elevated into the region which contains only essentially non-bonding MOs in OsO_4 and the tetrahalides. This is not without precedent, in that the first

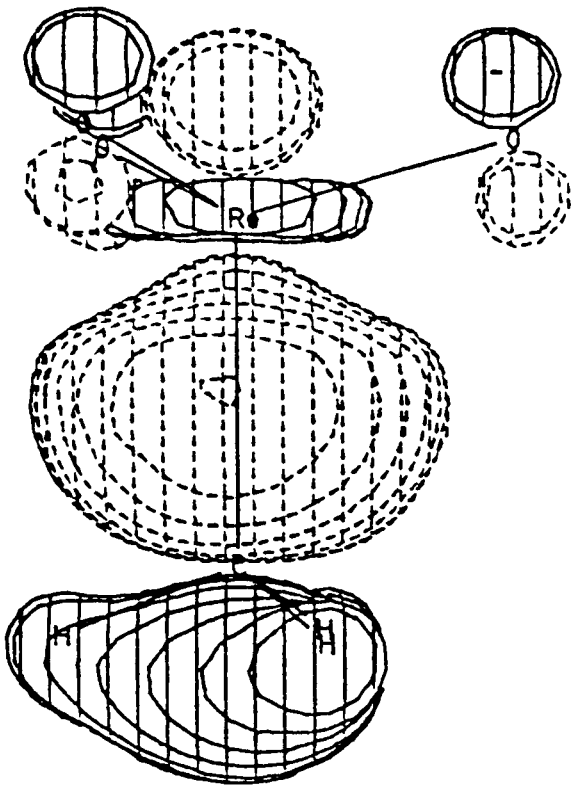

a

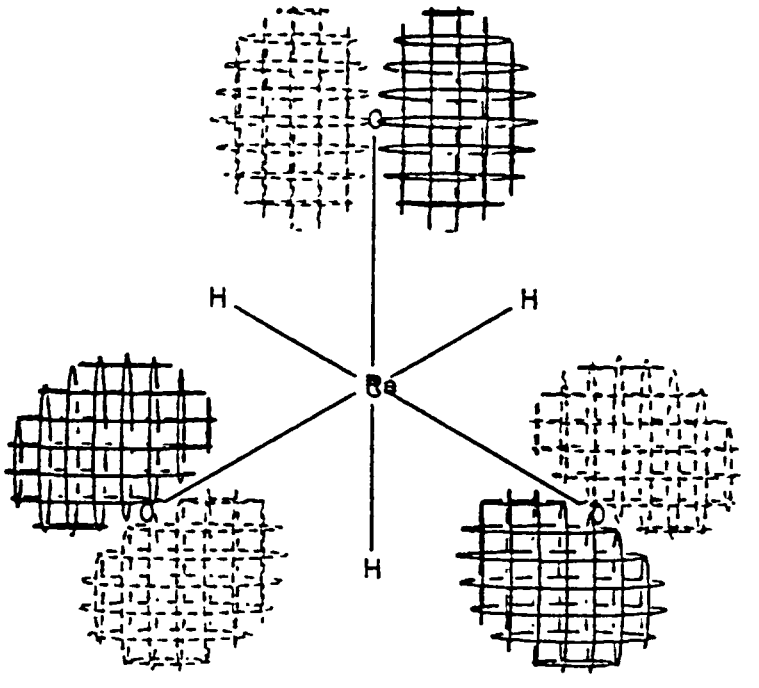

b

c

d

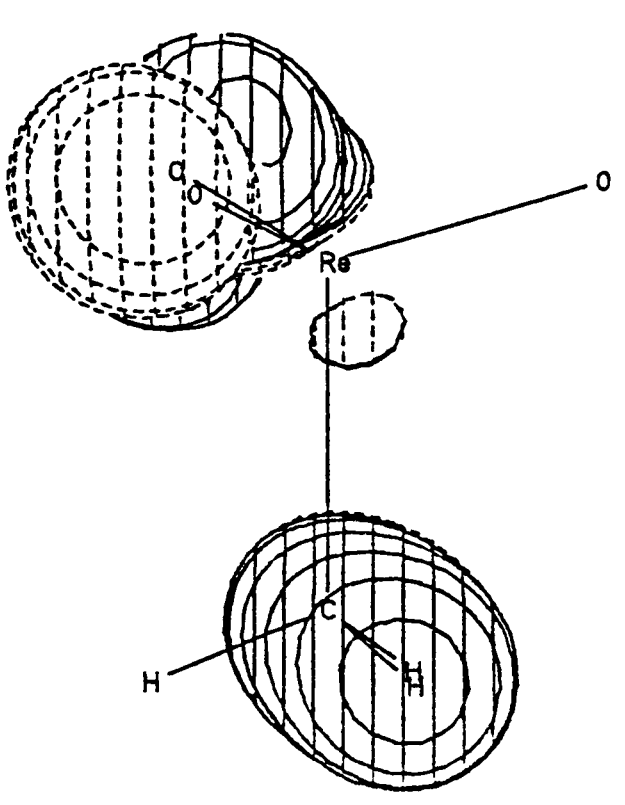

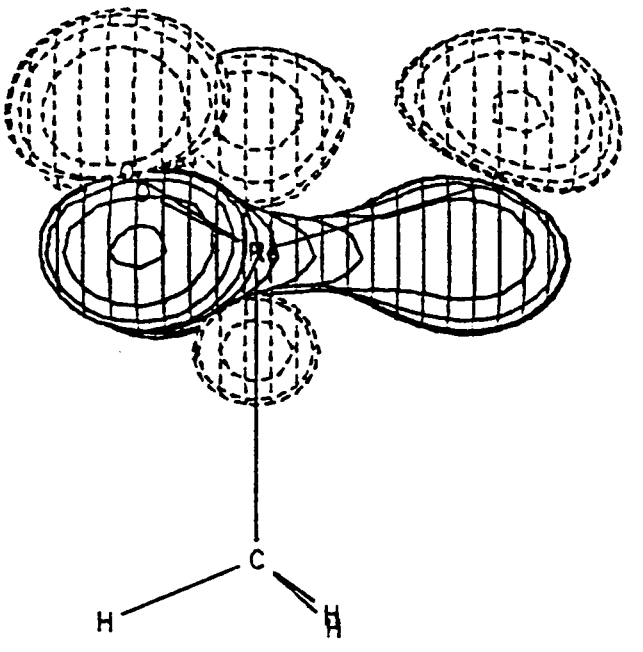

Figure 4.23 : contour plots of some of the valence MOs of $[(CH_3)ReO_3]$, taken from the EHMO calculation (a) MO 13 - $5a_1$ (b) MO 14 - $1a_2$ (c) MO 18 - 4e (d) MO 20 - $3a_1$ ((a), (c) and (d) viewed in a plane containing the Re-C bond, one Re-O and one C-H bond; (b) viewed along the Re-C bond from above)

band in the PE spectrum of $[(CH_3)TiCl_3]$ is unambiguously assigned to the titanium-carbon σ bond [46]. The subsequent two MOs in the EHMO calculation are the $1a_2$ and 5e (using the numbering scheme of Herrmann et al.), which can be equated with the $^2T_1(\pi)$ ionisation of OsO_4. Both are heavily localised on the oxygen atoms, the $1a_2$ rigorously so from symmetry restrictions (Figure 4.23 (b)).

Table 4.14 : descent in symmetry from T_d to C_{3v}

T_d	C_{3v}
A_1	A_1
A_2	A_2
E	E
T_1	$A_2 + E$
T_2	$A_1 + E$

The first three bands in the PE spectrum (A-C) may be assigned to the $5a_1$, 5e and $1a_2$ MOs respectively. This differs from the previous assignment, which places only the non-bonding oxygen lone pairs under the first band system. This is inconsistent with the He I/He II behaviour of bands A-C, which reveals a relative increase of band A, implying different AO localisation properties. The rhenium 5d AO character of the $5a_1$ MO readily explains the enhancement of band A as the incident photon energy is increased.

There is some fine structure to the high IE side of band C, with two shoulders at 12.44 and 12.62 eV. It is most likely that this arises from a vibrational progression of interval 0.18 eV. Although the $1a_2$ MO is a non-bonding MO, the Franck-Condon Factors for transitions to higher vibrational levels in the molecular ion will not be zero, and it is clear that the 0-0 transition is the most intense. It may be that the localisation of the hole upon the oxygen atoms is the driving force behind the vibrations of the molecular ion.

Bands D and E are assigned to the $4a_1$ and 4e MOs respectively, which may be considered as being derived from the $^2T_2(3t_2)$ primary ion state of OsO_4. The $4a_1$ MO is

once more oxygen-based, but the 4e contains some degree of carbon-hydrogen σ bonding character in the EHMO calculation (Figure 4.23 (c)). This may explain the stabilisation of the 4e MO relative to the $4a_1$. The assignment of bands D and E is as given by Herrmann et al.

The band at 14.54 eV is assigned to the $3a_1$ MO, which correlates well with the $^2A_1$ band of OsO_4, and which is bonding between rhenium and oxygen (Figure 4.23 (d)). The metal-oxygen bonding nature of this MO is readily understood by the fact that both the rhenium 6s and $5d_{z^2}$ AOs transform as a_1 symmetry in C_{3v}. No carbon-hydrogen or rhenium-carbon σ bonding character is predicted for this MO.

The broad band with a maximum at 15.30 eV (band G) is assigned to two overlapping ^2E ion states, arising from the 3e and 2e MOs. It may be equated with band E of OsO_4, which contains the ^2E and $^2T_2$ ionisations, the parent MOs of which are strongly osmium-oxygen bonding. The 2e and 3e MOs of $[(CH_3)ReO_3]$ are also found to be metal-oxygen bonding, and to contain some carbon-hydrogen σ bonding character. It is likely that the carbon 2p and hydrogen 1s AO contributions to the 2e and 3e MOs prevent band G from gaining in relative intensity in the He II spectrum to the same extent as band E of OsO_4.

The calculation suggests a gradation in AO nature of MOs 13-24. With the exception of the HOMO, the highest lying MOs are essentially oxygen p lone pairs. As the binding energy increases, there is a shift toward significant carbon-hydrogen σ bonding and increasing rhenium 5d AO character. As with OsO_4, the main metal-oxygen bonding MOs are found to lie at high binding energy, consistent with a significant degree of multiple bonding. Perturbing the T_d geometry with a CH_3 group causes one of the bonding levels to be strongly destabilised. Hence only four MOs lie at high binding energy (3e and 2e), with the fifth (expected from a descent in symmetry of the ^2E and $^2T_2$ states of OsO_4) becoming the rhenium-carbon σ bonding HOMO. It may be concluded that the introduction of a CH_3 group represents a strong perturbation to the T_d system, i.e. that $[(CH_3)ReO_3]$ is a "genuine" C_{3v} molecule.

4.5.2 ReO_3Cl

In the light of the reassignment of the PE spectrum of OsO_4 and the investigation of $[(CH_3)ReO_3]$, it seemed appropriate to re-examine the PE spectrum of ReO_3Cl. The He I and He II spectra have been measured by Egdell [5] and are given in Figure 4.24. They bear a striking resemblance to those of OsO_4, the major exception being the pronounced low IE shoulder to band A. IEs and band assignments are given in Table 4.15.

Table 4.15 : IEs and band assignments of the PE spectrum of ReO_3Cl. All data taken from reference [5].

Band	IE (ev)	Assignment [a]
A	12.05	$1a_2$ ($^2T_1(1t_1)$)
A	12.26	$5e$ ($^2T_1(1t_1)$)
B	12.95	$5a_1$+$4e$ ($^2T_2(3t_2)$)
C	13.26	
D	14.45	$4a_1$ ($^2A_1(2a_1)$)
E	15.70	$3e$+$3a_1$+$2e$ ($^2T_2(2t_2)$+$^2E(1e)$)

[a] Assignment (which differs from that given in reference [5]) given in terms of MO from which ionisation is occurring and related primary ion state of OsO_4

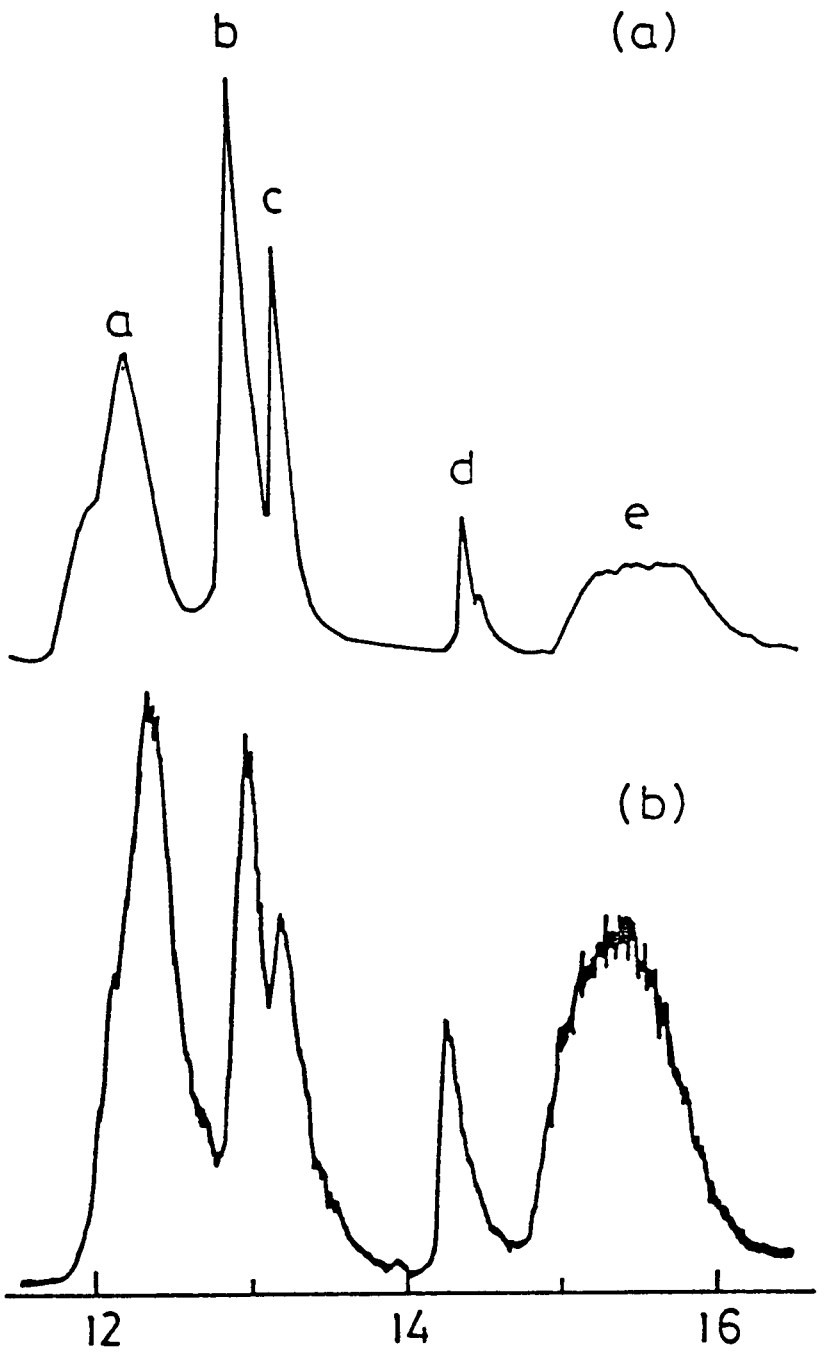

Figure 4.24 : (a) He I and (b) He II PE spectra of ReO_3Cl (from reference [5])

An EHMO calculation was performed on ReO_3Cl; input parameters are given in Appendix One and Table 4.16 presents the results. Contour plots of some of the valence MOs are given in Figure 4.25. An interpretation of the EHMO calculation in terms of the gross primary ion state ordering of OsO_4 is straightforward. The principal rhenium-oxygen bonding is concentrated in the 2e, $3a_1$ and 3e MOs, all five of which lie in the higher binding energy region. No significant destabilisation of the $3a_1$ MO is found, unlike the calculation of $[(CH_3)ReO_3]$. The $4a_1$ MO is seen to be bonding between all of the atoms in the molecule, with a significant rhenium-chlorine σ bonding contribution. This is also different from $[(CH_3)ReO_3]$, in which the $4a_1$ MO was found to be rhenium-oxygen bonding only. The 4e and $1a_2$ MOs are oxygen-localised p lone pair MOs. The 5e is also a

non-bonding MO, but contains a large amount of chlorine 3p AO character. The $5a_1$ MO has significant rhenium-chlorine σ bonding character, together with more oxygen lone pair.

Table 4.16 : results of the EHMO calculation of ReO_3Cl

MO Number/ Symmetry		Energy (eV)	AO character (%) Re	O	Cl	Principal bonding characteristics
10,11	5e	-14.32	2.15	33.35	64.20	Cl/O p lone pair
12	$1a_2$	-14.72	0.00	100.00	0.00	O p lone pair
13	$5a_1$	-14.94	9.99	41.14	48.87	Re-Cl σ bonding / O p lone pair
14,15	4e	-14.99	3.29	90.97	5.75	O p lone pair
16	$4a_1$	-15.24	7.23	61.67	31.10	Re-O σ/π / Re-Cl σ bonding
17,18	3e	-15.49	20.75	68.21	11.05	Re-O σ/π bonding / Re-Cl π bonding
19	$3a_1$	-15.50	21.62	76.11	2.27	Re-O σ/π bonding
20,21	2e	-15.89	28.87	66.41	4.73	Re-O σ/π bonding

Perhaps the main point arising from a comparison of the EHMO calculations on $[(CH_3)ReO_3]$ and ReO_3Cl is that ReO_3Cl represents a much gentler perturbation to T_d symmetry than does $[(CH_3)ReO_3]$. An interpretation of the PE spectrum of ReO_3Cl in these terms is not unreasonable, and indeed was the approach of Egdell. In the light of the reinterpretation of the spectrum of OsO_4, however, the assignment of that of ReO_3Cl is called into question.

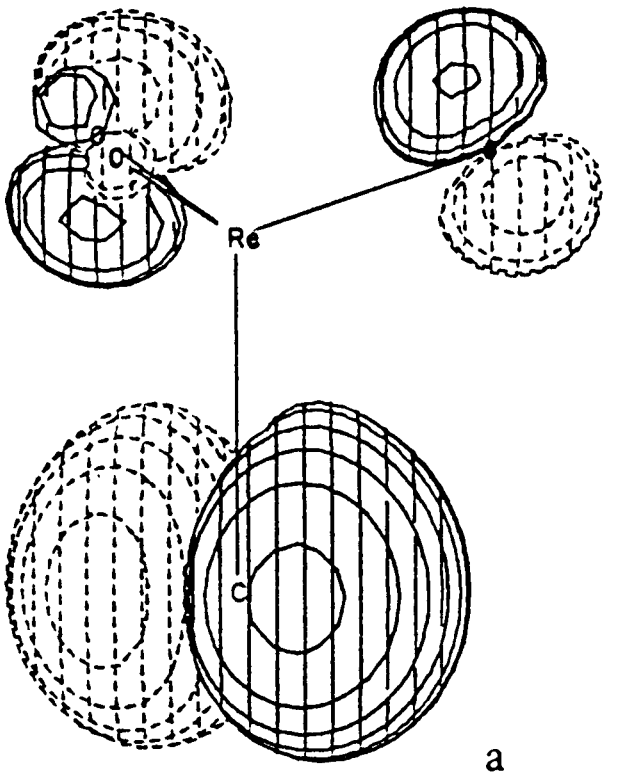

a

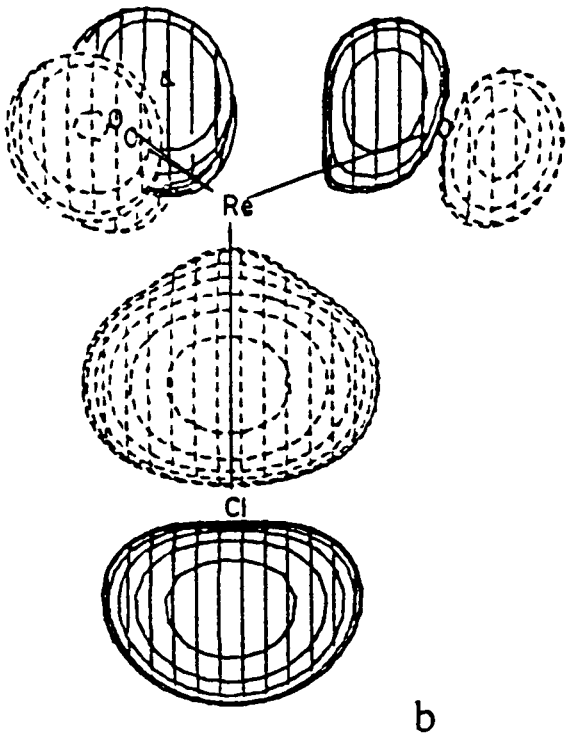

b

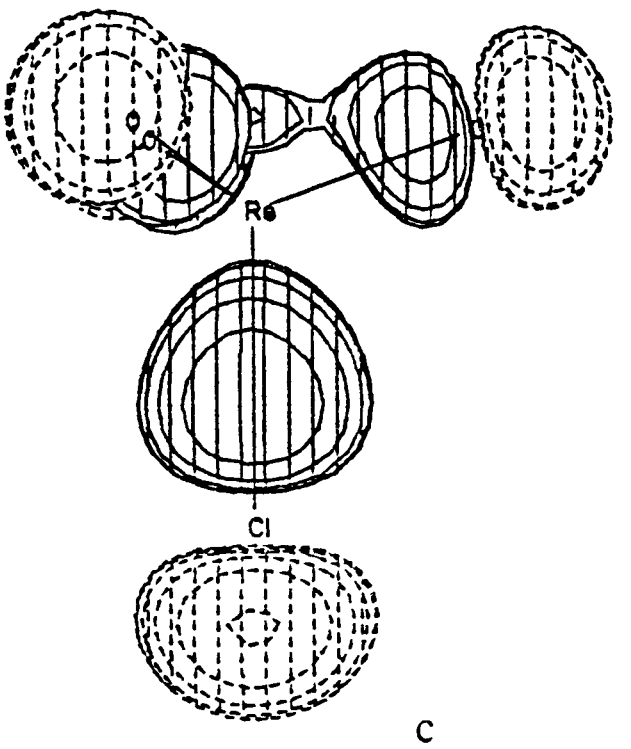

c

Figure 4.25 : contour plots of some of the valence MOs of ReO_3Cl, taken from the EHMO calculation (a) MO 10 - 5e (b) MO 13 - $5a_1$ (c) MO 16 - $4a_1$ (viewed in a plane containing the Re-Cl bond and one Re-O bond)

Band A is assigned to the MOs arising from the formerly $^2T_1(\pi)$ primary ion state of OsO_4, the $1a_2$ MO being the low IE component with the 5e lying to higher IE. Bands D and E arise from the $4a_1$ and 3e, $3a_1$ and 2e MOs respectively, stemming from the $^2A_1$ and $^2E+^2T_2(2t_2)$ ionisations of OsO_4. It is tempting to assign bands B and C to the 4e and $5a_1$ MOs respectively, which come from the descent in symmetry of the $^2T_2(3t_2)$ ion state. However, the He I/He II behaviour of the two bands is very similar, at odds with the EHMO calculation in which the $5a_1$ MO is predicted to have a much greater chlorine 3p AO contribution that the 4e. A collapse of band C relative to band B would therefore be expected. Furthermore, if the assertion that ReO_3Cl is a pseudo-tetrahedral molecule is correct, it may be expected that the significant spin-orbit splitting of the $^2T_2$ ion state of OsO_4 should carry through to ReO_3Cl. This suggests that bands B and C arise from a pseudo-spin-orbit splitting of the weakly perturbed $^2T_2$ primary ion state, a situation not observed in $[(CH_3)ReO_3]$ on account of the much greater perturbation to T_d symmetry generated by the methyl group.

Figure 4.26 illustrates the relationship between the ionisation bands of OsO_4, $[(CH_3)ReO_3]$ and ReO_3Cl in the light of the preceding discussion. The spectra can be divided into groups of ionisations which are closely related between the molecules (N.B. the lines on the diagram seek to illustrate how the OsO_4 MOs correlate with those of $[(CH_3)ReO_3]$ and ReO_3Cl on lowering the symmetry from T_d to C_{3v}, and the non-crossing rule is deliberately broken in order to emphasise the orbital correlation between OsO_4 and $[(CH_3)ReO_3]$). The metal-ligand bonding is concentrated mainly in the high IE bands, with the exceptions of the $5a_1$ MOs of the rhenium compounds, which have significant rhenium-carbon and rhenium-chlorine σ bonding character. Moving from T_d to C_{3v} also introduces some metal d AO-ligand bonding into the $2a_1$ MO of OsO_4. At lower IE lie the bands associated with the non-bonding electrons of the ligand atoms. As stressed before, this interpretation implies a high degree of metal-oxygen double bonding.

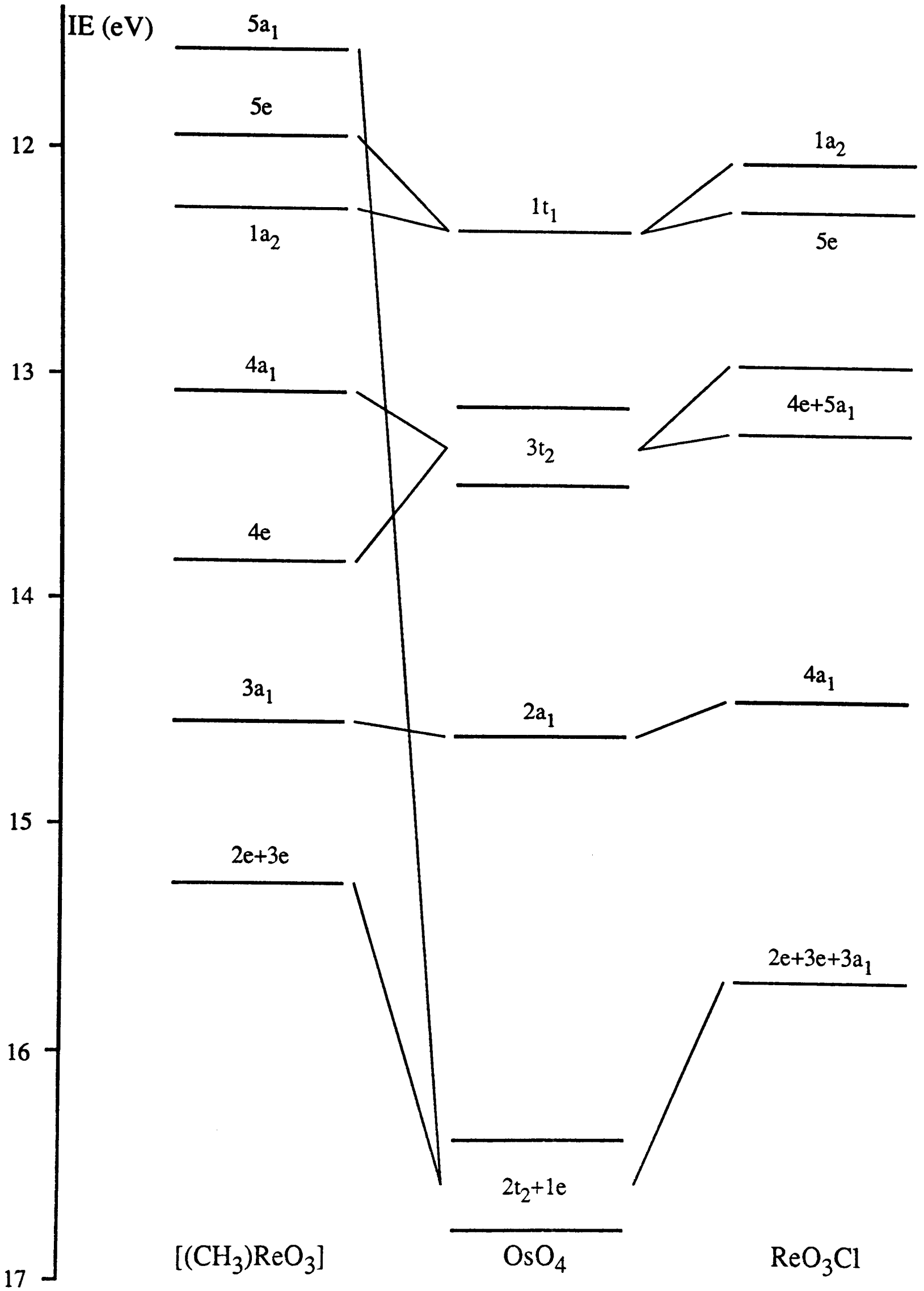

Figure 4.26 : relationship between the valence ionisations of $[(CH_3)ReO_3]$, OsO_4 and ReO_3Cl

4.6 Summary and Conclusions

Although it did not prove possible to obtain data on all of the members of the originally-targeted series, those which were collected have allowed a substantial re-evaluation of the electronic structures of the molecules in question. In the case of OsO_4, the synchrotron study (in conjunction with theoretical work) has provided strong support for multiple bonding, a conclusion which requires a degree of osmium np (n=5 and/or 6) AO character to the $3t_2$ MO. The resulting $^2T_2$ primary ion state is split by spin-orbit coupling derived from this p AO admixture.

The work on $TiCl_4$, $TiBr_4$ and $ZrBr_4$ indicates that their PE spectra may be interpreted via a common approach. The $2a_1$ MO is found to be the most tightly bound of the valence orbitals, resolving the debate as to the assignment of the $TiCl_4$ spectrum. Significant metal d AO character is found in the $2t_2$ and 1e MOs of $TiCl_4$ and in the corresponding spin-orbit coupled levels of $ZrBr_4$. Evidence for metal d orbital contributions to the equivalent MOs of $TiBr_4$ is less conclusive.

Measurement of the He I and He II spectra of $[(CH_3)ReO_3]$, together with an EHMO calculation, has resulted in a reassignment of the spectrum. The rhenium-carbon σ bonding MO is assigned to the lowest IE band. A comparison of the spectrum of OsO_4 with those of $[(CH_3)ReO_3]$ and ReO_3Cl suggests that the introduction of a methyl group may be treated as a major perturbation to T_d symmetry, while ReO_3Cl is little different from the tetroxide.

4.7 References for Chapter Four

[1] E. Diemann and A. Müller: *Chem. Phys. Lett.* **19** (1973) 538.

[2] S. Foster, S. Phelps, L. C. Cusachs and S. P. McGlynn: *J. Am. Chem. Soc.* **95** (1973) 5521.

[3] S. Evans, A. Hamnett and A. F. Orchard: *J. Am. Chem. Soc.* **96** (1974) 6621.

[4] P. Burroughs, S. Evans, A. Hamnett, A. F. Orchard and N. V. Richardson: *J. Chem. Soc., Farad. Trans. II* **70** (1974) 1895.

[5] R. G. Egdell: *D. Phil. Thesis* Oxford (1977).

[6] R. G. Egdell, A. F. Orchard, D. R. Lloyd and N. V. Richardson: *J. Electron Spectr. Relat. Phenom.* **12** (1977) 415.

[7] P. A. Cox, S. Evans, A. Hamnett and A. F. Orchard: *Chem. Phys. Lett.* **7** (1970) 414.

[8] J. C. Green, M. L. H. Green, P. J. Joachim, A. F. Orchard and D. W. Turner: *Phil. Trans. Roy. Soc. Lond. A* **268** (1970) 111.

[9] R. G. Egdell and A. F. Orchard: *J. Chem. Soc., Farad. Trans. II* **74** (1978) 485.

[10] G. M. Bancroft, E. Pellach and J. S. Tse: *Inorg. Chem.* **21** (1982) 2950.

[11] T. A. Carlson, M. O. Krause, F. A. Grimm, P. Keller and J. W. Taylor: *J. Chem. Phys.* **77** (1982) 5340.

[12] T. A. Carlson, A. Fahlman, W. A. Svensson, M. O. Krause, T. A. Whitley, F. A. Grimm, M. N. Piancastelli and J. W. Taylor: *J. Chem. Phys.* **81** (1984) 3828.

[13] T. A. Carlson, A. Fahlman, M. O. Krause, T. A. Whitley, F. A. Grimm, M. N. Piancastelli and J. W. Taylor: *J. Chem. Phys.* **84** (1986) 641.

[14] H. E. Wetzel: *Ph. D. Thesis* Hamburg (1987).

[15] A. Rauk, T. Ziegler and D. E. Ellis: *Theoret. Chim. Acta* **34** (1974) 49.

[16] J. Weber: *Chem. Phys. Lett.* **45** (1977) 261.

[17] S. A. Jarrett-Sprague: *Ph. D. Thesis* Manchester (1991).

[18] J. C. Green, M. F. Guest, I. H. Hillier, S. A. Jarrett-Sprague, N. Kaltsoyannis, M. A. MacDonald and K. H. Sze: *Inorg. Chem.* **31** (1992) 1588.

[19] D. Briggs: *Handbook of X-ray and Ultraviolet Photoelectron Spectroscopy* Heyden, London (1977).

[20] J. J. Yeh and I. Lindau: *At. Data Nucl. Data Tables* **32** (1985) 1.

[21] G. Cooper, J. C. Green and M. P. Payne: *Mol. Phys.* **63** (1988) 1031.

[22] R. McDowell and M. Goldblatt: *Inorg. Chem.* **10** (1971) 625.

[23] D. W. Turner, C. Baker, A. D. Baker and C. R. Brundle: *Molecular Photoelectron Spectroscopy* Wiley-Interscience, London (1970).

[24] J. S. Griffith: *The Theory of Transition Metal Ions* Cambridge University Press, London (1964).

[25] B. R. Higginson, D. R. Lloyd, P. Burroughs, D. M. Gibson and A. F. Orchard: *J. Chem. Soc., Farad. Trans. II* **74** (1973) 234.

[26] R. D. Cowan: *The Theory of Atomic Structure and Spectra* Chemical Abstracts Service, Columbus, Ohio (1981).

[27] N. Edelstein: *personal communication.*

[28] S. Evans, J. C. Green, P. J. Joachim, A. F. Orchard, D. W. Turner and J. P. Maier: *J. Chem. Soc., Farad. Trans. II* **68** (1972) 905.

[29] P. M. Boerrigter, J. G. Snijders and J. M. Dyke: *J. Electron Spectr. Rel. Phenom.* **46** (1988) 43.

[30] J. M. Dyke, N. K. Fayad, A. Morris, I. R. Trickle and G. C. Allen: *J. Chem. Phys.* **72** (1980) 3822.

[31] J. M. Dyke, G. D. Josland, A. Morris, P. M. Tucker and J. W. Tyler: *J. Chem. Soc., Farad. Trans. II* **77** (1981) 1273.

[32] P. Pyykkö and J. Li: *unpublished results.*

[33] C. A. L. Becker and J. P. Dahl: *Theor. Chim. Acta* **14** (1969) 26.

[34] C. A. L. Becker, C. J. Ballhausen and I. Trajberg: *Theor. Chim. Acta* **13** (1969) 355.

[35] F. Choplin and G. Kaufmann: *Theor. Chim. Acta* **25** (1972) 54.

[36] D. R. Truax, J. A. Geer and T. Ziegler: *J. Chem. Phys.* **59** (1973) 6662.

[37] F. R. Fenske and D. D. Radtke: *Inorg. Chem.* **7** (1968) 479.

[38] D. E. Ellis and T. Parameswan: *Int. J. Quantum Chem., Symp.* **5** (1971) 443.

[39] T. Parameswan and D. E. Ellis: *J. Chem. Phys.* **58** (1973) 2088.

[40] J. A. Tossell: *Chem. Phys. Lett.* **65** (1979) 371.

[41] A. E. Foti, V. H. Smith and M. A. Whitehead: *Mol. Phys.* **45** (1982) 385.

[42] I. H. Hillier and J. Kendrick: *Inorg. Chem.* **15** (1976) 520.

[43] W. von Niessen: *Inorg. Chem.* **26** (1987) 567.

[44] G. Cooper: *D. Phil. Thesis* Oxford (1987).

[45] W. A. Herrmann, P. Kiprof, K. Rypdal, J. Tremmel, R. Blom, R. Alberto, J. Behm, R. A. Albach, H. Bock, B. Solouki, J. Mink, D. Lichtenberger and N. E. Gruhn: *J. Am. Chem. Soc.* **113** (1991) 6527.

[46] M. Basso-Bert, P. Cassoux, F. Crasmier, D. Gervais, J. F. Labarre and P. De Loth: *J. Organomet. Chem.* **136** (1977) 201.

CHAPTER FIVE

COMPLEXES OF THE 3,4-BIS(TRIFLUOROMETHYL)-1,2-DITHIOLENE LIGAND - $[Fe_2(CO)_6S_2C_2(CF_3)_2]$ AND $[Ni(S_2C_2(CF_3)_2)_2]$

5.1 Introduction

Complexes of bidentate, unsaturated sulphur-donor ligands of the type S-C(R)-C(R)-S have been the subject of extensive investigations for almost thirty years [1]. The motives for such studies are manifold, and include the inability to assign formal oxidation states to the transition metal and the discovery of a rare structural type - the trigonal prism - in the tris complexes [2]. As part of an on-going study into the valence electronic structure of complexes of the S-C(CF_3)-C(CF_3)-S ligand, this Chapter presents PE spectroscopic data for two such systems $[Fe_2(CO)_6S_2C_2(CF_3)_2]$ and $[Ni(S_2C_2(CF_3)_2)_2]$, together with the results of Extended Hückel Molecular Orbital (EHMO) calculations.

Two limiting situations may be envisaged for the bonding in 1,2-dithiolene complexes, namely that the ligand may be regarded as neutral (I) or as a dianion (II)

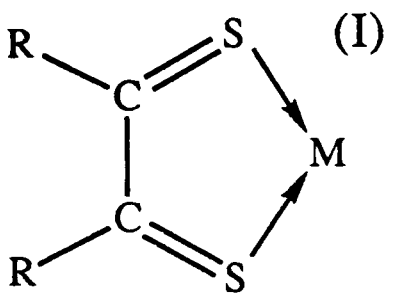

(I)

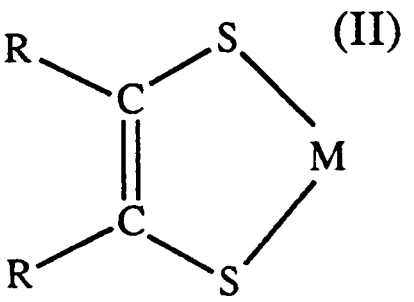

(II)

In the former the oxidation state of the metal is zero, while in the latter it is +2n, where n is the number of dithiolene ligands bonded to the metal centre. Clearly a range of intermediate situations is possible, and the configuration adopted by a given complex will be governed by factors such as the relative energies of metal and dithiolene valence MOs, and the electronic requirements of any other ligand types present in the molecule. The electronic

structure of $S_2C_2(CF_3)_2$ is discussed first, with a view to presenting the orbitals which it brings to complex formation, before a treatment of the title compounds is given.

5.2 $S_2C_2(CF_3)_2$

3,4-bis(trifluoromethyl)-1,2-dithiolene is known to possess the dithiete structure (III) and not the dithione structure (IV) [3]

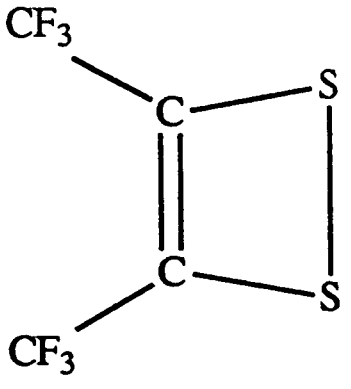

(III)

(IV)

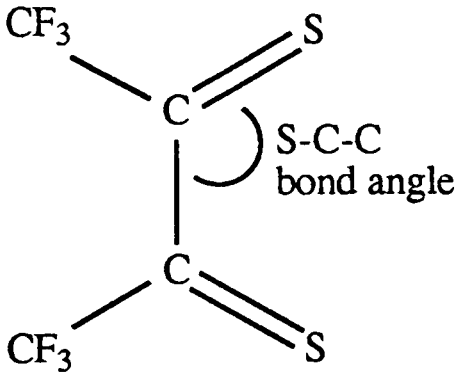

The sulphur-sulphur bond is broken upon complex formation, with a corresponding increase in the S-C-C bond angle from 100.8° in the free ligand to between 115° and 120° in its complexes [3, 4]. This opening of the ring is of critical importance to the relative energies of the valence MOs of the ligand. Figure 5.1, derived from EHMO calculations on $S_2C_2(CF_3)_2$, shows how the energies of the highest-lying MOs change as the internal S-C-C bond angle is increased from 100° to 120°. The input parameters used in the calculations are given in Appendix One. $S_2C_2(CF_3)_2$ has C_{2v} symmetry, and the symmetry labels used in Figure 5.1 are based upon the following axis system

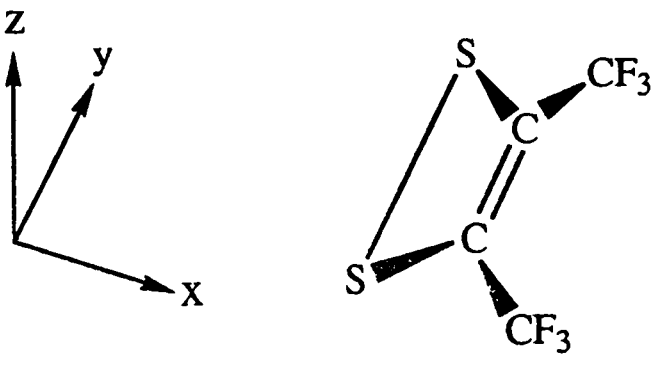

The valence MOs of $S_2C_2(CF_3)_2$ can be divided into those of σ symmetry and those of π symmetry. There are four butadiene-like π orbitals, π_1 through π_4, as shown in Figure 5.1. It is important to note that the contributions of the sulphur and carbon atoms to these π orbitals is not equal in all four cases. This is illustrated in Table 5.1, which is taken from the EHMO calculation at a S-C-C bond angle of 120°. π_1 and π_4 are to a large extent localised upon the carbon atoms, whereas π_2 and π_3 are more sulphur-based. Lying between π_1 and π_2 are two MOs which are out of phase combinations of carbon-carbon and carbon-sulphur σ bonding orbitals. The two remaining MOs, termed n_+ and n_-, are clearly bonding and antibonding respectively between the two sulphur atoms. The n_+ MO is not affected greatly by the opening of the four-membered ring, but the n_- MO is stabilised to a large extent by this process. Hence it lies inaccessibly high in energy in the free ligand (III), but is of comparable energy to the other ligand valence MOs at the S-C-C bond angles found in the dithiolene complexes.

Table 5.1: the percentage sulphur and carbon AO contributions to the π type valence MOs of $S_2C_2(CF_3)_2$. (Values determined from the EHMO calculation of $S_2C_2(CF_3)_2$ at an internal S-C-C bond angle of 120°)

Orbital	Sulphur 3p contribution (%)	Carbon 2p contribution (%)
π_1	23.0	76.2
π_2	79.4	20.4
π_3	76.9	23.3
π_4	20.5	78.0

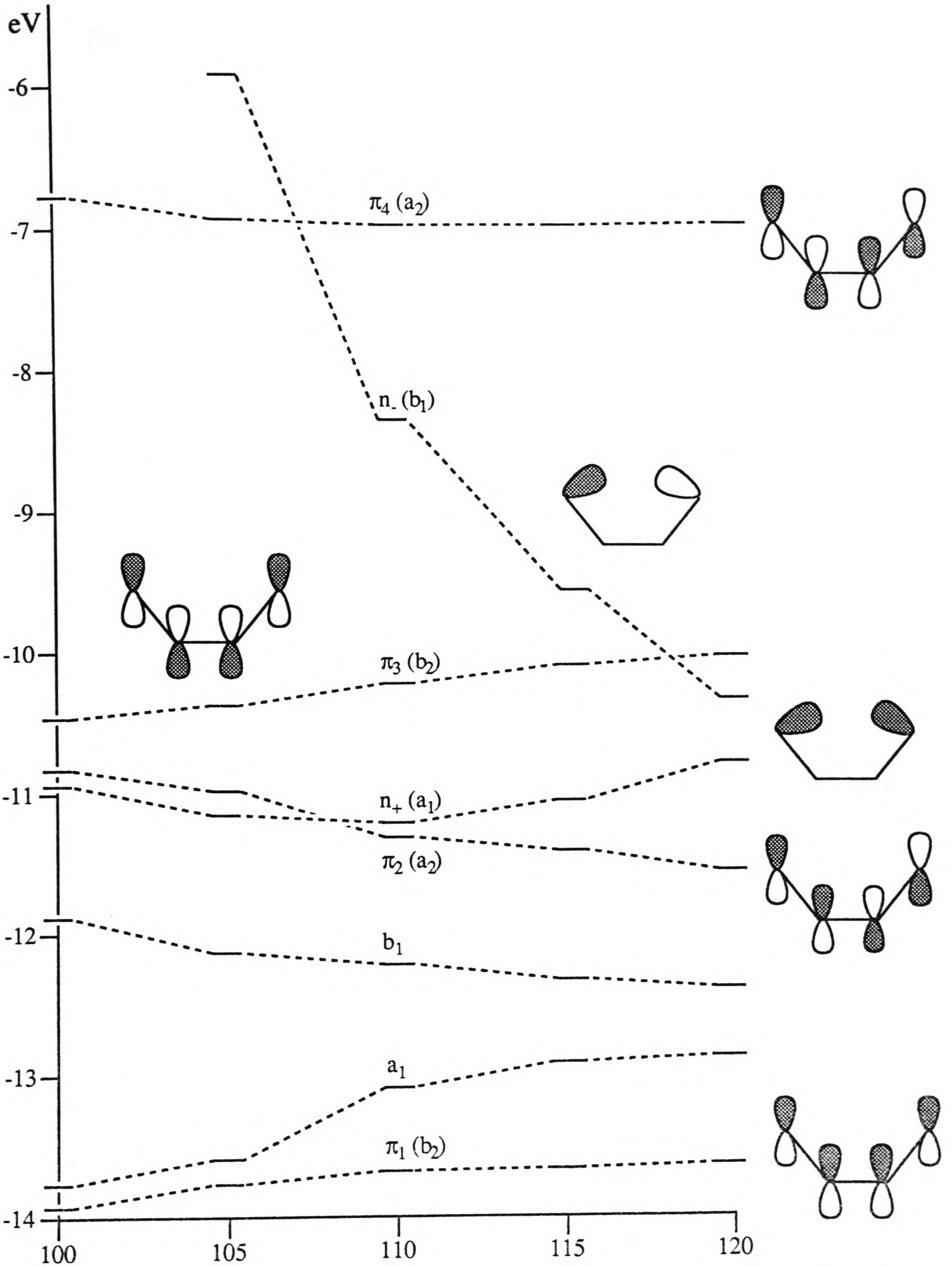

Figure 5.1: the variation in the energies of the valence MOs of $S_2C_2(CF_3)_2$ with internal S-C-C bond angle

The He I and He II PE spectra of the free ligand have been measured [5]. The MOs are filled up to and including the π_3 level, and the authors have assigned the top four ionisations to the π_3 (b_2), π_2 (a_2), b_1 and n_+ (a_1) MOs respectively. CNDO and MNDO calculations support the MO ordering inferred from Koopmans' Theorem, and differ from the EHMO calculation (at an S-C-C angle of 100°) in reversing the order of the n_+ and b_1 MOs. Nevertheless, all of the calculations are in agreement as to the number and nature of the valence MOs of (III) and it is these, together with the previously unoccupied n. MO, that form the valence MOs of the $S_2C_2(CF_3)_2$ ligand in its complexes. It should be stressed that the π_2, n_+, n. and π_3 MOs are all strongly localised upon the sulphur atoms.

5.3 $[Fe_2(CO)_6S_2C_2(CF_3)_2]$

5.3.1 Bonding and interpretation of the photoelectron spectrum

The structure of the molecule is shown in Figure 5.2. No crystallographic data exist for this particular complex, although the structure of the closely related $[Fe_2(CO)_6S_2C_2(C_6H_5)_2]$ has been determined [6]. Distortions from the idealised C_{2v} molecular symmetry are small enough so as to allow a bonding model in this point group to be established.

The bonding in complexes of the type $[M_2(CO)_6L]$ (where L is one of a wide range of π systems) has been thoroughly treated by Thorn and Hoffmann [7], and expanded upon by a number of other workers [8-13]. The $Fe_2(CO)_6$ molecular fragment has six valence orbitals of predominantly metal character which contain four electrons. In C_{2v} symmetry the valence electronic structure is given by $(1a_1)^2(1b_1)^2(1a_2)^0(1b_2)^0(2a_1)^0(2b_2)^0$ (using the numbering scheme of Hoffmann), although the $2b_2$ orbital lies much higher in energy than the other five and is unavailable for bonding with the dithiolene ligand. Lying slightly lower in energy are six more MOs, the description of which has varied between authors. Thorn and Hoffmann [7] and Van Dam et al. [10] refer to them as "heavily Fe→CO back-bonding", implying significant carbonyl localisation, whereas Anderson et al. [9] and Granozzi et al. [11] treat them as "iron lone pair orbitals". A more extensive discussion of this topic is given in connection with the cross section results presented later. Of central

importance, however, is that the overlap of these orbitals with those of the incoming ligand is small.

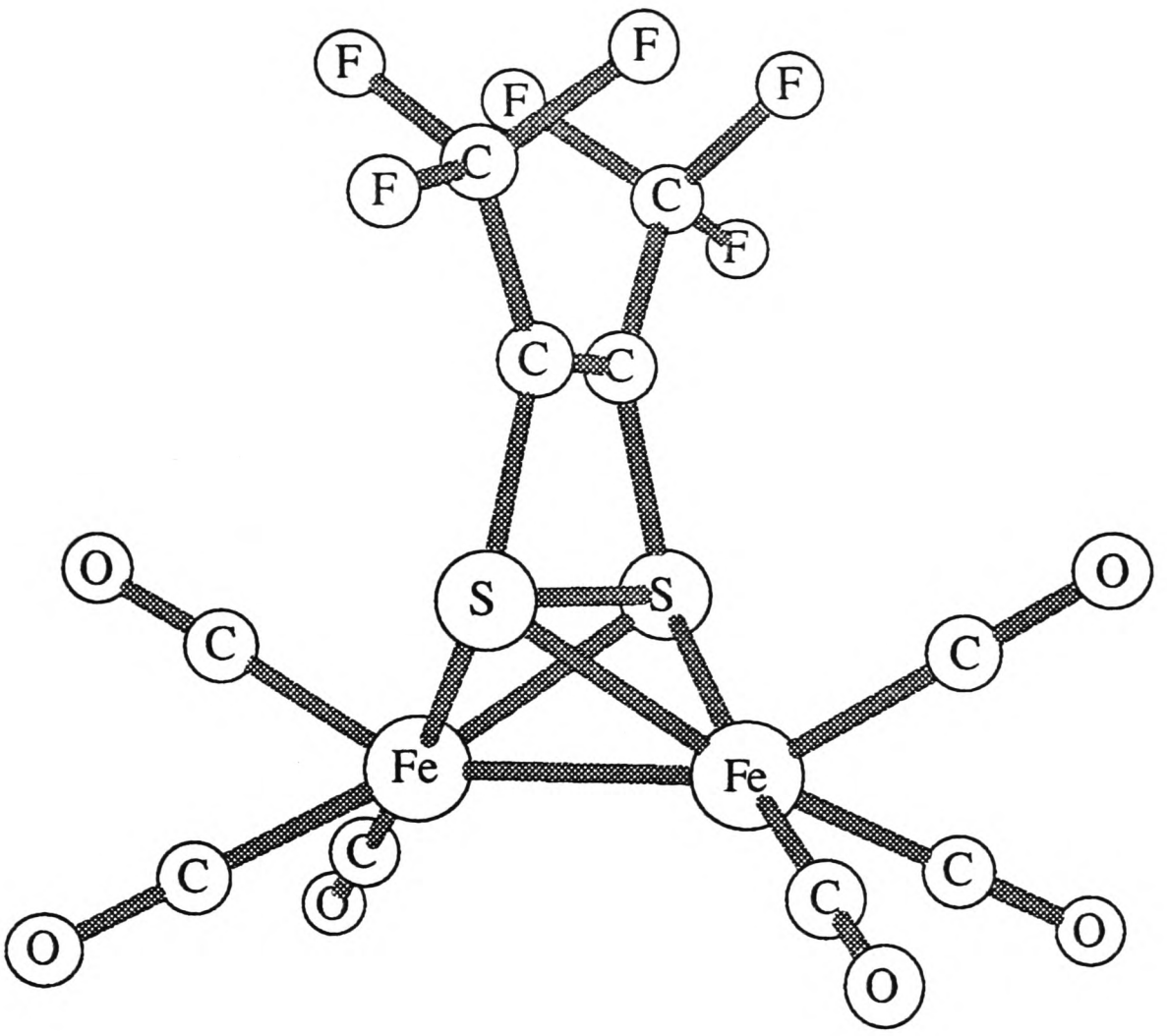

Figure 5.2 : the molecular structure of $[Fe_2(CO)_6S_2C_2(CF_3)_2]$

A qualitative orbital scheme resulting from interaction of these fragment MOs with those of the $S_2C_2(CF_3)_2$ ligand is given in Figure 5.3. The co-ordinate system employed is chosen so as to match that used in discussing $S_2C_2(CF_3)_2$, i.e. with the dithiolene ligand lying in the xy plane and the iron-iron axis as the z axis. The ligand valence orbital ordering is that predicted by the EHMO calculation for a S-C-C bond angle of 115°, which is that found in $[Fe_2(CO)_6S_2C_2(C_6H_5)_2]$ [6]. The highest occupied complex MO is predicted to be the $5a_1$ iron-iron bonding MO (using the numbering scheme of Figure 5.3), with the electrons in the $1b_1$ $Fe_2(CO)_6$ fragment MO being transferred into the dithiolene b_1 (n_-) LUMO. This interaction is believed to be the main source of metal-ligand bonding within this type of complex (see page 189). Figure 5.4 shows contour plots of the b_1 symmetry

MOs of the $Fe_2(CO)_6$ and $S_2C_2(CF_3)_2$ fragments (taken from the EHMO calculation on $S_2C_2(CF_3)_2$ at a S-C-C bond angle of 115° and from a fragment analysis of the EHMO calculation performed upon $[Fe_2(CO)_6S_2C_2(CF_3)_2]$ - page 195) from which it may be clearly seen how metal-ligand bonding is generated. The $Fe_2(CO)_6$-based b_1 fragment MO is strongly localised in the region between the iron atoms, with the iron-iron axis lying in a nodal plane which bisects the carbon-carbon bond of the S-C-C-S backbone of the dithiolene ligand in the complex.

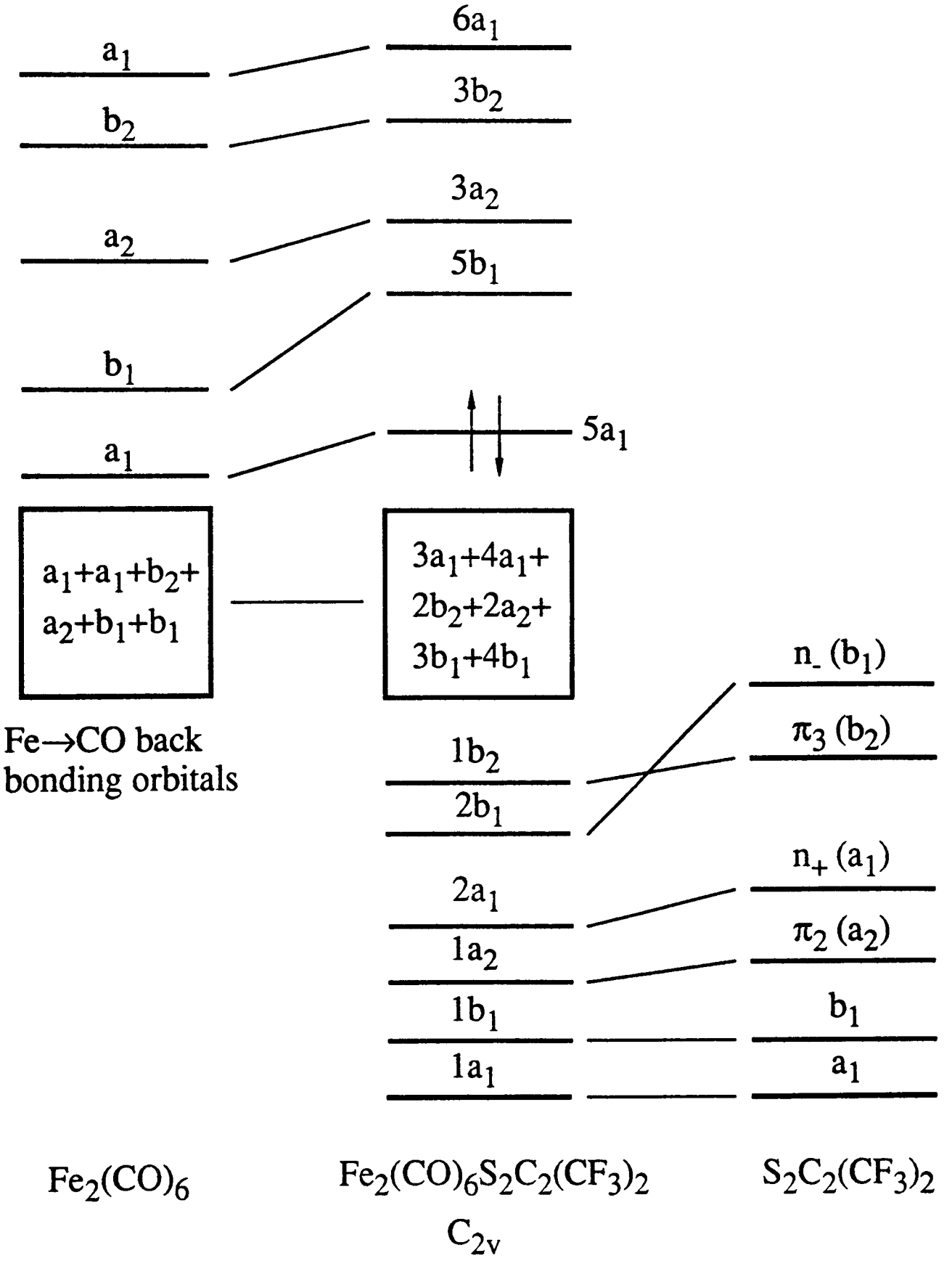

Figure 5.3 : qualitative MO diagram for $[Fe_2(CO)_6S_2C_2(CF_3)_2]$

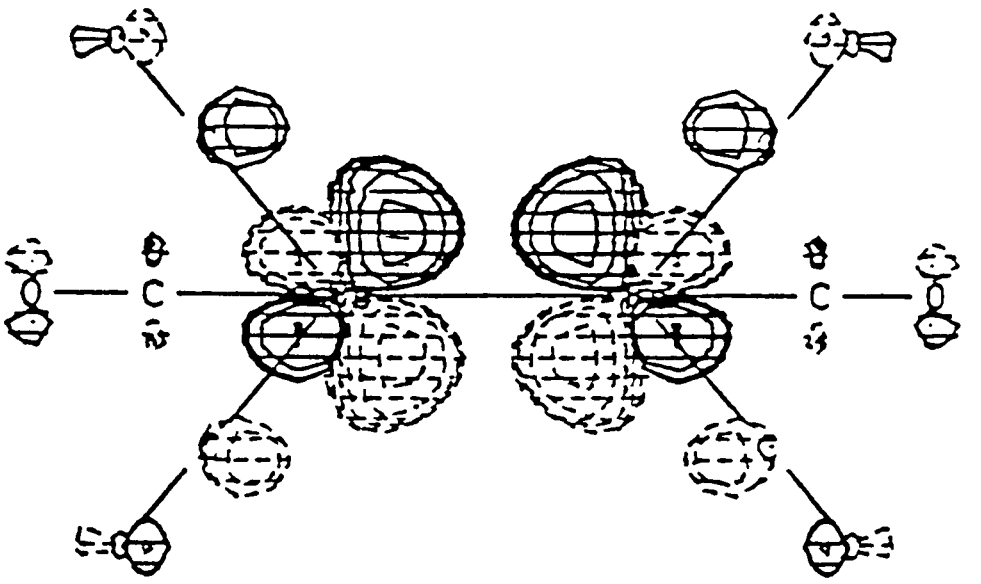

a

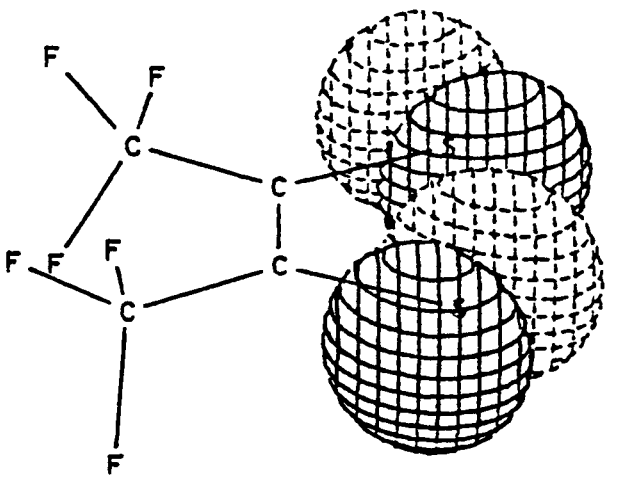

b

Figure 5.4 : the b_1 symmetry fragment MOs of the (a) $Fe_2(CO)_6$ (viewed from above) and (b) $S_2C_2(CF_3)_2$ moieties of $[Fe_2(CO)_6S_2C_2(CF_3)_2]$, illustrating the origin of the principal iron-dithiolene bonding

The He I and He II spectra of $[Fe_2(CO)_6S_2C_2(CF_3)_2]$ are presented in Figure 5.5, and the IEs and band assignments are given in Table 5.2. A number of PE spectroscopic studies of molecules of the form $[Fe_2(CO)_6L]$ have been carried out, and these are summarised in Table 5.3, together with the MO calculations that have been performed on these systems. In addition, $[Ru_2(CO)_6L]$ (L=$((C_2H_5)C^*=C(C_2H_5)$-C(O)-

$(C_2H_5)C=C^*(C_2H_5)$) (asterisked carbon atoms bind to the iron atoms)) has received attention [12], together with the heterobinuclear compound $[FeRu(CO)_6(N(^iPr)CH_2\text{-}CH_2N(^iPr))]$ [13]. There are no reports of L=dithiolene. The assignment given in Table 5.2 is in agreement with those reported previously, in so far as the differences in L allow. Of the ionisations occurring above 13.5 eV, bands G and H are assigned to carbon-fluorine, carbon-carbon and carbon-sulphur σ orbitals, together with the fluorine 2p lone pair and carbonyl 5σ and 1π orbitals [9, 14]. Peak I, at 18.01 eV, is assigned to the carbonyl 4σ MOs. The large number of MOs ionising in this region makes detailed assignment impossible, and the bands above 13.5 eV will not be discussed further.

Six bands can be distinguished in the He I spectrum with IEs below 13 eV, and these are assigned to the occupied MOs presented in Figure 5.3. Band A is due to ionisations from the six Fe→CO back-bonding MOs, together with the $5a_1$ iron-iron bonding MO. A similar band is seen in all of the PE spectra of the $[Fe_2(CO)_6L]$ systems. In some cases, e.g. L=(μ-butatriene) [11], the iron-iron bonding MO is clearly distinguished as a low IE shoulder to the first band. Moving to higher IE, a "window" is found in the ionisations of the $Fe_2(CO)_6$ fragment, in which bands due to ligand-based MOs occur. In $[Fe_2(CO)_6S_2C_2(CF_3)_2]$, bands B, C, D and E are assigned to the four ligand-based MOs $1b_2$ (π_3), $2b_1$ (n_-), $2a_1$ (n_+) and $1a_2$ (π_2) respectively. The justification for this orbital ordering is discussed below. Band F is assigned to the $1a_1$ and $1b_1$ MOs. It is impossible to tell whether the a_1 (π_1) ligand MO is ionising in this region as well, but it is more likely that it lies under the main CF_3/CO band above 13.5 eV.

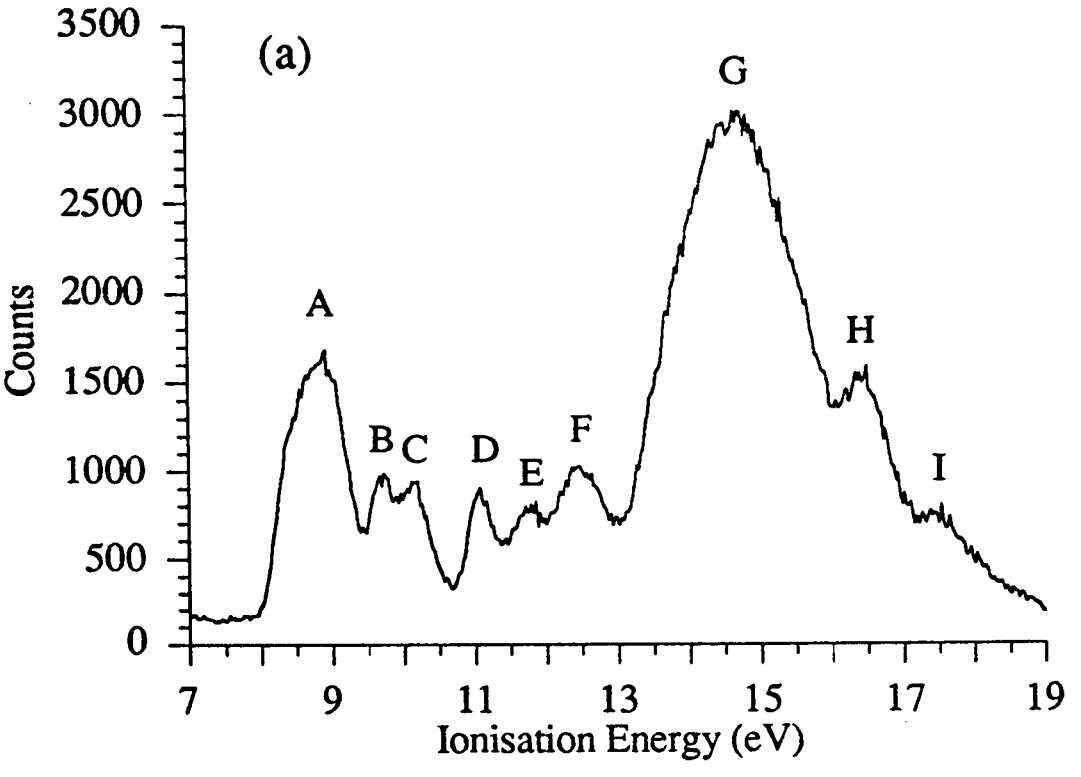

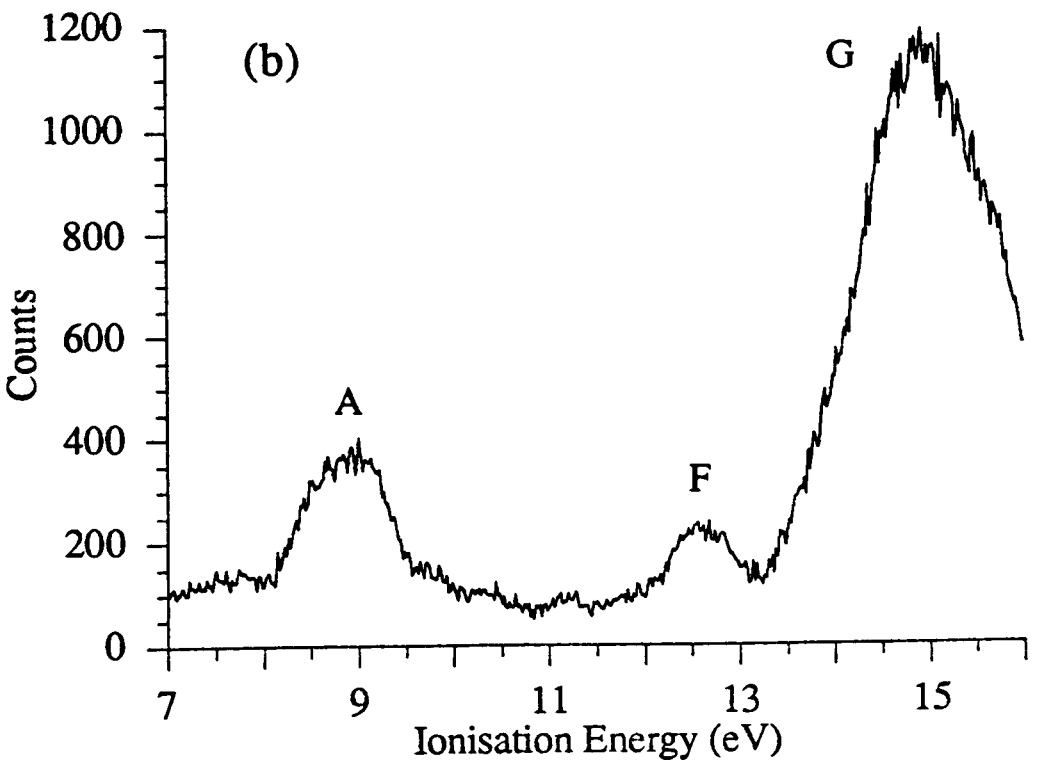

Figure 5.5 : the (a) He I and (b) He II PE spectra of $[Fe_2(CO)_6S_2C_2(CF_3)_2]$

Table 5.2 : IEs and band assignments of the PE spectra of $[Fe_2(CO)_6S_2C_2(CF_3)_2]$ and $S_2C_2(CF_3)_2$

Compound	Band	IE (eV)	Assignment
$[Fe_2(CO)_6S_2C_2(CF_3)_2]$	A	9.00	$5a_1$ + six Fe→CO back-bonding MOs
	B	9.89	$1b_2$ (π_3)
	C	10.36	$2b_1$ (n_-)
	D	11.30	$2a_1$ (n_+)
	E	12.15	$1a_2$ (π_2)
	F	12.74	$1b_1 + 1a_1$ σ bonding orbitals of the dithiolene ligand, fluorine 2p lone pair, CO 5σ and 1π
	G	15.13	
	H	16.98	
	I	18.01	CO 4σ
$S_2C_2(CF_3)_2$ [a]		10.2	$\pi_3 + \pi_2$
		12.95	$1b_1$
		13.45	n_+

[a] Data from reference [5]

Table 5.2 also presents the energies of the first four ionisations of $S_2C_2(CF_3)_2$. The ligand-based ionisations in the spectrum of $[Fe_2(CO)_6S_2C_2(CF_3)_2]$ (bands B-F) generally have lower IEs than the corresponding bands in the free ligand, which is almost certainly due to a shift of charge from the $Fe_2(CO)_6$ fragment to the ligand. This is in agreement with the previous studies [10], in which it was concluded that metal-ligand bonding is generated primarily through the donation of electrons from the $Fe_2(CO)_6$ moiety to empty orbitals on the bridging ligands. Formally two electrons are transferred from the $1b_1$ iron-iron bonding

fragment MO into the n- orbital of $S_2C_2(CF_3)_2$ (the ligand is functioning as a dianion), and this provides a good example of how the low-lying unoccupied ligand MOs become filled upon complexation. It is this availability of unoccupied MOs lying very close in energy to the ligand HOMO that can make the assignment of oxidation state problematic in dithiolene complexes.

Table 5.3 : summary of the previous PE spectroscopic and MO calculational studies of $[Fe_2(CO)_6L]$ systems

L	Type of study	Reference
B_2H_6	PES	[8]
(μ-butatriene)	PES/CNDO calculation	[11]
$(C_2H_5\text{-}C_2\text{-}C_2H_5)_2CO$	PES/ab initio calculation	[12]
S_2	PES/SCF-Xα-SW, ab initio calculations	[8, 10]
$(({}^iPr)S)_2$	PES/CNDO calculation	[10]
$(({}^tBu)NS)_2$	PES/CNDO calculation	[10]

5.3.2 RPPICS results

The He II spectrum reveals a dramatic collapse of bands B-E, to the extent that only bands A and F can still be distinguished. A similar effect was observed for the sulphur-based orbitals of $[Fe_2(CO)_6S_2]$, $[Fe_2(CO)_6({}^iPrS)_2]$ and $[Fe_2(CO)_6({}^tBuNS)_2]$ [10]. To explore these intensity changes more fully, the PE spectrum of $[Fe_2(CO)_6S_2C_2(CF_3)_2]$ was measured over the photon energy range 24-80 eV using synchrotron radiation, and this effect was observed in all of the spectra obtained above a photon energy of ca. 35 eV. Figure 5.6 shows the RPPICS of the six valence bands of $[Fe_2(CO)_6S_2C_2(CF_3)_2]$ over the photon energy range employed and these are given individually in Figure 5.7. There are marked differences in cross section behaviour between the orbitals localised on sulphur and those with significant iron, carbon and oxygen contributions. It must be noted that the very

small cross sections of bands B-E above a photon energy of ca. 35 eV make band area measurements difficult to obtain with certainty. Thus it is not possible to tell whether minor variations in the RPPICS of bands B-E above 35 eV are real or induced by the curve fitting program.

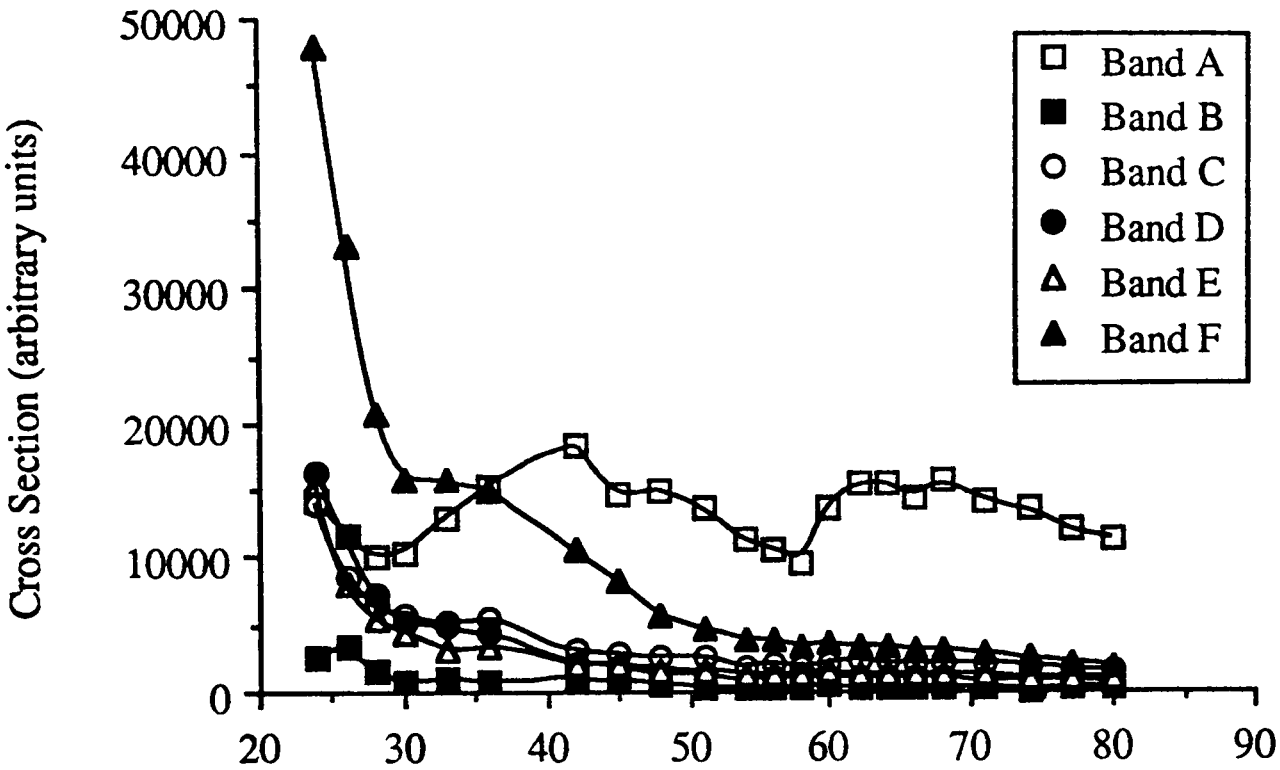

Figure 5.6 : RPPICS of bands A-F in the PE spectrum of $[Fe_2(CO)_6S_2C_2(CF_3)_2]$

The cross section of band A has two major features - a maximum at 42 eV and another enhancement with separate maxima at 64 and 68 eV. The origin of these can be traced to the high iron 3d AO contribution to the seven MOs ionising under this band. The maximum at 42 eV is due to the delayed maximum (Chapter 1.4.3 (b)) in the cross section of the 3d AO, calculated to occur at an incident photon energy of ca. 45 eV in the element [15]. Another possible explanation is a shape effect, and indeed the maximum in the RPPICS of the $1a_1'$ (Fe $3d_{z^2}$) band of ferrocene at 45 eV was attributed to this cause [16]. It is unlikely, however, that the molecular potential field of ferrocene is similar to that of $[Fe_2(CO)_6S_2C_2(CF_3)_2]$, and consequently an atomic effect is the more plausible explanation.

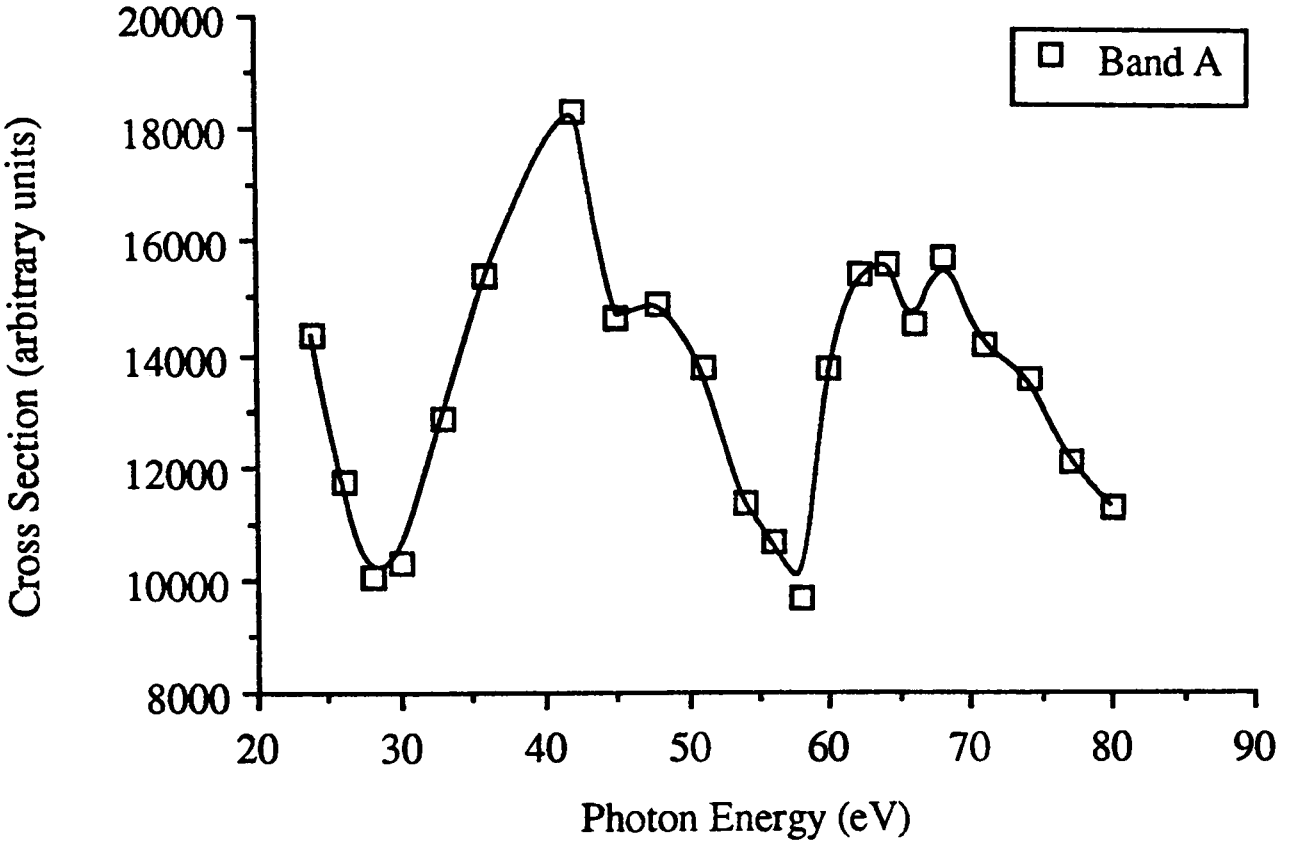

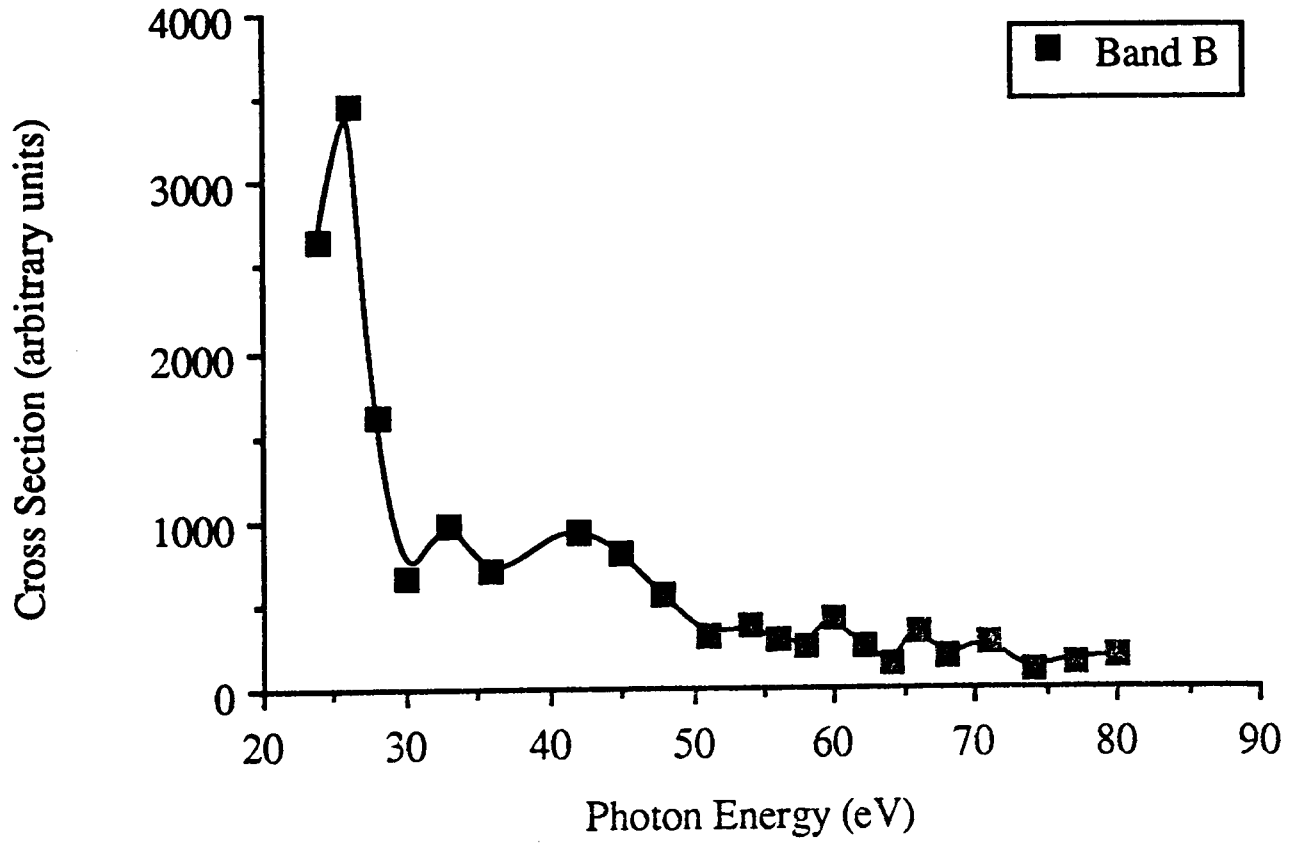

Figure 5.7 : individual RPPICS of bands A-F in the PE spectrum of $[Fe_2(CO)_6S_2C_2(CF_3)_2]$

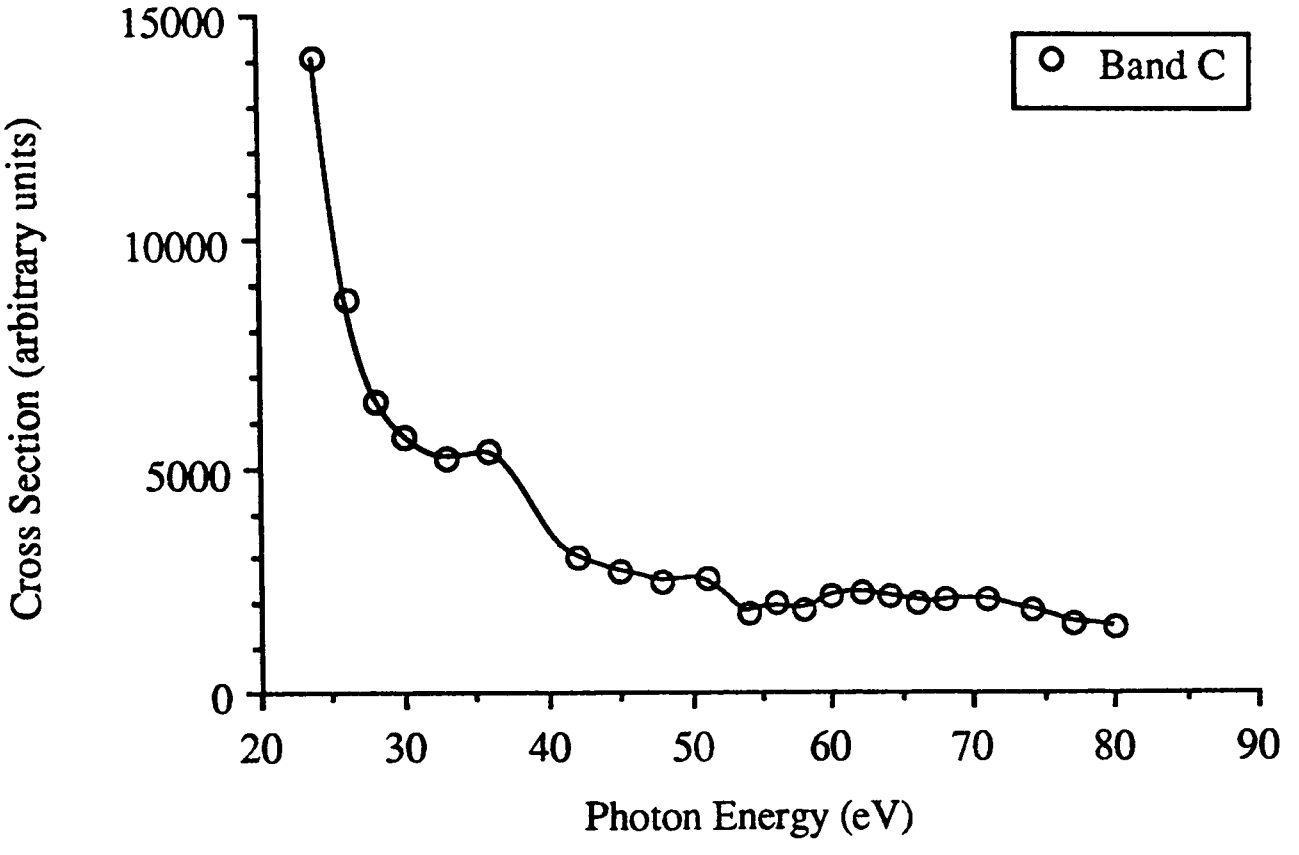

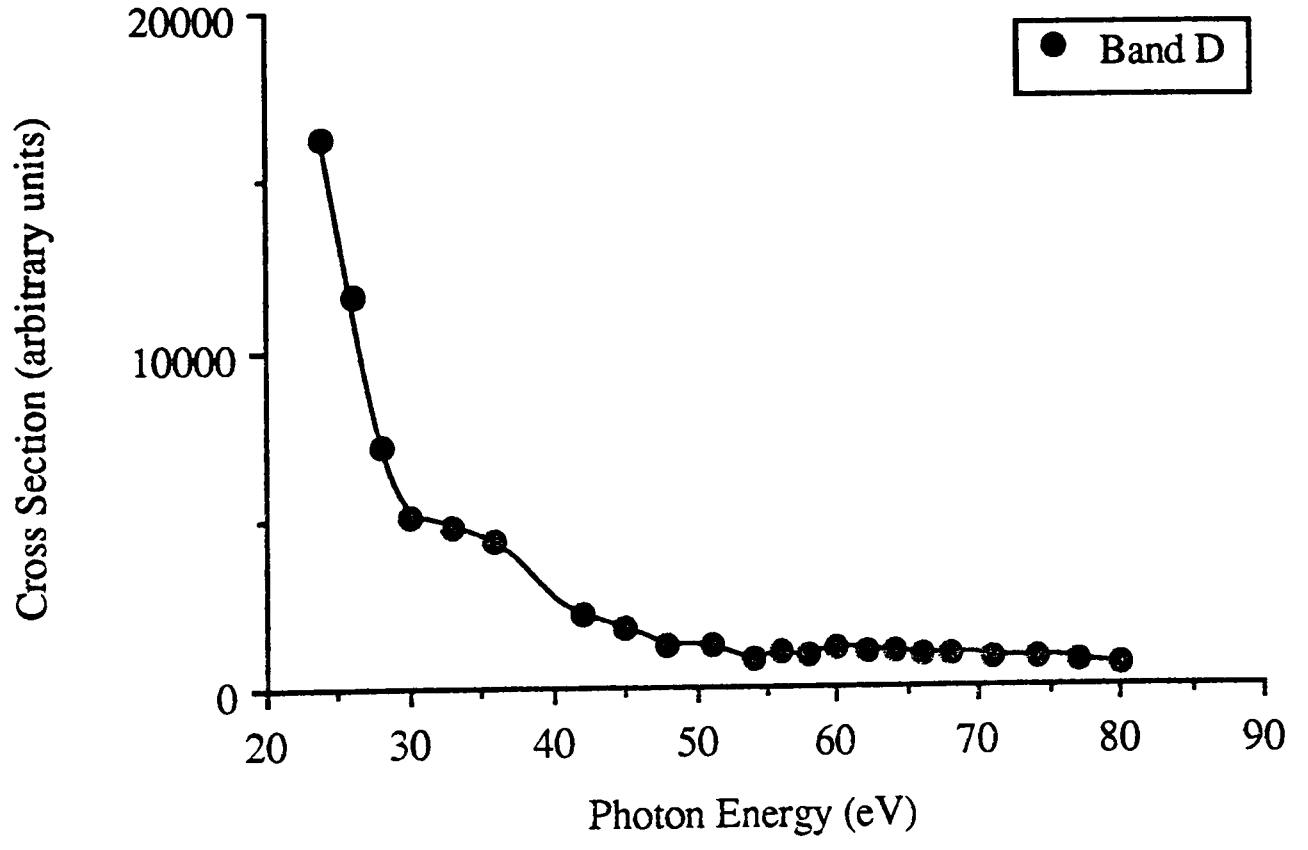

Figure 5.7 : individual RPPICS of bands A-F in the PE spectrum of $[Fe_2(CO)_6S_2C_2(CF_3)_2]$ (continued)

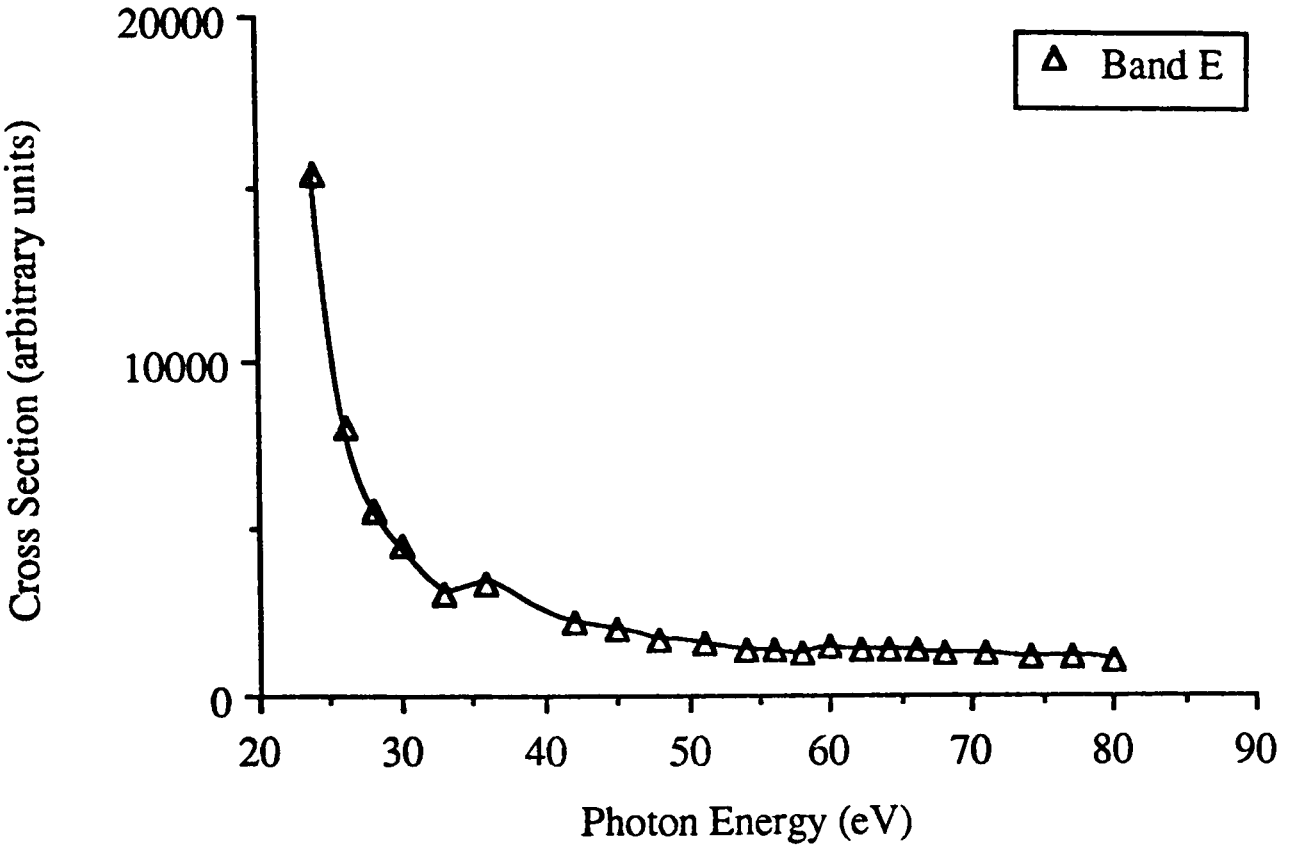

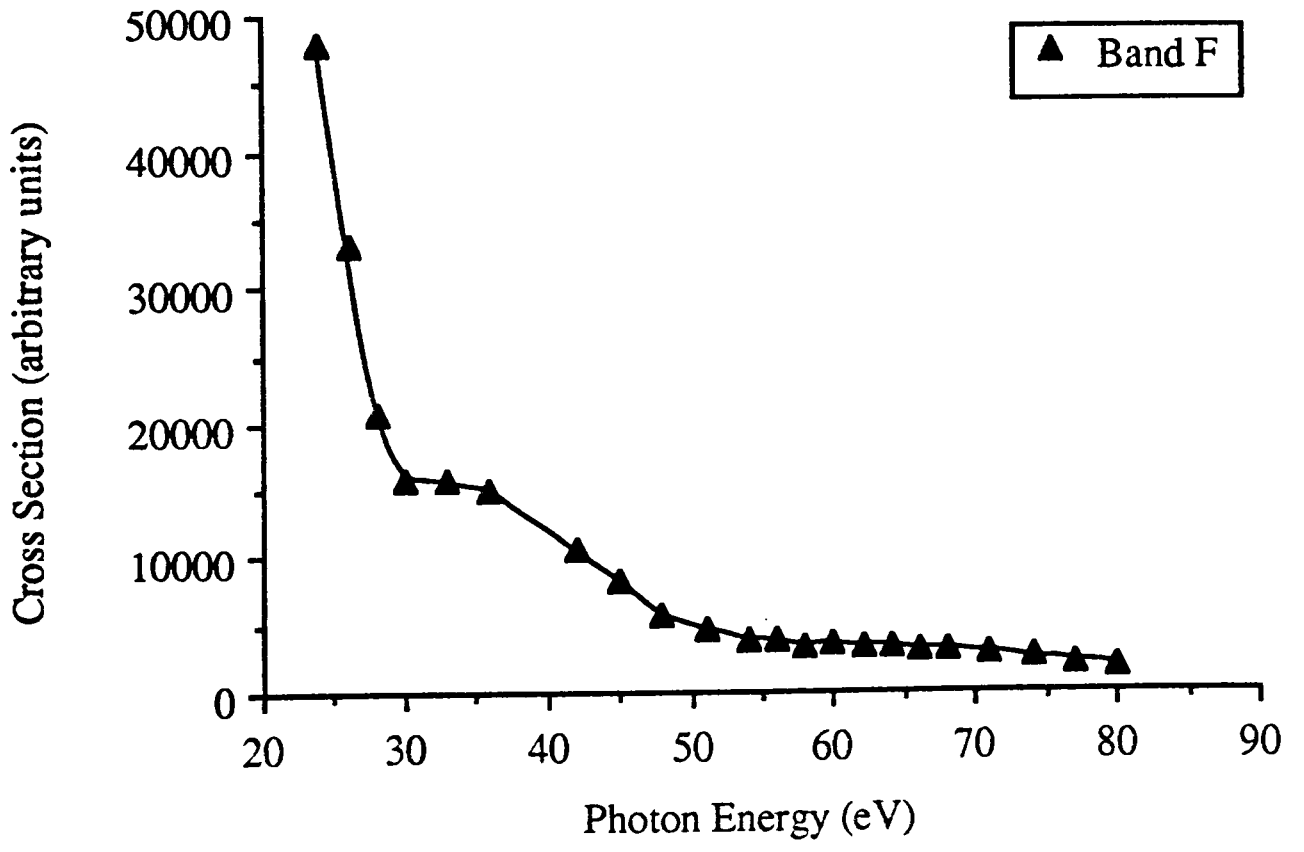

Figure 5.7 : individual RPPICS of bands A-F in the PE spectrum of $[Fe_2(CO)_6S_2C_2(CF_3)_2]$ (continued)

At low photon energies, the RPPICS of band A has a steep fall off. This is important in that it implies some AO contribution other than iron 3d to the MOs giving rise to band A. If the seven MOs, $3a_1$ through $5a_1$, were entirely metal-localised, their cross sections would be expected to rise from threshold to the delayed maximum. If, however, there is a significant carbon and oxygen 2p AO contribution, such as would arise if the MOs were Fe→CO back-bonding, then the observed RPPICS are readily explained. The carbon and oxygen 2p cross sections (which have a monotonic fall off with increasing photon energy) dominate the RPPICS at low photon energies, when the iron 3d cross section is small. As the photon energy is increased, the carbon and oxygen cross sections decrease, while the iron increases to produce the maximum at 42 eV. The origin of the shoulder at 46 eV is unclear.

A number of calculations has been performed upon $[Fe_2(CO)_6L]$ systems, usually in conjunction with the PES results detailed earlier (Table 5.3). Ab initio SCF calculations upon $[Fe_2(CO)_6S_2]$ [10] give iron 3d contributions of between 65 and 84% to the six MOs $3a_1$-$4b_1$. The $5a_1$ HOMO is calculated to have only 53% iron character, and to be delocalised over the carbonyl ligands. CNDO calculations on $[Fe_2(CO)_6(\mu\text{-butatriene})]$ [11] and SCF-Xα-SW calculations on $[Fe_2(CO)_6S_2]$ [9] produce iron contributions of 62-88% and 50-79% respectively for the $3a_1$ through $4b_1$ MOs.

A series of EHMO calculations was performed upon $[Fe_2(CO)_6S_2C_2(CF_3)_2]$. The one which most closely reproduced the energy ordering of the bands in the PE spectrum followed a charge iteration on the iron atoms only. The parameters used in this calculation are given in Appendix One.

Analysis of the reduced charge matrix of this EHMO calculation reveals the $3a_1$-$4b_1$ MOs to have iron contributions ranging from 48-73%. The other AO contributors are predominantly the carbonyl ligands. Thus all of the calculations are in broad agreement as to the iron content of these MOs, and yet differences exist as to their description. The RPPICS results presented here suggest that it is incorrect to refer to them as "iron lone pair" orbitals, as significant carbon and oxygen contributions are found.

The second major feature in the RPPICS of band A, with maxima at 64 and 68 eV, arises from resonant photoemission of iron 3d-based electrons in the vicinity of 3p→3d giant resonant absorption (Chapter 1.4.3 (c)), which occurs close to the 3p subshell IEs ($^2P_{3/2}$ = 59 eV $^2P_{1/2}$ = 61 eV [17]). For $[Fe_2(CO)_6S_2C_2(CF_3)_2]$, 3p→3d giant resonant absorption is represented by the process

$$3p^63a_1^24a_1^22b_2^22a_2^23b_1^24b_1^25a_1^25b_1^0 + h\nu \rightarrow 3p^53a_1^24a_1^22b_2^22a_2^23b_1^24b_1^25a_1^25b_1^1$$

(considering absorption to the LUMO only). The irreducible representations of the $3p^5$ configuration transform as $(A_1 + B_1 + B_2)$ in C_{2v} symmetry, and hence the states arising from the $3p^53a_1^24a_1^22b_2^22a_2^23b_1^24b_1^25a_1^25b_1^1$ configuration are given by the direct product

$$(A_1 + B_1 + B_2) \times B_1 = {}^1B_1 + {}^1A_1 + {}^1A_2 + {}^3B_1 + {}^3A_1 + {}^3A_2$$

The electric dipole selection rule allows transitions to A_1, B_1 and B_2 excited states only, and in the LS coupling limit we have that $\Delta S = 0$, giving the allowed final states as $^1B_1$ and $^1A_1$. Autoionisation

$$3p^53a_1^24a_1^22b_2^22a_2^23b_1^24b_1^25a_1^25b_1^1 \rightarrow 3p^53a_1^24a_1^22b_2^22a_2^23b_1^24b_1^25a_1^25b_1^0 + e^-$$

is possible, together with the super-Coster-Kronig decay processes

$$3p^5 3a_1^2 4a_1^2 2b_2^2 2a_2^2 3b_1^2 4b_1^2 5a_1^2 5b_1^1 \rightarrow \begin{cases} 3p^6 3a_1^2 4a_1^2 2b_2^2 2a_2^2 3b_1^2 4b_1^2 5a_1^1 5b_1^0 + e^- \\ 3p^6 3a_1^2 4a_1^2 2b_2^2 2a_2^2 3b_1^2 4b_1^1 5a_1^2 5b_1^0 + e^- \\ 3p^6 3a_1^2 4a_1^2 2b_2^2 2a_2^2 3b_1^1 4b_1^2 5a_1^2 5b_1^0 + e^- \\ 3p^6 3a_1^2 4a_1^2 2b_2^2 2a_2^1 3b_1^2 4b_1^2 5a_1^2 5b_1^0 + e^- \\ 3p^6 3a_1^2 4a_1^2 2b_2^1 2a_2^2 3b_1^2 4b_1^2 5a_1^2 5b_1^0 + e^- \\ 3p^6 3a_1^2 4a_1^1 2b_2^2 2a_2^2 3b_1^2 4b_1^2 5a_1^2 5b_1^0 + e^- \\ 3p^6 3a_1^1 4a_1^2 2b_2^2 2a_2^2 3b_1^2 4b_1^2 5a_1^2 5b_1^0 + e^- \end{cases}$$

the final states of which are identical to those produced by direct photoionisation

$$3p^6 3a_1^2 4a_1^2 2b_2^2 2a_2^2 3b_1^2 4b_1^2 5a_1^2 5b_1^0 + h\nu \rightarrow 3p^6 3a_1^2 4a_1^2 2b_2^2 2a_2^2 3b_1^2 4b_1^2 5a_1^1 5b_1^0 + e^-$$

$$3p^6 3a_1^2 4a_1^2 2b_2^2 2a_2^2 3b_1^2 4b_1^2 5a_1^2 5b_1^0 + h\nu \rightarrow 3p^6 3a_1^2 4a_1^2 2b_2^2 2a_2^2 3b_1^2 4b_1^1 5a_1^2 5b_1^0 + e^-$$

$$3p^6 3a_1^2 4a_1^2 2b_2^2 2a_2^2 3b_1^2 4b_1^2 5a_1^2 5b_1^0 + h\nu \rightarrow 3p^6 3a_1^2 4a_1^2 2b_2^2 2a_2^2 3b_1^1 4b_1^2 5a_1^2 5b_1^0 + e^-$$

$$3p^6 3a_1^2 4a_1^2 2b_2^2 2a_2^2 3b_1^2 4b_1^2 5a_1^2 5b_1^0 + h\nu \rightarrow 3p^6 3a_1^2 4a_1^2 2b_2^2 2a_2^1 3b_1^2 4b_1^2 5a_1^2 5b_1^0 + e^-$$

$$3p^6 3a_1^2 4a_1^2 2b_2^2 2a_2^2 3b_1^2 4b_1^2 5a_1^2 5b_1^0 + h\nu \rightarrow 3p^6 3a_1^2 4a_1^2 2b_2^1 2a_2^2 3b_1^2 4b_1^2 5a_1^2 5b_1^0 + e^-$$

$$3p^6 3a_1^2 4a_1^2 2b_2^2 2a_2^2 3b_1^2 4b_1^2 5a_1^2 5b_1^0 + h\nu \rightarrow 3p^6 3a_1^2 4a_1^1 2b_2^2 2a_2^2 3b_1^2 4b_1^2 5a_1^2 5b_1^0 + e^-$$

$$3p^6 3a_1^2 4a_1^2 2b_2^2 2a_2^2 3b_1^2 4b_1^2 5a_1^2 5b_1^0 + h\nu \rightarrow 3p^6 3a_1^1 4a_1^2 2b_2^2 2a_2^2 3b_1^2 4b_1^2 5a_1^2 5b_1^0 + e^-$$

Inter-channel coupling between the corresponding final states in the resonant and direct ionisation processes should lead to two overlapping Fano profiles (resulting from absorption to the $^1B_1$ and$^1A_1$ excited states) for the RPPICS of band A. A good fit was obtained using equation (1.8) to two Fano profiles over the photon energy range 58-80 eV. The values of the Fano parameters are given in Table 5.4. The large value of q, the line profile index, for the lower photon energy profile, indicates a strong contribution of the giant resonant ionisation process to the RPPICS in this region. (N.B. when fitting two profiles to equation (1.8), the Fano function fitting program allows the q values of the two profiles to vary independently). That two Fano profiles were required to fit the RPPICS of band A in the p→d resonance region suggests that the $^1B_1$ and $^1A_1$ excited states are well separated in energy. The spin-orbit splitting of the iron 3p subshell is not great enough to

explain the two maxima at 64 and 68 eV. An alternative explanation, which cannot be discounted, is the presence of intermediate states arising from absorption to MOs other than the LUMO.

Table 5.4 : Fano parameters obtained from the RPPICS of band A in the PE spectrum of $[Fe_2(CO)_6S_2C_2(CF_3)_2]$

Profile number	q	E_r (eV)	Γ
1	1.92	60	13.65
2	0.30	65	4.55

Background cross section = 3195 hν range = 58-80 eV

The RPPICS of bands C, D and E are very similar to one another, with an essentially monotonic fall off from 24-80 eV. The Cooper minimum of the 3p subshell of atomic sulphur is calculated to occur at a photon energy of 36 eV [15] (corresponding to a PE KE of 26 eV) and the recovery of the cross section after this minimum is not great. Hence the observed cross section behaviour of bands C, D and E is in agreement with their being due to sulphur-based MOs. This is also true of the RPPICS of band B, which is similar to those of bands C, D and E but which has a small maximum at 42 eV and is more animated in the region of the p→d resonance. Both of these features suggest a small iron 3d AO contribution to the MO ionising under band B.

The ligand valence orbital ordering at a S-C-C bond angle of 115° is π_2, n_+, π_3, n_-. Simple overlap arguments suggest that the chief $Fe_2(CO)_6$-ligand interaction will be between the n_+ (a_1) and n_- (b_1 - Figure 5.4) ligand valence orbitals and the metal-based MOs of the same symmetry, with the π type MOs being less perturbed and with the interaction of the n_- MO being greater than that of the n_+ as it lies closer energetically to the metal fragment valence orbitals. Thus while bands D and E may be assigned with some confidence to the $2a_1$ (n_+) and $1a_2$ (π_2) MOs, it is not clear whether the π_3/n_- ordering in the free ligand is reversed in the complex.

The EHMO calculation performed upon $[Fe_2(CO)_6S_2C_2(CF_3)_2]$ indicates that the n- MO is indeed stabilised below the π_3 on complex formation and gives 42% iron and 32% sulphur contribution to the $1b_2$ (π_3) MO and a 17% iron and 73% sulphur contribution to the $2b_1$ (n-). While these numbers must be treated with caution, given the approximations inherent in the EHMO approach, they suggest a much greater sulphur AO character to the $2b_1$ MO than the $1b_2$, and vice versa for their iron components. This is in agreement with the RPPICS data, and hence band B is assigned to the $1b_2$ (π_3) MO and band C to the $2b_1$ (n-) MO which is bonding between the $Fe_2(CO)_6$ and $S_2C_2(CF_3)_2$ fragments.

Band F has RPPICS behaviour which is qualitatively similar to that of bands C, D and E, but which is quantitatively different. The fall off in cross section in the region 30-60 eV is much less steep than the other bands and can be explained by assigning band F to the more carbon-based $1a_1$ and $1b_1$ MOs. These are calculated to have approximately equal sulphur and carbon character (ca. 30%) in the EHMO calculation on $[Fe_2(CO)_6S_2C_2(CF_3)_2]$. There is no radial node in the carbon 2p wavefunction and hence no Cooper minimum in its cross section. Hence the RPPICS of the $1a_1$ and $1b_1$ MOs hold up much better with increasing photon energy than those of bands B-E.

All five bands B-F share a feature in their cross sections between 30 and 36 eV which in some cases is a distinct maximum (bands B, C and E) and in others (D and F) is less pronounced. This is tentatively assigned to a molecular shape resonance, as there are no atomic effects which readily explain it.

5.4 $[Ni(S_2C_2(CF_3)_2)_2]$

Complexes of the type $[Ni(S_2C_2R_2)_2]$, where R = H, CN, CF_3 and Ph, have been shown to possess a square planar structure (Figure 5.8) [4]. Thus the co-ordination symmetry about the nickel atom is D_{2h}, and the bonding in $[Ni(S_2C_2(CF_3)_2)_2]$ will be developed in this point group. For consistency, the axis system employed is that used in the discussions of $S_2C_2(CF_3)_2$ and $[Fe_2(CO)_6S_2C_2(CF_3)_2]$, with the ligands lying in the xy plane.

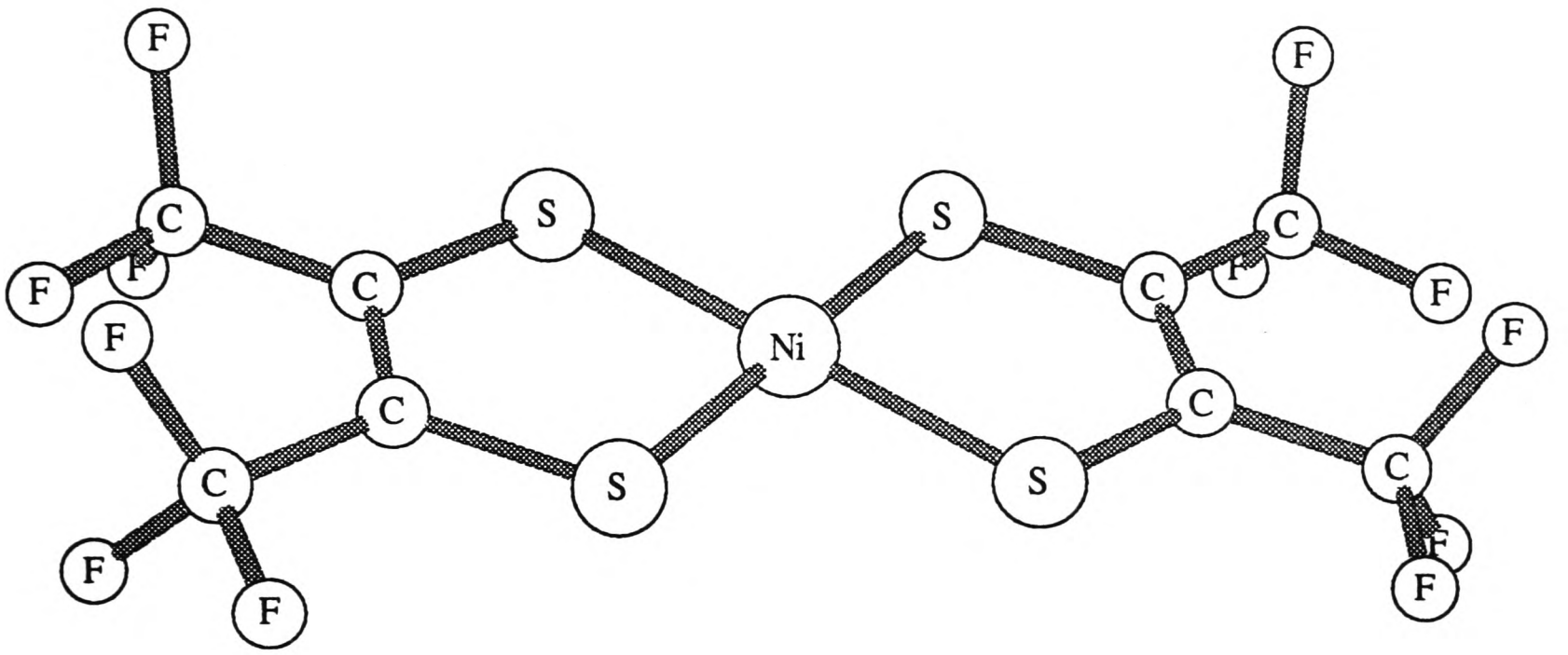

Figure 5.8 : the molecular structure of $[Ni(S_2C_2(CF_3)_2)_2]$

A qualitative MO scheme for $[Ni(S_2C_2(CF_3)_2)_2]$ is presented in Figure 5.9. The π_3 ligand orbital now lies above the n_-, as the S-C-C bond angle has increased to 119° [18] from the 115° found in $[Fe_2(CO)_6S_2C_2(CF_3)_2]$. Each valence MO of $S_2C_2(CF_3)_2$ interacts with its counterpart on the other ligand to produce an orbital of u symmetry and one of g symmetry. The energy splitting between these will be greatest for the n_+ and n_- ligand valence MOs, on simple overlap considerations. Whether the energy ordering of the ligand valence orbitals is altered by this mixing, or whether it is essentially preserved, is not certain. For clarity, the parent ligand orbital ordering is maintained in Figure 5.9.

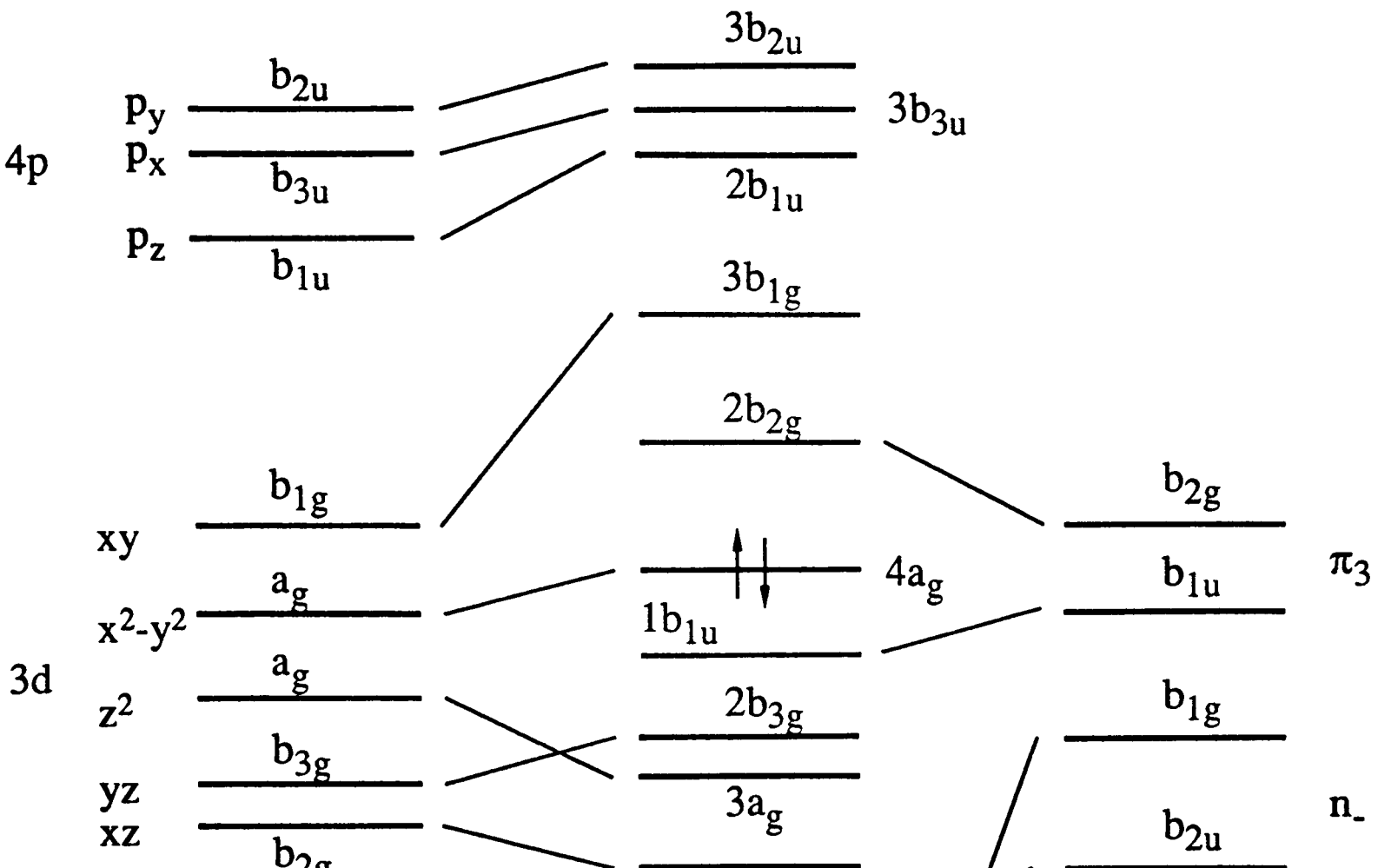

Figure 5.9 : qualitative MO diagram for $[Ni(S_2C_2(CF_3)_2)_2]$

The nickel 3d orbitals are more tightly bound than those of iron, and thus are of comparable energy to the highest filled ligand orbitals. The nickel 4p orbitals are also included in the MO scheme of the complex, as previous workers have suggested that they may be involved in metal-ligand bonding in these systems [19]. The scheme shows nickel to be formally in the +2 oxidation state, with two electrons being transferred from the nickel $3d_{xy}$ orbital into the empty ligand π_3 (b_{1u}) orbital (i.e. each ligand is formally monoanionic). This is consistent with the square planar structure of the complex, given the preference of a d^8 species for this geometry.

Several techniques have been used to study the electronic structure of $[Ni(S_2C_2R_2)_2]$, although no UV-PES work has been reported. The evidence from both electrochemical and optical spectroscopic studies [19-22] is that the LUMO is a largely ligand-based combination of nickel $3d_{xz}$ and ligand π_3 (b_{2g}) orbitals. ESR measurements on $[Ni(S_2C_2(CN)_2)_2]^-$ suggest that this MO is approximately 25-50% nickel 3d in character [23, 24]. The valence electronic stucture of the complex may be probed more deeply using PES, and Figure 5.10 shows the He I and He II PE spectra of $[Ni(S_2C_2(CF_3)_2)_2]$. The IEs of the bands and their assignments are given in Table 5.5. Although several attempts were made to record the spectrum of $[Ni(S_2C_2(CF_3)_2)_2]$ (and other transition metal complexes containing only dithiolene ligands) using synchrotron radiation, the compound had a deleterious effect upon the channel plates used in the spectrometer, and no useful data were obtained.

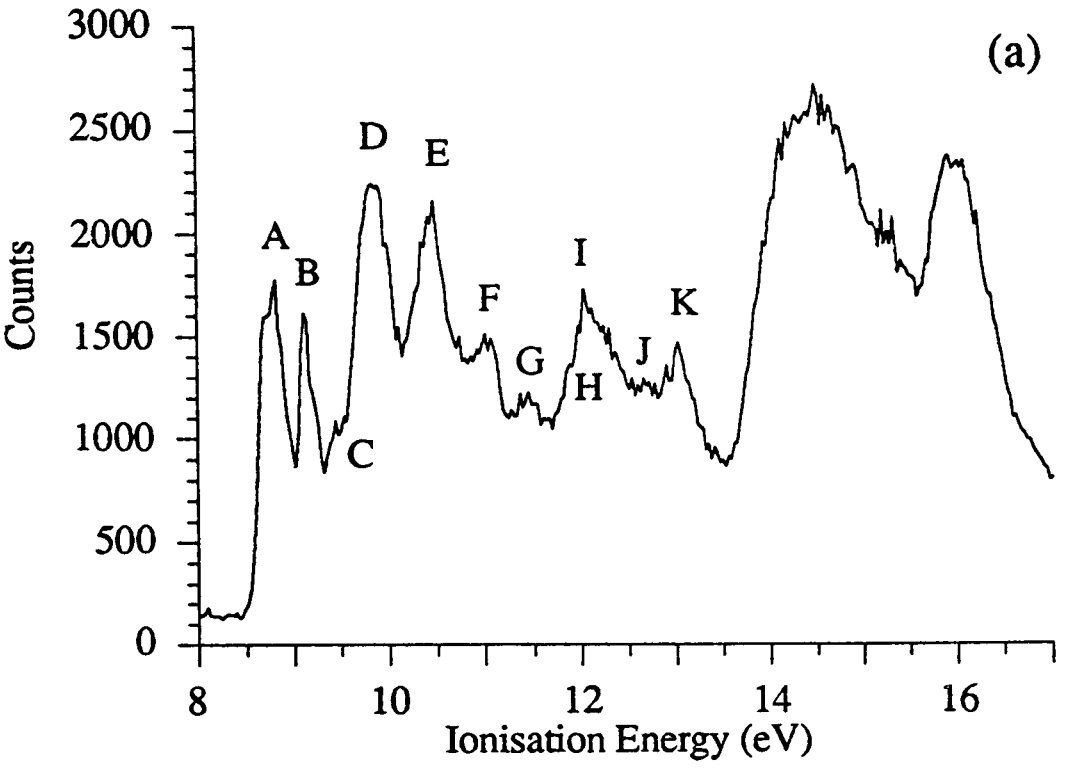

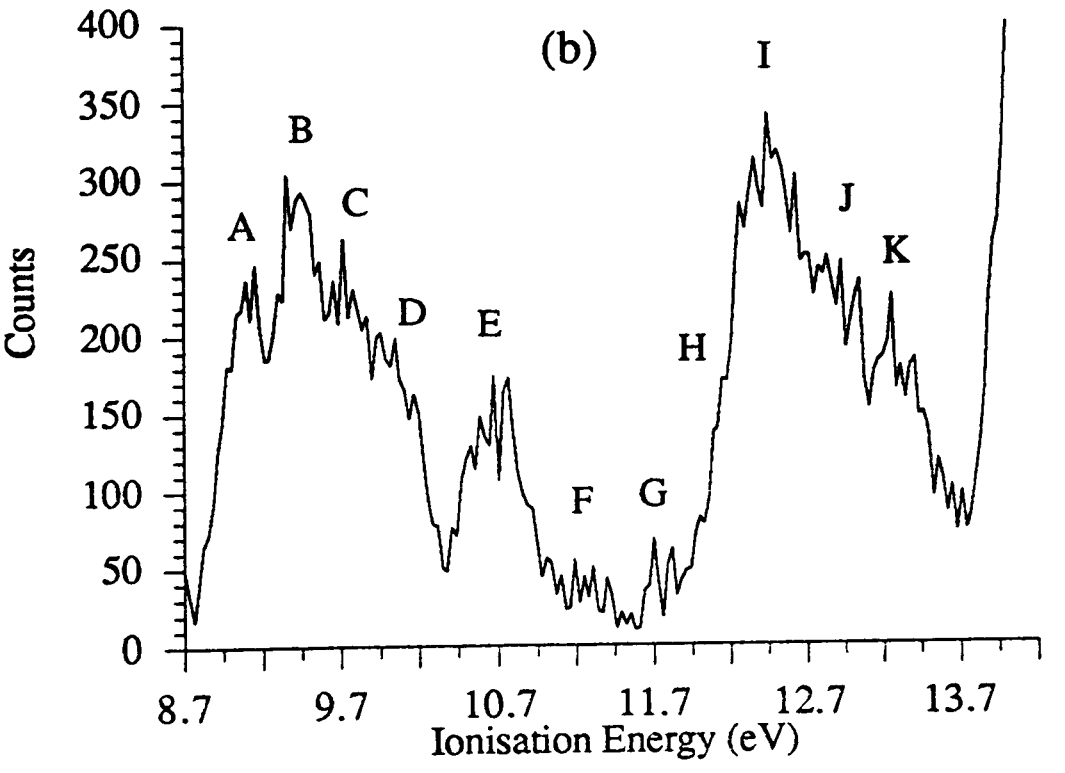

Figure 5.10 : the (a) He I and (b) He II PE spectra of $[Ni(S_2C_2(CF_3)_2)_2]$

Table 5.5 : IEs and band assignments of the PE spectrum of $[Ni(S_2C_2(CF_3)_2)_2]$

Band	IE (eV)	Assignment
A	9.13	$4a_g$, $1b_{1u}$
B	9.45	$2b_{3g}$, $3a_g$
C	9.81	$1b_{2g}$
D	10.27	$2b_{3u}$, $2b_{2u}$
E	10.92	$2b_{1g}$
F	11.50	$1b_{3g}$, $1a_u$, $2a_g$
G	12.12	
H	12.61	$1b_{1g}$
I	12.84	$1b_{2u}$
J	13.23	$1b_{3u}$
K	13.69	$1a_g$

The large number of ligand valence orbitals and the lack of degenerate MOs in the D_{2h} point group combine to produce a complicated PE spectrum. Ionisations above 13.5 eV are assigned in a manner analogous to those in the spectrum of $[Fe_2(CO)_6S_2C_2(CF_3)_2]$, with the exception of the carbonyl 4σ signal at 18 eV. Below 13.5 eV, eleven bands can be distinguished in the He I spectrum, and these are labelled A-K. There is a dramatic change in the form of the spectrum as the photon energy is increased from 21.22 eV (He I) to 40.81 eV (He II), but the same eleven bands are marked in the latter spectrum. Assignment of the spectrum in the absence of synchrotron studies relies heavily on the intensity changes of the bands between the He I and He II spectra, and hence the two will be discussed simultaneously.

The IEs and He I/He II behaviour of bands H-K suggests strongly that they are due to ionisations from the σ ligand valence orbitals with significant carbon character, the b_1 and a_1 free ligand MOs that lie between π_1 and π_2. The precise assignment of these bands is

not possible with any degree of certainty, but if the energy ordering found in the free ligand is maintained in the complex, H and I are due to ionisations from the $1b_{1g}$ and $1b_{2u}$ MOs, while J and K are due to the $1b_{3u}$ and $1a_g$ MOs.

Bands A-G must therefore arise from ionisations of the eleven highest-lying complex MOs. The collapse of bands D, F and G in the He II spectrum is strongly reminiscent of bands B-E in that of $[Fe_2(CO)_6S_2C_2(CF_3)_2]$, and suggests that these bands arise from sulphur-based MOs. The exception is band E, which clearly has an AO contribution from an atom other than sulphur. It is assigned to the $2b_{1g}$ complex MO, which is formed by interaction of the nickel $3d_{xy}$ AO with the b_{1g} (n_) ligand valence orbital. The greater metal character of this MO in the nickel complex in comparison with the b_1 (n_) MO in $[Fe_2(CO)_6S_2C_2(CF_3)_2]$ is a reflection of the nickel 3d electrons being more strongly bound than the iron, as alluded to earlier. The comparatively large width of band E may well reflect the bonding nature of the $2b_{1g}$ MO.

Bands F and G are assigned to the $1b_{3g}$ and $1a_u$ (π_2) orbitals, together with the $2a_g$ (n_+) orbital. Any nickel character to the $1b_{3g}$ and $2a_g$ orbitals is clearly small. Band D collapses from being the most prominent band in the He I spectrum to being almost a shoulder on band C in the He II, and is therefore assigned to the $2b_{3u}$ (n_+) and $2b_{2u}$ (n_) MOs, neither of which can have a metal d orbital contribution by symmetry.

Of the five remaining unassigned MOs, all bar the $1b_{1u}$ (π_3) have large nickel 3d contributions. Band C is assigned to the $1b_{2g}$ MO, the bonding counterpart of the $2b_{2g}$ complex LUMO. If the ESR measurements of $[Ni(S_2C_2(CN)_2)_2]^-$ - which suggest a 25-50% nickel $3d_{xz}$ contribution to the $2b_{2g}$ MO - are correct, then the $1b_{2g}$ could have as much as 75% nickel $3d_{xz}$ character. This would certainly account for the relative intensity increase of band C between the He I and He II spectra. Band B, which clearly has two components, also increases, and is assigned to the $3a_g$ ($3d_{z^2}$) and $2b_{3g}$ ($3d_{yz}$) MOs. The width of band B suggests that these are not strongly antibonding. Band A, which also appears to have two components, falls in relative intensity with respect to bands B and C. This is not surprising given that one of the two MOs assigned to band A is the $1b_{1u}$ (π_3) MO, which can have no nickel 3d contribution.

Several complexes of the type $[M(S_2C_2R_2)_2]^{z-}$ (where M = Ni, Pd, Pt; R = Ph, CN; z = 0, -1, -2) have been studied using X-ray PES [25-27]. The evidence from these studies suggests that the metal is in the +2 oxidation state, with the extra negative charge in the anions residing essentially upon the ligands. The UV-PES data presented here is consistent with nickel being formally in the +2 oxidation state in the complex. It appears that the main source of the nickel-sulphur bonding is between the nickel $3d_{xy}$ AO and the b_{1g} (n_-) ligand valence orbital, which is not surprising given that there is significant spacial overlap between these two orbitals.

The PE spectrum of $[Ni(S_2C_2(CH_3)_2)_2]$ has also been measured, by Lea Harris of this laboratory [28]. It is very similar to that of the perfluorinated analogue in both form and He I/He II behaviour and has been interpreted in the same manner. Unsurprisingly it is a more electron rich system (its first IE is 7.22 eV as compared with 9.00 eV in $[Ni(S_2C_2(CF_3)_2)_2]$), reflecting the relative inductive properties of CH_3 and CF_3.

5.5 Summary and Conclusions

The PE spectra of $[Fe_2(CO)_6S_2C_2(CF_3)_2]$ and $[Ni(S_2C_2(CF_3)_2)_2]$ have been obtained for the first time, and have been interpreted in terms of qualitative MO schemes derived from the valence MOs of the dithiolene ligands. A synchrotron study of $[Fe_2(CO)_6S_2C_2(CF_3)_2]$ has shown that the first band in the PE spectrum, which is believed to be due to ionisation from six Fe→CO back-bonding MOs together with the iron-iron bonding HOMO, has cross section behaviour which may be adequately explained in terms of AO contributions from carbon and oxygen 2p and iron 3d orbitals, a result supported by EHMO calculations. The four highest-lying complex MOs which are localised on the dithiolene ligand are found to be largely sulphur-based. He I/He II studies of $[Ni(S_2C_2(CF_3)_2)_2]$ also identify bands with strong sulphur character, but greater mixing of metal and ligand valence MOs produces a more complicated PE spectrum.

The results on $[Fe_2(CO)_6S_2C_2(CF_3)_2]$ suggest strongly that the dithiolene ligand is doubly reduced. This has also been found in the trigonal prismatic compounds $[M(S_2C_2(CF_3)_2)_3]$ (M=Mo and W) [29], in which no indication of metal d character was

found in any of the valence ionisation bands. The PE evidence for $[Ni(S_2C_2(CF_3)_2)_2]$ is consistent with the proposal that each ligand is singly reduced, with a dipositive metal centre, reflecting the closer energy match of metal and ligand valence MOs at the right hand end of the transition series.

5.6 References for Chapter Five

[1] R. P. Burns and C. A. McAuliffe: *Adv. Inorg. Chem. Radiochem.* **22** (1979) 303.

[2] R. Eisenberg and J. A. Ibers: *Inorg. Chem.* **5** (1966) 411.

[3] J. L. Hencher, Q. Shen and D. G. Tuck: *J. Am. Chem. Soc.* **98** (1976) 899.

[4] R. Eisenberg: *Prog. Inorg. Chem.* **12** (1970) 295.

[5] R. Schulz, A. Schweig, K. Hartke and J. Koster: *J. Am. Chem. Soc.* **105** (1983) 4519.

[6] H. P. Weber and R. F. Bryan: *J. Chem. Soc. (A)* (1967) 182.

[7] D. L. Thorn and R. Hoffmann: *Inorg. Chem.* **17** (1978) 126.

[8] E. L. Anderson and T. P. Fehlner: *Inorg. Chem.* **18** (1979) 2325.

[9] E. L. Anderson, T. P. Fehlner, A. E. Foti and D. R. Salahub: *J. Am. Chem. Soc.* **102** (1980) 7422.

[10] H. Van Dam, J. N. Louwen, A. D. Oskam, M. Doran and I. H. Hillier: *J. Electron Spectr. Relat. Phenom.* **21** (1980) 57.

[11] G. Granozzi, M. Casarin, S. Aime and D. Osella: *Inorg. Chem.* **21** (1982) 4073.

[12] M. Casarin, A. Vittadini, G. Granozzi, R. Bertoncello and D. Osella: *Inorg. Chem.* **25** (1986) 511.

[13] M. Casarin, G. A. Rizzi, A. Gulino, M. J. A. Kraakman, A. Vittadini and K. Vrieze: *Inorg. Chem.* **30** (1991) 1906.

[14] K. Kimura, S. Katsumata, Y. Achiba, T. Yamazaki and S. Iwata: *Handbook of He I Photoelectron Spectra of Fundamental Organic Molecules* Japan Scientific Societies Press, Tokyo (1981).

[15] J. J. Yeh and I. Lindau: *At. Data Nucl. Data Tables* **32** (1985) 1.

[16] G. Cooper, J. C. Green and M. P. Payne: *Mol. Phys.* **63** (1988) 1031.

[17] D. Briggs: *Handbook of X-ray and Ultraviolet Photoelectron Spectroscopy* Heyden, London (1977).

[18] R. D. Schmidt, R. M. Wing and A. H. Maki: *J. Am. Chem. Soc.* **91** (1969) 4394.

[19] D. C. Olson, V. P. Mayweg and G. N. Schrauzer: *J. Am. Chem. Soc.* **88** (1966) 4876.

[20] G. N. Schrauzer and V. P. Mayweg: *J. Am. Chem. Soc.* **87** (1965) 1483.

[21] G. N. Schrauzer and V. P. Mayweg: *J. Am. Chem. Soc.* **87** (1965) 3585.

[22] A. Davison, D. V. Howe and E. T. Shawl: *Inorg. Chem.* **6** (1967) 458.

[23] R. D. Schmidt and A. H. Maki: *J. Am. Chem. Soc.* **86** (1964) 4580.

[24] R. D. Schmidt and A. H. Maki: *J. Am. Chem. Soc.* **90** (1968) 2288.

[25] L. J. Mateinzo, S. O. Grim and W. E. Swartz: *J. Am. Chem. Soc.* **94** (1972) 5116.

[26] L. J. Mateinzo, S. O. Grim, W. E. Swartz and L. I. Yin: *Inorg. Chem.* **13** (1974) 447.

[27] L. J. Mateinzo, S. O. Grim, W. E. Swartz Jr and L. I. Yin: *Inorg. Chem.* **14** (1975) 2762.

[28] L. Harris: *Part II Thesis* Oxford (1991).

[29] N. Kaltsoyannis: *Part II Thesis* Oxford (1989).

CHAPTER SIX

EXPERIMENTAL DETAILS

6.1 Synthesis

Many of the compounds studied are air- and/or water-sensitive. All preparations and handling were carried out on a dual nitrogen/vacuum line using standard Schlenk techniques. Solvents were dried conventionally then distilled and degassed before use.

6.1.1 Chapter Two

$[Mo(\eta\text{-}C_6H_5Me)_2]$ was synthesised in conjunction with Peter Scott according to the literature procedure [1]. $[Mo(\eta\text{-}C_7H_7)(\eta\text{-}C_5H_5)]$, $[V(\eta\text{-}C_7H_7)(\eta\text{-}C_5H_5)]$, $[Nb(\eta\text{-}C_7H_7)(\eta\text{-}C_5H_5)]$ and $[Ta(\eta\text{-}C_7H_7)(\eta\text{-}C_5H_4Me)]$ were synthesised by Peter Scott following his recently developed method [2]. $[Ti(\eta\text{-}C_7H_7)(\eta\text{-}C_5H_5)]$ was made by Sally Jackson by the published procedure [3].

6.1.2 Chapter Three

PF_3 was obtained from Fluorochem Ltd., and used without further purification.

6.1.3 Chapter Four

OsO_4 was obtained from the Johnson Mathey Chemical Company, and used without further purification. $TiCl_4$ was obtained from Fluorochem Ltd. and purified by Tracey Frankcom by fractionation in vacuo [4]. $TiBr_4$ and $ZrBr_4$ were obtained from Fluorochem Ltd. and purified by sublimation in vacuo.

$[(CH_3)ReO_3]$ was prepared according to the published procedure [5].

6.1.4 Chapter Five

$S_2C_2(CF_3)_2$ was prepared by the method of Krespan [6]. $[Fe_2(CO_6)S_2C_2(CF_3)_2]$ was synthesised by Bill Heuer [7]. $[Ni(S_2C_2(CF_3)_2)_2]$ was made according to the published procedure [8].

The He I and He II PE spectra of all of the compounds studied were measured on the spectrometer described in Section 6.3, in order to check their spectral purity prior to running at the Synchrotron Radiation Source.

6.2 The photoelectron spectra and RPPICS calculations

6.2.1 The spectrometer

The photoionisation cross section data presented in this Thesis were obtained on beam line 3.3 of the Synchrotron Radiation Facility at the SERC's Daresbury Laboratory. An angle-resolved PE spectrometer was designed, set up and developed by J.B. West (Daresbury Laboratory), B.R. Dobson (Manchester University) and F. Quinn (Daresbury Laboratory/Aberdeen University) [9].

The monochromator on line 3.3 is a toroidal grating monochromator (TGM). Different photon energies are selected by altering the incidence angle of the radiation beam on the surface of the grating. Either of two gratings can be used in the TGM; one is ruled with 2400 lines/mm (grating 1), the other with 710 lines/mm (grating 2). These gratings can be interchanged with the TGM under vacuum as they are mounted on parallel bars attached to a rotation mechanism. They are interchanged by being moved sideways into the beam. Their angular orientations with respect to the synchrotron beam are under computer control. Resolution varies from 50-300 meV for each grating when operated at its low and high energy limits respectively. Grating 2 gives radiation of useful bandwidth and intensity from 15-50 eV while grating 1 is generally used from 50-130 eV. Grating 2 also produces high intensity radiation from 50-80 eV which can be used where resolution is not critical (bandwidth 400-600 meV). Alternatively, bandwidths of 50 meV or less can be achieved at any photon energy by adjustment of the TGM entrance and exit slits with subsequent

reduction in light intensity. The TGM was operated with wide open entrance and exit slits for the spectra collected for this Thesis as count rates were often low (particularly when using grating 1) and this did not noticeably affect the resolution.

A schematic diagram of the spectrometer is shown in Figure 6.1 (a). Photoelectrons produced by interaction of the monochromated synchrotron radiation beam with gaseous sample molecules are analysed in a hemispherical electron energy analyser, which is constructed of aluminium. All surfaces which are exposed to electrons are coated with colloidal graphite spray ("Aerodag G") and lightly polished. A three element, cylindrical, copper electrostatic lens (Figure 6.1 (b)) focuses electrons from the ionisation region onto the entrance aperture of the analyser. The lens stack and gas cell are also graphite coated. The analyser is operated in constant pass energy mode. A retarding or accelerating voltage applied to the analyser entrance aperture is scanned as is the lens focusing potential, while the voltage between the hemispheres is kept fixed. The pass energy of the analyser is defined as the KE of the electrons that will follow the centre line of the hemispheres. When electrons entering the analyser have a KE equal to the pass energy they will be detected at the centre of the multichannel plates. The analyser collection efficiency increases almost linearly with pass energy but the electron energy resolution decreases (the electron KE window width of the analyser is one-fifth of the pass energy). Pass energies of 3.2 and 6.4 eV were used in conjunction with grating 2, while 6.4 and 12.8 eV were employed with grating 1 up to photon energies of 80 eV. Above 80 eV, a pass energy of 14.7 eV was used. Electrons could not be retarded to less than one-tenth of their original KE.

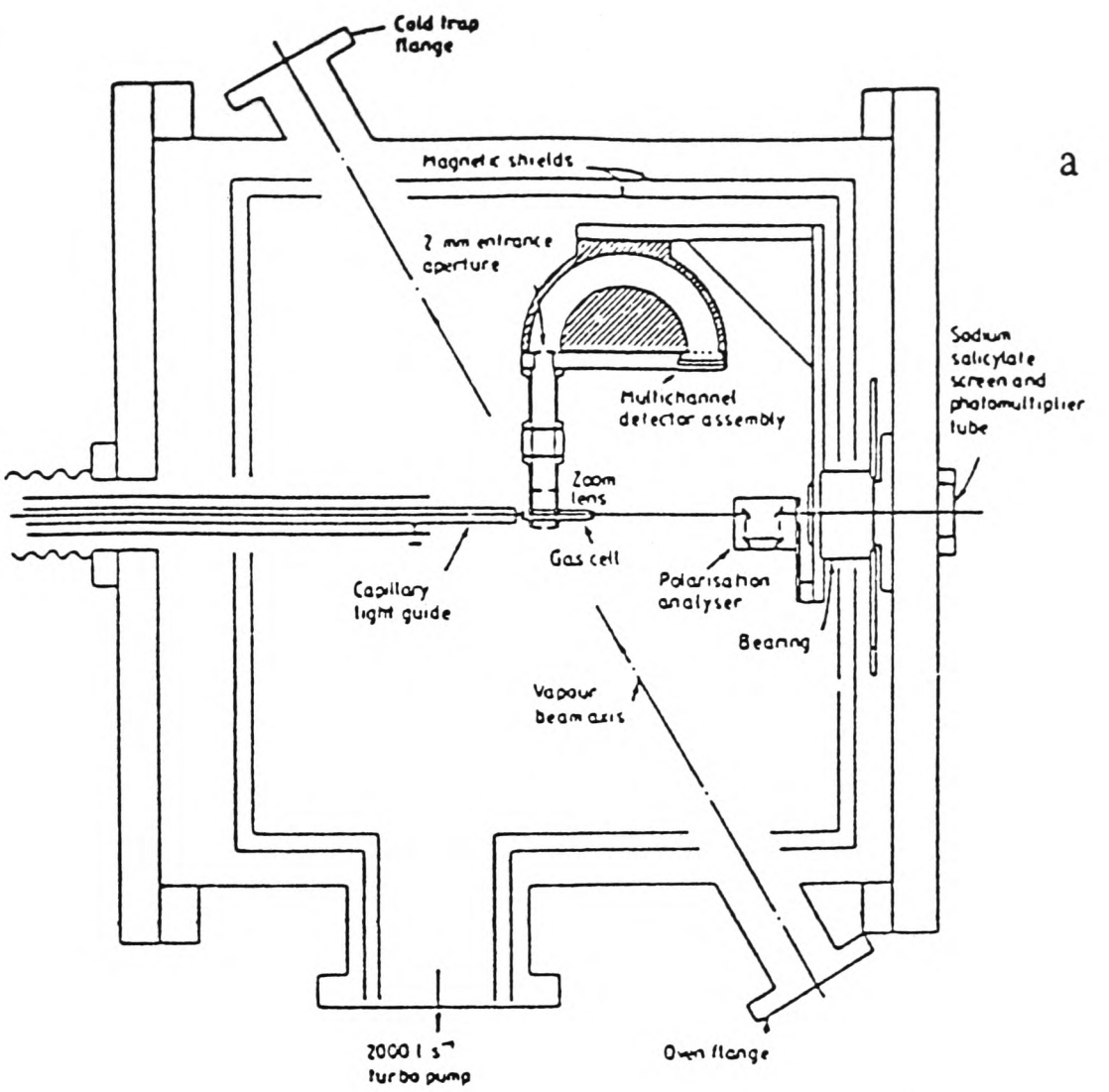

Figure 6.1 : (a) schematic diagram of the spectrometer used in Daresbury (b) three element lens assembly and gas cell

Electrons are detected using a multichannel plate/resistive anode encoder position sensitive detector [10]. The difference in rise-time between pulses leaving the two ends of the encoder due to the arrival of an electron on the multichannel plates is linearly dependent on its distance from their centre. By delaying the signal from one end of the resistive anode by the time taken for a pulse to travel along its length, it is possible to determine from where on the detector surface the signal originated. The dwell time at each spectrum step is determined by counting a preset number of pulses from a photomultiplier or photodiode which is positioned to intersect the radiation beam after it has passed through the ionisation region. This allows for fluctuations in photon flux which result mainly from storage ring beam decay. The whole analyser/detector assembly can be rotated from 0-270° with respect to the plane of polarisation of the radiation via computer control.

The data acquisition program runs on a PDP-11/04 minicomputer. The FORTRAN program was written by D. Croft and updated by M. Hayes (Daresbury Laboratory data acquistion group) from an earlier CATEX version by B.R. Dobson. As well as initiating spectral accumulation, the software allows automated movement of the monochromator and analyser angles, spectrum peak integration and transfer of stored data to a Convex Corporation C220 Supercomputer (mainframe).

All samples, with the exception of $TiCl_4$, OsO_4 and PF_3, were loaded into 2" long 1/4" diameter copper tubes which were sealed with a naphthalene plug. The tube was attached to the gas cell which fitted into the first lens element as shown in Figure 6.1 (b). A second inlet on the gas cell was for the inert gas calibration line. The samples were heated using Semflex non-inductively wound heating wire wrapped around the sample tube, the couplings and the first lens element. The electrical current needed to raise the temperature to the required levels was low (<1A). The gas cell temperature was monitored with a Matronics Digimat thermocouple, although temperature measurements are extremely sensitive to the position of the thermocouple on the gas cell wall and were taken as a rough guide only. $TiCl_4$ and OsO_4 are sufficiently volatile so that they could be attached externally and sublimed at ambient temperatures into the gas cell via the inert gas line. PF_3 was also

admitted in this manner. A liquid nitrogen cooled cold finger was fitted to the spectrometer to prevent diffusion of compound into the pumps.

As the spectrometer was initially designed for studying inert, air-stable, gaseous samples, no precautions were taken for preventing the ionising gas from reaching the detection system. Consequently, certain samples caused irrevocable damage to the detector. In particular, it was found that on exposure to the very water-sensitive oxy-chlorides $VOCl_3$ and CrO_2Cl_2, the performance of the detector immediately deteriorated, presumably due to reaction of the compounds with any moisture present on the detector surface.‡ $TiCl_4$ had a similar, though less marked effect. Furthermore, it was discovered that while good data might have been acquired for an air-sensitive sample, opening the spectrometer to the atmosphere resulted in very low signals on future operation, presumably due to deposition of the previous sample upon the detector and its subsequent reaction with oxygen/water. This problem was overcome by heating the copper box which surrounds the detector after the end of the experiment but while the spectrometer was still under vacuum. This volatilised any compound off the detector, allowing air to be admitted safely. It is possible that this technique may also work for measuring the oxy-chlorides, but has not yet been attempted.

6.2.2 Calibration

In order to eliminate the effects of the asymmetry parameter, β, from the RPPICS results, the analyser was positioned at the "magic angle". In previous studies [11-13], the magic angle was determined for each incident photon energy. This was achieved by measuring the degree of polarisation, P, of the radiation by recording the PE spectrum of helium at 90° and 180° with respect to the plane of polarisation of the radiation beam, and using $\beta = 2$ to calculate P. However, this technique gave values for the magic angle of 120 ± 3° for all of the compounds over all of the incident photon energies employed. Given that the measured polarisation varied from 60-90%, it is clear that large differences in

‡ The data collected for these compounds are of poor quality, and are not included in Chapter Four.

polarisation result in minimal changes in magic angle. It was therefore decided to dispense with polarisation measurements, and to use a fixed analyser angle of 120°. It is unlikely that this approach incurs errors in the angle greater than the ≤ 3° estimated in the previous technique.

The variations in analyser collection efficiency with electron kinetic and analyser pass energy, and the sensitivity of the photomultiplier/photodiode to different photon energies, had to be corrected for. This was achieved by recording spectra of the $1s^{-1}$ ionisation of helium and the np^{-1} ionisations of neon, argon and xenon at all photon and analyser pass energies used in data collection for each compound studied. The derived peak areas were divided by the appropriate photoionisation cross sections [14, 15]. Thus a photon energy intensity dependence was derived for electrons having IEs of 24.6, 21.2, 15.8 and 12.6 eV for helium, neon, argon and xenon (mean IE) respectively. Combination of these independent sets of results yielded separate calibration factors in terms of the PE KE and the radiation energy.

Absolute photoionisation cross sections could not be obtained as the pressure of the sample in the ionisation region could not be measured. Sample pressure fluctuations were allowed for by collecting a standard spectrum (a spectrum with fixed photon energy, number of scans and IE range) between each data run. The intensities of the bands in the standard spectra were determined by integration and these were used to correct for intensity variations caused by differences in the rate of sample sublimation. When a mode change occurred, i.e. at alterations in the analyser pass energy and at grating and wiring changes, sample and calibration spectra were recorded at the same photon energy under both sets of conditions. This enabled any discontinuity at the grating and mode changes to be corrected for.

6.2.3 Errors

Quantitative estimates of the errors involved in the experiment are not easy to obtain. Several sets of photon and KE calibration factors were gathered during each visit to Daresbury, and were usually reasonably reproducible, the KE factors less so than the

photon factors. Between visits, however, the form of these calibration curves varied significantly. Consequently a good measure of the response of the spectrometer to photon and PE energies could be made for each visit to Daresbury, but it is not valid to use calibrations obtained during one visit on data sets acquired at other times.

Uncertainties introduced into the RPPICS data by the photon calibration are small but derivation of the KE calibration factors is subject to considerable error. The analyser sensitivity decreases rapidly below ca. 10-15 eV PE KE but is approximately constant above this value. The errors introduced by the KE factors at very low PE KEs are the dominant factor in determining the accuracy of the corresponding RPPICS data. RPPICS closer than ca. 10-15 eV to the ionisation threshold of a band are therefore subject to larger uncertainties than those at higher PE KEs, and conclusions drawn from them should be treated accordingly.

The BR data are independent of the photomultiplier/photodiode sensitivity to photon energy and the long term variation in sample pressure. BRs are corrected only with the KE calibration so are subject to less overall error than RPPICS. For the RPPICS data the scales, although in arbitrary units, are internally consistent for each compound.

The errors quoted in Appendix Two are statistical errors associated with band area measurements, i.e. standard errors which assess sampling variability [16].

6.2.4 Data analysis

The analyses of spectra used to determine RPPICS were carried out using a set of programs initially developed by G. Cooper [11] to run on a Research Machines Ltd. NIMBUS microcomputer and J.C. Green to run on the OUCS VAX cluster. These were extended and incorporated into a suite of programs running on the Convex C220 Supercomputer at Daresbury by K.H. Sze. Inert gas calibration spectra were integrated using this program suite. Fano profiles were fitted using the program "Crossfit", written by G. Cooper [11] to run on a Research Machines Ltd. Nimbus microcomputer. Plots of RPPICS and BR data were generated using "Cricket Graph" on an Apple Macintosh microcomputer, and spectral plots were produced using "Kaleidagraph".

To calculate RPPICS, peak areas rather than peak heights were used as instrumental resolution varied between spectra of different photon energies. Where bands were clearly separated their areas were found by integration after subtraction of a linear background. Overlapping peaks were treated by fitting Gaussian curves. Both symmetric and asymmetric Gaussian functions are available, but in the majority of cases asymmetric functions were employed. Peak positions, heights and widths can be independently fixed, either absolutely or relative to those of any other peaks in the spectrum.

Curve fitting is a somewhat subjective exercise, in that by imposing suitable conditions upon the fit the eventual outcome can be heavily influenced. The approach adopted was to obtain good fits on the spectra acquired at low incident photon energies, as these are usually best resolved and have the highest counts. These fits were then used as guides for deconvoluting the more poorly resolved spectra. There are several examples, however, where this method is not completely successful. In both [Ti(η-C_7H_7)(η-C_5H_5)] and OsO_4 (Chapters Two and Four) the relative areas of bands B and C change significantly at the photon energy of a pass energy increase, after which a deterioration in resolution occurred. Corrections for this, however, cannot be made with any justification, in that the answer obtained is strongly prejudiced by the input parameters. Hence BR variations of overlapping bands at high incident photon energies should be treated with greater caution than those in the better resolved spectra. In certain cases, notably $ZrBr_4$ and [$Fe_2(CO)_6S_2C_2(CF_3)_2$] (Chapters Four and Five), the band area measurements are very heavily reliant upon the curve fitting program.

6.3 He I and He II photoelectron spectra

6.3.1 The spectrometer

He I and He II spectra were obtained on a PES Laboratories PE spectrometer model 0078 interfaced with a Research Machines Ltd. 380Z microcomputer for data collection. The spectrometer consists of a photon source, an ionisation chamber and an electron analyser. The photon source is a Helectros Developments Ltd. helium discharge lamp that can generate both He I and He II radiation (hν = 21.22 and 40.81 eV respectively). The

lamp is also used to heat the samples and probe temperatures from 20-300°C can be obtained by using water and air cooling. The analyser operates by electrostatic deflection of the electrons in a 127° cylindrical sector across which the potential is varied to scan through the range of electron KEs. The electrons are detected by a Channeltron electron multiplier. Spectra were collected by repeated scans of about 45 seconds duration in order to minimise relative intensity changes of the bands due to temperature fluctuations. There was no apparent drift during data collection.

6.3.2 Calibration

Surface charging and pressure effects necessitate that the spectra be calibrated for position and expansion by reference to inert gases. The helium self-ionisation peak at a KE of 16.23 eV resulting from ionisation of helium atoms by He IIα radiation appears in all He I spectra run with the present experimental arrangement and is used to set the position of the KE scale. The peak at a KE of 23.78 eV due to 2s ionisation by He IIβ radiation can be used to calibrate He II spectra. The KE scale expansion is determined by recording spectra of N_2 and xenon immediately after a data accumulation.

6.4 References for Chapter Six

[1] M. L. H. Green: *J. Organomet. Chem.* **200** (1980) 119.

[2] P. Scott: *D. Phil. Thesis* Oxford (1991).

[3] H. O. van Oven and H. J. de Liefde Meijer: *J. Organomet. Chem.* **23** (1970) 159.

[4] T. M. Frankcom: *Part II Thesis* Oxford (1989).

[5] W. A. Herrmann, J. G. Kuchler, G. Weichselbaumer, E. Herdtweck and P. Kiprof: *J. Organomet. Chem.* **372** (1989) 351.

[6] C. G. Krespan: *J. Am. Chem. Soc.* **83** (1961) 3434.

[7] W. B. Heuer: *personal communication.*

[8] A. Davison and R. H. Holm: *Inorg. Synth.* **10** (1967) 18.

[9] A. W. Potts, I. Novak, G. V. Quinn, B. R. Dobson and I. H. Hillier: *J. Phys. B* **18** (1985) 3177.

[10] A. A. MacDowell, I. H. Hillier and J. B. West: *J. Phys. E* **16** (1983) 487.

[11] G. Cooper: *D. Phil. Thesis* Oxford (1987).

[12] C. M. Redfern: *D. Phil. Thesis* Oxford (1988).

[13] N. Kaltsoyannis: *Part II Thesis* Oxford (1989).

[14] J. B. West and G. V. Marr: *Proc. R. Soc. London A* **349** (1976) 397.

[15] J. B. West and J. Morton: *At. Data Nucl. Data Tables* **22** (1978) 103.

[16] S. Dowdey and S. Wearden: *Statistics for Research (2nd ed.)* Wiley-Interscience, New York (1981).

APPENDIX ONE

MOLECULAR ORBITAL THEORY AND THE EXTENDED HÜCKEL METHOD

A1.1 Fundamentals of molecular orbital theory

All quantum mechanical descriptions of the electronic structures of atoms and molecules are obtained by solving the time independent Schrödinger equation for the system in question [1, 2]

$$\hat{H}\Psi = E\Psi$$

where $\hat{H}$ is the Hamiltonian operator (comprising kinetic and potential energy terms) which acts on the (atomic or molecular) wavefunction (Ψ) to regenerate the wavefunction multiplied by its energy (E). Equations of this type are known as eigenvalue equations, and the wavefunctions and their energies are often called eigenfunctions and eigenvalues respectively.

For polyelectronic molecules it is not possible to find an exact solution for the Schrödinger equation [1, 2], since all of the constituent particles are influenced by each other. It is possible, however, to circumvent this many body problem by making a number of simplifying assumptions.

Nucleus-electron interactions may be simplified by making the assumptions inherent in the Born-Oppenheimer approximation [3]. This approach uses the fact that the atomic nuclei in a molecule are far more massive than the electrons. Thus the electrons may be treated as moving in an attractive potential field due to fixed nuclei (i.e. molecular vibrations are ignored).

Electron-electron interactions are simplified by making the one-electron orbital approximation of Hartree and Fock [4-6]. In this approximation, electronic motions are not

correlated, but each electron experiences a time-averaged repulsive potential field due to the others.

The wavefunction which describes the spatial distribution of an electron throughout a molecule is known as a molecular orbital (MO). Each MO (Ψ_i) is the eigenfunction of a one-electron Hamiltonian ($\hat{H}_i$)

$$\hat{H}_i\Psi_i = E_i\Psi_i$$

Solutions of this one-electron (Hartree-Fock) Schrödinger equation are generally obtained by first making an initial guess as to the form of the MOs and then applying the variation principle to refine this initial guess [1, 2]. The important premise of the variation principle is that for any trial wavefunction the associated energy is always greater than the lowest eigenvalue of the Hamiltonian (i.e. the true ground state energy of the system).

A further simplification, introduced by Roothan [7], is to write each trial function as a linear combination of known functions (ϕ_1, ϕ_2, ... ϕ_n), which constitute the basis set. If weighting coefficients are introduced, the following expression is obtained

$$\Psi_i = c_1\phi_1 + c_2\phi_2 + \ldots\ldots + c_n\phi_n$$

Taking the one-electron Schrödinger equation, premultiplying both sides by Ψ_i^* (the complex conjugate of Ψ_i), rearranging and integrating over all space yields the energy (E_i) as the expectation value of the Hamiltonian operator

$$E_i = \frac{\int \Psi_i^* \hat{H}_i \Psi_i \, d\tau}{\int \Psi_i^* \Psi_i \, d\tau}$$

The value of E_i is minimised by altering the values of the coefficients until all of the partial differential functions ($\partial E_i/\partial c_i$) are equal to zero. From the variation principle, the set of coefficients which yield this (the minimum energy) constitute the best approximate wavefunction of the particular functional form originally chosen.

Calculating the expectation value of the one electron Hamiltonian, while constraining the energy to be a minimum, yields the following set of n homogeneous linear equations (homogeneous, all equal zero; linear, all c_is to the first power) known as the secular equations

$$c_1(H_{i1}-ES_{i1}) + c_2(H_{i2}-ES_{i2}) + \ldots\ldots + c_n\,(H_{in}-ES_{in}) = 0$$

where i = 1 to n; $H_{ij} = \langle\phi_i|\hat{H}|\phi_j\rangle = \int\phi_i^*\hat{H}\phi_j d\tau$; $S_{ij} = \langle\phi_i|\phi_j\rangle = \int\phi_i^*\phi_j d\tau$ (if all of the ϕ_i are real, then $\phi_i^*=\phi_i$ and the complex conjugate notation may be omitted). The latter integral reflects the extent of overlap between two orbitals, and is therefore known as the overlap integral.

It can be shown that non-trivial solutions to these equations are obtained when the following secular determinant is equal to zero [8]

$$\begin{vmatrix} H_{11}-ES_{11} & H_{12}-ES_{12} & \ldots\ldots & H_{1n}-ES_{1n} \\ H_{21}-ES_{21} & H_{22}-ES_{22} & \ldots\ldots & H_{2n}-ES_{2n} \\ \vdots & \vdots & \vdots & \vdots \\ H_{n1}-ES_{n1} & H_{n2}-ES_{n2} & \ldots\ldots & H_{nn}-ES_{nn} \end{vmatrix} = 0$$

Expanding the secular determinant yields a polynomial which is n^{th} order in E and has, therefore, n solutions. Any value of E satisfying this equation is associated with a set of non-trivial coefficients. The lowest value of E is the minimum average energy achievable by variation of the coefficients. Substitution of this E value back into the secular equations enables the determination of the coefficients, c_i, corresponding to the trial wavefunction that is the best approximation to the true ground state wavefunction of the system.

In most MO treatments, molecular wavefunctions are constructed from a basis set of atomic orbitals (AOs). This is known as the linear combination of AOs (LCAO) approach [9]. For polyelectronic atoms, these AOs are again only approximate functions. Two alternative functional forms of AOs are commonly used; Slater type orbitals (STOs) and gaussian orbitals. The angular parts of the STOs are identical to those of the hydrogenic orbitals (i.e. the spherical harmonics $\phi_{lm}(\theta,\phi)$). The radial part of a STO possesses no nodes [10] (many of the hydrogenic orbitals have radial nodes, and this mathematical aspect causes increased complexity in solving quantum chemical equations)

$$\Psi(r) = r^{n-1}\exp(-\zeta r)$$

where n is the principal quantum number of the orbital and the Slater exponent, ζ, is a function of the nuclear charge, Z, the screening constant, s and n

$$\zeta = (Z - s)/n$$

The $\exp(-\zeta r)$ dependence of the radial wavefunction means that the more electronegative elements, i.e. those with high effective nuclear charges (Z - s) and low principal quantum numbers, possess the more contracted orbitals.

The radial form of the AOs is often made more realistic by taking linear combinations of STOs. For reasons of computational simplicity, however, gaussian functions (which include a term of the form $\exp(-\alpha r^2)$) are sometimes used to mimic the radial functions of STOs. By choosing several values of α in $\exp(-\alpha r^2)$, one can create a set

of "primitive" gaussian functions and then take a linear combination of these to build up an approximation to the radial part of an STO function. Thus a calculation described as "STO-3G" has each STO approximated as a linear combination of three gaussian primitives.

The various types of MO calculation, though based on the same principles, have differing degrees of sophistication and accuracy [8]. Differences in approach can arise at two stages. First, a large basis set of atomic functions (e.g. multiple STO functions for each AO) leads, as mentioned above, to a more realistic representation of the radial part of the AOs and hence a more accurate calculation of the interaction between AOs. A second source of differences is the form of the Hamiltonian operator. In the more precise ab initio ("from the beginning") methods the integrals H_{ij} are evaluated explicitly, depending on the precise mathematical form of the Hamiltonian. In the more approximate semi-empirical methods the form of the Hamiltonian is ignored and the integrals H_{ij} are assigned empirical numerical values, on the basis of spectroscopic data. The advantage of semi-empirical methods is that they require shorter computation times, due to the assumptions made for H_{ij} and the choice of small AO basis sets, though they obviously lose out on accuracy.

A1.2 The extended Hückel method

The MO calculations described in this Thesis are of the extended Hückel type. This is an example of a semi-empirical MO method and is based on simple Hückel theory, which provides an estimate of the energies and approximate forms of the π MOs of planar, unsaturated molecules [11-13].

In Hückel theory the secular determinant is considerably simplified by making the following approximations

$H_{ii} = \alpha$ (Coulomb integral)

$H_{ij} = \beta$ (Resonance integral) when atoms i and j are bonded

$H_{ij} = 0$ when i and j are not bonded.

S_{ij} (Overlap integral) = 1 when i = j, otherwise $S_{ij} = 0$

The energies of the MOs are obtained from the secular determinant in the form

$$E = \alpha \pm \lambda\beta$$

where λ is a function of the geometry and connectivity of the framework atoms. The analysis is further simplified by the choice of a very limited basis set, i.e. only the p AOs which are perpendicular to the plane of the molecule.

In extended Hückel theory the basis set includes all of the valence orbitals of the constituent atoms in the molecule [14]. These orbitals are generally STOs of the form

$$\Psi_{nlm} = r^{n-1}\exp(-\zeta r)\phi_{lm}(\theta,\phi)$$

The radial properties of s and p orbitals are quite adequately reproduced by single STOs. For the more contracted valence d orbitals, however, linear combinations of two STOs ("double-zeta functions") are required. These have the following radial form

$$\Psi(r) = r^{n-1}[c_1\exp(-\zeta_1 r) + c_2\exp(-\zeta_2 r)]$$

where the coefficients (c_1 and c_2) and orbital exponents (ζ_1 and ζ_2) are defined empirically.

In the extended Hückel method the overlap integrals, S_{ij}, are evaluated explicitly, since the zero-overlap approach of simple Hückel theory does not yield sufficiently accurate values for the energies of the MOs.

The elements of the Hamiltonian matrix, H_{ij}, are estimated in the following way. The diagonal terms, H_{ii} (Coulomb integrals), are set equal to the energy (defined as negative), in eV, of an electron in the ith AO of the isolated atom in a given valence state. These energies are obtained from experimental data and the values used are known as the Valence Shell Ionisation Energies (VSIEs). A VSIE is obtained as the weighted mean of the states arising from a particular valence state configuration [15].

The off-diagonal terms of the Hamiltonian matrix, H_{ij} (Resonance integrals), are taken to be orbital interaction energies. It is assumed that the interaction between two AOs is roughly proportional to their overlap and is greater for high energy orbitals than low

energy ones. The most commonly used method of evaluating the H_{ij} terms is the arithmetic mean formula of Wolfsberg and Helmholtz [16]

$$H_{ij} = kS_{ij}(H_{ii} + H_{jj})/2$$

though geometrical and reciprocal mean formulae have been utilised [17]

$$H_{ij} = -kS_{ij} \sqrt{H_{ii}H_{jj}}$$

$$H_{ij} = 2kS_{ij}\frac{H_{ii}H_{jj}}{H_{ii} + H_{jj}}$$

Hoffmann has suggested a value of 1.75 for the Wolfsberg-Helmholtz constant k, on the grounds that this value gives the correct value for the rotational barrier in ethane [14]. Most extended Hückel calculations use a value of 1.75 for k, as generally these calculations are fairly insensitive to the value of k in the region $1.5 < k < 2.0$. Woolley has suggested, however, that k values in the range 2.0 - 4.0 may be more appropriate for d orbitals, as a value of 1.75 leads to an underestimation of d-d resonance integrals and d bandwidths for metal clusters [18].

In this methodology the total energy is simply taken as the sum of the one-electron energies. The absolute value of the energy, therefore, is generally inaccurate, as electron-electron and nuclear-nuclear repulsion terms are neglected, as are the effects of inner shell electrons. The relative energies of molecules in related conformations or geometries are, however, often quite accurately reproduced by this method. As the EHMO approach is based on a single configuration, problems are encountered when the system in question is not accurately representable by a single configuration wavefunction (e.g. systems containing unpaired electrons). In addition, it is found that the method works best when applied to uncharged, non-polar systems in which the nuclei undergoing relative motion are not too close to each other.

The electron density is partitioned according to the Mulliken population analysis [19]. For a normalised MO, Ψ_j, written as an LCAO

$$\Psi_j = c_{kj}\phi_k + c_{lj}\phi_l$$

the electron density is proportional to the square of the wavefunction

$$\Psi_j^2 = c_{kj}^2\phi_k^2 + c_{lj}^2\phi_l^2 + 2c_{kj}c_{lj}\phi_k\phi_l$$

Since all of the orbitals are normalised, integration over all space yields

$$1 = c_{kj}^2 + c_{lj}^2 + 2c_{kj}c_{lj}S_{kl}$$

Thus, one electron in Ψ_j contributes c_{kj}^2 to the net AO electron population of ϕ_k, c_{lj}^2 to the population of ϕ_l and $2c_{kj}c_{lj}S_{kl}$ to the overlap population between AOs ϕ_k and ϕ_l.

The total net AO population of ϕ_k, q_k, is obtained by summing over all MOs

$$q_k = \sum_j n_j c_{kj}^2$$

where n_j is the electron occupation (0, 1 or 2) of MO Ψ_j.

Similarly, the Mulliken overlap population for the pair of orbitals ϕ_k and ϕ_l, p_{kl} is obtained by making the summation

$$p_{kl} = 2\sum_j n_j c_{kj} c_{lj} S_{kl}$$

The sum of all the q_k and p_{kl} values must equal the total number of valence electrons in the system. Mulliken populations are useful indices of the location of electronic charge in a molecule and its bonding or antibonding nature. Antibonding interactions have a negative

Mulliken overlap population, interpreted to mean that the amount of charge in the overlap region is less than would exist if one squared the two AOs and then combined them.

The reduced Mulliken overlap population between atoms K and L, P_{KL}, is obtained by summing p_{kl} over all of the AOs on K and L

$$P_{KL} = \sum_{k} \sum_{l} p_{kl}$$

where P_{KL} constitutes a two-centre bond order.

The gross atomic population (i.e. total electron density) on atom K is obtained by dividing P_{KL} equally between K and L and adding this to the net atomic population of K ($= \sum_{k} q_k$). When all the Mulliken overlap populations have been reassigned in this way, the electronic charge is all in the AOs. The resultant atomic charge is simply calculated as the sum of the electronic and nuclear charges.

As is the case for orbital and total energies, Mulliken populations are sensitive to the choice of AO parameters and k. The relative values of the Mulliken populations are, however, reasonably parameter-independent, so that they may be used in a comparative, if not an absolute, sense. Another limitation of the Mulliken population analysis is encountered for diffuse orbitals, where there is significant orbital overlap in regions other than the internuclear region [20, 21].

It is sometimes found that large, unrealistic atomic charges are calculated in molecules consisting of atoms with very different electronegativities. This problem, which arises because the VSIE values used in the estimation of H_{ii} refer to neutral atoms, may be circumvented by the method of charge iteration.

The charge iteration method involves a series of extended Hückel calculations, with the VSIEs for the nth cycle of calculations defined as a function of the atomic charges (q) calculated in the $(n-1)^{th}$ cycle

$$\text{VSIE}\ (q) = Aq^2 + Bq + C$$

where the parameters A, B and C are obtained from multiconfigurational spectral data on the atoms and their charged ions [15]. The cycles are continued until self-consistent charges result. Such iterative calculations are known as Self Consistent Charge and Configuration (SCCC) calculations.

In certain cases, extended Hückel calculations have been found to suffer from a defect known as "counter-intuitive orbital mixing" (COM) [22]. COM (which has also been observed in ab initio calculations) occurs when there are large overlap integrals between orbitals, on different atomic centres, which are widely separated in energy. The orbital mixing which takes place does so in an antibonding fashion, contrary to that expected from perturbation theory, and some MOs possess small antibonding contributions from these orbitals. Although the effect on orbital energies is insignificant, COM results in anomalous Mulliken populations. COM is particularly significant in transition metal complexes with π acid ligands, such as cyclopentadienyl and CO.

The effects of COM may be minimised by using a modified Wolfsberg-Helmholtz relationship, the "weighted H_{ij} formula ". The basis of this approach is the replacement of k (in the equation for H_{ij}) by a new constant k´ [22]

$$k' = k + \Delta^2 + \Delta^4(1 - k)$$

where $\Delta = (H_{ii} - H_{jj})/(H_{ii} + H_{jj})$. In this way H_{ij} is effectively weighted in favour of the less diffuse orbitals (i.e. those with the most negative H_{ii} value).

A1.2.1 Description of the programs used for performing extended Hückel calculations

The extended Hückel calculations reported in this Thesis were performed using the ICON8 package of FORTRAN computer programs developed by Hoffmann and co-workers [22].

The input to ICON8, the main calculational program, consists of the cartesian co-ordinates and orbital parameters (H_{ii}s, Slater orbital exponents (ζ), and contracted d orbital coefficients (c_1 and c_2) and exponents (ζ_1 and ζ_2)) of the constituent atoms. Optional

features include the possibility of performing calculations using weighted H_{ij}s, charge iteration and non-default (1.75) values of k. If charge iteration calculations are to be performed, values of A, B and C must be specified. The program COORDINATE can be used to convert from polar co-ordinates (i.e. bond lengths and angles) into cartesian co-ordinates, suitable for input into ICON8.

The output from ICON8 is completely user controlled, depending on the information required. The input co-ordinates and parameters may be printed out, as a check. Most of the information is presented in matrix form, and includes the following items; interatomic distances, atomic overlap integrals, wavefunctions, orbital energies and occupations, total energy, overlap populations, reduced overlap populations, charge matrix, total atomic charges and orbital populations.

The charge matrix elements (Q_{ij}) correspond to the proportion of the electronic charge for a given MO (normalised to two electrons regardless of the actual orbital occupancy) which may be apportioned to each of its constituent AOs

$$Q_{ij} = 2c_{ij}\sum_{k} c_{kj}S_{ik}$$

where c_{ij} is the coefficient of the ith AO in the jth MO and S_{ik} is the overlap integral between AOs ϕ_i and ϕ_k. The reduced charge matrix elements are obtained by summing the values of Q_{ij} over all the orbitals (ϕ_i) of each atom.

In certain cases it is informative to divide conceptually a molecule into fragments and study the interaction between the orbitals of these fragments. The program FMO transforms the results of an ICON8 calculation from an AO basis set to a basis set consisting of such fragments. The input for FMO consists of ICON8 calculations on the fragments, as well as the complete molecule.

The programs MOPLOT and MOSHOW were used to generate the MO contour plots.

A1.3 Input data used in the EHMO calculations described in this Thesis

Table A1.1 : structural input data for $[(CH_3)ReO_3]$ [23]

Atom to atom	Bond Length (Å)	Bond Angle (°)	Dihedral Angle (°)
Re1 to C2	2.060	180.0	0.0
Re1 to O3	1.709	74.0	0.0
Re1 to O4	1.709	74.0	120.0
Re1 to O5	1.709	74.0	240.0
C2 to H6	1.105	112.0	60.0
C2 to H7	1.105	112.0	180.0
C2 to H8	1.105	112.0	300.0

Atom	x	y	z
Re1	0.000000	0.000000	0.000000
C2	0.000000	0.000000	2.060000
O3	1.642796	0.000000	-0.471064
O4	-0.821398	1.422703	-0.471064
O5	-0.821398	-1.422703	-0.471064
H6	0.512269	0.887276	2.473940
H7	-1.024538	0.000000	2.473940
H8	0.512269	-0.887276	2.473940

Table A1.2 : structural input data for ReO_3Cl [24]

Atom to atom	Bond Length (Å)	Bond Angle (°)	Dihedral Angle (°)
Re1 to Cl2	2.230	180.00	0.0
Re1 to O3	1.702	70.529	0.0
Re1 to O4	1.702	70.529	120.0
Re1 to O5	1.702	70.529	240.0

Atom	x	y	z
Re1	0.000000	0.000000	0.000000
Cl2	0.000000	0.000000	2.230000
O3	1.604663	0.000000	-0.567327
O4	-0.802332	1.389679	-0.567327
O5	-0.802331	-1.389679	-0.567327

Table A1.3 (a) : structural input data for $S_2C_2(CF_3)_2$, $\Theta = 100^o$ [25, 26]

Atom to atom	Bond Length (Å)	Bond Angle (°)	Dihedral Angle (°)
C1 to C2	1.370	180.00	0.00
C2 to S3	1.700	100.00	0.00
C1 to S4	1.700	80.00	0.00
C2 to C5	1.500	240.00	0.00
C5 to F6	1.300	110.80	0.00
C5 to F7	1.300	110.80	120.00
C5 to F8	1.300	110.80	240.00
C1 to C9	1.500	300.00	0.00
C9 to F10	1.300	110.80	0.00
C9 to F11	1.300	110.80	120.00
C9 to F12	1.300	110.80	240.00

Atom	x	y	z
C1	0.000000	0.000000	0.000000
C2	0.000000	0.000000	1.370000
S3	1.674173	0.000000	1.665202
S4	1.674173	0.000000	-0.295202
C5	-1.299038	0.000000	2.120000
F6	-2.306466	0.000000	1.298362
F7	-1.395011	-1.052457	2.877048
F8	-1.395011	1.052458	2.877048
C9	-1.299038	0.000000	-0.750000
F10	-1.091193	0.000000	-2.033277
F11	-2.002648	-1.052457	-0.454591
F12	-2.002648	1.052458	-0.454591

Table A1.3 (b) : structural input data for $S_2C_2(CF_3)_2$, $\Theta = 105^o$

Atom to atom	Bond Length (Å)	Bond Angle (°)	Dihedral Angle (°)
C1 to C2	1.370	180.00	0.00
C2 to S3	1.700	105.00	0.00
C1 to S4	1.700	75.00	0.00
C2 to C5	1.500	240.00	0.00
C5 to F6	1.300	110.80	0.00
C5 to F7	1.300	110.80	120.00
C5 to F8	1.300	110.80	240.00
C1 to C9	1.500	300.00	0.00
C9 to F10	1.300	110.80	0.00
C9 to F11	1.300	110.80	120.00
C9 to F12	1.300	110.80	240.00

Atom	x	y	z
C1	0.000000	0.000000	0.000000
C2	0.000000	0.000000	1.370000
S3	1.642074	0.000000	1.809992
S4	1.642074	0.000000	-0.439992
C5	-1.299038	0.000000	2.120000
F6	-2.306466	0.000000	1.298362
F7	-1.395011	-1.052457	2.877048
F8	-1.395011	1.052458	2.877048
C9	-1.299038	0.000000	-0.750000
F10	-1.091193	0.000000	-2.033277
F11	-2.002648	-1.052457	-0.454591
F12	-2.002648	1.052458	-0.454591

Table A1.3 (c) : structural input data for $S_2C_2(CF_3)_2$, $\Theta = 110^o$

Atom to atom	Bond Length (Å)	Bond Angle (°)	Dihedral Angle (°)
C1 to C2	1.370	180.00	0.00
C2 to S3	1.700	110.00	0.00
C1 to S4	1.700	70.00	0.00
C2 to C5	1.500	240.00	0.00
C5 to F6	1.300	110.80	0.00
C5 to F7	1.300	110.80	120.00
C5 to F8	1.300	110.80	240.00
C1 to C9	1.500	300.00	0.00
C9 to F10	1.300	110.80	0.00
C9 to F11	1.300	110.80	120.00
C9 to F12	1.300	110.80	240.00

Atom	x	y	z
C1	0.000000	0.000000	0.000000
C2	0.000000	0.000000	1.370000
S3	1.597478	0.000000	1.951434
S4	1.597478	0.000000	-0.581434
C5	-1.299038	0.000000	2.120000
F6	-2.306466	0.000000	1.298362
F7	-1.395011	-1.052457	2.877048
F8	-1.395011	1.052458	2.877048
C9	-1.299038	0.000000	-0.750000
F10	-1.091193	0.000000	-2.033277
F11	-2.002648	-1.052457	-0.454591
F12	-2.002648	1.052458	-0.454591

Table A1.3 (d) : structural input data for $S_2C_2(CF_3)_2$, $\Theta = 115^o$

Atom to atom	Bond Length (Å)	Bond Angle (°)	Dihedral Angle (°)
C1 to C2	1.370	180.00	0.00
C2 to S3	1.700	115.00	0.00
C1 to S4	1.700	65.00	0.00
C2 to C5	1.500	240.00	0.00
C5 to F6	1.300	110.80	0.00
C5 to F7	1.300	110.80	120.00
C5 to F8	1.300	110.80	240.00
C1 to C9	1.500	300.00	0.00
C9 to F10	1.300	110.80	0.00
C9 to F11	1.300	110.80	120.00
C9 to F12	1.300	110.80	240.00

Atom	x	y	z
C1	0.000000	0.000000	0.000000
C2	0.000000	0.000000	1.370000
S3	1.540723	0.000000	2.088451
S4	1.540723	0.000000	-0.718451
C5	-1.299038	0.000000	2.120000
F6	-2.306466	0.000000	1.298362
F7	-1.395011	-1.052457	2.877048
F8	-1.395011	1.052458	2.877048
C9	-1.299038	0.000000	-0.750000
F10	-1.091193	0.000000	-2.033277
F11	-2.002648	-1.052457	-0.454591
F12	-2.002648	1.052458	-0.454591

Table A1.3 (e) : structural input data for $S_2C_2(CF_3)_2$, $\Theta = 120^o$

Atom to atom	Bond Length (Å)	Bond Angle (°)	Dihedral Angle (°)
C1 to C2	1.370	180.00	0.00
C2 to S3	1.700	120.00	0.00
C1 to S4	1.700	60.00	0.00
C2 to C5	1.500	240.00	0.00
C5 to F6	1.300	110.80	0.00
C5 to F7	1.300	110.80	120.00
C5 to F8	1.300	110.80	240.00
C1 to C9	1.500	300.00	0.00
C9 to F10	1.300	110.80	0.00
C9 to F11	1.300	110.80	120.00
C9 to F12	1.300	110.80	240.00

Atom	x	y	z
C1	0.000000	0.000000	0.000000
C2	0.000000	0.000000	1.370000
S3	1.472243	0.000000	2.220000
S4	1.472243	0.000000	-0.850000
C5	-1.299038	0.000000	2.120000
F6	-2.306466	0.000000	1.298362
F7	-1.395011	-1.052457	2.877048
F8	-1.395011	1.052458	2.877048
C9	-1.299038	0.000000	-0.750000
F10	-1.091193	0.000000	-2.033277
F11	-2.002648	-1.052457	-0.454591
F12	-2.002648	1.052458	-0.454591

Table A1.4 : structural input data for $[Fe_2(CO)_6(S_2C_2(CF_3)_2)]$ [26, 27]

Atom to atom	Bond Length (Å)	Bond Angle (°)	Dihedral Angle (°)
D27 to Fe1	1.2535	90.000	0.000
Fe1 to C3	1.7780	151.525	0.000
C3 to O9	1.1520	180.000	0.000
Fe1 to D28	1.2780	146.580	180.000
D28 to C4	1.2360	90.000	90.000
C4 to O10	1.1520	134.050	180.000
D28 to C5	1.2360	90.000	-90.000
C5 to O11	1.1520	134.050	180.000
D27 to Fe2	1.2535	90.000	180.000
Fe2 to C6	1.778	151.525	0.000
C6 to O12	1.152	180.000	0.000
Fe2 to D29	1.278	146.580	180.000
D29 to C7	1.236	90.000	90.000
C7 to O13	1.152	134.050	180.000
D29 to C8	1.236	90.000	-90.000
C8 to O14	1.152	134.050	180.000
D27 to S15	1.879	49.922	90.000
D27 to S16	1.879	49.922	-90.000
S15 to C17	1.771	105.451	0.000
C17 to C19	1.500	122.437	180.000
C19 to F21	1.326	110.800	0.000
C19 to F22	1.326	110.800	120.000
C19 to F23	1.326	110.800	240.000
S16 to C18	1.771	105.451	0.000
C18 to C20	1.500	122.437	180.000
C20 to F24	1.326	110.800	0.000
C20 to F25	1.326	110.800	120.000
C20 to F26	1.326	110.800	240.000

D27 is a dummy atom lying midway along the Fe-Fe axis

D28 is a dummy atom lying in the plane defined by Fe1, C4 and C5 and situated midway between C4 and C5

D29 is a dummy atom lying in the plane defined by Fe2, C7 and C8 and situated midway between C7 and C8

Atom	x	y	z
Fe1	1.253500	0.000000	0.000000
Fe2	-1.253500	0.000000	0.000000
C3	2.816407	0.000000	-0.847707
C4	2.320190	-1.236000	0.703887
C5	2.320190	1.236000	0.703887
C6	-2.816407	0.000000	-0.847707
C7	-2.320190	1.236000	0.703887
C8	-2.320190	-1.236000	0.703887
O9	3.829044	0.000000	-1.396952
O10	3.011269	-2.036969	1.159916
O11	3.011269	2.036969	1.159915
O12	-3.829044	0.000000	-1.396952
O13	-3.011269	2.036969	1.159916
O14	-3.011269	-2.036969	1.159915
S15	0.000000	1.437752	-1.209756
S16	0.000000	-1.437752	-1.209756
C17	0.000000	0.699760	-2.819666
C18	0.000000	-0.699760	-2.819666
C19	0.000000	1.515313	-4.078584
C20	0.000000	-1.515313	-4.078584
F21	0.000000	2.811678	-3.799815
F22	1.073507	1.251151	-4.810757
F23	-1.073507	1.251151	-4.810757
F24	0.000000	-2.811678	-3.799815
F25	-1.073507	-1.251151	-4.810757
F26	1.073507	-1.251151	-4.810757

Table A1.5 : Orbital exponents, H_{ii}s and coefficients used in the EHMO calculations

Atom	Orbital	Exponent	H_{ii} (eV)
Hydrogen	1s	1.300	-13.6
Carbon	2s	1.625	-21.4
	2p	1.625	-11.4
Oxygen	2s	2.275	-32.3
	2p	2.275	-14.8
Fluorine	2s	2.425	-40.0
	2p	2.425	-18.1
Chlorine	3s	2.183	-26.3
	3p	1.733	-14.2
Sulphur	3s	2.122	-20.0
	3p	1.827	-11.0
Iron [a,b]	4s	1.900	-9.274
	4p	1.900	-4.442
	3d	5.35, 2.00	-11.529
Rhenium [c]	6s	2.398	-9.36
	6p	2.372	-5.96
	5d	5.343, 2.277	-12.66

[a] Iron H_{ii} values taken from a charge iteration of $[Fe_2(CO)_6(S_2C_2(CF_3)_2)]$ (charge iteration performed on the iron atoms only)

[b] Iron 3d orbital coefficients 0.5505, 0.6260

[c] Rhenium 5d orbital coefficients 0.63775, 0.56576

A1.4 References for Appendix One

[1] L. Pauling and E. B. Wilson: *Introduction to Quantum Mechanics* McGraw-Hill, New York (1935).

[2] A. S. Davydov: *Quantum Mechanics* Pergamon Press, Oxford (1965).

[3] M. Born and J. R. Oppenheimer: *Ann. Phys. (Leipzig)* **84** (1927) 457.

[4] D. R. Hartree: *Proc. Cambridge Phil. Soc.* **24** (1928) 328.

[5] V. A. Fock: *Ann. Phys. (Leipzig)* **61** (1930) 126.

[6] P. O. Lowdin: *Phys. Rev.* **97** (1955) 1474.

[7] C. C. J. Roothan: *Rev. Mod. Phys.* **32** (1960) 179.

[8] J. P. Lowe: *Quantum Chemistry* Academic Press, New York (1978).

[9] R. S. Mulliken: *J. Chem. Phys.* **3** (1935) 375.

[10] J. C. Slater: *Phys. Rev.* **36** (1930) 57.

[11] E. Hückel: *Z. Physik* **70** (1931) 204.

[12] E. Hückel: *Z. Physik* **72** (1931) 310.

[13] E. Hückel: *Z. Physik* **76** (1932) 628.

[14] R. Hoffmann: *J. Chem. Phys.* **39** (1963) 1397.

[15] C. J. Ballhausen and H. B. Gray: *Molecular Orbital Theory* Benjamin, New York (1965).

[16] M. Wolfsberg and L. Helmholtz: *J. Chem. Phys.* **20** (1952) 837.

[17] W. A. Yerranos: *J. Chem. Phys.* **44** (1966) 2207.

[18] R. G. Woolley: *Nouv. J. Chim.* **5** (1981) 219.

[19] R. S. Mulliken: *J. Chem. Phys.* **23** (1955) 1833, 1841, 2338, 2343.

[20] A. Streitweiser, J. E. Williams, S. Alexandratos and J. M. McKelvey: *J. Am. Chem. Soc.* **98** (1976) 4778.

[21] A. Streitweiser, C. M. Berke, G. W. Schriver, D. Grier and J. B. Collins: *Tetrahedron Suppl. No. 9* **37** (1981) 345.

[22] H. B. Börgi, J. H. Ammeter, J. C. Thibeault and R. Hoffmann: *J. Am. Chem. Soc.* **100** (1978) 3686.

[23] W. A. Herrmann, P. Kiprof, K. Rypdal, J. Tremmel, R. Blom, R. Alberto, J. Behm, R. A. Albach, H. Bock, B. Solouki, J. Mink, D. Lichtenberger and N. E. Gruhn: *J. Am. Chem. Soc.* **113** (1991) 6527.

[24] A. Guest, H. E. Howard-Lock and C. J. L. Lock: *J. Mol. Spectr.* **72** (1978) 143.

[25] J. L. Hencher, Q. Shen and D. G. Tuck: *J. Am. Chem. Soc.* **98** (1976) 899.

[26] R. Eisenberg: *Prog. Inorg. Chem.* **12** (1970) 295.

[27] H. P. Weber and R. F. Bryan: *J. Chem. Soc. (A)* (1967) 182.

APPENDIX TWO

RELATIVE PARTIAL PHOTOIONISATION CROSS SECTION DATA TABLES‡

A2.1 Rppics of bands A-D in the PE spectrum of [Mo(η-$C_6H_5Me)_2$]

hν (eV)	Band A	Band B	Band C	Band D
24.00	9085.993±134.353	33358.926±259.730	40385.262±292.110	30356.418±254.759
27.00	9990.053±132.654	32049.531±237.600	33448.383±244.644	24928.510±212.390
30.00	11907.494±146.256	27147.303±220.834	29146.150±228.819	22162.105±199.530
33.00	11153.487±127.416	21950.350±178.748	24438.572±188.607	17082.857±157.689
36.00	6362.627±90.927	14658.773±138.014	20251.553±162.220	13457.908±132.240
38.00	3233.246±59.605	11791.436±113.827	19985.064±148.189	14993.093±128.353
40.00	3973.023±67.431	13486.300±124.236	18516.039±145.571	15054.596±131.260
42.00	8099.897±99.123	20998.498±159.598	11324.161±117.202	22711.039±165.978
44.00	10628.097±111.705	24960.377±171.186	10228.192±109.583	19222.508±150.227
46.00	10563.431±110.134	25561.510±171.322	9179.074±102.664	17494.131±141.732
48.00	12687.003±124.794	28603.639±187.381	7837.911±98.087	18750.205±151.711
50.00	13851.367±123.311	28223.281±176.018	6490.189±84.408	17588.051±138.952
52.00	12775.526±113.122	25600.988±160.135	7484.221±86.583	15031.023±122.702
54.00	10444.258±97.480	21825.549±140.915	6596.023±77.467	13463.062±110.674
56.00	8642.252±87.421	17767.363±125.347	6558.285±76.155	11368.069±100.265
58.00	6974.313±63.522	14753.398±92.388	5824.638±58.050	9793.921±75.274
60.00	5713.021±49.517	12096.047±72.051	5324.015±47.801	8725.947±61.197
62.00	4837.785±100.030	10024.814±143.994	4995.799±101.651	8288.713±130.933
64.00	3904.656±87.295	8514.286±128.907	4748.365±96.266	7475.951±120.791
66.00	3366.428±65.452	7300.248±96.384	4705.994±77.386	7051.546±94.728
68.00	2678.428±59.628	6275.315±91.270	4372.915±76.190	6183.972±90.603
70.00	2252.052±52.284	5323.754±80.388	3825.236±68.141	5715.939±83.296
73.00	1695.084±46.626	4609.068±76.884	3351.174±65.558	5310.826±82.530
76.00	1326.128±37.691	4013.628±65.572	3610.917±62.195	5015.687±73.302
80.00	847.777±29.799	2548.254±51.663	2714.830±53.325	3926.869±64.133
85.00	541.238±19.750	1802.682±36.044	2085.946±38.773	2992.275±46.438
90.00	418.196±16.187	1369.957±29.298	1818.926±33.759	2411.646±38.872
95.00	278.691±15.233	979.902±28.565	1600.528±36.507	2152.661±42.338
100.00	272.964±17.814	974.039±33.650	1510.484±41.905	2075.824±49.125

‡ Error values are statistical errors associated with band area measurements (see Chapter 6.2.3)

A2.2 Rppics of bands A-D in the PE spectrum of [Mo(η-C_7H_7)(η-C_5H_5)]

hν (eV)	Band A	Band B	Band C	Band D
21.00	14750.856±260.867	62656.656±553.140	89030.914±790.797	121931.313±695.949
24.00	13290.790±303.422	47448.586±583.822	72860.258±739.681	55580.652±663.388
27.00	14992.031±324.028	39833.559±528.174	53466.941±611.921	42928.598±557.994
28.50	15500.162±359.604	32826.547±523.322	43904.137±605.215	33201.949±526.306
30.00	16812.666±350.935	33861.984±498.040	40683.141±545.903	31082.113±477.160
31.50	15036.388±313.619	30423.389±446.102	35642.012±482.849	27866.406±426.944
33.00	11676.214±273.943	25142.377±401.987	31223.760±447.973	26321.730±411.307
34.00	10053.305±240.712	23622.289±368.981	30478.531±419.122	23737.570±369.881
36.00	5491.247±122.880	17219.197±217.597	24365.463±258.841	20391.570±236.795
38.00	4357.469±102.890	16981.258±203.114	24876.355±245.838	23553.238±239.211
40.00	5060.490±119.620	17777.094±224.200	21553.012±246.865	22811.006±253.967
42.00	10323.893±218.694	25098.871±340.991	21439.527±315.154	23035.408±326.673
44.00	14046.542±307.747	29513.109±446.084	20633.207±372.985	21565.051±381.315
46.00	15489.443±324.362	32651.758±470.939	20304.594±371.372	21416.449±381.404
48.00	16445.205±329.273	31934.494±458.846	17848.893±343.039	18755.971±351.646
50.00	19099.289±389.392	35163.566±528.354	18073.590±378.792	19478.041±393.235
52.00	14980.104±207.651	28921.145±288.526	15784.918±213.156	14621.688±205.151
54.00	14251.900±285.272	25796.045±383.795	15319.115±295.760	14299.309±285.746
56.00	10714.808±155.343	20289.676±213.764	13087.204±171.681	11923.689±163.871
58.00	9341.124±118.153	18419.631±165.916	13720.885±143.198	10990.303±128.159
60.00	7903.599±120.048	15947.604±170.526	11939.354±147.548	10958.534±141.357
65.00	5382.318±170.119	12356.160±257.756	10531.241±237.961	9070.876±220.847
70.00	2916.705±121.815	8471.706±207.605	8369.983±206.355	7319.394±192.970
75.00	2072.489±107.295	6909.668±195.914	7337.313±201.884	6392.464±188.438
80.00	1231.871±76.708	4778.971±151.087	6006.611±169.385	4994.399±154.454

A2.3 RPPICS of bands A-D in the PE spectrum of [Nb(η-C_7H_7)(η-C_5H_5)]

hν (eV)	Band A	Band B	Band C	Band D
21.00	3116.718±72.298	22711.277±199.073	31920.152±243.406	37916.648±272.471
24.00	2179.040±50.941	14020.406±131.214	19153.051±157.701	22536.553±175.222
27.00	2464.631±54.650	11570.676±118.410	14825.612±134.034	16082.813±142.121
30.00	1456.383±38.493	7961.690±90.001	10501.146±103.363	9664.040±99.158
33.00	783.322±26.968	6068.920±75.063	7668.359±84.377	7806.833±85.135
36.00	968.319±28.505	6786.309±75.460	7518.138±79.425	8818.342±86.019
38.00	1696.375±33.281	8576.778±74.834	7709.354±70.949	9462.336±78.602
40.00	2583.401±45.244	11358.216±94.869	7789.973±78.566	10094.790±89.437
42.00	2774.757±44.883	10526.087±87.417	6392.583±68.125	8157.769±76.958
44.00	3029.604±45.325	10588.984±84.735	5407.885±60.556	7091.921±69.346
46.00	3170.698±51.308	10233.814±92.178	5211.165±65.777	6247.689±72.022
48.00	2412.913±38.317	8297.624±71.057	4203.063±50.572	4978.457±55.039
50.00	1922.008±36.063	7039.224±69.015	3811.348±50.783	4431.790±54.761
52.00	1797.137±34.709	6785.703±67.444	3842.713±50.753	4348.499±53.990
54.00	1446.903±29.856	5882.007±60.197	3624.843±47.256	3989.150±49.573
56.00	915.724±21.914	4015.146±45.887	2721.502±37.779	2985.218±39.566
58.00	902.594±18.086	3954.905±37.859	3029.722±33.136	3101.710±33.528
60.00	636.147±13.979	3190.224±31.306	2640.432±28.481	2637.660±28.466
62.50	485.433±21.497	2675.063±50.467	2409.750±47.899	2257.065±46.357
65.00	397.685±17.849	2367.679±43.551	2109.091±41.104	2270.831±42.651
70.00	198.314±11.655	1677.241±33.898	1678.707±33.913	1751.471±34.640
75.00	175.715±10.666	1337.656±29.426	1488.384±31.040	1458.113±30.722
77.50	122.851±8.208	1026.604±23.726	1301.299±26.713	1347.390±27.181
80.00	88.675±7.346	855.497±22.813	1106.413±25.943	1131.971±26.241

A2.4 Rppics of bands A-D in the PE spectrum of [Ta(η-C_7H_7)(η-C_5H_4Me)]

hν (eV)	Band A	Band B	Band C	Band D
20.00	2090.493±78.901	14509.938±220.619	27898.867±326.012	40766.414±416.214
22.00	2150.445±69.514	14946.473±189.114	25837.773±262.775	25490.445±273.478
24.00	1977.243±67.979	13744.244±179.230	22651.676±235.155	23017.869±246.911
26.00	1692.175±57.206	10878.626±145.046	16613.592±179.246	15607.212±173.818
28.00	2234.818±62.295	11722.617±142.673	15437.895±163.728	14634.278±159.410
30.00	2202.143±61.123	11135.441±137.448	13847.268±153.274	12278.474±144.331
32.00	1429.320±42.112	8005.695±99.665	10967.441±116.652	8940.884±105.325
34.00	1063.403±34.109	7377.623±89.841	9489.064±101.889	8721.662±97.682
36.00	775.965±26.678	6188.972±75.341	8104.970±86.219	7507.518±82.980
38.00	907.432±29.772	5951.718±76.246	7398.658±85.011	7308.306±84.490
40.00	1603.313±42.774	7657.471±93.478	6925.995±88.902	7034.246±89.594
42.00	1322.447±35.651	6823.994±80.984	5944.115±75.582	6081.687±76.452
44.00	998.293±30.986	5391.255±72.008	4827.535±68.139	4881.079±68.516
46.00	1113.813±26.763	5515.525±59.557	4773.112±55.404	5317.793±58.480
48.00	1483.672±30.110	6473.103±62.893	4522.397±52.569	4834.461±54.353
50.00	2032.697±41.329	7451.917±79.132	4426.311±60.987	4491.708±61.436
52.50	1551.083±31.694	5893.467±61.780	3655.628±48.657	3391.432±46.866
55.00	1194.832±25.268	4712.273±50.181	3281.434±41.875	2786.619±38.589
57.50	898.246±21.032	3696.448±42.666	2724.630±36.631	2431.254±34.602
60.00	738.461±16.959	2937.908±33.828	2422.511±30.717	2081.910±28.476
62.50	596.335±13.268	2604.926±27.731	2223.985±25.624	1686.973±22.317
65.00	491.890±11.052	2271.630±23.750	2077.970±22.715	1582.483±19.822
67.50	439.035±11.408	2037.387±24.575	1714.775±22.546	1446.121±20.705
70.00	376.003±10.181	1842.881±22.540	1594.602±20.967	1434.415±19.886
75.00	275.598±8.890	1398.363±20.026	1292.190±19.250	1120.416±17.925
80.00	210.297±6.627	1161.855±15.577	1067.841±14.933	1044.470±14.769
85.00	176.970±5.627	893.601±12.645	871.981±12.491	863.309±12.428
90.00	148.442±4.515	732.592±10.029	735.847±10.052	752.884±10.167
95.00	120.226±3.868	610.753±8.718	674.187±9.160	696.187±9.308

A2.5 RPPICS of bands A-C in the PE spectrum of [Ti(η-C_7H_7)(η-C_5H_5)]

hν (eV)	Band A	Band B	Band C
20.00	63272.441±545.740	100138.391±717.782	131012.063±851.622
22.00	51763.957±446.743	77884.453±559.673	102821.656±664.643
24.00	48093.754±408.429	64795.328±474.071	70637.961±497.854
26.00	42270.355±345.900	58829.129±408.065	61053.355±415.707
28.00	35103.000±322.470	47543.926±375.288	44151.449±361.651
30.00	33349.457±306.633	42650.445±346.765	43886.434±351.754
32.00	29621.033±270.089	36276.566±298.896	33415.617±286.868
34.00	24172.221±244.241	33255.180±286.477	32590.330±283.599
36.00	24025.002±254.854	27750.375±273.901	29993.670±284.757
38.00	25094.311±275.449	26871.252±285.035	28418.654±293.127
40.00	29063.238±275.983	27839.293±270.109	29970.770±280.259
42.00	37794.867±353.288	30884.713±319.363	32946.715±329.852
44.00	52846.559±419.407	31569.479±324.161	34555.523±339.145
46.00	71973.602±533.477	35045.297±372.258	37657.852±385.884
48.00	74952.898±494.593	32525.107±325.809	34327.273±334.713
50.00	72678.766±497.615	33016.844±335.396	30383.490±321.743
52.00	56496.605±402.146	30640.799±296.158	29386.178±290.031
54.00	43284.582±311.120	25318.945±237.949	27100.070±246.176
56.00	33120.816±274.818	20518.535±216.306	21688.766±222.389
58.00	24497.941±197.649	16673.371±163.057	16542.379±162.416
60.00	19774.283±163.291	13514.110±134.991	13500.530±134.924
62.50	19627.146±188.908	13487.023±156.595	9332.499±130.263
65.00	18472.123±175.680	11898.172±140.995	9127.399±123.491
67.50	18508.822±173.058	12663.098±143.143	9120.346±121.480
70.00	17813.137±167.916	12387.498±140.028	9397.835±121.965
72.50	16971.018±156.458	12023.010±131.689	8707.944±112.073
75.00	16396.848±155.529	10802.139±126.237	9165.898±116.283
77.50	15773.693±149.427	9985.228±118.889	8022.336±106.565
80.00	15696.018±143.513	9427.006±111.220	8392.975±104.943

A2.6 Rppics of bands A-F in the PE spectrum of PF_3

hν (eV)	Band A	Band B	Band C
30.00	2767.526±80.847	24702.186±249.375	11668.187±174.849
33.00	2865.798±75.555	22964.359±213.877	10475.338±145.895
36.00	2603.049±67.999	21195.256±194.038	8723.216±124.482
39.00	2409.903±68.818	19481.070±195.662	7599.489±122.206
42.00	2297.751±62.238	17650.439±172.499	6824.828±107.264
45.00	2018.869±53.224	14643.544±143.344	5979.730±91.600
48.00	1860.407±49.654	13459.142±133.556	6169.999±90.427
50.00	2296.013±75.140	13115.975±179.592	6302.887±124.496
55.00	2284.117±71.126	12126.007±163.880	6890.474±123.536
60.00	1778.721±59.245	9839.482±139.342	6440.266±112.732
65.00	1029.623±39.138	6701.442±99.849	5054.395±86.715
70.00	844.306±36.113	4807.722±86.174	3543.966±73.987
72.50	568.991±24.331	3537.566±60.667	2687.772±52.881
75.00	394.497±18.265	2931.668±49.791	2115.890±42.300
77.50	306.218±12.455	2097.355±32.594	1451.497±27.115
80.00	241.951±8.924	1508.339±22.282	997.717±18.122
82.50	192.032±7.023	1319.215±18.407	761.333±13.983
85.00	129.529±5.676	1103.081±16.563	604.945±12.266
87.50	115.392±4.684	829.999±12.562	516.627±9.911
90.00	87.819±3.624	664.680±9.971	413.198±7.862
95.00	43.019±1.869	394.360±5.657	231.926±4.338

A2.6 Rppics of bands A-F in the PE spectrum of PF_3 (continued)

hν (eV)	Band D	Band E	Band F
30.00	5003.037±116.678	12659.345±187.974	3258.454±99.740
33.00	5117.643±103.761	11138.756±154.871	3526.394±90.773
36.00	4044.783±84.764	9431.424±129.436	3552.885±82.316
39.00	3974.345±88.376	8596.457±129.975	3363.777±81.304
42.00	3438.905±76.141	8022.189±116.293	3863.440±80.704
45.00	3189.010±66.894	6859.528±98.107	3205.990±67.072
48.00	3584.124±68.920	6970.963±96.118	3023.658±63.303
50.00	3169.510±88.284	6731.737±128.662	2712.888±81.678
55.00	3533.751±88.468	6515.017±120.122	2238.534±70.413
60.00	2965.873±76.502	6400.985±112.388	2294.562±67.289
65.00	2412.341±59.907	5095.571±87.068	1910.793±53.317
70.00	1304.563±44.889	3456.241±73.066	1209.112±43.216
72.50	918.033±30.905	2698.915±52.990	929.307±31.095
75.00	529.219±21.155	2381.392±44.875	774.094±25.585
77.50	524.681±16.303	1588.938±28.370	579.491±17.133
80.00	270.409±9.434	1075.921±18.819	342.843±10.623
82.50	320.452±9.072	796.238±14.300	265.757±8.262
85.00	261.220±8.060	717.973±13.362	239.184±7.713
87.50	256.083±6.978	525.245±9.993	198.742±6.147
90.00	150.665±4.748	409.012±7.822	150.909±4.751
95.00	54.885±2.110	273.102±4.707	93.744±2.758

A2.7 Rppics of bands A-E in the PE spectrum of OsO_4

hv (eV)	Band A	Band B	Band C
24.00	80670.813±779.506	44668.633±586.270	25736.184±447.853
27.00	73212.578±738.862	46580.656±595.142	25199.453±440.297
30.00	54856.324±615.897	45111.773±558.521	24053.650±407.835
33.00	50858.750±628.907	53108.566±642.667	26552.711±454.421
36.00	45851.488±562.864	44512.391±554.584	23936.961±406.688
39.00	41864.535±451.929	37154.301±425.747	19917.328±311.719
42.00	36785.625±388.214	29563.438±348.024	16218.278±257.771
45.00	31399.162±280.067	23556.367±242.581	12558.060±177.118
48.00	29134.412±245.042	19052.674±198.159	11005.186±150.603
50.00	29903.816±250.741	18853.840±199.096	10751.412±150.347
52.50	32050.389±501.222	17600.314±371.427	9800.335±277.162
55.00	30467.279±468.019	16070.460±339.907	8625.162±249.018
57.50	25552.475±376.599	13943.206±278.192	5978.884±182.168
60.00	25874.576±427.641	12357.369±295.533	6633.126±216.522
62.00	23609.262±370.883	11536.057±259.254	5202.883±174.108
64.00	23835.252±369.786	11655.776±258.590	5541.919±178.308
66.00	23983.428±350.461	11552.827±243.236	5801.216±172.362
67.50	22228.186±337.209	10604.590±232.913	4600.426±153.407
70.00	19076.018±232.021	10072.820±168.601	3260.915±95.930
72.50	17975.490±189.057	9321.622±136.144	2425.430±69.446
75.00	15925.636±172.248	8674.323±127.123	2566.111±69.143
77.50	14941.771±163.223	8177.153±120.748	2178.854±62.329
80.00	15243.273±170.345	9482.342±134.353	2677.085±71.388
82.50	13210.309±186.688	7793.169±143.389	2177.635±75.797
85.00	12953.993±189.580	7868.107±147.749	2219.300±78.469
87.50	12003.090±183.717	7337.516±143.641	2157.625±77.892
90.00	11018.791±187.433	6626.268±145.350	2176.311±83.299
92.50	10567.001±182.293	6924.437±147.566	2087.148±81.015
95.00	11117.878±185.760	7731.704±154.910	2183.488±82.323
97.50	10286.047±172.981	7387.531±146.597	2226.301±80.476
100.00	9939.963±164.381	6825.151±136.212	2250.570±78.217
102.50	9465.370±158.336	6755.567±133.764	2171.356±75.836
105.00	8981.922±140.749	6772.386±122.217	2120.866±68.394
110.00	7584.077±123.260	6098.055±110.527	1747.082±59.160
115.00	7055.841±109.802	5378.082±95.863	1660.561±53.268

A2.7 Rppics of bands A-E in the PE spectrum of OsO_4 (continued)

hv (eV)	Band D	Band E
24.00	11005.991±298.004	74595.523±802.632
27.00	11261.994±299.052	82466.664±834.620
30.00	10320.023±270.681	77268.961±761.927
33.00	11215.872±295.339	76988.672±774.055
36.00	10861.222±273.947	77632.953±732.403
39.00	11233.910±234.106	67861.555±575.385
42.00	10830.399±210.647	53810.160±469.531
45.00	10966.867±165.518	38755.219±311.149
48.00	11859.296±156.339	29921.072±248.328
50.00	14532.297±174.795	31192.846±256.088
52.50	13694.405±327.630	43535.160±584.162
55.00	10107.568±269.569	45086.168±569.335
57.50	9714.298±232.203	24594.947±369.475
60.00	7901.830±236.323	33547.332±486.935
62.00	7540.979±209.609	30844.957±423.924
64.00	7758.053±210.968	36363.027±456.741
66.00	6458.323±181.863	39101.063±447.485
67.50	5647.608±169.973	35595.703±426.723
70.00	4367.693±111.022	25704.467±269.332
72.50	3977.396±88.931	21457.936±206.559
75.00	3273.829±78.097	19518.598±190.691
77.50	3072.308±74.013	17473.672±176.511
80.00	3358.401±79.957	17942.039±184.810
82.50	2953.797±88.277	14597.541±196.245
85.00	2948.165±90.441	14712.988±202.041
87.50	2858.648±89.657	13283.651±193.269
90.00	2865.035±95.576	11650.081±192.728
92.50	2643.480±91.176	10692.149±183.369
95.00	2916.284±95.139	11210.646±186.533
97.50	2832.233±90.769	10644.201±175.967
100.00	2688.277±85.487	9392.183±159.787
102.50	2921.717±87.969	9264.863±156.650
105.00	2569.017±75.273	8407.623±136.175
110.00	2245.126±67.065	7458.273±122.234
115.00	2002.151±58.491	6366.752±104.303

A2.8 Rppics of bands A-E in the PE spectrum of $TiCl_4$

hν (eV)	Band A	Band B	Band (C+D)	Band E
17.00	58396.375±349.653	54414.574±362.362	149590.055±893.359	16906.090±223.823
18.00	48671.203±335.111	50942.402±364.850	120754.062±829.448	14836.000±214.986
19.00	45617.031±334.916	49244.957±367.788	103724.398±784.055	12451.821±199.713
20.00	39369.238±320.078	48217.973±372.339	93494.426±757.581	14558.025±219.044
21.00	39192.457±336.932	46836.695±385.421	81051.586±739.123	13313.906±218.505
24.00	28533.068±210.311	30168.355±224.112	54768.835±436.127	10935.669±141.450
25.00	27208.297±180.112	28330.934±190.018	49122.469±360.774	11583.053±126.940
26.00	20971.654±134.742	23138.238±146.024	39036.613±272.988	10222.999±101.111
27.00	20440.723±145.270	21594.863±153.773	36748.051±288.349	10178.532±109.695
28.00	18189.160±135.073	19446.193±143.599	33105.410±268.188	9109.841±101.893
30.00	12158.378±97.209	12600.922±101.470	22544.139±194.507	5816.593±71.199
32.00	7580.958±62.262	7630.893±63.205	14154.700±122.506	3496.516±44.051
34.00	4810.288±46.167	4432.597±44.317	13220.138±129.728	2181.628±30.343
36.00	3320.048±34.238	3054.944±32.842	11559.380±136.288	1742.028±24.800
38.00	2170.561±25.095	2234.138±25.460	12479.221±73.812	1559.854±21.274
40.00	1954.943±16.672	3849.164±23.394	15011.327±88.059	3137.161±21.120
41.50	1871.389±38.312	3006.863±48.563	12487.652±139.019	3106.927±49.364
43.00	1813.941±40.102	2712.627±49.040	15660.653±166.371	2144.558±43.604
46.00	1772.581±41.319	3210.438±55.608	16745.298±177.680	1925.742±43.068
49.00	2053.042±47.503	3651.316±63.350	17926.333±198.078	1893.342±45.618
52.00	3012.094±49.194	3989.913±56.618	16600.711±163.098	2038.015±40.465
55.00	3371.785±47.319	3955.559±51.252	13913.418±135.818	1672.312±33.324
58.00	3261.020±43.256	4079.600±48.382	10614.045±110.209	1372.890±28.067
62.00	3265.999±37.155	3658.824±39.326	8371.013±83.25	1065.944±21.226
64.00	3502.358±37.363	3745.063±38.635	7655.944±77.688	1024.539±20.208
66.00	3213.651±33.161	3223.563±33.213	7495.832±67.534	877.806±17.331
69.00	2342.858±23.371	2494.293±24.114	4573.745±46.028	657.423±12.380

A2.9 RPPICS of bands A-F in the PE spectrum of $TiBr_4$

hν (eV)	Band A	Band B	Band C
20.00	83519.258±762.506	49932.680±595.285	153853.531±1073.413
22.00	70051.766±673.942	37298.570±495.976	97520.992±821.211
24.00	66514.102±724.935	34899.664±529.141	102375.531±925.670
26.00	45839.598±461.690	22811.893±327.959	74835.109±605.487
28.00	40266.066±388.686	18923.336±268.151	54052.004±461.180
30.00	28161.424±290.932	13022.002±197.835	36849.301±334.669
32.00	21768.801±235.576	11005.493±167.501	31152.428±281.812
34.00	16510.094±202.221	8975.189±149.099	22592.539±236.556
36.00	13790.113±184.945	6959.931±131.390	17715.004±209.618
38.00	11047.384±185.465	5380.580±129.433	13500.278±205.023
40.00	8351.500±149.334	4539.444±110.098	12616.794±183.549
42.00	7234.226±150.520	4129.655±113.725	11332.146±188.388
44.00	5829.445±132.242	3180.254±97.676	12962.915±197.199
46.00	4501.566±111.967	2567.911±84.565	12379.518±185.677
48.00	4980.420±65.534	2386.190±45.361	13444.879±107.674
50.00	4242.184±61.078	2165.108±43.634	12618.533±105.340
55.00	2937.393±79.651	1296.402±52.917	9621.902±144.159
60.00	1884.033±50.235	830.753±33.358	5684.937±87.260

A2.9 RPPICS of bands A-F in the PE spectrum of $TiBr_4$ (continued)

hν (eV)	Band D	Band E	Band F
20.00	109618.125±917.026	235512.156±1362.216	46045.555±617.020
22.00	96529.742±825.695	174316.094±1122.605	39930.750±548.677
24.00	74035.266±794.619	151929.516±1150.173	43209.652±624.870
26.00	49984.984±499.057	81837.984±644.551	33033.344±416.373
28.00	48888.180±441.992	65172.457±514.664	30143.885±355.338
30.00	30470.320±306.486	43097.445±367.341	18266.520±242.472
32.00	18619.898±217.873	35728.773±301.803	14220.227±190.400
34.00	16492.004±202.110	23455.270±241.031	9696.729±154.976
36.00	11978.951±172.372	19054.428±217.398	7750.895±138.654
38.00	9880.038±175.392	17672.816±234.577	6951.717±147.122
40.00	9937.394±162.897	20835.336±235.873	5832.968±124.803
42.00	9895.271±176.040	20543.188±253.649	3980.861±111.657
44.00	8358.729±158.353	20347.010±247.062	2923.120±93.644
46.00	6793.482±137.547	20865.615±241.058	3376.666±96.972
48.00	7280.136±79.232	27372.729±153.635	2907.073±50.068
50.00	6309.648±74.489	25273.684±149.081	2753.567±49.208
55.00	3647.162±88.755	13996.696±173.870	1930.899±64.579
60.00	2239.941±54.775	10794.373±120.241	940.888±35.499

A2.10 RPPICS of bands A-G in the PE spectrum of $ZrBr_4$

hν (eV)	Band A	Band B	Band C	Band D
20.00	15284.176±148.796	6779.011±99.886	28641.842±208.504	5162.634±89.547
22.00	11252.448±116.665	4991.053±78.262	19723.885±157.744	4430.859±75.531
24.00	8927.137±86.703	3880.382±57.534	13952.980±110.487	3066.552±52.282
26.00	6476.987±56.562	2461.271±35.078	9099.313±68.232	2337.953±34.872
28.00	5344.313±59.614	2121.046±37.803	6887.520±68.842	2065.872±37.988
30.00	4352.957±42.364	1498.413±24.856	4905.844±44.975	1469.782±24.721
32.00	3212.157±33.697	1093.112±19.656	3696.857±36.143	1178.308±20.405
34.00	2848.760±32.408	941.713±18.624	3486.243±35.856	1328.896±22.127
36.00	2341.851±26.589	934.669±16.791	3029.231±30.248	1194.286±18.991
38.00	1949.507±25.359	658.855±14.728	2449.550±28.427	994.328±18.112
40.00	1402.502±13.942	492.292±7.821	1960.208±16.560	768.977±10.396
42.00	960.072±9.952	475.095±7.000	1602.429±12.855	699.343±8.491
44.00	620.672±6.930	420.544±5.703	1085.608±3.995	412.902±5.646
46.00	539.870±4.874	205.730±3.003	835.995±6.067	352.288±3.940
48.00	405.711±3.181	134.506±1.828	638.068±3.995	231.951±2.399
50.00	277.418±3.244	118.546±1.951	521.205±4.450	118.241±1.904
53.00	245.225±2.668	136.244±1.987	409.018±3.449	148.092±2.074
55.00	180.233±2.153	84.201±1.471	333.484±2.929	114.367±1.712
57.00	199.006±2.655	102.468±1.897	366.718±3.596	141.533±2.231
60.00	154.974±2.100	78.262±1.495	245.887±2.643	73.921±1.454
70.00	104.878±2.210	78.622±1.914	154.125±2.699	52.511±1.562
75.00	106.449±2.259	62.005±1.732	150.677±2.687	36.336±1.314
80.00	61.749±1.220	93.307±1.513	198.015±2.211	92.704±1.502

A2.10 RPPICS of bands A-G in the PE spectrum of $ZrBr_4$ (continued)

hν (eV)	Band E	Band F	Band G
20.00	27305.156±207.800	12116.967±139.773	6396.197±102.262
22.00	19707.820±160.602	7814.683±102.015	6324.670±92.610
24.00	15029.452±116.595	5466.526±70.868	6184.234±70.005
26.00	9805.407±71.913	2993.858±40.014	4545.056±49.685
28.00	7674.112±73.693	2066.893±38.484	3510.941±50.510
30.00	6154.335±50.894	1646.424±26.489	2766.814±34.545
32.00	5582.328±44.421	1344.365±21.797	2361.836±28.885
34.00	8324.693±55.407	2682.854±31.449	2469.090±30.177
36.00	6967.613±45.873	2306.532±26.391	1640.047±22.158
38.00	4653.108±39.189	1273.957±20.490	1041.371±18.533
40.00	4130.725±24.681	1412.233±14.410	812.812±9.462
42.00	3228.041±18.250	1025.740±10.280	1017.612±10.241
44.00	2181.405±13.003	669.249±7.201	713.823±7.432
46.00	1582.800±8.354	538.924±4.869	390.733±4.146
48.00	1151.871±5.365	377.591±1.757	255.682±1.731
50.00	847.015±5.683	324.897±3.474	175.536±2.697
53.00	700.135±4.511	270.348±2.800	130.678±1.939
55.00	582.974±3.870	224.652±2.400	101.913±1.607
57.00	547.317±4.401	180.666±2.521	77.913±1.607
60.00	356.211±3.190	130.168±1.928	88.122±1.586
70.00	203.180±3.099	90.142±2.063	52.751±1.558
75.00	141.268±2.608	72.368±1.861	46.049±1.491
80.00	192.354±2.176	80.941±1.397	54.402±1.151

A2.11 Rppics of bands A-F in the PE spectrum of $[Fe_2(CO)_6S_2C_2(CF_3)_2]$¶

hν (eV)	Band A	Band B	Band C	Band D	Band E	Band F
24.00	14356.547	2647.140	14077.880	16307.357	15485.460	47940.797
26.00	11746.328	3469.164	8673.186	11593.100	7944.147	33141.797
28.00	10023.122	1609.354	6456.533	7153.315	5470.236	20779.242
30.00	10292.983	653.322	5661.782	5104.740	4465.790	15706.139
33.00	12834.547	980.166	5183.642	4813.914	2990.051	15699.811
36.00	15376.795	696.362	5364.548	4304.107	3364.316	15093.051
42.00	18303.205	937.130	3017.075	2155.449	2183.676	10571.855
45.00	14678.907	817.626	2735.443	1788.028	2015.705	8255.274
48.00	14919.368	557.009	2516.347	1258.766	1683.460	5763.237
51.00	13811.318	320.099	2581.874	1259.526	1556.951	4734.614
54.00	11343.626	363.298	1820.551	820.451	1296.283	3937.875
56.00	10657.188	285.442	2019.667	993.498	1322.835	3918.312
58.00	9667.900	254.233	1854.017	935.927	1214.259	3340.524
60.00	13765.697	421.269	2171.210	1132.823	1460.515	3748.239
62.00	15460.173	256.853	2250.290	1086.767	1331.987	3248.826
64.00	15641.568	146.069	2204.172	1085.880	1348.855	3305.938
66.00	14616.534	339.003	2055.248	927.367	1383.209	3119.391
68.00	15761.930	176.280	2062.393	931.048	1225.445	3042.871
71.00	14235.583	266.636	2101.243	869.721	1237.392	2878.089
74.00	13615.682	107.868	1872.443	852.462	1134.558	2488.053
77.00	12131.450	151.849	1588.881	742.189	1125.724	2184.485
80.00	11275.170	179.284	1497.584	627.732	1046.940	1847.588

¶ Statistical errors not available